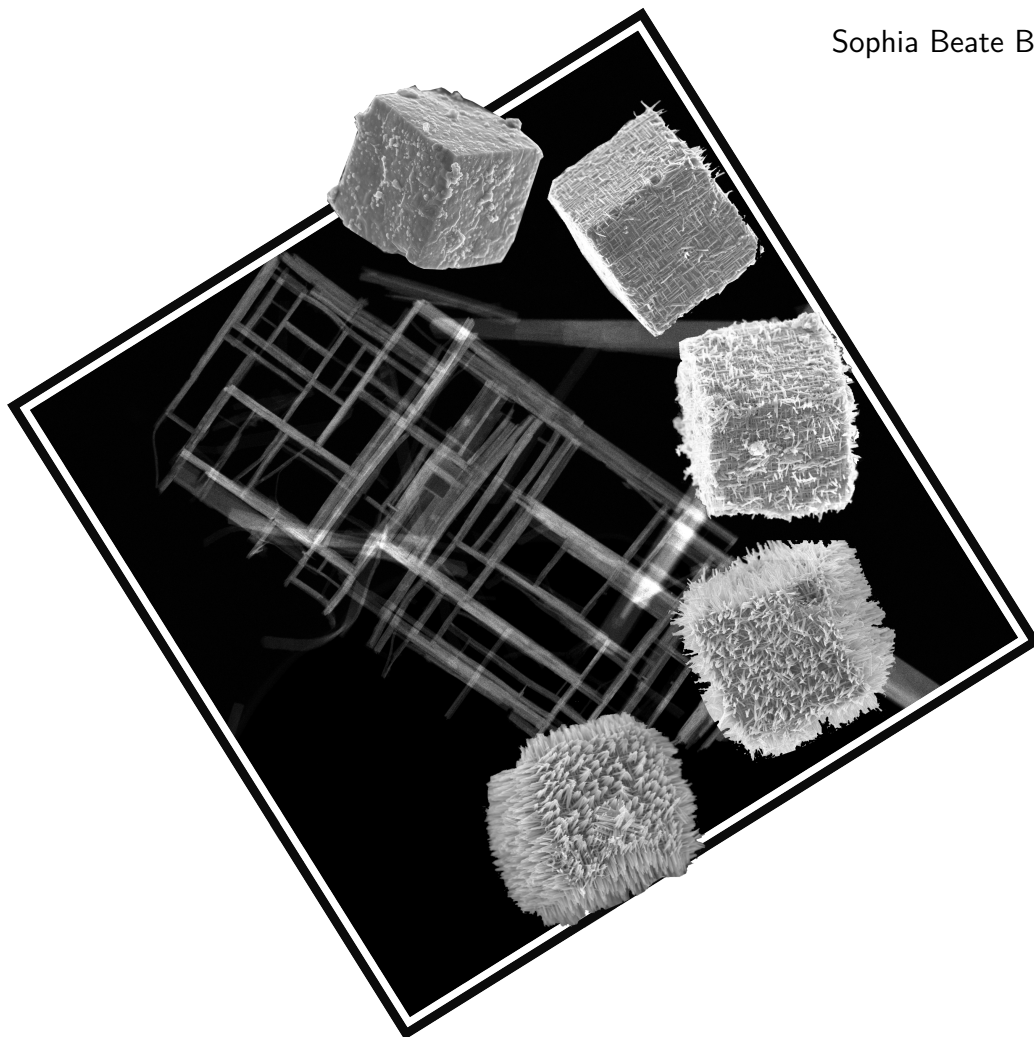




3D Hierarchical $\text{Nb}_3\text{O}_7(\text{OH})$ Superstructures:

Synthesis, Structural Characterization and
Photophysical Properties

Sophia Beate Betzler



München 2015

Dissertation zur Erlangung des Doktorgrades
der Fakultät für Chemie und Pharmazie
der Ludwig-Maximilians-Universität München

3D Hierarchical Nb₃O₇(OH) Superstructures:

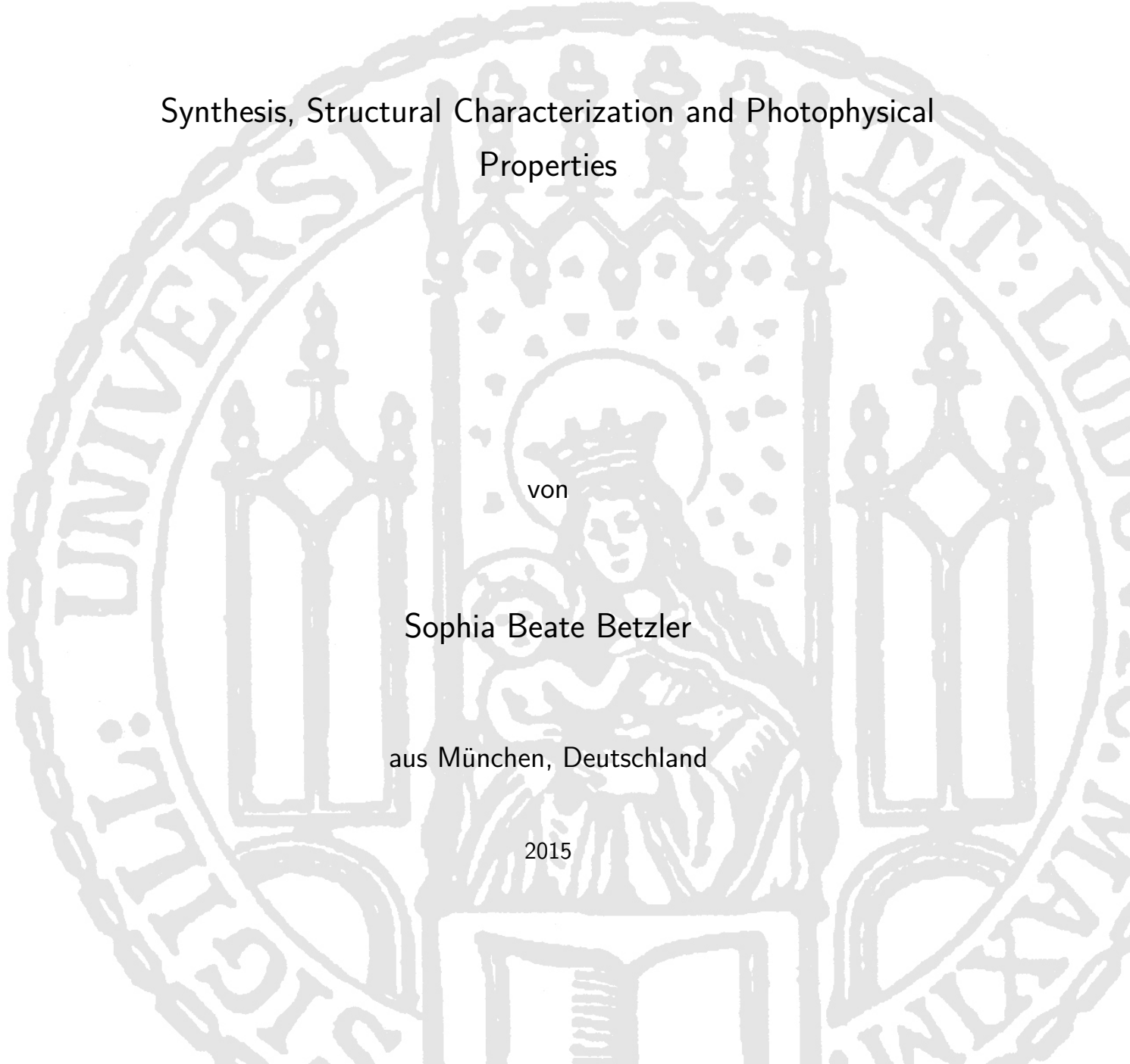
Synthesis, Structural Characterization and Photophysical
Properties

von

Sophia Beate Betzler

aus München, Deutschland

2015



Erklärung

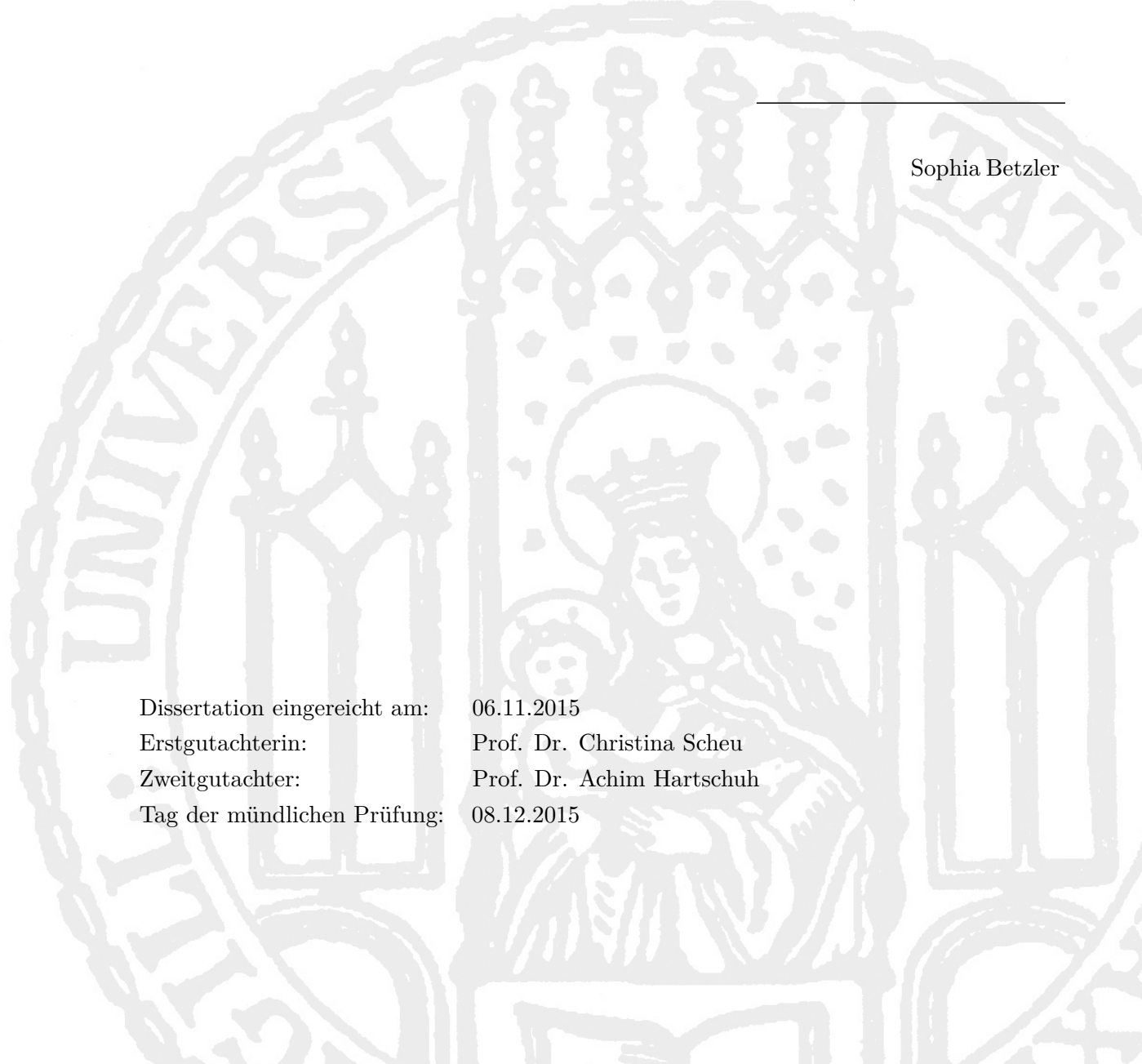
Diese Dissertation wurde im Sinne von § 7 der Promotionsordnung vom 28. November 2011 von Frau Prof. Dr. Christina Scheu betreut.

Eidesstattliche Versicherung

Diese Dissertation wurde eigenständig und ohne unerlaubte Hilfe erarbeitet.

München, den

Sophia Betzler



Dissertation eingereicht am: 06.11.2015
Erstgutachterin: Prof. Dr. Christina Scheu
Zweitgutachter: Prof. Dr. Achim Hartschuh
Tag der mündlichen Prüfung: 08.12.2015

Global warming caused by continuous emission of greenhouse gases is omnipresent. Anthropogenic CO₂ resulting from the combustion of fossil fuels adds the largest mass to the scales. Therefore, new technologies for power generation and energy storage are required. This study focuses on the synthesis and characterization of novel materials to be used as photoelectrode in dye-sensitized solar cells or as photocatalyst for water splitting. Hydrothermal conditions feature the formation of 3D hierarchical Nb₃O₇(OH) superstructures which are composed of highly-ordered nanowire networks. Despite their complexity these superstructures form self-organized starting from amorphous hollow cubes. Advanced transmission electron microscopy is applied for the characterization of the crystallographic structure, atomic arrangement and bonding characteristics of the nanostructures. 3D reconstruction of the nanowire arrangement, based on a combination of local thickness measurements and electron tomography, indicates suitable charge transport paths. The stabilization of the superstructures is based on the nanowire junctions. Even though no complete interpenetration of the nanowires was observed these networks exhibit a very high thermal stability. The morphology remains stable for temperatures up to 850 °C despite of the phase transformation of Nb₃O₇(OH) to H-Nb₂O₅. This phase transformation was investigated in detail with ex situ and in situ experiments yielding a good understanding of the impact of temperature, atmospheric condition and electron beam on the crystal structure. The morphological and photophysical properties of the nanostructures determine their performance in functional devices and promising hydrogen production rates are observed for the superstructures. These rates can be further enhanced by the incorporation of titanium into the crystal lattice. The capacity of the Nb₃O₇(OH) crystal lattice to incorporate titanium is limited to about 12 at% and the formation of anatase TiO₂ plates is observed for titanium excess. The presence of titanium in the crystal lattice has two main effects. It slows down the crystallization of Nb₃O₇(OH) leading to superstructures composed of smaller nanocrystals and furthermore it reduces the surface defects resulting in lower charge recombination rates. Therefore, the hydrogen production rate of titanium doped (5.5 at% Ti) superstructures was by a factor of two higher than the one observed for undoped Nb₃O₇(OH).

Contents

Abstract	I
List of Figures	V
List of Tables	VII
Abbreviations	VIII
Symbols	X
1 Introduction	1
1.1 Aim of the Thesis	2
1.2 Outline of the Thesis	3
1.3 References	4
2 Materials and Synthesis Procedure	6
2.1 Metal Oxides for Photochemistry	6
2.2 Titanium Oxide	6
2.3 Niobium Oxide	7
2.4 Solvothermal Synthesis Strategy	8
2.4.1 Synthesis of Nb ₃ O ₇ (OH) Nanostructures	9
2.4.2 Doping with Titanium	9
2.5 References	10
3 Analytical Techniques	13
3.1 Electron-Matter Interaction	13
3.2 Electron Microscopy – Imaging and Diffraction	14
3.2.1 Transmission Electron Microscopy	14
3.2.1.1 Setup of a Transmission Electron Microscope	14
3.2.1.2 Diffraction and Bright/Dark Field Imaging	15
3.2.1.3 High Resolution TEM	16
3.2.1.4 In Situ TEM Heating Experiments	19
3.2.2 Scanning Transmission Electron Microscopy	20
3.2.3 Scanning Electron Microscopy	20
3.3 Electron Microscopy – Spectroscopy	22
3.3.1 Electron Energy-Loss Spectroscopy	22
3.3.1.1 Thickness Measurements	23

3.3.1.2	Band Gap Determination	23
3.3.1.3	Analysis of the Near Edge Fine Structure	24
3.3.1.3.1	Nb-M _{2,3} Edge	26
3.3.1.3.2	Ti-L _{2,3} Edge	27
3.3.1.3.3	O-K Edge	28
3.3.1.4	Quantification of the Elemental Composition	29
3.3.2	Energy-Dispersive X-ray Spectroscopy	30
3.4	X-ray Diffraction and Photon Based Spectroscopy	31
3.4.1	X-ray Diffraction	31
3.4.2	UV/Vis and PL Spectroscopy	32
3.5	Instrumentation	33
3.6	References	34
4	Template-Free Synthesis of Novel, Highly-Ordered 3D Hierarchical Nb₃O₇(OH) Superstructures with Semiconductive and Photoactive properties	36
4.1	Introduction	36
4.2	Results and Discussion	37
4.2.1	Hydrothermal Conditions Enable the Self-Organized Formation of Nb ₃ O ₇ (OH) Superstructures	37
4.2.2	Analysis of the Superstructure Formation	38
4.2.3	Investigation of the Structure of the Superstructures at Atomic Scale	41
4.2.4	Suitability of the Nb ₃ O ₇ (OH) Superstructures as New Electrode Material	44
4.3	Conclusion	45
4.4	Additional Information	47
4.4.1	Analysis of the Diffraction Pattern of the Network	47
4.4.2	Local Thickness Measurements and FFT Analysis at Nanowire Junctions	48
4.5	Experimental	49
4.6	References	50
5	3D vs 2D – New Insights into the Nanowire Arrangement in Nb₃O₇(OH) Superstructures	52
5.1	Introduction	52
5.2	Application for Nb ₃ O ₇ (OH)	55
5.3	Conclusion	58
5.4	Experimental	59
5.5	References	60
6	In-Depth Characterization of Planar Defects in the Crystal Lattice	61
6.1	Introduction	61
6.2	Results	62
6.3	Discussion	64

6.4	Experimental	64
6.5	References	65
7	Heat Induced Phase-Transformation of 3D Nb₃O₇(OH) Superstructures – Effect of Atmosphere and Electron Beam	66
7.1	Introduction	66
7.2	Results and Discussion	67
7.2.1	Ex Situ Studies of the Phase Transformation at Ambient Conditions	67
7.2.2	In Situ TEM Investigation of Phase Transformation in Reducing Atmosphere	70
7.2.3	Electron Energy-Loss Spectroscopy Analysis of the Different Samples	73
7.3	Conclusion	76
7.4	Experimental	77
7.5	References	78
8	Titanium Doping and its Effect on the Morphology of 3D Hierarchical Nb₃O₇(OH) Nanostructures for Enhanced Light-Induced Water Splitting	80
8.1	Introduction	80
8.2	Results and Discussion	81
8.2.1	Effect of the Incorporation of Titanium on the Morphology and Crystal Structure	81
8.2.2	In-Depth TEM Characterization of the Nanowire Networks	83
8.2.3	Electron Energy-loss Spectroscopy Study of Titanium Doped Samples	86
8.2.4	Photocatalytic Activity of the Different Morphologies	87
8.3	Conclusion	89
8.4	Experimental	90
8.5	References	91
9	Summary and Conclusion	93
	Appendices	96
A	Appendix	96
B	Appendix	100
C	Appendix	107
	Bibliography	118
	Curriculum Vitae	131
	Acknowledgments	135

List of Figures

2.1	Crystal structures of rutile, anatase and brookite TiO_2	7
2.2	Crystal structures of $\text{H-Nb}_2\text{O}_5$ and $\text{Nb}_3\text{O}_7(\text{OH})$	8
2.3	SEM images of different morphologies accessible by slight variation of the hydrothermal synthesis conditions (pH value, temperature, synthesis time).	9
3.1	Schematic illustration of electron beam-matter interaction and the emitted irradiation.	13
3.2	Schematic illustration of the setup of a transmission electron microscope.	15
3.3	Schematic drawing showing elastic scattering at crystals which illustrates the Bragg equation.	16
3.4	Illustration of the CTF with and without C_s correction.	18
3.5	Schematic illustration of STEM detectors which detect electrons for different scattering angles.	20
3.6	Schematic illustration of the setup and image generation of a SEM.	21
3.7	Schematic illustration of an EEL spectrometer and spectrum.	22
3.8	The sample thickness is encoded in the intensity of the plasmon peak.	23
3.9	Low-loss EEL spectrum acquired for $\text{H-Nb}_2\text{O}_5$ used for the determination of the band gap.	24
3.10	Schematic illustration of the band structure and the origin of the ELNES.	25
3.11	Experimental and theoretical ELNES of the Nb-M _{2,3} of $\text{Nb}_3\text{O}_7(\text{OH})$	26
3.12	Experimental Ti-L _{2,3} edge recorded for anatase and rutile TiO_2	27
3.13	Experimental O-K edge recorded for anatase TiO_2 and $\text{Nb}_3\text{O}_7(\text{OH})$	28
3.14	Schematic drawing illustrating the formation of characteristic X-rays and Bremsstrahlung.	30
4.1	Table of contents graphic.	36
4.2	SEM images of $\text{Nb}_3\text{O}_7(\text{OH})$ cube morphologies obtained for different synthesis times and respective XRD pattern.	39
4.3	Electron microscopic investigation of the $\text{Nb}_3\text{O}_7(\text{OH})$ mesocrystals.	42
4.4	Electron microscopic investigation of one single $\text{Nb}_3\text{O}_7(\text{OH})$ nanowire on a holey carbon film, which broke off from a network, and of the different nanowire junctions in the network.	43
4.5	Measurement of the optoelectronic properties of $\text{Nb}_3\text{O}_7(\text{OH})$ superstructures.	45
4.6	TEM image and electron diffraction pattern detected of a small network fragment.	47

4.7	Analysis of the junctions appearing in the network.	48
5.1	Schematic illustration of the electron tomographic reconstruction technique.	53
5.2	Selected images of a tilt series detected for a single $\text{Nb}_3\text{O}_7(\text{OH})$ nanowire network and the respective reconstruction.	55
5.3	Analysis of the 3D nanowire arrangement in the network using electron tomography.	56
5.4	Investigation of the nanowire spikes on the cube surface which increase the surface area of the morphology.	57
6.1	TEM images of $\text{Nb}_3\text{O}_7(\text{OH})$ nanowires which reveal planar defects in the crystal lattice of individual nanowires.	62
6.2	HRTEM analysis of the defect structure in a very thin nanowire.	63
7.1	Table of contents graphic.	66
7.2	Electron micrographs of samples heated ex situ at ambient condition. . .	69
7.3	In situ TEM heating experiments which shows the effect of heat and electron bombardment on the structure of nanowire networks.	70
7.4	HRTEM images detected during the in situ TEM heating experiments. . .	72
7.5	EEL spectra recorded for samples achieved by different heat treatments. .	74
8.1	Table of content graphic.	80
8.2	Morphology and crystal structure of $\text{Nb}_3\text{O}_7(\text{OH})$ superstructures which form for different Ti(IV) concentration in the reaction solution.	83
8.3	Electron microscopy analysis of the superstructures achieved for different Ti(IV) concentrations in the reaction solution.	84
8.4	EEL spectra detected for morphology A, B and the wall of the cubes and TiO_2 plate of morphology C.	87
8.5	Semi-log plot of TCSPC transients detected for the three morphologies and intensity averaged lifetimes.	89

List of Tables

3.1	Used electron microscopes.	33
5.1	Measurement parameters used for the acquisition of tilt series for 3D tomography of single Nb ₃ O ₇ (OH) nanowire networks.	59
7.1	EELS data recorded for the samples calcined at different temperatures ex situ and in situ in the presence of the electron beam.	76
8.1	H ₂ production rate, surface area and PL lifetime for different Nb ₃ O ₇ (OH) superstructures which comprise different titanium amounts.	88

Abbreviations

ADF	Annular dark field
AE	Auger electron
ART	Algebraic reconstruction technique
BF	Bright field
BFP	Back focal plane
BSE	Back-scattered electron
CB	Conduction band
CTF	Contrast transfer function
DART	Discrete algebraic reconstruction technique
DSSC.....	Dye-sensitized solar cell
DOS	Density of states
EELS	Electron energy-loss spectroscopy
ELNES	Energy-loss near edge fine structure
EDX	Energy dispersive X-ray spectroscopy
FEG	Field emission gun
FFT	Fast Fourier transformation
HAADF	High angle annular dark field
HRTEM	High resolution transmission electron microscopy
HOMO	Highest occupied molecular orbital
LUMO	Lowest unoccupied molecular orbital
MFP	Mean free path
OD	Optical density
PL	Photoluminescence
SAED	Selected area electron diffraction
SAGB	Small angle grain boundary
SE	Secondary electron
SEM	Scanning electron microscopy
SIRT	Simultaneous iterative reconstruction technique
STEM	Scanning transmission electron microscopy

TCSPC	Time correlated single photon counting
TEAM	Transmission electron aberration-corrected microscopy
TEM	Transmission electron microscopy
UV	Ultraviolet
VB	Valence band
Vis	Visible
XRD	X-ray diffraction
ZLP	Zero loss peak

Symbols

A	Absorbance
a	Absorption coefficient
β	Collection angle
$\chi(u)$	Contrast transfer function
c	Concentration
C_c	Chromatic aberration coefficient
C_s	Spherical aberration coefficient
D	Spacing
d_{hkl}	Lattice spacing
δ	Tilt angle tomography
Δ	Energy window
ΔE	Energy difference
Δf	Defocus
$\Delta f_{Scherzer}$	Scherzer defocus
ϵ	Absorptivity coefficient
E	Energy
$E_c(u)$	Chromatic aberration envelope function
$E_d(u)$	Drift envelope function
$E_D(u)$	Detector envelope function
E_g	Band gap energy
$E_s(u)$	Spatial envelope function
$E_t(u)$	Total envelope function
$E_v(u)$	Vibration envelope function
f	Scattering factor
F_{hkl}	Structure factor
h	Planck constant
h^+	Hole
hkl	Miller indices

I	Intensity
I_e	Beam current of electron beam
I_0	Intensity zero loss peak
I_t	Intensity low loss region
J	Emission current density
k	Boltzmann factor
K	Tailing parameter of the Tauc method
$k_{a,b}$	Cliff-Lorimer factor
l	Length
λ	Wavelength
λ_p	Mean free path
$M(\Delta E)$	Transition matrix element
n	Diffraction order
N	Atoms per unit area
N_A	Elemental composition
$N(\Delta E)$	Density of states
ν	Frequency
$P_{j,k,\delta}$	Projection
ϕ	Work function
q	Iteration cycle
$R_{j,k,\delta}$	Reprojection
ρ	Voxel
σ	ionization cross-section
T	Temperature
T_{melt}	Melting temperature
t	Acquisition time EELS
t_s	Sample thickness
τ	PL lifetime
θ_B	Bragg angle
u	Spatial frequency
x, y, z	Coordinates
$W(\Delta E)$	Transition rate
Z	Atomic number

1 Introduction

"*There is plenty of room at the bottom*" entitles a talk given by Richard Feynman in 1959 where he introduced the ideas and concepts behind nanoscience. In his talk, Feynman described processes which allow scientists to manipulate and control matter at the nanoscale. However, more than a decade had passed before Norio Taniguchi introduced the term *nanotechnology*. In the early 2000s the field gained increasing scientific attention. Today, we can't imagine our world without nanotechnology, as many modern technologies make use of the superior properties of nanostructures^[1,2] which are not observed for their bulk counterparts.

Working at the nanoscale requires vision at the nanoscale, which is made possible by electron microscopes. The replacement of light with electrons features a drastically increased resolution and structures below 1 nm can be resolved. Several different electron microscope types were developed which allow to analyze the properties of nanostructures e.g. their crystal structure, elemental composition, and morphology.^[3] Knowledge about material properties at the nanoscale leads to a better understanding of their performance in functional devices.^[4] Nanostructured materials can be fabricated in a controlled manner by chemical^[5-9] or physical approaches^[10,11] which led to advancements in various fields of technology like gas^[1] and data storage,^[12] medicine,^[13,14] or green energy.^[15] The latter becomes increasingly important as the atmospheric CO₂ concentration, which is mainly caused by the combustion of fossil fuels, reached a new record value in May 2015.^[16] CO₂ is the main anthropogenic greenhouse gas causing the greenhouse effect which is associated with severe environmental damage. To reduce the demand for fossil fuel photovoltaic cells become more and more attractive as the sun continuously delivers 120000 TW of solar energy to the earth.^[17] Nanostructured devices, like dye-sensitized solar cells (DSSC) attract increasing attention.^[18] The original DSSC consists of a semi-conducting TiO₂ nanoparticle film on a transparent electrode, which is decorated with a dye and immersed with an iodide electrolyte.^[19] DSSCs mimic the photosynthesis: the dye is excited by sunlight leading to the transition of electrons from the highest occupied molecular orbital (HOMO) to the lowest unoccupied molecular orbital (LUMO). The charges are separated at the dye-semiconductor-interface as the electron relaxes into the conduction band (CB) of the semiconductor and subsequently diffuses to the electrode. The hole which was left behind in the HOMO is simultaneously filled with the help of the I₃⁻/I⁻ redox system.^[18,19] Solar cells suffer from weather-dependent intermittency and novel materials to chemically store the energy are therefore needed. Hydrogen gas which can be stored and later used in e.g. fuel cells is listed as one of the most promising future fuels. Semiconductor photocatalysts use solar power to split water and form hydrogen, utilizing photons to excite electrons from the valence band (VB) to the CB

of the semiconductor. The photo generated charges are used up for the water splitting redox reaction happening at the surface of the semiconductor.^[20–23] The efficiency of nanostructured materials for DSSC and photocatalysis is determined by their absorption behavior, their band gap and their charge separation/transport properties.^[24–26] Charge recombination processes at grain boundaries^[27–29] or defects^[4,30,31] are the major loss mechanism in photochemistry and therefore have a large impact on the performance of materials. On this account it is important to study nanostructures on a local scale using various electron microscopic techniques. High resolution transmission electron microscopy (HRTEM) and high angle annular dark field (HAADF) imaging enables the investigation of crystal lattices at the atomic scale e.g. featuring new insights into their defect structure. Electron energy-loss (EEL) and energy-dispersive X-ray (EDX) spectroscopy further extend the knowledge about materials yielding information about the elemental composition, bonding behavior and oxidation state of atoms. The combination of these methods can help at identifying loss mechanisms of nanostructured functional devices.

As mentioned above, the original DSSCs were based on TiO_2 nanoparticles and achieved a light power-conversion efficiency of 7.1 – 7.9% under simulated solar light.^[19] Since then several different TiO_2 morphologies were investigated to optimize the performance. Next to nanoparticles 1D materials like nanowires and nanotubes were applied to accelerate charge mobility along improved transport paths.^[32–34] This concept was extended to three dimensions by the preparation of mesoporous TiO_2 single crystals.^[35] By optimizing the different cell components^[36] a new record efficiency of 13% was achieved for TiO_2 based DSSC.^[37] However, undoped TiO_2 has a band gap size of 3.0 – 3.2 eV^[38] which constrains the exploitation of the solar spectrum. This illustrates why the research of new materials and morphologies is inevitable.

1.1 Aim of the Thesis

In this study a one-step, template-free synthesis strategy is developed which can be used to grow novel $\text{Nb}_3\text{O}_7(\text{OH})$ nanostructures with exceptional morphologies. $\text{Nb}_3\text{O}_7(\text{OH})$ can serve as an alternative material to TiO_2 and was recently introduced as promising material for photoelectrodes and photocatalysis.^[39] Hydrothermal conditions are applied and the reaction product is studied as function of the synthesis time to establish a growth model. For this, the morphology of the nanostructures is investigated by scanning electron microscopy (SEM) while the crystallinity is determined by X-ray and electron diffraction experiments. Since nanostructure junctions might act as obstacles for charge transport they are studied in detail by local thickness measurements based on EELS and electron tomography. Defects and grain boundaries in the crystal lattice are also expected to have a strong impact on the photophysical properties, thus HRTEM and HAADF imaging are used to visualize them and to uncover their structure. The distribution of the atomic species is studied by EDX while the bonding behavior and oxidation state is investigated with EELS. To further modify the properties of the nanostructures both the effect of dopants and heat is investigated. Calcination temperatures

above 500 °C are reported to provoke the phase transformation from $\text{Nb}_3\text{O}_7(\text{OH})$ to $\text{H-Nb}_2\text{O}_5$.^[39] Annealing experiments are therefore performed ex situ at elevated temperatures up to 1200 °C and in situ in the TEM. The addition of titanium(IV) salts to the reaction solution is used to modify the morphological properties. The photophysical properties of the different morphologies are analyzed with different optical spectroscopy methods and correlated to the results obtained with electron microscopy. Dye-bleaching and water splitting experiments are conducted to predict the suitability of the different morphologies for application as photocatalyst or photoelectrode material.

1.2 Outline of the Thesis

Besides the introduction, the present thesis has eight chapters. Chapter 2 introduces common metal oxides investigated for photocatalysis and DSSCs, followed by a description of the properties of niobium- and titanium oxide. Furthermore, the fundamentals of solvothermal synthesis strategies and the developed synthesis protocols are introduced in this chapter. The analytical techniques applied to investigate the samples are given in chapter 3 with a focus on electron microscopy and its related techniques. It also contains a brief section about the applied photophysical characterization methods. The developed hydrothermal synthesis route to fabricate $\text{Nb}_3\text{O}_7(\text{OH})$ superstructures is described in detail in chapter 4. The growth mechanism, which is determined from SEM and XRD analysis, along with their morphological and crystallographic characteristics is also presented in this chapter. In addition, the suitability of $\text{Nb}_3\text{O}_7(\text{OH})$ superstructures as photoelectrode or photocatalyst material is investigated. Their cubic morphology is composed of highly ordered nanowire networks. The 3D nanowire arrangement in these networks is further analyzed by 3D electron tomography as described in chapter 5. Chapter 6 focuses on HRTEM analysis of planar defects visible in the crystal lattice of $\text{Nb}_3\text{O}_7(\text{OH})$ nanowires. The effects of the heat induced phase transformation of $\text{Nb}_3\text{O}_7(\text{OH})$ to $\text{H-Nb}_2\text{O}_5$ on the superstructure morphology and crystal structure is investigated in chapter 7 applying in situ and ex situ electron microscopy methods. The performance of the superstructures as photocatalyst for water splitting is finally tested and the results are described in chapter 8. Additionally, the effect of Ti-doping on the photophysical, morphological and crystallographic properties of the superstructures is examined. Chapter 9 draws the main conclusions from this work and provides an outlook into future projects. The appendices contain additional information supporting the findings of this study.

1.3 References

- [1] R. E. Morris, P. S. Wheatley, *Angew. Chem.* **2008**, *47*, 4966.
- [2] I. Moreels, K. Lambert, D. Smeets, D. De Muynck, T. Nollet, J. C. Martins, F. Vanhaecke, A. Vantomme, C. Delerue, G. Allan, Z. Hens, *ACS Nano* **2009**, *3*, 3023.
- [3] D. B. Williams, C. B. Carter, *Transmission Electron Microscopy: A Textbook for Materials Science*, Springer, **2013**.
- [4] A. Wisnet, K. Bader, S. B. Betzler, M. Handloser, P. Ehrenreich, T. Pfadler, J. Weickert, A. Hartschuh, L. Schmidt-Mende, C. Scheu, J. A. Dorman, *Adv. Funct. Mater.* **2015**, *25*, 2601.
- [5] J. H. Fendler, F. C. Meldrum, *Adv. Mater.* **1995**, *7*, 607.
- [6] Y. Wang, A. S. Angelatos, F. Caruso, *Chem. Mater.* **2008**, *20*, 848.
- [7] Q. Yang, Z. Lu, J. Liu, X. Lei, Z. Chang, L. Luo, X. Sun, *Prog. Nat. Sci.* **2013**, *23*, 351.
- [8] C. C. Yec, H. C. Zeng, *J. Mater. Chem. A* **2014**, *2*, 4843.
- [9] M. R. Kim, Z. Xu, G. Chen, D. Ma, *Chemistry* **2014**, *20*, 11256.
- [10] S. K. Tripathi, N. Shukla, V. N. Kulkarni, *Nanotechnology* **2009**, *20*, 075304.
- [11] S. M. George, *Chem. Rev.* **2010**, *110*, 111.
- [12] S. S. Parkin, M. Hayashi, L. Thomas, *Science* **2008**, *320*, 190.
- [13] O. Salata, *J. Nanobiotechnology* **2004**, *2*, 3.
- [14] D. A. Giljohann, D. S. Seferos, W. L. Daniel, M. D. Massich, P. C. Patel, C. A. Mirkin, *Angewandte Chemie* **2010**, *49*, 3280.
- [15] In *Nanostructured Semiconductor Oxides for the Next Generation of Electronics and Functional Devices*, (Ed.: S. Zhuiykov), Woodhead Publishing, **2014**, pp. 267–320.
- [16] Mauna Loa Observatory, Scripps CO₂ data, **Oct. 2015**, <http://co2now.org/Current-CO2/CO2-Now/scripps-co2-data-mauna-loa-observatory.html>.
- [17] K. Yu, J. Chen, *Nanoscale Res. Lett.* **2008**, *4*, 1.
- [18] A. Hagfeldt, G. Boschloo, L. Sun, L. Kloo, H. Pettersson, *Chem. Rev.* **2010**, *110*, 6595.
- [19] B. O'Regan, M. Grätzel, *Nature* **1991**, *353*, 737.
- [20] A. Fujishima, K. Honda, *Nature* **1972**, *238*, 37.
- [21] M. G. Walter, E. L. Warren, J. R. McKone, S. W. Boettcher, Q. Mi, E. A. Santori, N. S. Lewis, *Chem. Rev.* **2010**, *110*, 6446.
- [22] X. Chen, S. Shen, L. Guo, S. S. Mao, *Chem. Rev.* **2010**, *110*, 6503.
- [23] F. E. Osterloh, *Chem. Soc. Rev.* **2013**, *42*, 2294.
- [24] A. C. Dodd, A. J. McKinley, M. Saunders, T. Tsuzuki, *J. Nanopart. Res.* **2006**, *8*, 43.
- [25] G. Xiong, U. Pal, J. G. Serrano, *J. Appl. Phys.* **2007**, *101*, 024317.
- [26] K. Kočí, L. Obalová, L. Matějová, D. Plachá, Z. Lacný, J. Jirkovský, O. Šolcová, *Appl. Catal. B-Environ* **2009**, *89*, 494.
- [27] A. K. Ghosh, C. Fishman, T. Feng, *J. Appl. Phys.* **1980**, *51*, 446.

-
- [28] C. R. M. Grovenor, *J. Phys. C: Solid State Phys.* **1985**, *18*, 4079.
- [29] P. Docampo, S. Guldin, U. Steiner, H. J. Snaith, *J. Phys. Chem. Lett.* **2013**, *4*, 698.
- [30] A. Testino, I. R. Bellobono, V. Buscaglia, C. Canevali, M. D'Arienzo, S. Polizzi, R. Scotti, F. Morazzoni, *J. Am. Chem. Soc.* **2007**, *129*, 3564.
- [31] W. A. Goddard, D. Brenner, S. E. Lyshevski, G. J. Iafrate, *Handbook of Nanoscience, Engineering, and Technology, Third Edition*, Taylor & Francis, **2012**.
- [32] J. Jiu, F. Wang, S. Isoda, M. Adachi, *Chem. Lett.* **2005**, *34*, 1506.
- [33] J. Jiu, S. Isoda, F. Wang, M. Adachi, *J. Phys. Chem. B* **2006**, *110*, 2087.
- [34] B. Liu, E. S. Aydil, *J. Am. Chem. Soc.* **2009**, *131*, 3985.
- [35] E. J. W. Crossland, N. Noel, V. Sivaram, T. Leijtens, J. A. Alexander-Webber, H. J. Snaith, *Nature* **2013**, *495*, 215.
- [36] J. Albero, P. Atienzar, A. Corma, H. Garcia, *Chem. Rec.* **2015**, *15*, 803.
- [37] S. Mathew, A. Yella, P. Gao, R. Humphry-Baker, B. F. Curchod, N. Ashari-Astani, I. Tavernelli, U. Rothlisberger, M. K. Nazeeruddin, M. Grätzel, *Nat Chem* **2014**, *6*, 242.
- [38] D. O. Scanlon, C. W. Dunnill, J. Buckeridge, S. A. Shevlin, A. J. Logsdail, S. M. Woodley, C. R. Catlow, M. J. Powell, R. G. Palgrave, I. P. Parkin, G. W. Watson, T. W. Keal, P. Sherwood, A. Walsh, A. A. Sokol, *Nat. Mater.* **2013**, *12*, 798.
- [39] H. Zhang, Y. Wang, D. Yang, Y. Li, H. Liu, P. Liu, B. J. Wood, H. Zhao, *Adv. Mater.* **2012**, *24*, 1598.

2 Materials and Synthesis Procedure

In this chapter a short summary on metal oxides, which are often used in photochemistry, is presented. Furthermore, a detailed description of niobium oxide and titanium oxide concerning their properties and crystallographic structure is given.

2.1 Metal Oxides for Photochemistry

TiO₂ nanoparticles were the first system for which the photocatalytic splitting of water could be shown,^[1] and the electrode material applied in the first DSSC.^[2] However, the absorption range of undoped TiO₂ is confined to the UV spectral region given by its band gap.^[3,4] Since then, many other metal oxides have been investigated intensively.^[5,6] Compared to TiO₂ ZnO benefits from both an order of magnitude higher electron mobility^[7] and a higher exciton binding energy.^[8] But unfortunately its band gap of 3.4 eV is larger than the one of TiO₂^[9] and its low stability in aqueous solution constrains its applicability further.^[10] SnO₂ is characterized by an even larger band gap of 3.6 eV^[11] but the energetic position of its conduction band facilitates the electron injection from the dye.^[12] However, despite its better electron transport properties SnO₂ underperforms TiO₂.^[12,13] Next to metal oxides organo-lead trihalide perovskites are investigated as photoelectrode materials,^[14] as they combine tunable band gaps between 1.5 eV and 2.3 eV^[15,16] with large charge carrier diffusion lengths.^[17] However, these perovskites suffer from a low stability leading to their rapid degradation when exposed to air.

2.2 Titanium Oxide

To date TiO₂ is still the most commonly applied material in the field of photochemistry.^[3,18,19] In the present work it forms as second phase when adding Ti(IV) to the synthesis protocol. Therefore, its crystal structure and properties are shortly summarized. It occurs in three main bulk phases: anatase, rutile and brookite. The polymorphs are based on TiO₆ octahedra which are linked differently for the three phases: Two edges of each octahedra are shared in rutile TiO₂, resulting in infinite chains of edge-sharing octahedras along the *c*-direction. In brookite the octahedra are connected by three shared edges whereas they share four in anatase (see fig. 2.1).^[20] Rutile has a tetragonal crystal structure with $a = 4.59 \text{ \AA}$ and $b = 2.95 \text{ \AA}$,^[21] anatase is likewise tetragonal with $a = 3.78 \text{ \AA}$, $c = 9.49 \text{ \AA}$ ^[21] and orthorhombic brookite TiO₂ is characterized by $a = 9.17 \text{ \AA}$, $b = 5.44 \text{ \AA}$ and $c = 5.14 \text{ \AA}$.^[22] The metastable phases anatase and brookite can be transformed into the thermodynamically stable rutile phase by calcination at about 1090 °C and 930 °C respectively.^[23] Anatase TiO₂ has a reported band gap of 3.2 eV which is

about 0.2 eV larger than the band gap of rutile TiO_2 , with the VB of anatase being about 0.4 eV higher in energy than that of rutile.^[4] The electron mobilities observed for TiO_2 cover a wide range dependent on the morphology and crystal phase.^[24,25]

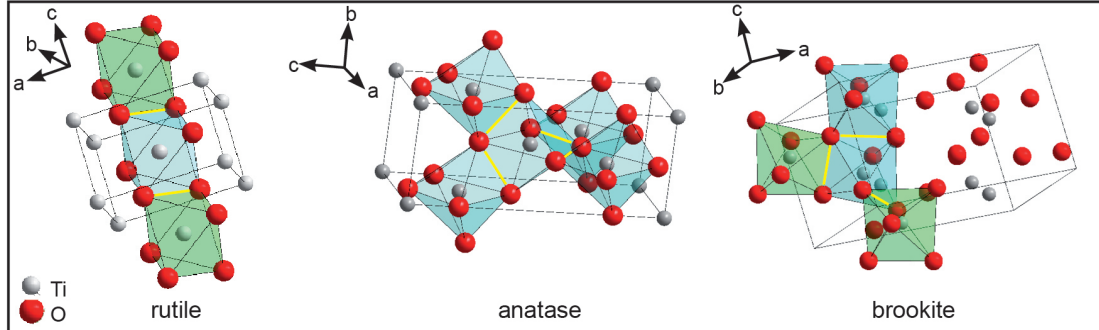


Figure 2.1 Crystal structures of rutile, anatase and brookite TiO_2 . Titanium ions are drawn in white, oxygen ions in red. The three crystal phases are characterized by different octahedra linkage and the shared edges are highlighted in yellow. Octahedra of neighboring unit cells are displayed in green.

2.3 Niobium Oxide

Niobium oxide is another metal oxide which has been investigated for application in photochemistry.^[26] Several interesting Nb_2O_5 nanostructure morphologies were synthesized^[27–35] and successfully tested as photocatalysts^[26,32,36,37] or electrode material in DSSCs.^[28,38–41] Niobium is known as non-corrosive metal. The same is true for its oxides which feature a high chemical stability.^[42,43] This is reflected in the photocatalytic stability of the material which does not lose its catalytic efficiency for repeating catalysis cycles.^[36,44] Unfortunately Nb_2O_5 suffers from large band gap sizes, which range from 4.35 eV observed for amorphous thin films to 4.87 eV depending on the annealing temperature.^[45]

Nb_2O_5 crystal phases are composed of ReO_3 -type structure units which consist of corner-sharing NbO_6 octahedra.^[46] Every arrangement of these blocks that constitutes a regular repeating pattern generates a distinct Nb_2O_5 phase, which is why more than 15 different polymorphs of Nb_2O_5 exist.^[47] In addition to the high variety of ordered structures disordered structures with corresponding gradients of the composition occur.^[48] $\text{H-Nb}_2\text{O}_5$ is the thermodynamically stable polymorph and has a monoclinic crystal structure with $a = 21.15 \text{ \AA}$, $b = 3.82 \text{ \AA}$, $c = 19.36 \text{ \AA}$, $\beta = 119.80^\circ$ (see fig. 2.2).^[49] Its crystal structure is composed of $(3 \times 5)(3 \times 4)$ blocks, connected via columns of tetrahedrally coordinated niobium cations. The crystal lattice of $\text{H-Nb}_2\text{O}_5$ has the ability to compensate non-stoichiometry by partly removing cations from the tetrahedron columns.^[48] The ability to compensate oxygen deficiency is a common scheme observed for many Nb_2O_5 phases. This is achieved by crystallographic shear on (100) and (001) planes of the ReO_3 substructure, by the rearrangement of the ReO_3 blocks or by lamella intergrowth of different structures. $\text{Nb}_3\text{O}_7(\text{OH})$ recently came up as new material for photochemistry.^[38] It is characterized by a smaller band gap of 3.1 eV,^[50] and its performance as

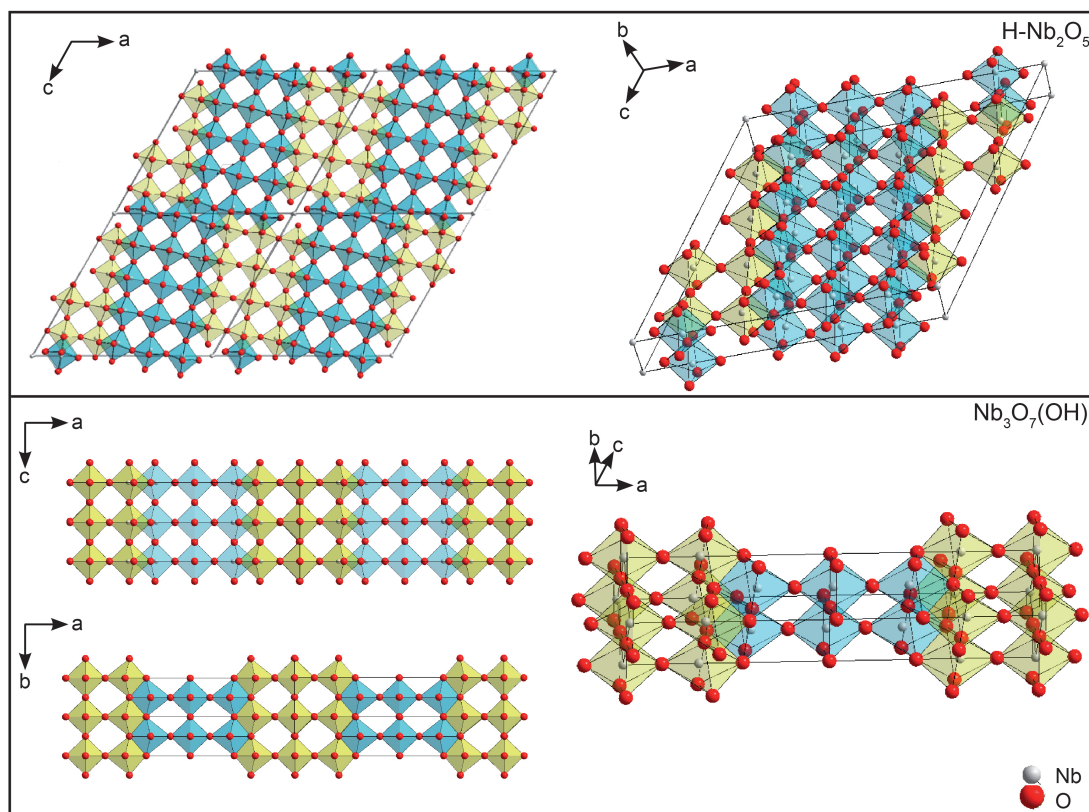


Figure 2.2 Crystal structures of $\text{H-Nb}_2\text{O}_5$ and $\text{Nb}_3\text{O}_7(\text{OH})$. Niobium ions are represented as white, oxygen ions as red spheres.

photoelectrode material in DSSCs exceeds Nb_2O_5 .^[38] Similar to most binary niobium oxides its orthorhombic crystal structure is composed of $(3 \times \infty)$ blocks of corner-sharing NbO_6 octahedra which expand infinite in b - and c -direction. Its unit cell dimensions are $a = 20.74 \text{ \AA}$, $b = 3.82 \text{ \AA}$, $c = 3.93 \text{ \AA}$.^[51] The structural resemblance of $\text{Nb}_3\text{O}_7(\text{OH})$ and $\text{H-Nb}_2\text{O}_5$ is manifested in the heat induced phase transformation observed at $500 \text{ }^\circ\text{C}$.^[38] Theoretical calculations indicate that this phase transformation goes along with significant changes of the optoelectronic properties.^[52]

This section based on an invited book chapter to be published 2016 in *Materials Development for Solar Fuels and Energy Conversion in Fuel Cells* by Springer Science (Editors: U. I. Kramm, H.-J. Lewerenz, D. Schmeißer).

2.4 Solvothermal Synthesis Strategy

Niobium and titanium oxide can be obtained by solvothermal synthesis strategies, which form an alternative to classical solid-solid reactions that require high temperatures in the range of $1000 \text{ }^\circ\text{C}$.^[53] Solvothermal synthesis is carried out in a closed vessel at moderate temperatures above the boiling point of the used solvent (water (hydrothermal), ammoniac (ammonothermal), ethanol). The resulting high pressure enables the crystallization of materials at comparably low temperatures. Solvothermal crystal growth involves three distinct stages: The dissolution of the reactants, seed formation and crystallization. The crystal growth is limited by the reactant concentration, as reactions on

the seed surface require supersaturation at the seed-solution interface.^[54] These conditions favor more complex structures of lower enthalpy, entropy and symmetry^[55] so that a large variety of morphologies of different materials were produced by hydrothermal synthesis strategies.^[55–58]

2.4.1 Synthesis of $\text{Nb}_3\text{O}_7(\text{OH})$ Nanostructures

In the present work a hydrothermal synthesis strategy to produce $\text{Nb}_3\text{O}_7(\text{OH})$ nanostructures was developed. All chemicals were used as supplied without further purification. Niobium(IV)-chloride-tetrahydrofuran complex (0.2 g, 0.5 mmol; supplied by *Sigma Aldrich*) was mixed with concentrated HCl (5 mL; 37% HCl, p.a., *Brenntag*) yielding a green suspension. After 20 minutes 5 mL H_2O were added to this solution causing a color change to dark blue. The mixture was transferred into a Teflon liner in a stainless steel autoclave and placed into an oven at 200 °C (reaction time 16–72 hours). The reaction product was collected after cooling down to room temperature and washed several times with ethanol to remove remaining starting material. Dependent on the applied synthesis conditions (changes of the pH value, temperature and reaction time) several different niobium oxide morphologies and polymorphs are accessible (fig. 2.3). These range from compact cubes, over compact spheres to hollow spheres and cubes.

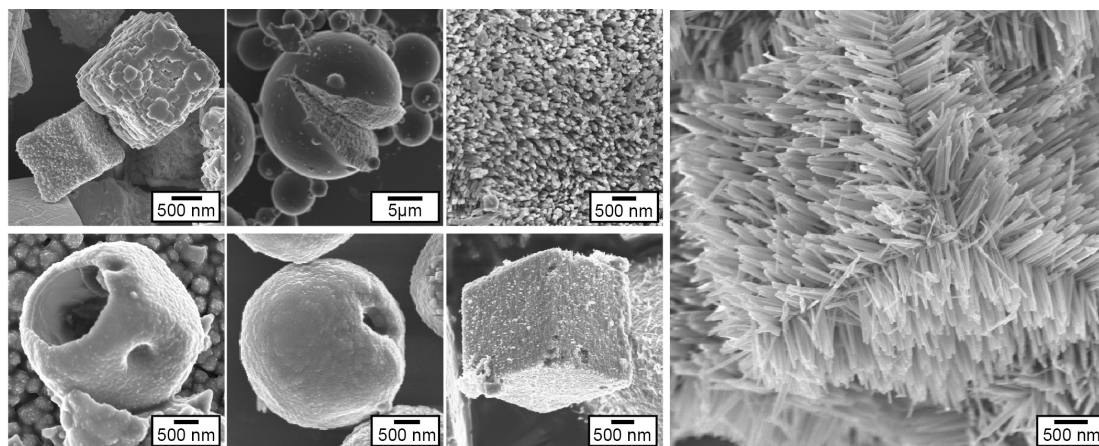


Figure 2.3 SEM images of different morphologies accessible by slight variation of the hydrothermal synthesis conditions (pH value, temperature, synthesis time) (image taken from reference^[59]).

2.4.2 Doping with Titanium

As described for the synthesis of $\text{Nb}_3\text{O}_7(\text{OH})$ nanostructures $\text{NbCl}_4 \cdot 4\text{THF}$ (0.2 g; supplied by *Sigma Aldrich*) was mixed with concentrated HCl (5 mL; p.a., *Brenntag*) and 5 mL H_2O . To this mixture between 0.03 and 0.11 molL^{-1} $\text{Ti}(\text{O}i\text{Bu})_4$ (supplied by *Sigma Aldrich*) were added. The mixture was stirred until a clear solution had formed which was transferred into a Teflon-lined autoclave and heated at 200 °C for 19 hours. After cooling down to room temperature the product was collected and washed with ethanol to remove impurities and left-over starting material.

2.5 References

- [1] A. Fujishima, K. Honda, *Nature* **1972**, *238*, 37.
- [2] B. O'Regan, M. Grätzel, *Nature* **1991**, *353*, 737.
- [3] X. Chen, S. S. Mao, *Chem. Rev.* **2007**, *107*, 2891.
- [4] D. O. Scanlon, C. W. Dunnill, J. Buckeridge, S. A. Shevlin, A. J. Logsdail, S. M. Woodley, C. R. Catlow, M. J. Powell, R. G. Palgrave, I. P. Parkin, G. W. Watson, T. W. Keal, P. Sherwood, A. Walsh, A. A. Sokol, *Nat. Mater.* **2013**, *12*, 798.
- [5] M. Dürr, S. Rosselli, A. Yasuda, G. Nelles, *J. Phys. Chem. B* **2006**, *110*, 21899.
- [6] I. Concina, A. Vomiero, *Small* **2015**, *11*, 1744.
- [7] A. K. Chandiran, M. Abdi-Jalebi, M. K. Nazeeruddin, M. Grätzel, *ACS Nano* **2014**, *8*, 2261.
- [8] Ü. Özgür, Y. I. Alivov, C. Liu, A. Teke, M. Reshchikov, S. Doan, V. Avrutin, S.-J. Cho, H. Morkoç, *J. Appl. Phys.* **2005**, *98*, 041301.
- [9] A. Janotti, C. G. Van de Walle, *Rep. Prog. Phys.* **2009**, *72*, 126501.
- [10] M. Liu, C.-Y. Nam, C. T. Black, J. Kamcev, L. Zhang, *J. Phys. Chem. C* **2013**, *117*, 13396.
- [11] W. Zhou, Y. Liu, Y. Yang, P. Wu, *J. Phys. Chem. C* **2014**, *118*, 6448.
- [12] P. Tiwana, P. Docampo, M. B. Johnston, H. J. Snaith, L. M. Herz, *ACS Nano* **2011**, *5*, 5158.
- [13] A. Birkel, Y.-G. Lee, D. Koll, X. V. Meerbeek, S. Frank, M. J. Choi, Y. S. Kang, K. Char, W. Tremel, *Energy Environ. Sci.* **2012**, *5*, 5392.
- [14] N. J. Jeon, J. H. Noh, W. S. Yang, Y. C. Kim, S. Ryu, J. Seo, S. I. Seok, *Nature* **2015**, *517*, 476.
- [15] J. H. Noh, S. H. Im, J. H. Heo, T. N. Mandal, S. I. Seok, *Nano Lett.* **2013**, *13*, 1764.
- [16] G. E. Eperon, S. D. Stranks, C. Menelaou, M. B. Johnston, L. M. Herz, H. J. Snaith, *Energy Environ. Sci.* **2014**, *7*, 982.
- [17] D. Shi, V. Adinolfi, R. Comin, M. Yuan, E. Alarousu, A. Buin, Y. Chen, S. Hoogland, A. Rothenberger, K. Katsiev, Y. Losovyj, X. Zhang, P. Dowben, O. F. Mohammed, E. Sargent, O. M. Bakr, *Science* **2015**, *347*, 519.
- [18] A. Hagfeldt, G. Boschloo, L. Sun, L. Kloo, H. Pettersson, *Chem. Rev.* **2010**, *110*, 6595.
- [19] B. E. Hardin, H. J. Snaith, M. D. McGehee, *Nat. Photonics* **2012**, *6*, 162.
- [20] E. P. Meagher, G. A. Lager, *Can. Mineral.* **1979**, *17*, 77.
- [21] F. Schoßberger, *Z. Kristallogr.* **1942**, *104*.
- [22] L. Pauling, J. H. Sturdivant, *Z. Kristallogr.* **1928**, *68*.
- [23] T. Mitsuhashi, O. J. Kleppa, *J. Am. Ceram. Soc.* **1979**, *62*, 356.
- [24] T. Dittrich, E. A. Lebedev, J. Weidmann, *Phys. Status Solidi A* **1998**, *165*, R5.
- [25] E. Hendry, M. Koeberg, B. O'Regan, M. Bonn, *Nano Lett.* **2006**, *6*, 755.
- [26] Y. Zhao, X. Zhou, L. Ye, S. C. E. Tsang, *Nano Rev.* **2012**, *3*, 1.
- [27] M. Mozetič, U. Cvelbar, M. K. Sunkara, S. Vaddiraju, *Adv. Mater.* **2005**, *17*, 2138.
- [28] M. Wei, Z.-m. Qi, M. Ichihara, H. Zhou, *Acta Mater.* **2008**, *56*, 2488.

- [29] C. Yan, D. Xue, *Adv. Mater.* **2008**, *20*, 1055.
- [30] C. Yan, L. Nikolova, A. Dadvand, C. Harnagea, A. Sarkissian, D. F. Perepichka, D. Xue, F. Rosei, *Adv. Mater.* **2010**, *22*, 1741.
- [31] A. Le Viet, M. V. Reddy, R. Jose, B. V. R. Chowdari, S. Ramakrishna, *J. Phys. Chem. C* **2010**, *114*, 664.
- [32] B. Gao, J. Fu, K. Huo, W. Zhang, Y. Xie, P. K. Chu, *J. Am. Ceram. Soc.* **2011**, *94*, 2330.
- [33] J. Wu, D. Xue, *CrystEngComm* **2011**, *13*, 1966.
- [34] J. He, Y. Hu, Z. Wang, W. Lu, S. Yang, G. Wu, Y. Wang, S. Wang, H. Gu, J. Wang, *J. Mater. Chem. C* **2014**, *2*, 8185.
- [35] F. Idrees, C. Cao, R. Ahmed, F. K. Butt, S. Butt, M. Tahir, M. Tanveer, I. Aslam, Z. Ali, *Sci. Adv. Mater.* **2015**, *7*, 1298.
- [36] H.-Y. Lin, H.-C. Yang, W.-L. Wang, *Catal. Today* **2011**, *174*, 106.
- [37] L. Li, J. Deng, R. Yu, J. Chen, Z. Wang, X. Xing, *J. Mater. Chem. A* **2013**, *1*, 11894.
- [38] H. Zhang, Y. Wang, D. Yang, Y. Li, H. Liu, P. Liu, B. J. Wood, H. Zhao, *Adv. Mater.* **2012**, *24*, 1598.
- [39] R. Ghosh, M. K. Brennaman, T. Uher, M.-R. Ok, E. T. Samulski, L. E. McNeil, T. J. Meyer, R. Lopez, *ACS Appl. Mater. Interfaces* **2011**, *3*, 3929.
- [40] K. Sayama, H. Sugihara, H. Arakawa, *Chem. Mater.* **1998**, *10*, 7.
- [41] H. Luo, W. Song, P. G. Hoertz, K. Hanson, R. Ghosh, S. Rangan, M. K. Brennaman, J. J. Concepcion, R. A. Binstead, R. A. Bartynski, R. Lopez, T. J. Meyer, *Chem. Mater.* **2013**, *25*, 122.
- [42] H. Paritong, I. Wadsworth, L. A. Donohue, W.-D. Münz, *Trans. Inst. Met. Finish.* **1998**, *76*, 4.
- [43] M. Ziolk, *Catal. Today* **2003**, *78*, 47.
- [44] A. G. S. Prado, L. Bolzon, C. P. Pedroso, A. O. Moura, L. L. Costa, *Appl. Catal. B-Environ.* **2008**, *82*, 219.
- [45] G. Agarwal, G. B. Reddy, *J. Mater. Sci.: Mater. in Electronics* **2005**, *16*, 21.
- [46] B. M. Gatehouse, A. D. Wadsley, *Acta Crystallogr.* **1964**, *17*, 1545.
- [47] J. S. Anderson, J. M. Browne, J. L. Hutchison, *J. Solid State Chem.* **1972**, *5*, 419.
- [48] J. S. Anderson, J. M. Browne, A. K. Cheetham, R. V. Dreele, J. L. Hutchison, F. J. Lincoln, D. J. M. Bevan, J. Straehle, *Nature* **1973**, *243*, 81.
- [49] K. Kato, S. Tamura, *Acta Crystallogr. B-Stru.* **1975**, *31*, 673.
- [50] J. Wu, J. Wang, H. Li, D. Xue, *Thin Solid Films* **2013**, *544*, 545.
- [51] F. Izumi, H. Kodama, *Z. Anorg. Allg. Chem.* **1978**, *441*, 8.
- [52] W. Khan, S. B. Betzler, O. Šipr, J. Ciston, P. Blaha, C. Scheu, J. Minar, *submitted* **2016**.
- [53] Q. Yang, Z. Lu, J. Liu, X. Lei, Z. Chang, L. Luo, X. Sun, *Prog. Nat. Sci.* **2013**, *23*, 351.
- [54] L. N. Demianets, A. N. Lobachev, *Krist. Tech.* **1979**, *14*, 16.
- [55] A. Stein, S. W. Keller, T. E. Mallouk, *Science* **1993**, *259*, 7.
- [56] B. Liu, E. S. Aydil, *J. Am. Chem. Soc.* **2009**, *131*, 3985.

-
- [57] J. S. Beck, J. C. Vartuli, W. J. Roth, M. E. Leonowicz, C. T. Kresge, K. D. Schmitt, C. T.-W. Chu, D. H. Olson, E. W. Sheppard, *J. Am. Chem. Soc.* **1992**, *114*, 10834.
- [58] M.-M. Titirici, M. Antonietti, A. Thomas, *Chem. Mater.* **2006**, *18*, 3808.
- [59] S. B. Betzler, C. Scheu in *Materials Development for Solar Fuels and Energy Conversion in Fuel Cells*, (Eds.: U. Kramm, H.-J. Lewerenz, D. Schmeißer), Springer Science to be printed, **2016**.

3 Analytical Techniques

This chapter introduces the analytical techniques applied in this PhD study. It starts with the description of electron-matter interaction which forms the basis for electron microscopy and related spectroscopy methods. The third part of the chapter focuses on analytical techniques which are used to determine the photophysical properties of the material.

3.1 Electron-Matter Interaction

When electrons hit a sample elastic and inelastic scattering processes occur, but in the case of thin samples electrons can also pass through unscattered (see fig. 3.1). Crystallographic investigations make use of electrons which are scattered elastically by the Coulomb potential within the sample, while inelastically scattered electrons transfer energy to the sample causing the excitation of inner shell electrons. These electrons subsequently relax via the emission of Auger electrons (AE) or X-rays giving rise to several analytical methods which focus on the elemental composition of a sample. In addition, secondary electrons (SE), which are emitted as side product of inelastic scattering in the material, and back-scattered electrons (BSE) are used for imaging. Besides these signals, the emission of cathodoluminescence is observed providing insights into electrical and optical properties of materials.

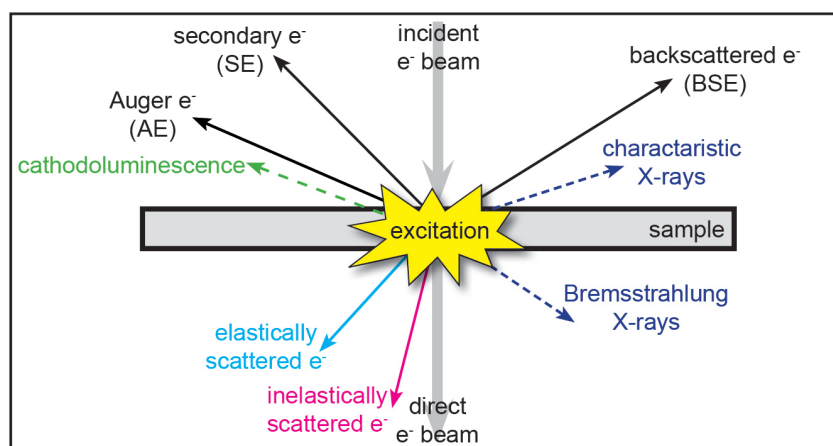


Figure 3.1 Schematic illustration of electron beam-matter interaction and the emitted irradiation.

3.2 Electron Microscopy – Imaging and Diffraction

In TEM elastically scattered electrons are used for imaging and apertures are applied to filter out electrons scattered in a certain angle regime resulting in a mixture of thickness and orientation contrast in the image. In SEM special detectors allow the detection of BSE and SE emitted from a sample due to quasi-elastic and inelastic scattering. This section briefly describes related techniques based on following textbooks.^[1-3]

3.2.1 Transmission Electron Microscopy

The Rayleigh or Abbe criterion defines the dependence of the resolution limit on the wavelength of the used irradiation. In 1932 Ruska and Knoll^[4] replaced light with electrons and built the first TEM. From then on new innovations continuously lowered the resolution limit with the transmission electron aberration-corrected microscopy (TEAM) project reaching 0.5 Å in 2008.^[5] In the following the setup of a TEM and the different factors determining the achieved resolution are described in more detail.

3.2.1.1 Setup of a Transmission Electron Microscope

The beam path through a TEM is shown schematically in figure 3.2. The electron beam is produced by the electron gun: Electrons are emitted from a cathode via thermal or field emission and accelerated towards the anode to obtain a specific kinetic energy. In the case of thermal emission, the Richardson equation ($J \approx T^2 e^{-\frac{\phi}{kT}}$) can be used to describe the dependence of the emission current density J on the work function of the metal ϕ and the temperature T , k is the Boltzmann factor. This effect provides the basis of thermionic electron guns which use tungsten ($\phi(\text{W}) = 4.5 \text{ eV}$) or lanthanum hexaboride ($\phi(\text{LaB}_6) = 2.5\text{--}2.9 \text{ eV}$) filaments heated to about 1800 °C to emit electrons. Field emission guns (FEG) on the contrary apply very strong electric fields (10^9 Vm^{-1}) to sharp tips to lower the work function and modify the potential barrier. If the field is strong enough efficient tunneling of the electrons through the potential barrier into the vacuum occurs. Compared to thermionic emitter FEGs benefit from higher intensity and a narrower energy width of the electron beam. A third gun type combines the basic principles of these two designs (Schottky emitter) featuring a higher intensity at the cost of energy width. The energy widths of the different gun types are summarized here together with the one achievable when using a monochromator:



The electron beam is focused onto the specimen by the condenser lens system which controls its intensity and convergence. The two-lens system is applied most commonly but alternative systems like the Köhler illumination exist as well. After trespassing through the specimen, at which a thickness below 100 nm is required for electron transparency, the electrons impinge on the objective lens which is located below the specimen. This lens projects an initial intermediate image of the sample region and the diffraction pat-

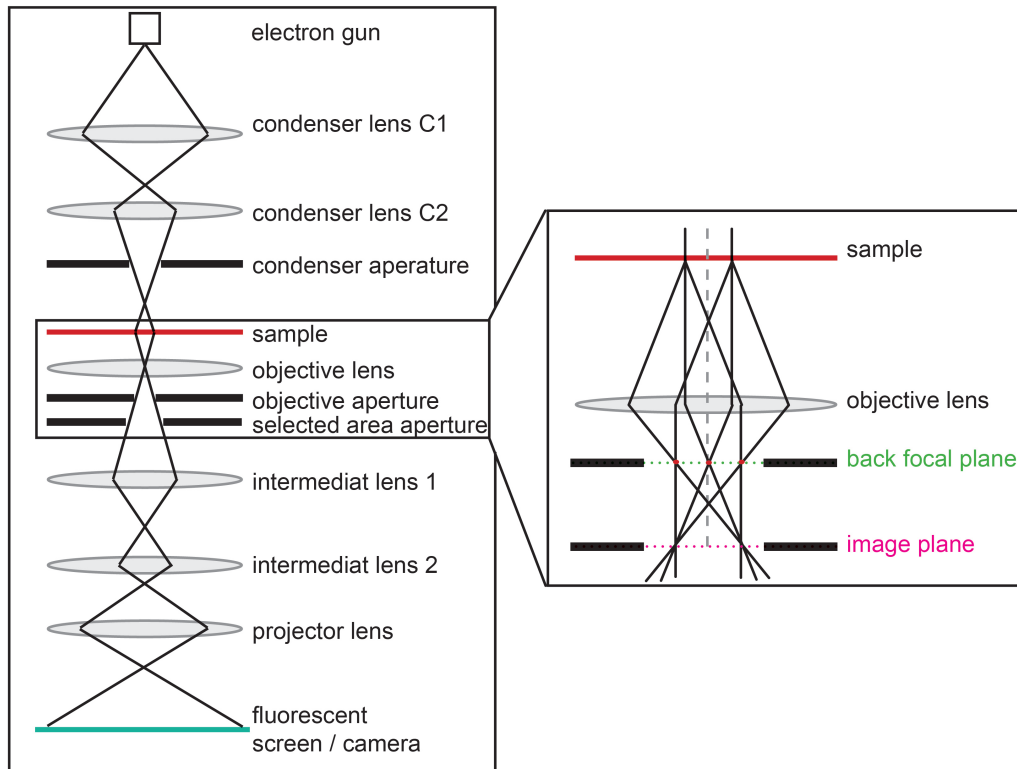


Figure 3.2 Schematic illustration of the setup of a TEM. The beam path of the electrons is given in detail for the objective lens.

tern of the samples occurs in its back focal plane (BFP). The final image is formed by the projector lens system which magnifies the intermediate image onto the fluorescent screen or a charge coupled device camera. Alternatively, the diffraction pattern obtained in the BFP is magnified and projected onto the screen.

3.2.1.2 Diffraction and Bright/Dark Field Imaging

The diffraction pattern of a sample forms in the BFP of the objective lens so that the insertion of an objective aperture in this plane features an enhanced contrast in the image as diffracted beams are blocked by the aperture and cannot contribute to the image formation.

Crystalline samples are characterized by defined reflections in the BFP which result from constructive interference of electrons scattered at atoms located at parallel lattice planes (see fig. 3.3). Constructive interference of the scattered beams occurs for path differences being an integer multiple (order of diffraction n) of the wavelength λ . The Bragg equation 3.1 describes the requirement for constructive interference as given by the scattering geometry in dependence on the lattice plane spacing d_{hkl} and scattering angle which is two times the Bragg angle θ_B .^[6]

$$n \cdot \lambda = 2d \cdot \sin(\theta_B) \quad (3.1)$$

Choosing different reflections for the image generation features different contrast modes. When the aperture is placed around the primary beam thick and strongly scattering

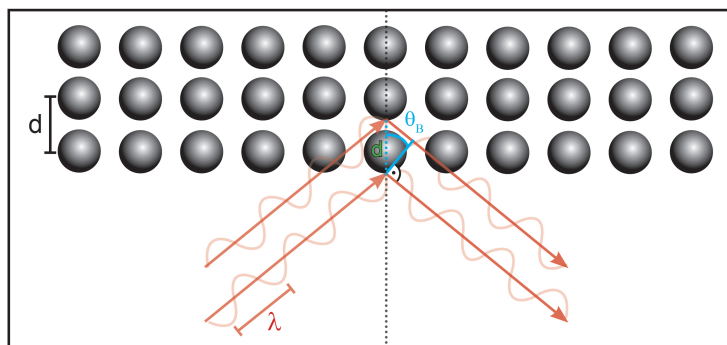


Figure 3.3 Schematic drawing showing elastic scattering at crystals which illustrates the Bragg equation.

areas appear dark in the image – this mode is called bright field (BF) mode. Alternatively the aperture can also be placed around distinct diffraction spots. The sample regions contributing to this reflection occur bright (off-axis dark field). However, aberrations are large in that case and to improve the image quality the beam is tilted such that the diffracted beam is parallel to the optical axis (on-axis dark field). The other mode of operation is the diffraction mode. The intensity variation and distances between the diffraction spots combined with the symmetry of the diffraction pattern are characteristic for a crystalline material and can be used to identify the crystal structure and orientation. When the diffraction pattern is projected onto the camera the lattice spacing d_{hkl} can be determined directly from the distance between primary beam and diffraction spot dependent on the camera constant of the microscope. The selected area electron diffraction (SAED) aperture which is inserted into the image plane of the objective lens allows to selectively choose a region of interest for the diffraction experiment which gives rise to a detailed analysis of the crystallographic properties of a sample.

3.2.1.3 High Resolution TEM

Electrons can be described as planar waves whose phases are modulated by interactions with the Coulomb potential of the atomic nucleus and propagation through space. The resulting exit wave experiences additional phase shifts by the optical system of the TEM due to aberration of the lens optics and different path lengths introduced by defocusing the lens. This is described in terms of spatial frequencies u by the contrast transfer function (CTF) which transforms the exit wave into the image wave. Thin samples are thought of as weak phase objects for which a constant amplitude of the electron wave is assumed and a simplified contrast transfer function can be used.

$$CTF = \sin\chi(u) \quad (3.2)$$

with

$$\chi(u) = \frac{2\pi}{\lambda} \left(\frac{1}{4} C_s \lambda^4 u^4 - \frac{1}{2} \Delta f \lambda^2 u^2 \right) \quad (3.3)$$

The shape of the contrast transfer function depends on the angular phase shift caused by the defocus Δf of the objective lens and the spherical aberration as well as on the

wavelength of the electrons λ given by the acceleration voltage. The spherical aberration (spherical aberration coefficient C_s) describes the fact that electrons are refracted more strongly at the outer part of a lens compared to its center so that they do not meet at a focal point behind the lens but form a disc of least confusion instead. The first zero-crossing of the CTF marks the transition from a region of similar contrast to regions where the contrast oscillates and contrast reversal occurs. The first zero defines the point resolution (see fig. 3.4a) – which is the resolution for which the phase contrast image is directly interpretable and where all atomic positions occur dark on a bright background. The maximum point resolution achievable by a microscope is given by the Scherzer defocus defined according to equation 3.4:

$$\Delta f_{Scherzer} = -1.2\sqrt{C_s\lambda} \quad (3.4)$$

However, the resolution of a microscope is further affected by the total envelope function $E_t(u)$ which describes the damping of spatial frequencies due to limited spatial and temporal coherence of the electron wave (see fig. 3.4b). $E_t(u)$ defines the information limit of a microscope. The spatial envelope is given by the electron source $E_s(u)$ which is not an ideal point source. The temporal coherence is determined by the chromatic aberration $E_c(u)$, the instability of the high tension/objective lens current and also by the energy width of the electron source. The chromatic aberration (chromatic aberration coefficient C_c) is caused by the failure of lenses to focus electrons of different wavelengths to the same spot. In addition to limited spatial and temporal coherence specimen drift $E_d(u)$, vibrations $E_v(u)$ and also detector instabilities $E_D(u)$ contribute to the envelope function and affect the information limit. The total envelope function is thus given by:

$$E_t(u) = E_c(u) \cdot E_s(u) \cdot E_d(u) \cdot E_v(u) \cdot E_D(u) \quad (3.5)$$

The spherical aberration causes the resolution of uncorrected microscopes to be limited by the point resolution. C_s correctors produce a negative spherical aberration coefficient C_s to cancel the positive C_s of the projection optics. Thus, the resolution of a C_s corrected microscope is no more limited by the point resolution but by the information limit of the microscope (see fig. 3.4c). In this regard the application of a C_c corrector in addition to a C_s corrector further improves the resolution of the microscope due to a higher information limit by reducing the damping of the temporal envelope. Double corrected machines feature the highest resolution possible today allowing to resolve up to 0.5 \AA .^[5]

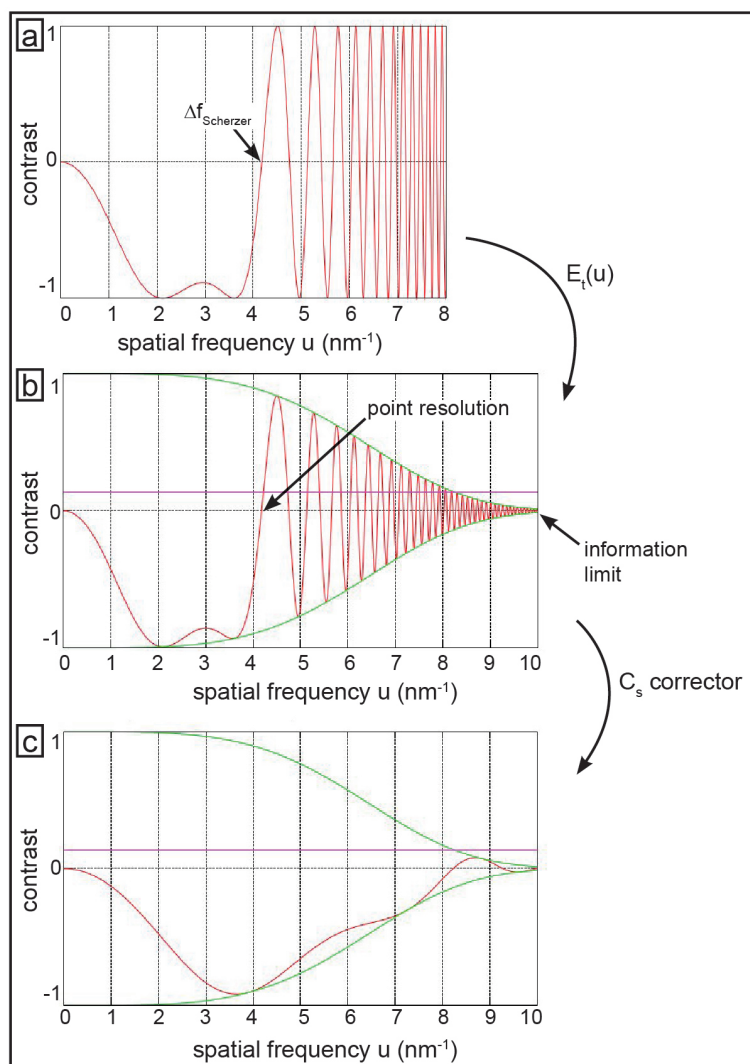


Figure 3.4 Illustration of the CTF with and without C_s correction. a) The initial CTF is calculated for $\lambda=0.0025$ eV, $\Delta f=60$ nm and $C_s=1.1$ mm. b) Damping of this CTF by spatial and temporal envelope functions for (b) ($C_c=1.6$ mm, $\Delta E=0.7$ eV, $E=300$ keV). c) Effect of correction of the spherical aberration on the CTF $\Delta f=23.92$ nm and $C_s=0.159$ mm, $C_c=1.6$ mm, $\Delta E=0.7$ eV (simulation taken from reference.^[7]).

To perfectly reconstruct the exit wave from the image both the phase and the amplitude information of the image wave are required. Unfortunately the phase information is lost due to the fact that the intensity of the image wave is detected by TEM. This problem is solved by the acquisition of defocus series with defined focus steps which allow to reconstruct the exit wave taking advantage of the focus dependence of the CTF. The reconstructed exit wave is compared to a simulated exit wave achieved by the multislice algorithm. This algorithm describes the propagation of the planar electron waves through the crystal which is considered a sequence of projected crystal potentials separated by vacuum. The comparison of reconstructed and simulated exit waves allows a detailed interpretation of HRTEM data.

3.2.1.4 In Situ TEM Heating Experiments

The effect of heat on the atomic structure of a material is an important factor which has to be taken into account at developing new material systems. In situ TEM investigations are challenging due to the thermal expansion of materials at elevated temperatures, causing drastically increased drift of the sample holder. Different heating holder designs were developed to allow controlled in situ heating of a specimen with minimal drift.^[8] Conventional heating holders are based on a small furnace located around the TEM grid to control the temperature at the sample. To minimize heating of the holder and related drift, the holder is cooled by water. Atomic resolution is possible,^[9,10] but challenging when operating these holders at temperatures above 500 °C. The relative low melting point of copper ($T_{melt} = 1083$ °C) prevents to use copper grids above 500 °C but more temperature stable grids made of molybdenum ($T_{melt} = 2625$ °C) should be used instead.^[11] Due to the increased temperature of the holder the objective aperture, which is located very close to the sample, should be removed. Furthermore, EDX measurements (in the case of a beryllium window in front of the detector) are not possible during the experiment.

To resolve these issues new holder designs are based on metal contacts embedded in silicon nitride chips. If a current flows through the material the temperature T can be regulated and determined from the measured resistance $R(T)$ according to the following equation

$$R(T) = a \cdot T^2 + b \cdot T + c \quad (3.6)$$

with a , b and c as chip related constants. Electron transparent windows in the chip enable the investigation of the sample. The low thermal expansion of silicon nitride results in a high stability of the holder at elevated temperatures even allowing the investigation of material at the atomic scale at temperatures of 1000 °C. The narrow localization of heat at the chip supersedes water-cooling of the holder and in situ EDX and BF investigations are possible during the heating experiment.

3.2.2 Scanning Transmission Electron Microscopy

In STEM a convergent electron beam is scanned over the specimen and the resolution of STEM images is defined by the quality of the condenser lens system which determines the size of the electron beam. The electrons which pass through the sample are scattered in different angles and are detected point by point by STEM detectors.

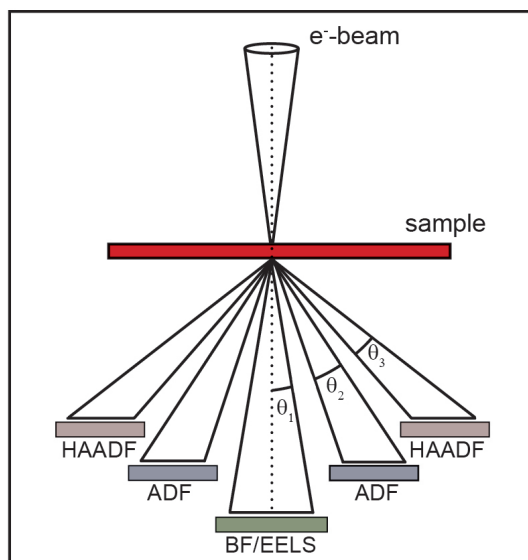


Figure 3.5 Schematic illustration of STEM detectors which detect electrons for different scattering angles.

STEM detectors consist of two or three ring detectors allowing to selectively detect certain scattering angles (see fig. 3.5). The inner detector (BF detector) records electrons scattered in small angles in forward direction ($\theta_1 < 10-25$ mrad), while the annular dark field (ADF) detector detects elastically scattered electrons for angles of $25 < \theta_2 < 50$ mrad. The contrast in BF mode equals the one of conventional BF images whereas thick and crystalline regions appear bright in ADF images.

Electrons scattered incoherently into angles larger than 50 mrad (θ_3) (Rutherford scattering) are detected with a HAADF detector. While HRTEM is based on the interference of coherently scattered electrons leading to a complicated interference pattern (sec-

tion 3.2.1.3) the contrast in HAADF can be interpreted intuitively. This is due to the Z -contrast in the image given by the Rutherford cross-section which scales with $I \approx Z^2$. Z is the atomic number which is why heavy elements appear bright in HAADF. Furthermore, STEM also enables the detection of analytical signals (see section 3.3) with high spatial resolution offering the possibility of simultaneous spectroscopy and image acquisition.

3.2.3 Scanning Electron Microscopy

Scanning electron microscopy is a technique which images the topology of a sample at the nano- to microscale by scanning the electron beam over the sample. The interaction of the electron beam with the sample material results in the emission of SE, BSE and X-rays due to inelastic scattering processes. These signals are used for imaging and qualitative composition analysis (see section 3.3.2). The small convergent angle of the electron beam yields a large depth of field, which is characteristic for SEM images and features an intuitive 3D impression of the sample surface.

The electron source (FEG or thermal emitters) generates an electron beam with typical energies in the range of 0.2 to 40 keV which is focused onto the sample surface by the condenser lens system reaching beam diameters between 0.4 and 5 nm. The scanning of the electron beam is managed by scanning coils or deflector plates (see fig. 3.6a). SE

and BSE emitted from the sample are collected by detectors mounted above the sample (Everhart-Thornley^[12] or In-lens detectors). The escape depth of secondary electrons is limited to the upper 50 nm of the sample volume due to their low energy. These electrons allow the investigation of the sample topology owing to edge and shadowing effects (see fig. 3.6b): SE have a high yield at edges and perturbations and are attracted to the detector by a positive potential applied to the Everhart-Thornley grid. Back-scattered electrons on the contrary result from quasi-elastic scattering processes and feature energies close to the energy of the incident beam, meaning that they are emitted from much deeper sample regions. Their yield strongly depends on the atomic number of the elements in the sample featuring a material contrast. Figure 3.6c shows the comparison of a SE with a BSE image detected for platinum decorated $\text{Nb}_3\text{O}_7(\text{OH})$ superstructures: While the Pt particles are invisible in the SE image they show up as bright spots in the BSE image.

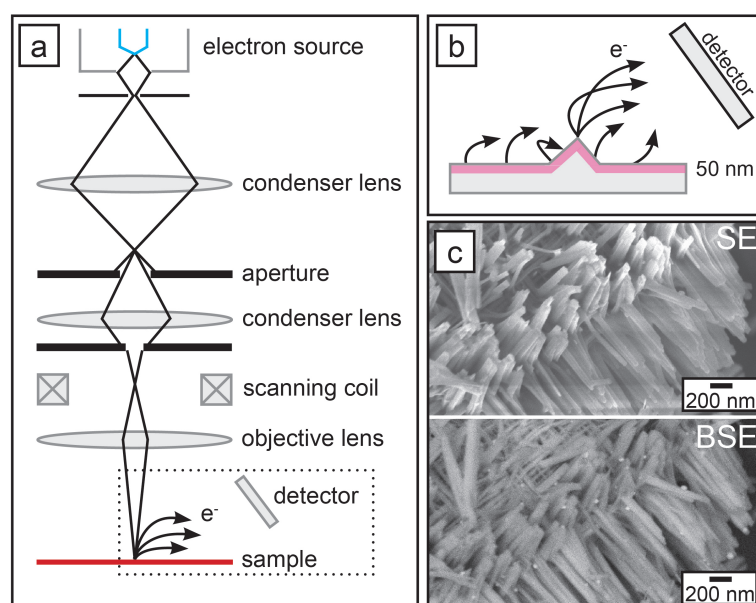


Figure 3.6 Schematic illustration of the setup (a) and image generation of a SEM. b) The principles of edge and shadowing effects, which form the basis of the image generation in SEM, are illustrated. c) Comparison of a BSE and a SE image detected for the same sample region of platinum decorated $\text{Nb}_3\text{O}_7(\text{OH})$ superstructures.

3.3 Electron Microscopy – Spectroscopy

Inelastically scattered beam electrons give rise to several analytical methods, either by directly measuring the lost energy or by indirectly detecting the X-rays excited by beam electrons. The following section gives further insights into the different features detected by EELS and introduces the working principle of EDX spectroscopy. The descriptions are based on the following references.^[1,3,13,14]

3.3.1 Electron Energy-Loss Spectroscopy

EELS detects the energy-loss of electrons which passed through a sample and were scattered inelastically. The electrons are filtered according to their energy using a magnetic prism (fig. 3.7a) which focuses electrons with the same energy to one point in the energy-dispersive plane. Several interactions of the beam electrons with the material are possible generating distinct features in an EEL spectrum. Generally, an EEL spectrum can be separated into two main regions: the low-loss region for energy losses smaller than 50 eV and the core-loss region for higher losses (fig. 3.7b).

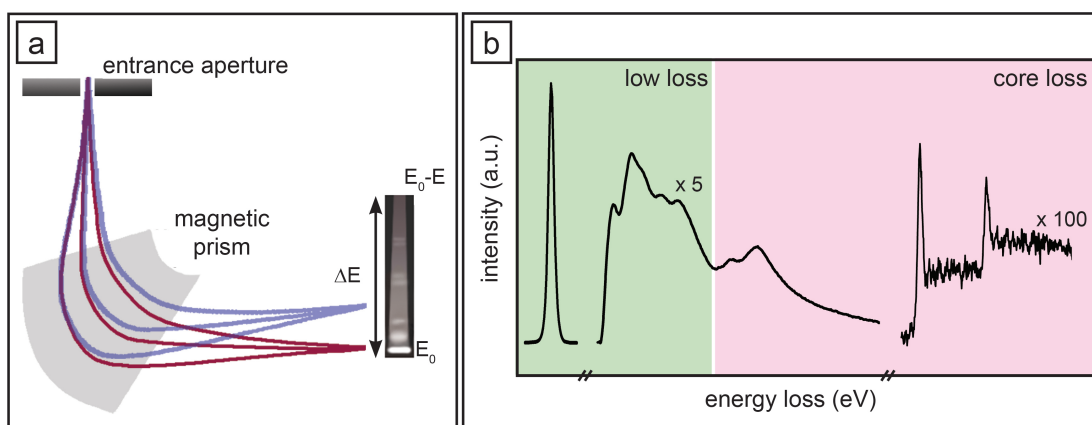


Figure 3.7 Schematic illustration of an EEL spectrometer and spectrum. a) Scheme showing the magnetic prism used to filter the electrons according to their energy. b) Exemplary EEL spectrum showing its main components. The low-loss region is composed of the zero loss peak, plasmon peak and intra- and interband transitions, while element specific edges show up in the core loss region.

Most electrons pass through the sample without losing energy resulting in a dominant feature in the spectrum, the so called zero-loss peak (ZLP). Together with the plasmon the ZLP forms the major component of the low-loss region. Next to features originating from collective oscillations of the free electron gas (plasmonic excitation) the low-loss region also comprises features caused by intra- and interband transitions. In this regard, the shape and intensity of the low-loss region encodes several sample properties, e.g. its thickness (see section 3.3.1.1), band gap (see section 3.3.1.2) and phase. In combination with the core-loss region, which contains element specific ionization edges showing the sample composition, EEL spectra allow a detailed analysis of the bonding behavior and oxidation states of ions. The resolution of an EEL spectrum is determined by the monochromacy of the electron beam and hence depends on the electron gun. However,

it can be improved further by using a monochromator, which allows energy resolutions below 0.2 eV.

3.3.1.1 Thickness Measurements

The intensity of the plasmon peak is determined by the probability of multiple scattering events which in turn depend on the mean free path of an electron in the material λ_p and the sample thickness. Figure 3.8 shows two low-loss spectra detected for two different thicknesses of the same material.

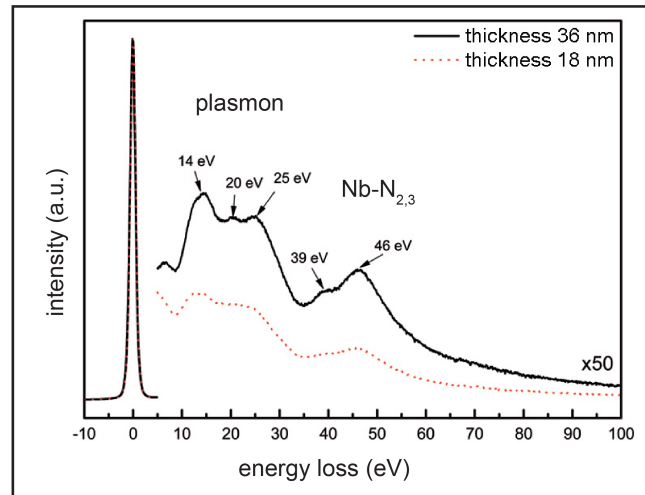


Figure 3.8 The sample thickness is encoded in the intensity of the plasmon peak. Two EEL spectra recorded for two different thicknesses of $\text{Nb}_3\text{O}_7(\text{OH})$ nanowires are shown. Taken from reference.^[15]

The altered intensity ratio of ZLP and plasmon peak forms the basis of the log-ratio method:^[16]

$$e^{-\frac{t_s}{\lambda_p}} = \frac{I_0}{I_t} \quad \Rightarrow \quad t_s = \lambda_p \cdot \ln\left(\frac{I_t}{I_0}\right) \quad (3.7)$$

here I_0 is the intensity of the zero-loss peak, I_t the intensity of the whole low-loss region, t_s the sample thickness and λ_p the mean free path.

3.3.1.2 Band Gap Determination

For semiconducting materials the onset of the first transition in an EEL spectrum equals the size of the band gap as the interband excitation of electrons from the VB to the CB requires the least amount of energy. The linear fit method^[17] estimates the band gap from the intersection of a straight line originating from the background level, achieved by removing the ZLP from the spectrum, with a linear fit to the onset of the transition. However, for materials with refraction indexes > 1.5 , certain acquisition conditions (small collection angles) and sample thicknesses the band gap determination is hindered by additional features in the spectrum region between 1 and 5 eV. These features are caused by the Čerenkov radiation which is emitted when electrically charged particles pass through a dielectric medium at greater speed than the phase velocity of light in this

medium.^[18,19] The measurement conditions applied for the band gap analysis in the present work minimize the contribution of Čerenkov losses. As an example figure 3.9 shows the band gap determination performed for H-Nb₂O₅ nanowires.

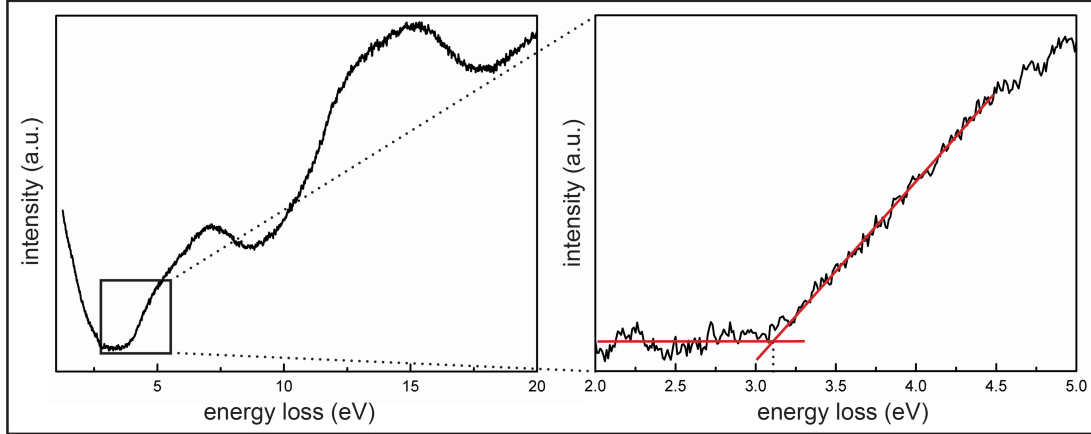


Figure 3.9 Low-loss EEL spectrum acquired for H-Nb₂O₅ used for the determination of the band gap. The band gap was determined with the linear fit method reported in literature.^[17]

3.3.1.3 Analysis of the Near Edge Fine Structure

The core-loss region of an EEL spectrum contains the ionization edges of each element present in the sample. These features evolve when a beam electron transfers energy onto a core-shell electron (K, L, M, N) which is then excited to unoccupied states above the Fermi level. Atoms are characterized by discrete energy levels. Due to electrostatic interactions of the electrons, these levels split up as soon as two atoms approach each other and molecular orbitals form. In a crystal many atoms interact causing a smearing of the atomic energy levels to energy bands due to superposition of the atomic orbitals of many atoms. The thickness of a band reflects the delocalization of electrons of the respective energy level throughout the crystal. Hence, as electrons of lower energy levels are bound stronger to the nucleus these bands are narrower than high energy level bands like the valence or conduction band (fig. 3.10a). The density of states (DOS) is defined as the number of states per energy interval and thus illustrates the band structure of a material.

The energy ΔE necessary for the excitation of an inner-shell electron to unoccupied states depends on the atomic bonding in the material of the element and the shell of the respective electron. Fermi's golden rule describes the probability for this excitation per time unit and area. The transition rate $W(\Delta E)$ depends on the transition matrix element $M(\Delta E)$, which correlates initial and final state, and the DOS of the conduction band $N(\Delta E)$.

$$W(\Delta E) \propto |M(\Delta E)|^2 \cdot N(\Delta E) \quad (3.8)$$

The energy-loss near edge fine structure (ELNES) describes the first 50 eV of the edge and is dominated by bonding effects. In the case of an only slightly varying $M(\Delta E)$ it represents the DOS above the Fermi level as illustrated in figure 3.10b. It thus depends on the oxidation number and local surrounding of the atom in the sample and theoretical calculations can be used for a detailed interpretation of the ELNES. Small oscillations observed at energy losses above the first 50 eV of the edge in the so called extended energy-loss fine structure are related to the atomic arrangement in the crystal. In the following a detailed description of the ELNES observed for the ionization edges investigated in this study is given.

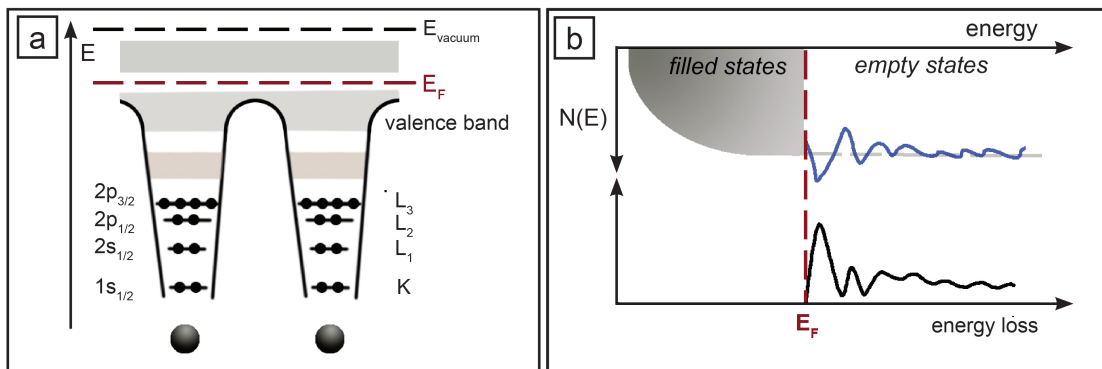


Figure 3.10 Schematic illustration of the band structure and the origin of the ELNES. a) Band structure of a crystal showing inner shell states as well as the VB and CB. b) The ELNES reflects the DOS of the material.

3.3.1.3.1 Nb-M_{2,3} Edge

This edge is associated to the excitation of Nb-3*p* electrons to unoccupied Nb-4*d* and Nb-5*s* states and is observed for energy losses between 350 and 440 eV. Its ELNES is characterized by two white lines which reflect the spin-orbital splitting of Nb-3*p*_{3/2} and Nb-3*p*_{1/2} states (fig. 3.11). For Nb₂O₅ and Nb₃O₇(OH) high-energy shoulders appear for both white lines. Theoretical calculations indicate that this double peak structure is caused by inequivalent niobium positions in the crystal lattice and different crystal field splitting.^[20] These shoulders are not visible for NbO and less pronounced in NbO₂ spectra.^[21,22]

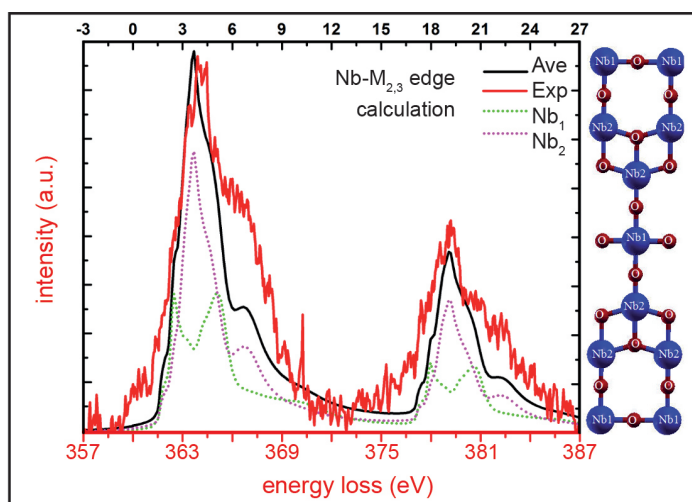


Figure 3.11 Experimental and theoretical ELNES of the Nb-M_{2,3} of Nb₃O₇(OH). The comparison of theory and experiment shows the contribution of inequivalent lattice sites Nb₁/Nb₂ to the ELNES of the edge (taken from reference^[20]).

3.3.1.3.2 Ti-L_{2,3} Edge

Several experimental and theoretical studies^[23–27] discussed the ELNES of the Ti–L_{2,3} edges of various titanium oxides leading to a better understanding of its shape. It is visible in the energy loss range of 450 to 500 eV and results from the transition of Ti-2*p* electrons to unoccupied Ti-3*d* states (fig. 3.12). A splitting of the edge into two white lines is observed, attributable to the spin-orbital splitting of the 2*p* orbital in 2*p*_{3/2} (L₃) and 2*p*_{1/2} (L₂) states,^[27] which is 5.4 eV for both anatase and rutile TiO₂.^[25] The crystal-field splitting of *t*_{2*g*} and *e*_g orbitals causes an additional splitting of these two white lines leading to two doublets, because electrons are excited from the 2*p*_{3/2} or 2*p*_{1/2} to unoccupied *t*_{2*g*}/*e*_g states. The shape and splitting of these doublets depends on the occupancy of the *t*_{2*g*} orbital which in turn reflects the oxidation state of titanium. Ti(IV)O₂ yields distinct doublets due to completely empty *t*_{2*g*} states, increasing occupation of the *t*_{2*g*} states results in decreasing intensities of the peaks *a* and *b* with no observable doublet splitting for fully occupied *t*_{2*g*} states (Ti(II)O). The shape alteration goes along with a shift of the onset of the L_{2,3} edge to lower energies with decreasing oxidation state of titanium reaching a minimum of 356 eV for metallic titanium.^[27] Two possible explanations for this shift were proposed: Either it is due to an incomplete screening of core hole formed as a result of the excited electron^[27] or caused to increased strength of the covalent Ti–O bond resulting from the decreasing number of d-electrons.^[28] Both crystal structures of anatase and rutile TiO₂ comprise TiO₆ octahedra leading to very similar short-range titanium and oxygen environments. Nevertheless, the ELNES of Ti–L_{2,3} shows a significant difference in the form of an additional low-energy (rutile) respectively high-energy (anatase) shoulder of peak *a*' (fig. 3.12). These features are related to a distortion of the TiO₆ octahedra in the crystal lattice in the form of an elongation of O–Ti–O bond in *c* direction and a deviation in the O–Ti–O angles from 90°.^[23,25]

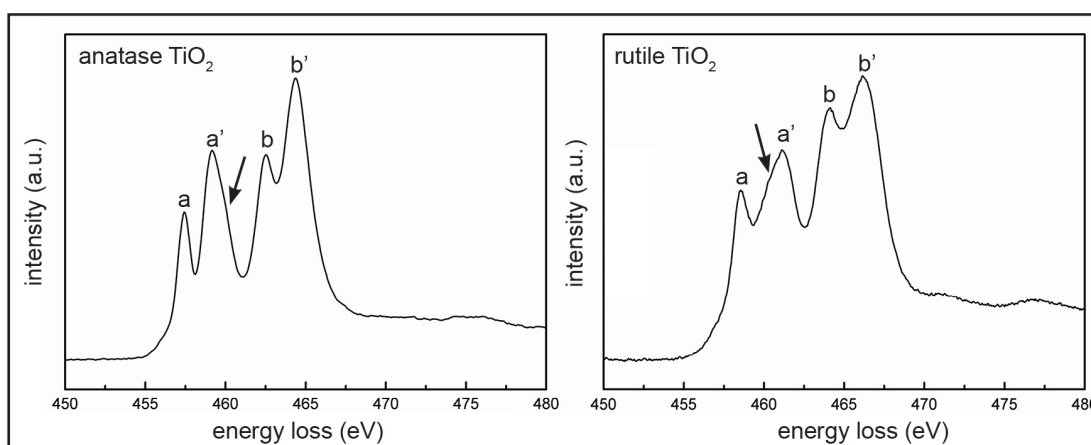


Figure 3.12 Experimental Ti-L_{2,3} edge recorded for anatase^[29] and rutile TiO₂. Additional high-energy (anatase) respectively low-energy (rutile) shoulders are marked with arrows.

3.3.1.3.3 O-K Edge

The O-K edge results from transitions of O-1s core-electrons to unoccupied O-2p states. In the case of titanium oxide these O-2p states form σ^* hybrid orbitals with empty Ti-3d states which are split into e_g and t_{2g} due to the octahedral coordination of titanium. Transitions from O-1s to $\sigma_{t_{2g}}^*$ yield peak *a*, the excitation to $\sigma_{e_g}^*$ peak *b*. The ligand field splitting of e_g and t_{2g} orbitals depends on the magnitude of covalency of the bonding which is determined by the number of *d*-electrons of titanium (the oxidation state). Empty *d* states feature a covalent bonding for TiO₂ which becomes ionic for Ti(II)O, thus a splitting of 2.5 eV is observed for rutile/anatase TiO₂ which decreases to 1.8–1.9 eV for TiO. The peaks *c*, *d*, *e* observed at higher energy losses result from excitations to O-2p, Ti-4s and Ti-4p hybrid orbitals (fig. 3.13).^[27,28]

In the case of niobium oxide the O-K edge (fig. 3.13) is characterized by a double peak-structure (*a* and *b*) just above the ionization edge followed by several other peaks offering the best fingerprint for different niobium oxides (fig. 3.13). The intensity ratio of peak *a*-to-*b* changes with the oxidation state of niobium (Nb(V)₂O₅, Nb(IV)O₂ and Nb(II)O) featuring a decreased intensity of peak *a* and a smaller peak splitting for lower oxidation states. The latter agrees with the observation for TiO₂. The altered ELNES goes along with a shift of the onset to higher energy losses with decreasing oxidation numbers, with a maximum of 533.2 eV observed for Nb(II)O.^[21,22] Theoretic calculations performed for Nb₃O₇(OH) reveal the contribution of inequivalent oxygen sites to the peaks of the O-K edge.^[20]

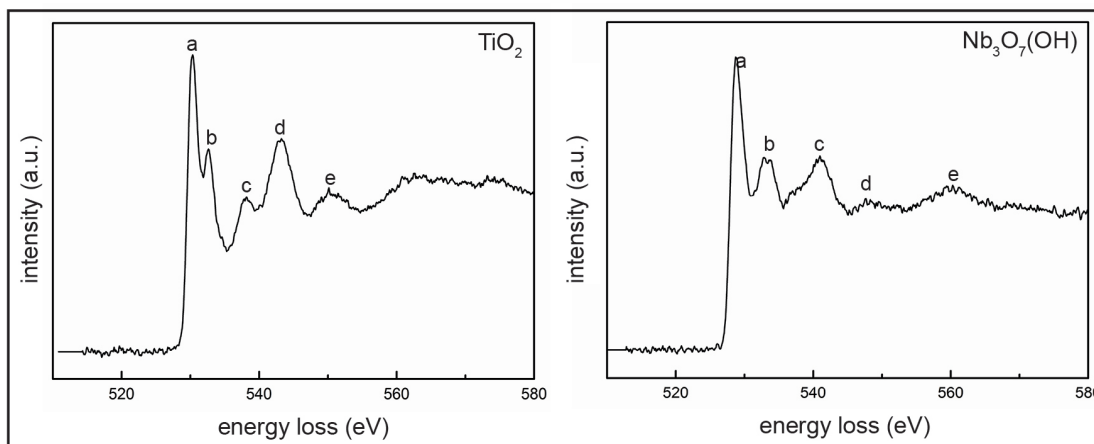


Figure 3.13 Experimental O-K edge recorded for anatase TiO₂ and Nb₃O₇(OH).

3.3.1.4 Quantification of the Elemental Composition

EELS can be used for quantitative analysis of the sample composition with a detection limit of 0.1 at%. The quantification is based on the following equation:

$$I_A(\beta, \Delta) = N_A \cdot \sigma_A(\beta, \Delta) \cdot I_e \cdot t. \quad (3.9)$$

The intensity I_A of the ionization edge depends on the partial ionization cross-section $\sigma(\beta, \Delta)$, which describes the excitation probability of core electrons to unoccupied states, and the elemental composition N_A of the specimen. EELS data are acquired for a certain collection angle β given by the spectrometer entrance aperture which blocks parts of the signal thus affecting the intensity in the spectrum. The background must be removed from the spectrum prior to the analysis, which is usually done by fitting a power law function ($I \approx A\Delta E^{-r}$; with r and A being fitting parameters). I_A is then obtained by integration over a defined energy loss window Δ . Equation 3.9 describes the dependence of the intensity of the edge I_A on σ_A , the beam current of the electron beam I_e , the acquisition time t and the number of atoms per unit area N_A .

Most commonly the atomic ratio of two elements is required which can be calculated according to following the equation.

$$\frac{I_A(\beta, \Delta)}{I_B(\beta, \Delta)} = \frac{N_A \cdot \sigma_A(\beta, \Delta) \cdot I_{e,A} \cdot t_A}{N_B \cdot \sigma_B(\beta, \Delta) \cdot I_{e,B} \cdot t_B} \quad (3.10)$$

I_e and t can be canceled for identical measurement condition which facilitates the analysis. The partial ionization cross-section σ can either be determined theoretically using the Hartree-Slater or the hydrogen model or experimentally with a reference sample. Quantification analysis via EELS has an uncertainty of about 5 at% caused by the background correction, determination of σ and the integration of the intensity of the different ionization edges.

3.3.2 Energy-Dispersive X-ray Spectroscopy

EDX is an alternative method to analyze the sample composition. The emission of characteristic X-rays is stimulated by beam electrons which excite an electron from the inner-shell to unoccupied states. The remaining unoccupied inner-shell state is

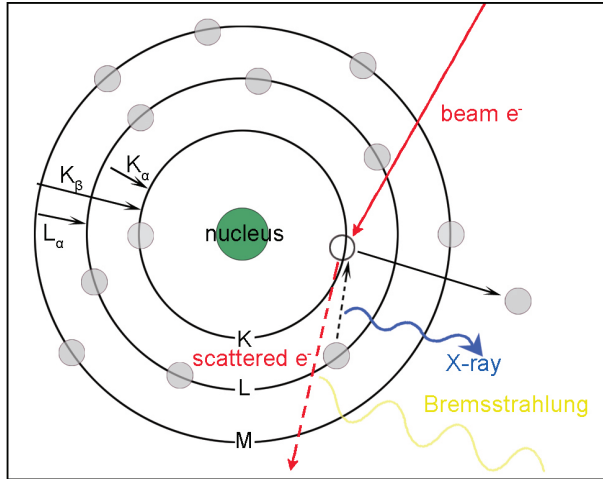


Figure 3.14 Schematic drawing illustrating the formation of characteristic X-rays and Bremsstrahlung.

subsequently filled with an outer shell electron and the excessive energy is emitted either in the form of an Auger electron or a photon (X-ray) (fig. 3.14). The emission of X-rays or AEs is a competing process with the probability of X-ray emission increasing with the atomic number Z of the element as given by the fluorescence yield. The positions of the energy shells are characteristic for each element and so are the energies of the emitted X-rays resulting in distinct peaks in the spectrum. Next to element specific peaks an X-ray continuum (Bremsstrahlung) is present in

EDX spectra, which results from X-rays emitted during deceleration of electrons due to interactions with the electric field of the atomic nucleus.

The element determines the peak position while its concentration is reflected in the intensity I of the peak enabling the semi-quantitative analysis of the sample composition $\frac{c_A}{c_B}$ ($c_{A/B}$ equals the concentration of element A/B).

$$\frac{c_A}{c_B} = k_{ab} \frac{I_A}{I_B} \quad (3.11)$$

The method developed by Cliff and Lorimer^[30] uses the Cliff-Lorimer factor k_{ab} (see equation 3.11) to approximate the influence of the element specific fluorescence yield and ionization cross-section. In addition, k_{ab} accounts for the efficiency of the applied detector and the fact that an ionized K-shell can relax both ways by emitting K_α or K_β irradiation. The k_{ab} value can be determined either experimentally or calculated from first principles. Unfortunately, the low X-ray yield and the enhanced absorption of low-energy X-rays in the detector prohibits quantitative analysis of light elements by EDX.

3.4 X-ray Diffraction and Photon Based Spectroscopy

Several spectroscopic and diffraction techniques exist which apply photons or X-rays as illumination source. The following section describes the basic principles of X-ray diffraction (XRD), Ultraviolet/visible light (UV/Vis) and photoluminescence (PL) spectroscopy experiments based on the following references.^[31–33]

3.4.1 X-ray Diffraction

X-rays can be scattered elastically by solid materials and in the case of a crystalline sample a diffraction pattern forms which contains information on the crystal structure. Amorphous materials lack ordered atomic arrangement resulting in diffuse scattering, while distinct reflections are observed for crystals, which form rings for polycrystalline samples. As it was described for elastic electron scattering the Bragg equation (equation 3.1) predicts in which directions θ_B reflections are to be expected. Their intensities are determined by the sum of scattering factors f of the atoms in the unit cell – called structure factor F_{hkl} .^[34]

$$F_{hkl} = \sum_j^N f_j \exp[2\pi i(hx_j + ky_j + lz_j)] \quad (3.12)$$

F_{hkl} is the sum over the atomic form factor f over all atoms N in the unit cell taking their coordinates xyz and Miller indices hkl into account. The intensity of the respective reflections is $I \propto |F_{hkl}|^2$.

Still, the shape of the reflections is affected by several parameters: Nanosized crystals cause a reflection broadening which allows to determine the crystallite size via the Scherrer equation.^[35] The shape of a crystal can furthermore affect the intensity of certain reflections.^[36] Dopants in the crystal lattice alter the peak position due to enhanced or decreased d_{hkl} lattice spacings caused by the incorporation of foreign atoms into the crystal lattice. Hugo Rietveld developed a technique to simulate measured diffraction pattern which allows the analysis of the shape of the reflections yielding in depth information about the sample characteristics.^[37] The method uses the least square fitting approach to refine a theoretical line profile until it matches the measured pattern taking account of the characteristics of the X-ray beam and experimental setup.

3.4.2 UV/Vis and PL Spectroscopy

Light absorption as a function of the wavelength provides information about electronic transitions occurring in a material. This forms the basis of UV/Vis spectroscopy which measures the optical absorbance A of materials in the wavelength regime of 250 to 800 nm (UV/Vis). Spectrometer detect the fraction of light transmitted through the investigated material I versus the incident light intensity I_0 and the absorbance is defined as the negative decadic logarithm of $\frac{I}{I_0}$. The Beer-Lambert law relates the absorbance with the molar absorptivity coefficient ϵ of the material, its concentration c and the length of light through the material l (e.g. film thickness):

$$A = \epsilon \cdot c \cdot l = -\log\left(\frac{I}{I_0}\right) \quad (3.13)$$

UV/Vis spectroscopy offers a convenient method to determine the band gap of semiconductors. A classical semiconductor mainly absorbs light exceeding its band gap energy E_g , which is illustrated in the sharp increase of ϵ at E_g . The absorption can be modeled by the Tauc formula,^[38] which describes the dependence of the absorption coefficient a on the energy of the illumination source given by the product of light frequency ν and Planck constant h .

$$a \cdot h\nu = K[(h\nu - E_g)]^{m/2} \quad (3.14)$$

K is called band tailing parameter and depends on the width of localized states in VB and CB, while the exponent m distinguishes between direct ($m = 1$) and indirect ($m = 2$) transitions. This relationship allows an estimation of the band gap energy E_g by extrapolating the linear region of the data achieved by plotting $h\nu$ versus $(a \cdot h\nu)^{1/m}$ to the baseline.^[39]

Photoluminescence is the radiative relaxation of photoexcited charge carriers and PL measurements are utilized to gain insight into radiative and non-radiative rate modifications of different materials. The applied time-resolved studies are able to distinguish between radiative and non-radiative relaxation channels. In general the combination of PL spectra and PL lifetime measurements allows to investigate semiconductor band structures and exciton binding energies. These material properties can be improved by different fabrication methods and different dopants allowing the optimization of the photophysical properties of materials to enhance the resulting device performance.

3.5 Instrumentation

Table 3.1 summarizes the different electron microscopes used in this thesis.

Table 3.1 Used electron microscopes.

Scanning electron microscopes	
<i>Zeiss Gemini Ultra Field</i>	Imaging with In-lens, BSE and SE detector (4 keV).
<i>Jeol JSM-6500F</i>	EDX measurements (15 to 30 keV) with <i>Oxford Instruments</i> EDX detector.
Transmission electron microscopes	
<i>Jeol 2011</i>	TEM imaging (200 keV) and EDX measurements with <i>EDAX</i> EDX detector.
<i>Jeol 3010</i>	In situ heating experiments with a conventional <i>Gatan</i> heating holder (300 keV).
<i>Jeol JEM-2200FS</i>	In situ heating experiments with a silicon nitride chip supplied by <i>DeNS solution</i> (200 keV).
<i>Philips CM200</i>	TEM & STEM imaging (200 keV), EDX with <i>Oxford Instruments</i> EDX detector & EELS measurements.
<i>Philips CM300</i>	HRTEM imaging (300 keV, $C_s = 0.6$ mm) & EELS measurements.
<i>FEI Tecnai G2 20 S-TWIN</i>	CTEM imaging (200 keV), EDX measurements with <i>EDAX</i> EDX detector.
<i>FEI Titan 80–300</i>	STEM & TEM imaging (300 keV), EDX measurements with <i>EDAX</i> EDX detector.
<i>FEI Titan3 G2 60-300</i>	Low-loss EELS investigation (80 keV).
<i>FEI Titan 60–300</i>	TEM & STEM imaging (300 keV), in situ heating with <i>Protochip</i> holder, tomography with <i>Hummingbird</i> holder, EDX measurements with <i>Bruker SuperX</i> EDX detector.
<i>FEI TEAM 0.5</i>	TEM & STEM imaging (80 keV, 300 keV) equipped with a monochromator, C_c and C_s corrector, low-loss EELS investigation.
<i>Zeiss Libra MC200</i>	Monochromated EELS investigation (200 keV).

3.6 References

- [1] P. J. Goodhew, J. Humphreys, R. Beanland, *Electron Microscopy and Analysis, Third Edition*, Taylor & Francis, **2000**.
- [2] P. Goodhew in *Aberration-Corrected Analytical Transmission Electron Microscopy*, John Wiley & Sons, Ltd, **2011**, pp. 1–19.
- [3] D. B. Williams, C. B. Carter, *Transmission Electron Microscopy: A Textbook for Materials Science*, Springer, **2013**.
- [4] M. Knoll, E. Ruska, *Z. Physik* **1932**, *76*, 21.
- [5] C. Kisielowski, B. Freitag, M. Bischoff, H. van Lin, S. Lazar, G. Knippels, P. Tiemeijer, M. van der Stam, S. von Harrach, M. Stekelenburg, M. Haider, S. Uhlemann, H. Müller, P. Hartel, B. Kabius, D. Miller, I. Petrov, E. A. Olson, T. Donchev, E. A. Kenik, A. R. Lupini, J. Bentley, S. J. Pennycook, I. Anderson, A. M. Minor, A. K. Schmid, T. Duden, V. Radmilovic, Q. M. Ramasse, M. Watanabe, R. Erni, E. A. Stach, P. Denes, U. Dahmen, *Microsc. Microanal.* **Oct. 2008**, *14*, 469.
- [6] W. H. Bragg, W. L. Bragg, *Proc R. Soc. Lond. A* **1913**, *88*, 428.
- [7] CEOS, Phase contrast and information limit, **Oct. 2015**, <http://www.ceos-gmbh.de/English/FAQ/informationlimit.html>.
- [8] G. Dehm, J. M. Howe, J. Zweck, *In-situ Electron Microscopy: Applications in Physics, Chemistry and Materials Science*, John Wiley & Sons, Ltd, **2012**.
- [9] S. H. Oh, Y. Kauffmann, C. Scheu, W. D. Kaplan, M. Rühle, *Science* **2005**, *310*, 661.
- [10] S. H. Oh, M. F. Chisholm, Y. Kauffmann, W. D. Kaplan, W. Luo, M. Rühle, C. Scheu, *Science* **2010**, *330*, 489.
- [11] Z. Zhang, D. Su, *Ultramicroscopy* **2009**, *109*, 766.
- [12] T. E. Everhart, R. F. M. Thornley, *J. Sci. Instrum.* **1960**, *37*, 246.
- [13] R. Egerton, *Electron Energy-Loss Spectroscopy in the Electron Microscope*, Springer, **2011**.
- [14] J. Goldstein, D. E. Newbury, D. C. Joy, C. E. Lyman, P. Echlin, E. Lifshin, L. C. Sawyer, J. R. Michael, *Scanning Electron Microscopy and X-ray Microanalysis: Third Edition*, Springer, **2002**.
- [15] S. B. Betzler, A. Wisnet, B. Breitbach, C. Mitterbauer, J. Weickert, L. Schmidt-Mende, C. Scheu, *J. Mater. Chem. A* **2014**, *2*, 12005.
- [16] T. Malis, S. C. Cheng, R. F. Egerton, *J. Electron. Microsc. Tech.* **1988**, *8*, 193.
- [17] J. Park, S. Heo, J.-G. Chung, H. Kim, H. Lee, K. Kim, G.-S. Park, *Ultramicroscopy* **2009**, *109*, 1183.
- [18] M. Stöger-Pollach, H. Franco, P. Schattschneider, S. Lazar, B. Schaffer, W. Grogger, H. W. Zandbergen, *Micron* **2006**, *37*, 396.
- [19] L. Gu, V. Srot, W. Sigle, C. Koch, P. van Aken, F. Scholz, S. B. Thapa, C. Kirchner, M. Jetter, M. Rühle, *Phys. Rev. B* **2007**, *75*.
- [20] W. Khan, S. B. Betzler, O. Šipr, J. Ciston, P. Blaha, C. Scheu, J. Minar, *submitted* **2016**.
- [21] D. Bach, H. Störmer, R. Schneider, D. Gerthsen, J. Verbeeck, *Microsc. Microanal.* **2006**, *12*, 416.

-
- [22] D. Bach, R. Schneider, D. Gerthsen, J. Verbeeck, W. Sigle, *Microsc. Microanal.* **2009**, *15*, 505.
- [23] R. D. Leapman, L. A. Grunes, P. L. Fejes, *Phys. Rev. B* **1982**, *26*, 614.
- [24] S. D. Berger, J. M. Macaulay, L. M. Brown, *Philos. Mag. Lett.* **1987**, *56*, 179.
- [25] R. Brydson, H. Sauer, W. Engel, J. M. Thomas, E. Zeitler, N. Kosugi, H. Kuroda, *J. Phys.: Condens. Matter.* **1989**, *1*, 797.
- [26] C. Heiliger, F. Heyroth, F. Syrowatka, H. S. Leipner, I. Maznichenko, K. Kokko, W. Hergert, I. Mertig, *Phys. Rev. B* **2006**, *73*.
- [27] E. Stoyanov, F. Langenhorst, G. Steinle-Neumann, *Am. Mineral.* **2007**, *92*, 577.
- [28] M. Yoshiya, I. Tanaka, K. Kaneko, H. Adachi, *J. Phys.: Condens. Matter* **1999**, *11*, 3217.
- [29] S. B. Betzler, F. Podjaski, K. Bader, M. Beetz, A. Wisnet, M. Handloser, A. Hartschuh, B. V. Lotsch, C. Scheu, *submitted* **2016**.
- [30] G. Cliff, G. W. Lorimer, *J. Microsc.* **1975**, *103*, 203.
- [31] Z. Chen, H. N. Dinh, E. Miller, *Photoelectrochemical Water Splitting Standards, Experimental Methods, and Protocols*, Springer, **2013**.
- [32] B. E. Warren, *X-ray Diffraction*, Dover Publications, **1969**.
- [33] C. S. S. R. Kumar, *UV-VIS and Photoluminescence Spectroscopy for Nanomaterials Characterization*, Springer, **2013**.
- [34] W. Borchardt-Ott, *Kristallographie*, Springer, **2009**.
- [35] P. Scherrer, *NGWG Math.-Phys.* **1918**, *1918*, 98.
- [36] D. Ariosa, F. Elhordoy, E. A. Dalchiele, R. E. Marotti, C. Stari, *J. App. Phys.* **2011**, *110*, 124901.
- [37] H. M. Rietveld, *J. Appl. Crystallogr.* **1969**, *2*, 65.
- [38] J. Tauc, R. Grigorovici, A. Vanacu, *Phys. Status Solidi B* **1966**, *15*, 627.
- [39] P. Sharma, I. Sharma, S. C. Katyal, *J. Appl. Phys.* **2009**, *105*, 053509.

4 Template-Free Synthesis of Novel, Highly-Ordered 3D Hierarchical $\text{Nb}_3\text{O}_7(\text{OH})$ Superstructures with Semiconductive and Photoactive properties

This chapter is based on the following publication: S. B. Betzler, A. Wisnet, B. Breitbach, C. Mitterbauer, J. Weickert, L. Schmidt-Mende, and C. Scheu, *J. Mater. Chem. A*. (2014) **2**, 12005-12013.

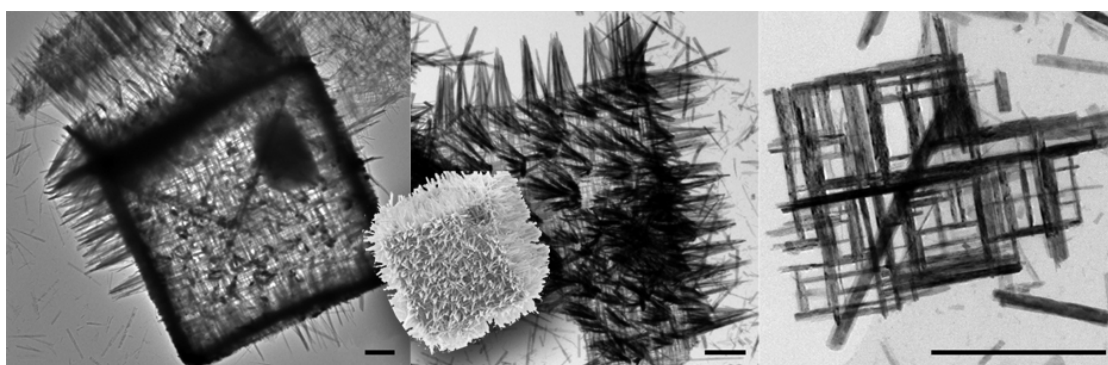


Figure 4.1 Table of contents graphic (scale bar 500 nm).

4.1 Introduction

Nanostructured materials find application in various fields, like functionalized nanoparticles in medicine^[1] or porous electrodes in photovoltaics.^[2] Next to the synthesis of nanoparticles and one-dimensional nanostructures of different materials much effort is made for the generation of more complex but highly-ordered three-dimensional superstructures. The developed synthesis strategies can generally be divided into template-based and template-free methods. In connection with this, Cölfen et al. introduce the term *mesocrystal*, which describes the self-assembly of non-spherical building blocks to ordered superstructures on the scale of several hundred nanometers to micrometers.^[3,4] To date, the self-organized formation of these mesocrystals is not fully understood. However, several models were proposed in literature, based on different driving forces like external and internal fields, organic matrices or interparticle forces.^[5-7] Solvothermal synthesis methods, which enable the fabrication of superstructures, belong to the class

of template-free methods. They utilize high pressures for the crystallization of materials at comparably low temperatures. These reaction conditions apparently favor the self-organized formation of nanostructures. Reports show solvothermally achieved structures like CuInS₂-spheres,^[8] hierarchical Co₃O₄ superstructures^[9] or TiO₂ nanowires.^[10] TiO₂ is one of the most commonly applied materials in the field of green energy and the decomposition of hazardous materials,^[11] some of the major tasks of this century. In general, materials applied in this field must fulfill certain preconditions like large accessible surface areas, long-range electronic connectivity, structural coherence and a suitable band structure.^[12] Next to the most commonly applied TiO₂ and ZnO various other materials are investigated.^[13–15] Niobium oxide is promising as it exists in many polymorphic phases with different oxidation numbers and crystal structures, most featuring a high chemical stability, corrosion resistance in both acidic and alkaline media and, dependent on the crystal phase, band gaps in the range of 3.1 eV^[16] to 4.9 eV.^[17] Several studies utilize solvothermal methods to achieve nanostructured niobium oxide,^[18–21] whose application in dye-sensitized solar cells^[22–24] results in power conversion efficiencies up to 7%.^[25] Besides being used in DSSCs, niobium oxide nanostructures find application in the field of electrochromics,^[26,27] catalysis,^[28] field-emission displays,^[29,30] gas sensing^[31] and lithium batteries.^[32]

Here we report on novel three-dimensional hierarchical Nb₃O₇(OH) superstructures, which were synthesized via a template-free, one-step hydrothermal approach. The focus of our study lies on the formation of these hierarchical structures by analyzing intermediate growth states combining XRD, SEM and UV/Vis spectroscopy. This provides deeper insights into the self-organized formation of mesocrystals. Further analyses were performed at the atomic scale to get a better understanding of the arrangement of these hierarchical structures. For this purpose TEM, EELS and STEM were performed. The presented superstructures prove to be viable for photochemical applications as shown in bleaching experiments with different dye molecules.

4.2 Results and Discussion

4.2.1 Hydrothermal Conditions Enable the Self-Organized Formation of Nb₃O₇(OH) Superstructures

The applied hydrothermal synthesis strategy yields different well-controllable cube morphologies without using a template. The one-step synthesis approach is based on the hydrothermal treatment of an aqueous Nb(IV)-chloride solution at temperatures between 150 and 200 °C. In dependence of the applied synthesis parameters (pH-value, temperature, synthesis time) a variety of cube morphologies can be achieved. These morphologies reach from compact to hollow cubes, with differently shaped surfaces. Amongst those, hollow cubes with surfaces consisting of nanowires stand out, as this unique morphology combines a large surface area (BET 53 m²g⁻¹) and a high crystallinity (fig. 4.2). Consequently, the investigation focuses on these superstructures aiming at a better understanding of their formation, stabilization and applicability. These nanowire-based

hollow cubes can be achieved using a pH of -0.8, a synthesis temperature of 200 °C and a growth time of 24 hours.

4.2.2 Analysis of the Superstructure Formation

For a better understanding of mechanisms involved in the formation of these novel superstructures, the intermediate steps of the cubes formation process were analyzed. The SEM images displayed in figure 4.2 show the morphology of the cubes depending on the reaction time. Note that cubes form in the reaction solution already at the initial growth state at room temperature. These cubes are characterized by blunt edges, which sharpen during the first hours of the hydrothermal synthesis. Substantial changes of the cube morphology were observed for a synthesis time of eight hours. The corresponding sample contains two morphologies emblematic for two different growth states: On the one hand tiny nanowires, which seem to lie loosely on the surface of the cubes and on the other hand larger nanowires occur. For synthesis times longer than eight hours the cubes are completely built up from nanowire networks, which grow at the expense of the material in the interspaces between the nanowires. The continuous changing of the morphology is accompanied by increasing mean cube sizes, reaching their maximum of $3.9 \pm 1.1 \mu\text{m}$ for a synthesis time of 24 hours. For very large synthesis times (72 hours) the stability of the cubes decreases, resulting in wreckage of nanowires and a decreased mean cube size of $2.9 \pm 0.6 \mu\text{m}$, which indicates a preferential breakdown of larger cubes (quantitative analysis see appendix fig. A.1).

Changes of the crystallographic properties which go along with the changing morphologies were analyzed using XRD (fig. 4.2). The analysis shows that the samples are X-ray amorphous for shorter synthesis times, as the corresponding pattern only contain broad features attributable to short-range order phenomena. Crystallization of the sample starts after a synthesis time of two hours. For longer synthesis duration the observed reflections become more pronounced. Rietveld analysis performed on the crystalline samples indicate that they all consist of pure $\text{Nb}_3\text{O}_7(\text{OH})$ phase. The changing crystallographic properties are also reflected in the band gap of the material, which was determined from UV/Vis data based Tauc plots (see section 3.4.2). Investigation of the band gap of the different morphologies shows a slightly decreasing trend for increasing synthesis time, spanning an energy range of 0.14 eV. Only the band gap of the cubes obtained for a synthesis time of one hour breaks from this trend, as it is 0.2 eV larger than the band gap of the amorphous starting phase (0h sample) (see appendix fig. A.2 & tab. A.1).

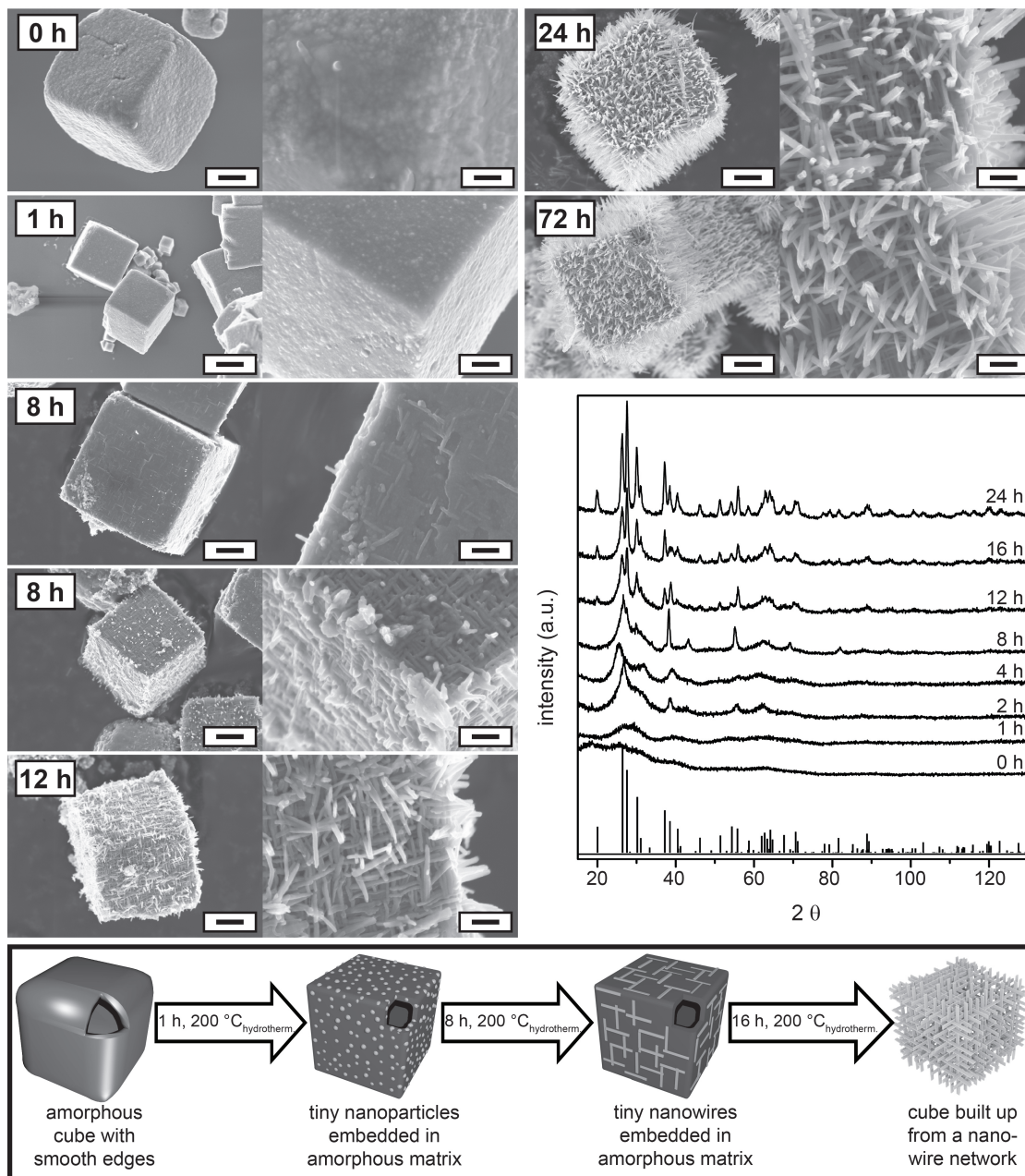
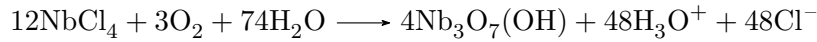


Figure 4.2 SEM images of $\text{Nb}_3\text{O}_7(\text{OH})$ cube morphologies obtained for different synthesis times and respective XRD pattern. The left row shows an overview SEM image of single cubes for different times of hydrothermal treatment – 0h, 1h, 8h, 12h, 24h, 72h – (scale bar 1 μm) and the right row shows a zoom in on one edge of the correspondent cube (scale bar 200 nm). The development of nanowires during the hydrothermal treatment can be observed. XRD pattern of the different morphologies and the reference data of $\text{Nb}_3\text{O}_7\text{F}$ (JCPDS, Card No. 74–2363), which is isomorphic to $\text{Nb}_3\text{O}_7(\text{OH})$,^[33] can be seen in the graph on the right. At the bottom a schematic drawing is shown, which summarizes the intermediate steps of the hydrothermal growth of the $\text{Nb}_3\text{O}_7(\text{OH})$ superstructures.

The morphological changes during the hydrothermal treatment coincide with a chemical reaction resulting in the formation of niobium oxide out of niobium chloride. The molecular formula of $\text{Nb}_3\text{O}_7(\text{OH})$ indicates the presence of niobium(V) in the cubes. Analysis of the bonding characteristic by EELS measurements in the TEM was performed to verify this oxidation state. Comparing the O-K-edge and the plasmon of EEL spectra

detected for single nanowires with spectra from literature^[34] indicates the pentavalence of niobium in $\text{Nb}_3\text{O}_7(\text{OH})$, as the shape of the accordant edges agree with the ones reported for Nb_2O_5 (see section 3.3.1). This reveals the oxidation reaction happening with the formation process of the cubes, resulting in the transformation of Nb(IV)chloride to Nb(V)oxide as given in the following equation:



Combining the results of these different analysis methods allows to set up a model for the formation mechanism of these cubes. A schematic drawing illustrating the growth is shown in figure 4.2. The growth starts from amorphous, hollow cubes with smooth surfaces, which already form at room temperature. With beginning of the hydrothermal treatment apparently tiny nanoparticles form, which are embedded in an amorphous matrix. These nanoparticles cause a quantum confinement effect resulting in an increased band gap. Comparable results were reported by Anpo et al.,^[35] who observed a blue shift of 0.16 eV for the band gap of anatase TiO_2 nanoparticles of 38 Å diameter compared to bulk anatase due to quantum confinement effects. The Nb_xO_y particles most likely serve as seed crystals for the formation of the nanowires via one-dimensional crystal growth. The formation of nanowires due to one-dimensional crystal growth was also reported to occur under hydrothermal conditions for rutile TiO_2 .^[10] Density functional theory calculations performed for rutile show that one-dimensional growth is thermodynamically favored as the size of high-energy crystal surfaces is reduced for the benefit of lower-energy surfaces.^[36,37] Similar reasons might cause the one-dimensional growth of $\text{Nb}_3\text{O}_7(\text{OH})$. Here, the one-dimensional growth starts with tiny nanowires, which are embedded in an amorphous matrix (observed for synthesis times of eight hours). With ongoing growth (for synthesis times larger than 16 hours), the nanowires increase in size at the expense of the amorphous material in the interspaces. These findings suggest the involvement of an Ostwald ripening process during the wire formation. Ostwald ripening was also reported to be the reason for the formation of hollow Nb_2O_5 spheres by Xue et al.^[21] and Li et al.^[38] Some steps of the mechanism found for the formation of the $\text{Nb}_3\text{O}_7(\text{OH})$ superstructures are in compliance with models of the self-organized formation of mesocrystals reported in literature.^[4,39] Similarity is found to a four-step mechanism proposed by Gong et al.^[4] and the formation mechanism reported by Zhang et al.^[40] The mechanism of Gong et al. is subdivided into the initial nucleation, the self-assembly via oriented aggregation, crystal growth via Ostwald ripening and a subsequent separation process.^[4] While Zhang et al. show the formation of nanostructured spheres starting from nanoparticles which transform to spheres built up of nanoparticles. With ongoing hydrothermal treatment first interlaced connected streak structures form, which are favored for further growth of nanosheets.^[40]

4.2.3 Investigation of the Structure of the Superstructures at Atomic Scale

For a better understanding of their structure, the morphology of the cubes consisting of a nanowire arrangement was investigated intensively. SEM (fig. 4.3a-c) and TEM (fig. 4.3d) images of the cubes show that their walls are composed of nanowire networks. TEM images of network fragments reveal a nearly perfect perpendicular arrangement of the nanowires in the network (fig. 4.3e). This regularity is reflected in the electron diffraction pattern of the network (fig. 4.3f), which consists of distinct reflections usually characteristic for single crystalline materials. However, TEM images reveal black contours within the wires, attributable to the presence of strain and defects in the network (fig. 4.3e). SEM images of broken cubes confirm the hollowness of the cubes. Cross-sections of the cube walls exhibit additional nanowires oriented perpendicular to the cube edges (fig. 4.3b,c). These nanowires appear as dark spots in TEM images of the network, because they are aligned parallel to the beam direction (three are marked with black arrows in figure 4.3e). EDX analysis performed in the TEM on single nanowires, which broke off from cubes synthesized for 24 hours, show that the nanowires homogeneously consist of niobium and oxygen (EDX data see appendix fig. A.3). Electron diffraction experiments performed for one nanowire indicate that it is single crystalline $\text{Nb}_3\text{O}_7(\text{OH})$ phase and grows in the $[010]$ direction (fig. 4.4a; the indexing was verified with simulations using the JEMS software, see appendix fig. A.4a,b). Comparable results were reported by Zhang et al.,^[25] who investigated $\text{Nb}_3\text{O}_7(\text{OH})$ nanowire arrays, which did not form three-dimensional assemblies. ADF images detected for one single nanowire reflect the crystal symmetry, which is characterized by NbO_6 octahedra connected tip- and edge-wise. A schematic drawing of the crystal structure showing these octahedra is included in the ADF image in figure 4.4b. Furthermore, it is worth noticing that the $\langle 001 \rangle$ zone axis is always observed for single nanowires lying on a holey carbon film, indicating an enlarged (001) crystal facet compared to the (100) facet (see schematic drawing of a nanowire in fig. 4.4c).

Analysis of the nanowire network reveals that it is built up from nanowires, all facing the same crystallographic orientation, displaying the $\langle 100 \rangle$ zone axis (the indexing of one single nanowire in the network was verified by simulations, see appendix fig. A.4c,d). In this regard, the diffraction pattern of the network shown in figure 4.3f was indexed as the superposition of the diffraction pattern of two nanowires rotated by 90° with respect to each other (detailed analysis see section 4.4.1). Fast Fourier transformation (FFT) analysis of HRTEM images confirm this indexing (see section 4.4.2). In addition, these HRTEM images of the network exhibit two different types of nanowire junctions, which were further analyzed using site selective EELS based thickness measurements (see section 4.4.2) and STEM. One junction type results from a T-shaped arrangement of two nanowires. As no thickness changes could be detected at these junctions, the corresponding nanowires do not seem to overlap (fig. 4.4d). The second junction type results from two nanowires overlaying each other, forming a crossing. The enhanced thickness at the overlap region, which corresponds to about 80% of the thickness sum of the respective nanowires, shows that the nanowires partly interpenetrate each other at the

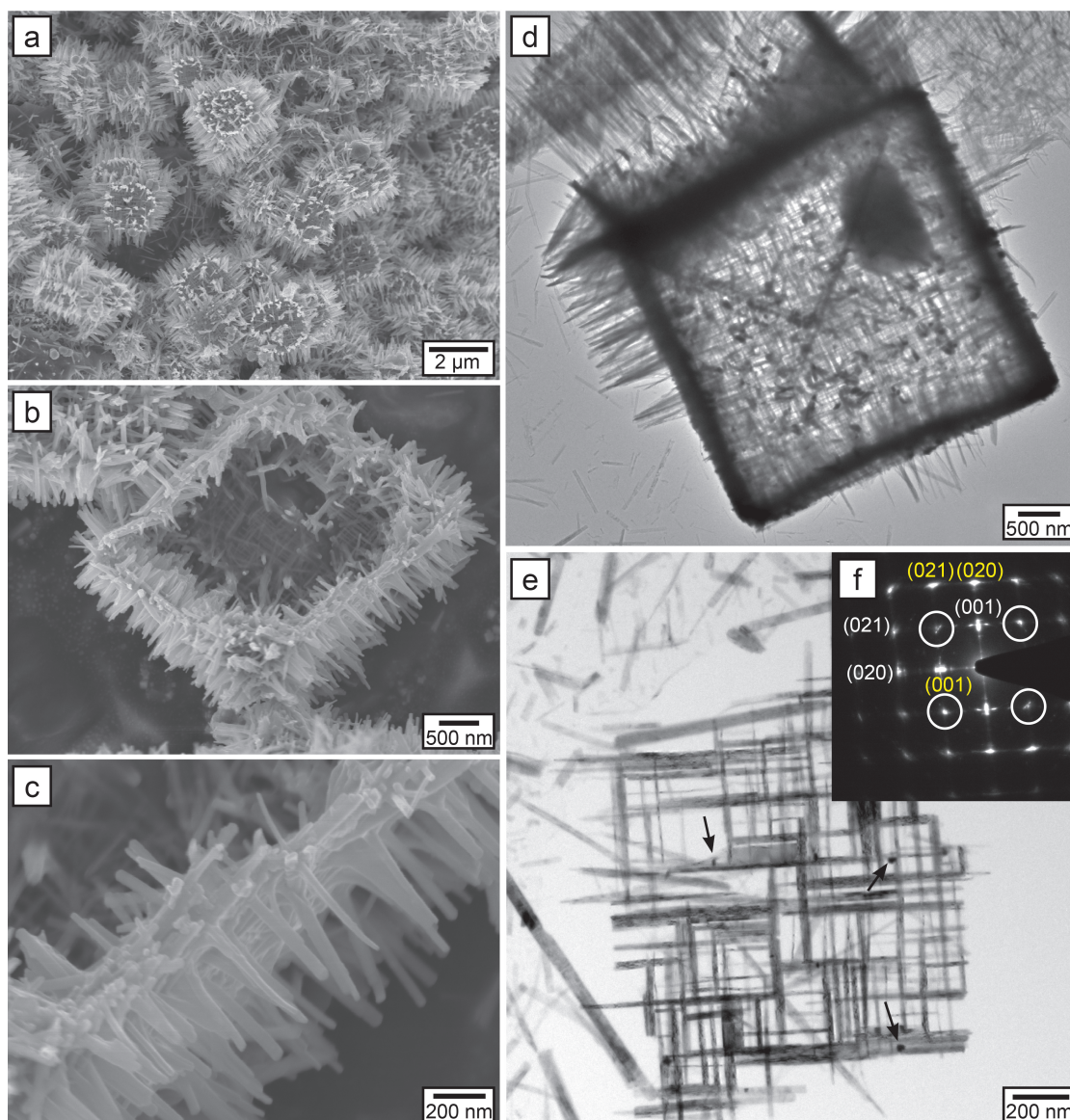


Figure 4.3 Electron microscopic investigation of the $\text{Nb}_3\text{O}_7(\text{OH})$ mesocrystals. a) An overview SEM image of the sample. b) SEM image of one cube with its top broken off, a higher magnification of the cube wall can be seen in c). d) Overlap TEM image of a topless cube lying on a carbon grid. e) TEM image of a fragment of one cube wall and the corresponding electron diffraction pattern (f), which is indexed as combined pattern of two nanowires.

overlap region (see fig. 4.4e and section 4.4.2). FFT analysis reveal that these overlap regions cause additional reflections appearing in the diffraction pattern of the network (marked with white circles in figure 4.3f). The intensity of those reflections depends on the network size, which corresponds to the quantity of crossings, in that way that it increases with growing network size.

The analysis indicates a faceted shape of the nanowires with preferred $\{001\}$ planes. These nanowires form the building blocks of 3D hierarchical cubes, which consist of nanowire-networks. The high degree of regularity of the nanowire arrangement results in a single crystalline appearance of the complex superstructures. This, and the fact that

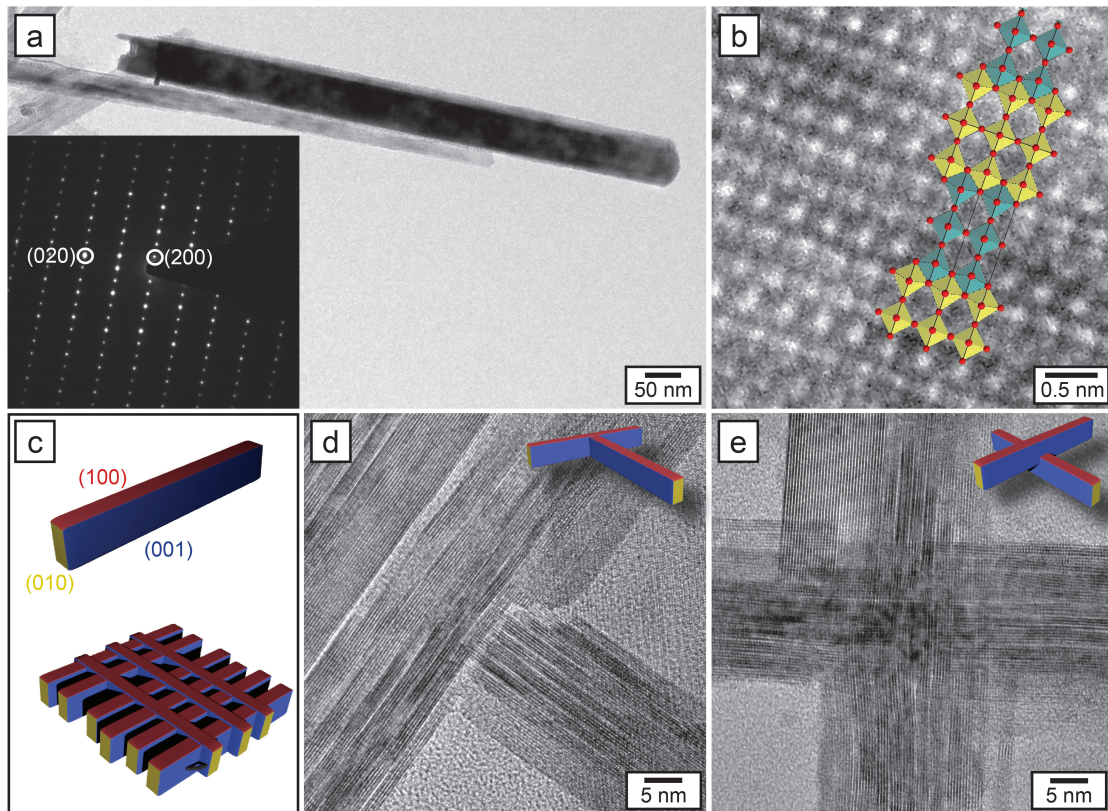


Figure 4.4 Electron microscopic investigation of one single $\text{Nb}_3\text{O}_7(\text{OH})$ nanowire on a holey carbon film, which broke off from a network, and of the different nanowire junctions in the network. a) Overlap bright field image of the investigated nanowire and corresponding electron diffraction pattern detected for this wire, which is indexed for $\text{Nb}_3\text{O}_7(\text{OH})$ in $\langle 001 \rangle$ zone axis (inset). b) ADF image of a single nanowire including a schematic drawing of the crystal symmetry. c) Schematic drawing illustrating the crystal shape of the nanowires and the crystallographic arrangement of the nanowires in the network. d) HRTEM image of a T-shaped nanowire junction and schematic drawing showing the arrangement of the nanowires at the junction (inset). e) HRTEM image of a nanowire crossing and schematic drawing of the junction (inset).

they form self-organized from solution proposes them categorizeable as *mesocrystals* following the definition of Cölfen et al.^[3] Neither the formation nor the stabilization of mesocrystals is generally understood in literature. The aforementioned results indicate a major role of the nanowire crossings at the stabilization of the networks, as a partial interpenetration of the nanowires could be shown for these junctions via site-selective thickness measurements. The resulting increased thickness at the overlap region compared to plain nanowires is also reflected in the diffraction pattern of the network, which show additional reflections most likely attributable to double diffraction. However, the partial interpenetration of the nanowires at the crossing is apparently enforced by the orthorhombic crystal symmetry of $\text{Nb}_3\text{O}_7(\text{OH})$ which is characterized by $a = 20.740 \text{ \AA}$, $b = 3.823 \text{ \AA}$ and $c = 3.936 \text{ \AA}$.^[33] The small lattice mismatch of the b and c -direction enables the preservation of the atomic columns in $[100]$ direction at the overlap regions of the crossing, thus the octahedral coordination of niobium can be preserved (see section 4.4.2). Nonetheless, the small difference between the two crystal directions causes strain in the network, which is visible in bright-field images (fig. 4.3e). Yet, the driving

forces involved in the perpendicular alignment of the nanowires are still unknown. Different polarities of the crystal surfaces might hint to an explanation,^[5] as buck charging of the (010) and (100) faces would explain the perpendicular arrangement due to balanced repulsion and attraction. The mechanism of formation of the additional nanowires, standing like spikes from the edges of the cubes, and their role in the stabilization of the mesocrystals is not yet understood and will be the subject of future investigations.

4.2.4 Suitability of the $\text{Nb}_3\text{O}_7(\text{OH})$ Superstructures as New Electrode Material

The $\text{Nb}_3\text{O}_7(\text{OH})$ superstructures benefit from their large surface area, high crystallinity and direct electron transport paths. In this regard their optoelectronic properties related to their application in photochemical devices were investigated. The band gap of a material is one important factor. Thus, UV/Vis data based Tauc plots (fig. 4.5a) were applied. They show a band gap of 3.19 ± 0.05 eV for the sample synthesized for 24 hours. Since UV/Vis spectroscopy averages over the whole sample, additional site-selective EELS measurements were performed in the TEM to determine the band gap of one single nanowire of the same sample. The corresponding low-loss EEL spectrum is shown in figure 4.5b after subtraction of the zero-loss peak. It confirms the size of the band gap, yielding a value of 3.2 ± 0.1 eV. However, the determined band gaps are slightly larger than the one reported by Wu et al.,^[16] who found a band gap of 3.03 eV for their $\text{Nb}_3\text{O}_7(\text{OH})$ thin films. The 2D photoluminescence spectrum of the cubes grown for 72 hours (fig. 4.5c) shows one major feature with an excitation maximum in the range of 4.1 to 3.1 eV and an emission range of 2.8 to 2.5 eV. This feature can be attributed to interband transitions from the valence to the conduction band, as the energy corresponds to the size of the band gap and electronic excitations to higher energetic states, thus likewise confirming the determined band gap. However, the emission range points towards a possible existence of trap states. The band gap of $\text{Nb}_3\text{O}_7(\text{OH})$ is smaller or in the range of common other metal oxides, like TiO_2 , Nb_2O_5 or ZnO which are used as electrode material in photovoltaics and photocatalysis.^[13] The photocatalytic degradation of dyes is an elegant method to investigate their suitability for photochemical applications. In the present study the analysis of three dyes with different colors and functionality shows a successful degradation. However, a strong pH value dependence of the kinetic degradation rate was observed (the kinetic rates correspond to the slope of the graphs summarized in figure 4.5d-f). While the adsorption of indigo carmine and methylene blue occurs for specific pH values, this was not the case for rhodamine B. For indigo carmine adsorption was best at a pH of 2, which is reflected in the highest photocatalytic degradation rate at this pH value, while methylene blue was best adsorbed at a pH of 10 (see appendix fig. A.5). Nevertheless, the investigations reveal that the adsorption of the dye is not necessary for the photocatalytic degradation, but increases its reaction kinetic. The photocatalytic degradation of rhodamine B by $\text{Nb}_3\text{O}_7(\text{OH})$ films was also shown by Wu et al.^[16] The pH dependence of its photocatalytic degradation might be related to the pH dependent intermediate formation of either hydroxyl- or

hydrogen radicals.^[41] These findings, namely an attractive band gap and photocatalytic activity, indicate the suitability of these $\text{Nb}_3\text{O}_7(\text{OH})$ superstructures as electrode material in functional devices. Correspondent testing goes beyond the scope of this work, but Zhang et al. already showed the successful integration of $\text{Nb}_3\text{O}_7(\text{OH})$ nanowire arrays into DSSC reaching efficiencies up to 7%.^[25]

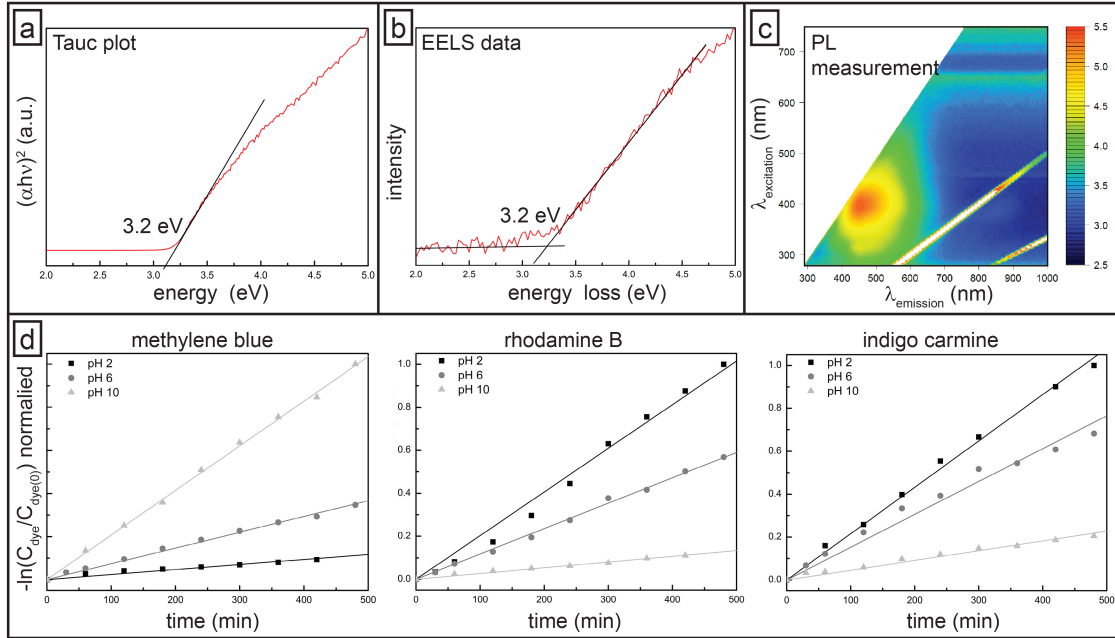


Figure 4.5 Measurement of the optoelectronic properties of $\text{Nb}_3\text{O}_7(\text{OH})$ superstructures. a) UV/Vis data based Tauc plot from which a band gap of 3.19 ± 0.05 eV was determined for cubes achieved for a synthesis time of 24 hours. b) Low-loss EEL spectrum detected for a single nanowire of the same sample (24 hours) after removing the zero-loss peak. The linear fit method^[42] was used to determine the band gap. The spectrum yields a band gap of 3.2 ± 0.1 eV. c) 2D PL spectrum of a sample synthesized for 72 hours, showing one intensive absorption peak between 400 and 500 nm. Emission intensity is shown in arbitrary units on a logarithmic scale. Spectral features labeled with an asterisk are experimental artifacts at the doubled and tripled excitation wavelengths and do not originate from the sample. d) Measurement of the photocatalytic degradation of three different dyes (methylene blue, rhodamine B, indigo carmine) at three different pH values (pH 2, pH 6, pH 10). The kinetic rate constant can be determined from the graph obtained by plotting $-\ln\left(\frac{C_{\text{dye}}}{C_{\text{dye}(0)}}\right)$ versus the irradiation time t .

4.3 Conclusion

This study reports on novel $\text{Nb}_3\text{O}_7(\text{OH})$ superstructures with hollow nanostructured cubic morphologies, which are grown in a one-step, template-free hydrothermal synthesis. Their self-organized assembly was investigated showing that initially amorphous hollow cubes with smooth surfaces form, which transform to cubes built up from crystalline $\text{Nb}_3\text{O}_7(\text{OH})$ nanowire-networks during the hydrothermal synthesis. The morphological changes go along with an oxidation reaction resulting in the formation of niobium(V)oxide. From our results we motivate a model for a new type of crystal growth which has not been observed before in literature and expands the numbers of reported

formation mechanisms. The construction of the walls was investigated at atomic scale, showing that the walls of the hollow cubes consist of a regular nanowire network. In the network the nanowires are aligned in a perpendicular fashion. This regularity is also reflected in the electron diffraction pattern, which shows distinct reflections. The self-organized formation and the high degree of regularity indicate that these superstructures fulfill the criteria for mesocrystals following the definition given by Cölfen et al.^[3] Their stabilization is most likely related to the partial interpenetration of the nanowires at crossings, which at the same time triggers the perpendicular arrangement. In addition the properties of the cubes, namely their large surface area, their band gap of 3.2 eV, their high chemical stability and photochemical activity render them attractive for photochemical and photophysical devices. Furthermore the reported synthesis strategy and mechanistic investigations support the development of superstructures of various materials and the understanding of the forces triggering self-assembly.

4.4 Additional Information

4.4.1 Analysis of the Diffraction Pattern of the Network

Figure 4.6a shows a TEM image of a network fragment and the corresponding diffraction pattern (fig. 4.6b). A diffraction pattern of one single nanowire of the network was used as basis for the analysis (fig. 4.6c). This pattern was rotated by 90° (fig. 4.6d) and added to the original pattern (fig. 4.6e). The resulting superposition coincides with the diffraction pattern detected of the network. Next to the major reflections smaller reflections can be seen in the diffraction pattern of the small network. These reflections result from the underlying nanowire, which displays the $\langle 001 \rangle$ zone axis (marked with an arrow in figure 4.6a) and does not belong to the fragment.

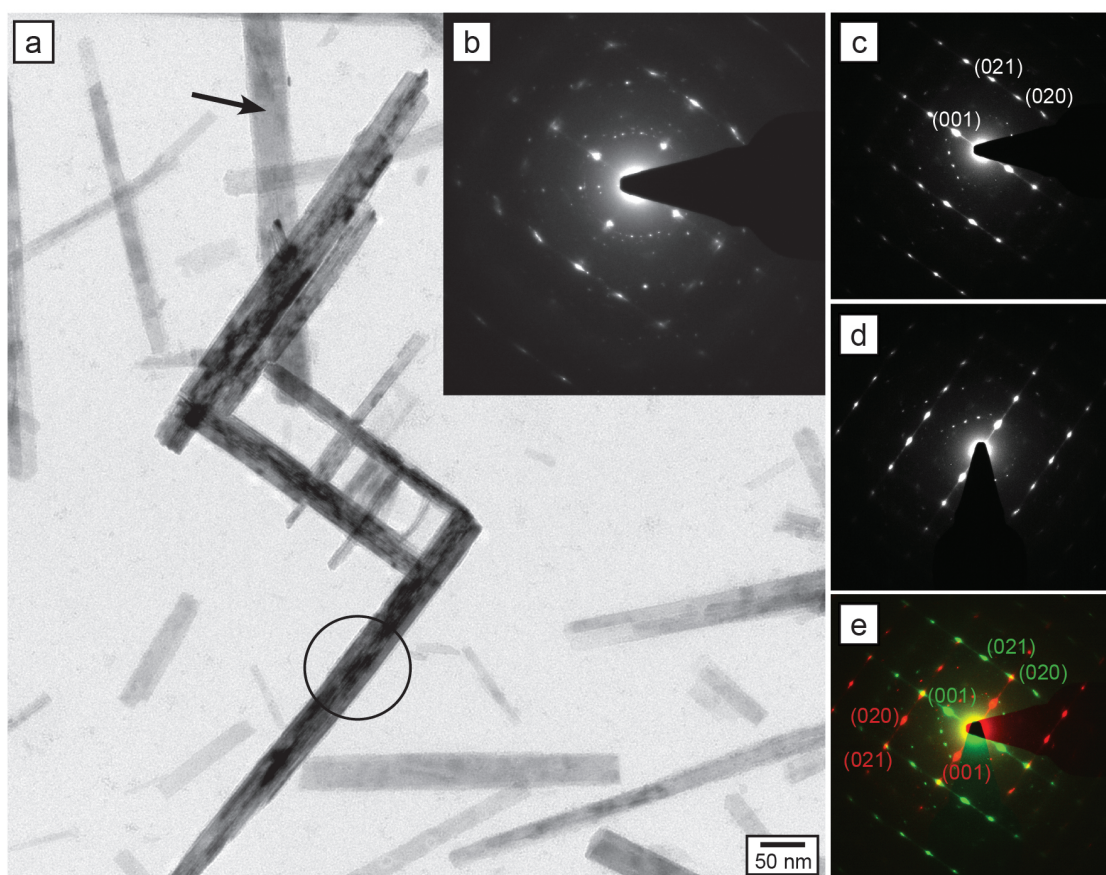


Figure 4.6 TEM image and electron diffraction pattern detected of a small network fragment. a) TEM image of the analyzed network fragment, which consists of nine nanowires. b) Electron diffraction pattern detected of the complete network. c) Diffraction pattern detected of one single wire in $\langle 100 \rangle$ zone axis, the investigated area is marked with a black circle in (a). d) Diffraction pattern shown in (c) rotated by 90° . e) Combination of the diffraction pattern shown in (c) and (d).

4.4.2 Local Thickness Measurements and FFT Analysis at Nanowire Junctions

Using FFT of different HRTEM images in combination with a masking tool enables the determination of the origin of the spots in the FFT via calculating the inverse FFT. The area and the corresponding spot in the FFT are colored the same (fig. 4.7a,b). This color-coding proves the indexing of the complex diffraction pattern of the networks, which is based on the assumption that these diffraction pattern are composed of the diffraction pattern of the distinct wires. The FFT of crossings shows additional reflections (fig. 4.7b), which are not observed for T-shaped junctions (fig. 4.7a). The analysis indicates that these spots originate from the area where the two nanowires overlap. In addition site-specific thickness measurements were performed using both STEM and EELS (see section 3.3.1.1). In figure 4.7d,e the achieved relative thicknesses are given as numbers related to the mean free path (MFP). The achieved results are confirmed by ADF investigations, as thicker region cause a higher brightness in the images (fig. 4.7c). In addition ADF images indicate the preservation of the atomic columns at the junction (fig. 4.7f).

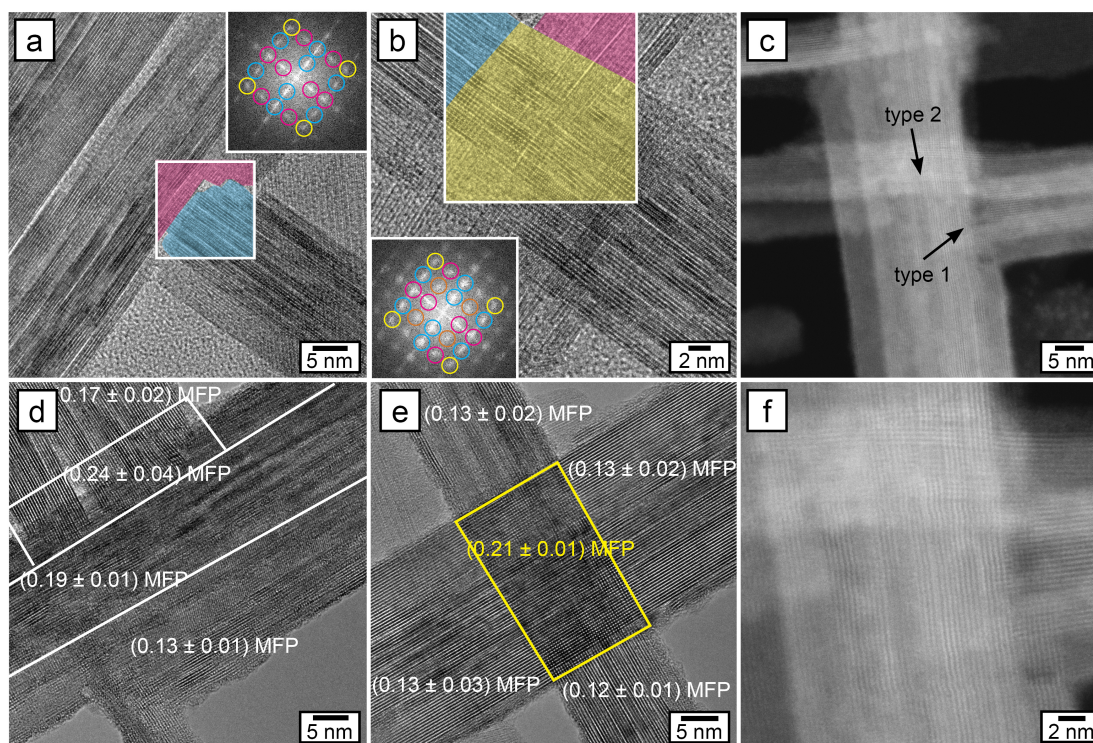


Figure 4.7 Analysis of the junctions appearing in the network. a) HRTEM image of a T-shaped junction and the corresponding FFT (inset) of the area marked in the HRTEM image. The color-coding correlates the origin of each spot in the FFT with the respective area in the HRTEM. b) HRTEM image of a crossing, color-coding and FFT like in (a), reflections marked yellow originate from the whole area. c) STEM image including both junction types. Site-specific thickness information were obtained from low-loss EEL spectra. The HRTEM image of the junctions (T-shaped (d), crossing (e)) include the calculated relative thicknesses in dependence of the MFP. f) ADF image of the two junctions types, showing the preservation of the atomic order at the junctions.

4.5 Experimental

$\text{Nb}_3\text{O}_7(\text{OH})$ superstructures were obtained from the hydrothermal treatment of a mixture of NbCl_4 , HCl and water performed at 200°C . Detailed description can be found in section 2.4.1. The morphologies were analyzed with a *Zeiss Gemini Ultra Field Emission SEM* equipped with an In-lens detector operated at 4 keV . To reduce charging effects the samples were fixed on silicon wafers and coated with carbon using a *BAL-TEC MED020* coating system. XRD analysis was performed with Co-K_α radiation using a *Seifert THETA/THETA-diffractometer (GE Inspection Technologies)* equipped with a *Meteor OD* detector. A 2θ detection range of $15\text{--}130^\circ$, a step size of $2\theta = 0.05^\circ$ and a count time of $30\text{ s}/(2\theta\text{-step})$ were used.

TEM samples were prepared by drop casting a suspension. This suspension was achieved by sonicating a mixture of powder sample and ethanol to crush the superstructures. HRTEM, STEM and EELS investigations were performed at 300 keV with a *FEI Titan 80-300 TEM* equipped with a *Gatan Tridiem EELS* and an *EDAX* ultra thin window $\text{Si}(\text{Li})$ EDX detector. The low-loss EEL spectra used for local thickness measurements (see section 3.3.1.1) were recorded in STEM mode averaging over small sample areas (in the range of $6\times 6\text{ nm}^2$), with a collection semi angle of 15.6 mrad , a convergence semi angle of 9.5 mrad , a total acquisition time of 5 s and a dispersion of 0.1 eV/channel . The low-loss spectra used for band gap determination (see section 3.3.1.2) were acquired with a *FEI Titan3 G2 60-300 TEM* operated at 80 keV which is equipped with an aberration-corrector for the probe-forming lens system, a high brightness field emission (*XFEGTM*) source, a monochromator and a high-resolution EEL spectrometer (*Gatan 966 GIF*). Data were acquired in STEM mode by scanning an area of about $20\times 20\text{ nm}^2$ and the EEL spectra were recorded with a dispersion of 0.025 eV/channel , a convergence semi angle of 18.7 mrad , collection semi angle 6.5 mrad and total acquisition times up to 10 s . The photophysical properties were recorded for samples fixed on quartz substrates. The UV/Vis spectra were detected with an *Agilent Cary 5000* spectrometer in the spectral range of 200 to 750 nm (step size 1 nm). PL measurements were performed on a *Horiba Jobin Yvon Fluorolog* Spectrometer equipped with a 500 W Xenon lamp. The two dimensional spectrum was detected for an emission range of 250 to 1000 nm and excitation range of 240 to 750 nm using a step size of 5 nm and an illumination angle of 60° .

Photocatalytic degradation of three different dyes (rhodamine B, methylene blue, indigo carmine) was investigated at three different pH values (2 , 6 and 10). For the measurements $\text{Nb}_3\text{O}_7(\text{OH})$ powder (0.5 mg , 0.001 mmol) was mixed with 3 mL aqueous dye solution (concentration: indigo carmine (57 mgL^{-1}), methylene blue (800 mgL^{-1}), rhodamine B (11 mgL^{-1})). The absorption of the different dye solutions was measured using an *Ocean Optics USB4000* spectrometer. To ensure the establishment of an adsorption-desorption equilibrium between $\text{Nb}_3\text{O}_7(\text{OH})$ and the dye, the mixtures were incubated for 1.5 hours in the dark. The catalytic degradation was started via UV irradiation using a *UVP UVGL-58* handheld UV lamp at long-wave UV irradiation. The kinetic constant was determined assuming a pseudo-first order kinetic model as the slope of the graph achieved by plotting $-\ln(\frac{C_{\text{dye}}}{C_0})$ versus the irradiation time t .

4.6 References

- [1] R. Ladj, A. Bitar, M. Eissa, Y. Mugnier, R. Le Dantec, H. Fessi, A. Elaissari, *J. Mater. Chem. B* **2013**, *1*, 1381.
- [2] H.-N. Kim, J. H. Moon, *ACS Appl. Mater. Interfaces* **2012**, *4*, 5821.
- [3] H. Cölfen, M. Antonietti, *Angew. Chem. Int. Ed. Engl.* **2005**, *44*, 5576.
- [4] Q. Gong, X. Qian, X. Ma, Z. Zhu, *Cryst. Growth Des.* **2006**, *6*, 1821.
- [5] R. Q. Song, H. Cölfen, *Adv. Mater.* **2010**, *22*, 1301.
- [6] K. J. M. Bishop, C. E. Wilmer, S. Soh, B. A. Grzybowski, *Small* **2009**, *5*, 1600.
- [7] S. J. Sedlmaier, T. Dennenwaldt, C. Scheu, W. Schnick, *J. Mater. Chem.* **2012**, *22*, 15511.
- [8] A. S. Wochnik, A. Frank, C. Heinzl, J. Häusler, J. Schneider, R. Hoffmann, S. Matich, C. Scheu, *Solid State Sci.* **2013**, *26*, 23.
- [9] L. Zhang, X. Zhao, W. Ma, M. Wu, N. Qian, W. Lu, *CrystEngComm* **2013**, *15*, 1389.
- [10] B. Liu, E. S. Aydil, *J. Am. Chem. Soc.* **2009**, *131*, 3985.
- [11] X. Chen, S. S. Mao, *Chem. Rev.* **2007**, *107*, 2891.
- [12] P. Docampo, S. Guldin, U. Steiner, H. J. Snaith, *J. Phy. Chem. Lett.* **2013**, *4*, 698.
- [13] R. Jose, V. Thavasi, S. Ramakrishna, *J. Am. Ceram. Soc.* **2009**, *92*, 289.
- [14] M. D. Hernández-Alonso, F. Fresno, S. Suárez, J. M. Coronado, *Energy Environ. Sci.* **2009**, *2*, 1231.
- [15] M. Wang, J. Ioccozia, L. Sun, C. Lin, Z. Lin, *Energ. Environ. Sci.* **2014**, *7*, 2182.
- [16] J. Wu, J. Wang, H. Li, D. Xue, *Thin Solid Films* **2013**, *544*, 545.
- [17] G. Agarwal, G. B. Reddy, *J. Mater. Sci.: Mater. in Electronics* **2005**, *16*, 21.
- [18] M. Wei, Z.-m. Qi, M. Ichihara, H. Zhou, *Acta Mater.* **2008**, *56*, 2488.
- [19] J. Liu, D. Xue, K. Li, *Nanoscale Res. Lett.* **2011**, *6*, 138.
- [20] C. Yan, L. Nikolova, A. Dadvand, C. Harnagea, A. Sarkissian, D. F. Perepichka, D. Xue, F. Rosei, *Adv. Mater.* **2010**, *22*, 1741.
- [21] D. Xue, F. Liu, *Modern Phys. Lett. B* **2009**, *23*, 3769.
- [22] K. Sayama, H. Sugihara, H. Arakawa, *Chem. Mater.* **1998**, *10*, 7.
- [23] P. Guo, M. A. Aegerter, *Thin Solid Films* **1999**, *351*, 290.
- [24] R. Ghosh, M. K. Brennaman, T. Uher, M.-R. Ok, E. T. Samulski, L. E. McNeil, T. J. Meyer, R. Lopez, *ACS Appl. Mater. Interfaces* **2011**, *3*, 3929.
- [25] H. Zhang, Y. Wang, D. Yang, Y. Li, H. Liu, P. Liu, B. J. Wood, H. Zhao, *Adv. Mater.* **2012**, *24*, 1598.
- [26] T. Maruyama, S. Arai, *Appl. Phys. Lett.* **1993**, *63*, 869.
- [27] N. Özer, D.-G. Chen, C. Lampert, *Thin Solid Films* **1996**, *277*, 162.
- [28] Y. Zhao, X. Zhou, L. Ye, S. C. E. Tsang, *Nano Rev.* **2012**, *3*, 1.
- [29] M. Žumer, V. Nemanič, B. Zajec, M. Remškar, A. Mrzel, D. Mihailovič, *Appl. Phys. Lett.* **2004**, *84*, 3615.
- [30] B. Varghese, S. C. Haur, C.-T. Lim, *J. Phys. Chem. C* **2008**, *112*, 10008.

-
- [31] D. Rosenfeld, P. E. Schmid, S. Széles, F. Lévy, V. Demarne, A. Grisel, *Sens. Actuators B* **1996**, *37*, 83.
- [32] A. Le Viet, M. V. Reddy, R. Jose, B. V. R. Chowdari, S. Ramakrishna, *J. Phys. Chem. C* **2010**, *114*, 664.
- [33] F. Izumi, H. Kodama, *Z. Anorg. Allg. Chem.* **1978**, *441*, 8.
- [34] D. Bach, R. Schneider, D. Gerthsen, J. Verbeeck, W. Sigle, *Microsc. Microanal.* **2009**, *15*, 505.
- [35] M. Anpo, T. Shima, S. Kodama, Y. Kubokawa, *J. Phys. Chem.* **1987**, *91*, 4305.
- [36] H. Perron, C. Domain, J. Roques, R. Drot, E. Simoni, H. Catalette, *Theor. Chem. Acc.* **2007**, *117*, 565.
- [37] M. Ramamoorthy, D. Vanderbilt, R. D. King-Smith, *Phys. Rev. B* **1994**, *49*, 16721.
- [38] L. Li, J. Deng, R. Yu, J. Chen, Z. Wang, X. Xing, *J. Mater. Chem. A* **2013**, *1*, 11894.
- [39] T. Wang, H. Cölfen, M. Antonietti, *J. Am. Chem. Soc.* **2005**, *127*, 3246.
- [40] H. Zhang, Y. Li, Y. Wang, P. Liu, H. Yang, X. Yao, T. An, B. J. Wood, H. Zhao, *J. Mater. Chem. A* **2013**, *1*, 6563.
- [41] U. G. Akpan, B. H. Hameed, *J. Hazard. Mater.* **2009**, *170*, 520.
- [42] J. Park, S. Heo, J.-G. Chung, H. Kim, H. Lee, K. Kim, G.-S. Park, *Ultramicroscopy* **2009**, *109*, 1183.

5 3D vs 2D – New Insights into the Nanowire Arrangement in Nb₃O₇(OH) Superstructures

This chapter is partly based on an invited book chapter to be published 2016 in *Materials Development for Solar Fuels and Energy Conversion in Fuel Cells* by Springer Science (Editors: U. I. Kramm, H.-J. Lewerenz, D. Schmeißer).

The hydrothermally grown Nb₃O₇(OH) superstructures described in chapter 4 possess a complex 3D morphology which consists of nanowire networks. Knowledge of the nanowire arrangement is important for the prediction of the performance of the superstructures in functional devices which strongly depends on the charge flow through the nanostructures. In the case of Nb₃O₇(OH) superstructures it furthermore yields new insights into the stabilization of the complex morphology. Local thickness measurements via EELS give a first hint to the 3D arrangement of the nanowires which can be extended upon reconstructing the 3D structure of the networks at the nanoscale using TEM tomography.

5.1 Introduction

Conventional TEM and STEM is limited to obtain 2D information due to the projection effect. Electron tomography is one promising method to reconstruct the 3D morphology of materials at the nanoscale.^[1] The method is based on tilt series which contain images of a single object recorded for distinct degree steps about a tilt axis. The limited tilt range of most tomography holders leads to the *missing wedge* effect of lost information causing artifacts in the reconstruction.^[1] This effect can be reduced by using large tilt angles up to 75–80°,^[2] by recording dual-axis tilt series^[3] or by applying the Saxton scheme,^[4] which uses smaller tilt increments at the outer limits of the tilt range.

Many different algorithms were developed to optimize the reconstruction of 3D information from tilt series.^[5] STEM images detected for certain tilt angles δ serve as original projections. The intensities in the image are Radon transformed line by line yielding projection $P_{j,(k=1,2,\dots),\delta}$ with k as slice and j as direction. The simplest method (called backprojection) to reconstruct the 3D information evenly distributes the value of each point of the projection $P_{j,k,\delta}$ over the reconstruction volume. This method suffers from strong artifacts which are reduced either by applying filters^[6] or by convoluting the projection or its Fourier transform with a weighting function.^[7] The application of itera-

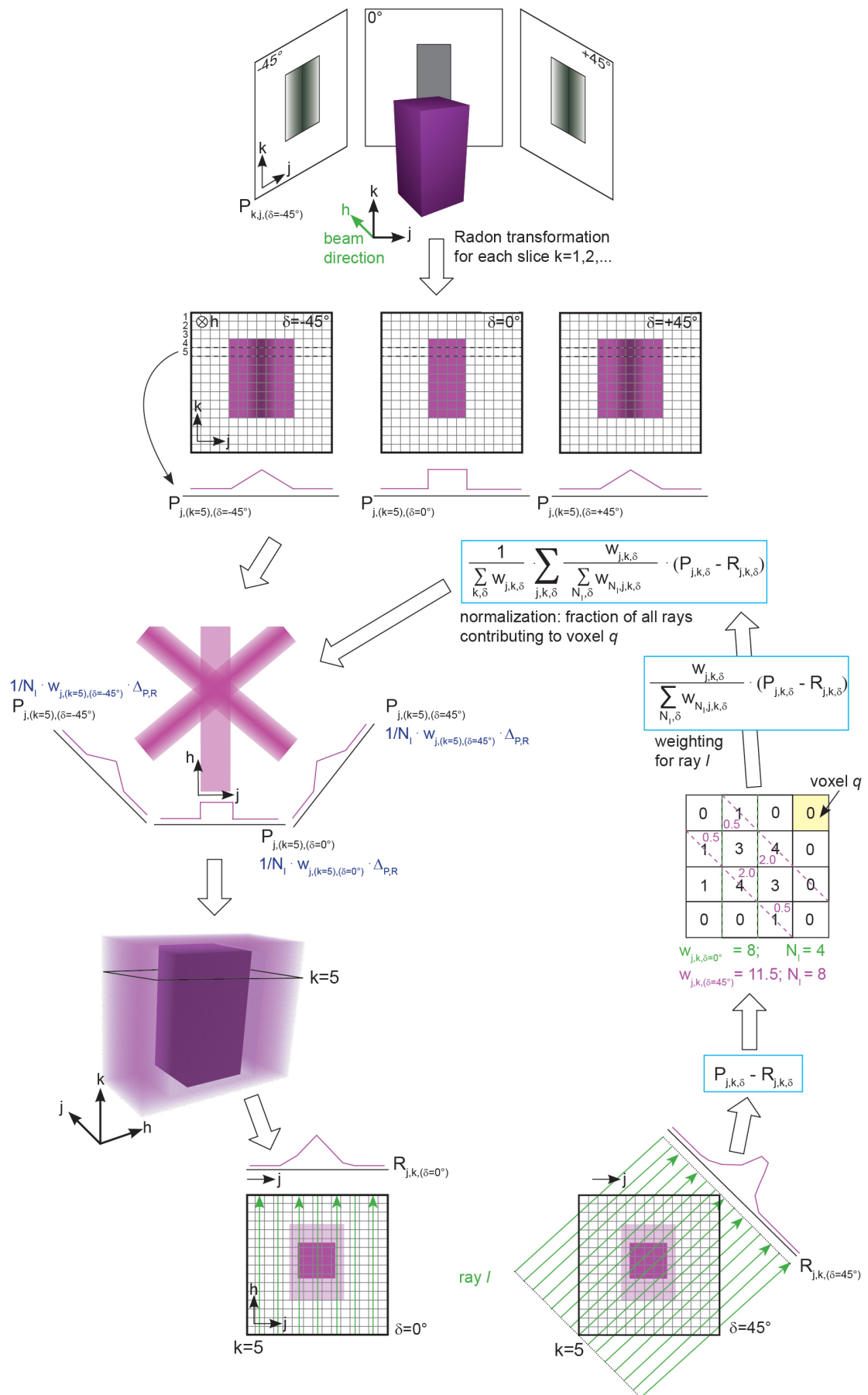


Figure 5.1 Schematic illustration of the electron tomographic reconstruction technique. One iteration loop of the SIRT algorithm is shown in detail (the distinct steps are highlighted in blue.)

tive techniques further reduces artifacts as they iteratively compare the original projections $P_{j,k,\delta}$, which are based on experimental data, with calculated reprojections $R_{j,k,\delta}$. $R_{j,k,\delta}$ is generated from the reconstructed volume by adding the values of voxels in the beam path of ray l . The algebraic reconstruction technique (ART)^[8] redistributes the density of the voxels contributing to the different rays by solving numerical equations so that the values of the reprojection $R_{j,k,\delta}$ equal the respective experimental $P_{j,k,\delta}$. The simultaneous iterative reconstruction technique (SIRT)^[9–11] is based on ART but extends it by two important factors: The reconstruction is not updated until all reprojections $R_{j,k,\delta}$ have been processed and an additional weighting is applied which takes into account that some voxels are truncated by the rays and therefore do not fully contribute to the respective projection. The algorithm is described in equation 5.1 for the alteration of one single voxel ρ per iteration q .

$$\rho_j^{q+1} = \rho_j^q + \frac{1}{\sum_{k,\delta} w_{j,k,\delta}} \sum_{j,k,\delta} \frac{w_{j,k,\delta}}{\sum_{N_l,\delta} w_{N_l,j,k,\delta}} (R_{j,k,\delta} - P_{j,k,\delta}^q) \quad (5.1)$$

The difference $(R_{j,k,\delta} - P_{j,k,\delta}^q)$ determined for each ray l is allocated to all voxels l touches using a weighting factor. This weighting factor takes the varying number of voxels N_l which different rays penetrate into account as given by the term $\frac{w_{j,k,P}}{\sum_{N_k,P} w_{N_k,P}}$. The fact that rays penetrate diverging numbers of voxels N_l dependent on δ is corrected by a normalization factor $\frac{1}{\sum_{k,\delta} w_{j,k,\delta}}$. The distinct steps of a SIRT reconstruction are illustrated in figure 5.1.

To further improve the reconstruction obtained with the SIRT algorithm the discrete algebraic reconstruction technique (DART)^[12,13] can be used. This technique is based on two main assumptions. One is that objects consist of a given low number of different densities (materials). Hence, certain intervals of gray values of the reconstruction are assigned to the different densities/materials existing in the object. Second, only regions at the surface of an object need to be refined, meaning that the algorithm does not affect voxel surrounded by the same material (density) as they are attributed to the interior of an object. By this the computing power is reduced strongly because neither voxels of the bulk nor the vacuum are considered.

The 3D structure of many different objects and materials were successfully reconstructed with these techniques. Amongst other it was possible to elucidate the 3D morphology of gold^[14,15] and magnetite nanoparticles,^[16] but also of more complex structures like NiO roses.^[17] Novel techniques furthermore allow tomographic reconstructions at the atomic scale so that the shape of gold nanoparticles could be investigated with a resolution of 2.8 Å^[18] and individual atomic positions could be resolved in a gold nanorod^[19] and a tungsten needle.^[20]

5.2 Application for Nb₃O₇(OH)

STEM tomography was applied to obtain 3D reconstructions of fragments of Nb₃O₇(OH) nanowire networks using tilt angles between -75° and $+75^\circ$. The alignment of the tilt series was performed with the help of *TomoJ*.^[21] A first SIRT reconstruction is followed by the restriction of the volume using a mask filter. The mask is created by setting the values of distinct projections to zero or one using the average intensity of the image as threshold value and removing all values set to zero from the reconstruction volume.^[13] This mask is applied for a subsequent SIRT loop which yields the basis for a DART algorithm used to reduce artifacts caused by the missing wedge effect (further details into the reconstruction routine can be found elsewhere^[22]). A tilt series and the respective reconstruction of a Nb₃O₇(OH) network is shown in figure 5.2.

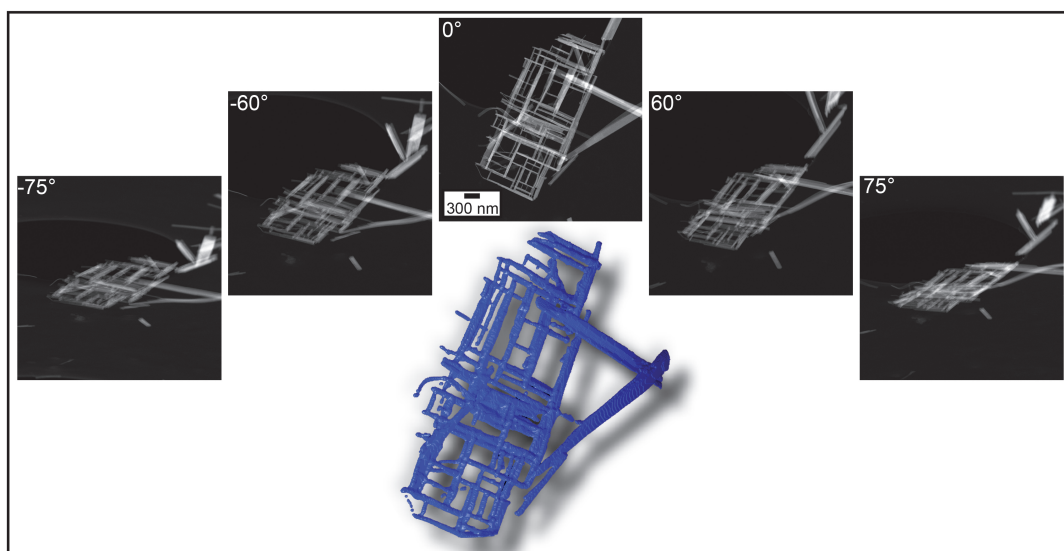


Figure 5.2 Selected images of a tilt series detected for a single Nb₃O₇(OH) nanowire network and the respective reconstruction achieved with the DART algorithm.

The arrangement of the nanowires at the junctions is crucial for both mechanical stabilization and charge transport (fig. 5.3b). Two junction types can be distinguished in the TEM images and local thickness measurements via EELS allow a first interpretation of their 3D structure (for more details see chapter 4). Additional 3D information about the nanowire arrangement was obtained by tomographic reconstruction. The DART algorithm sets the gray values in the reconstruction to defined values rendering the distinction of artifact from object impossible. Therefore, a tomographic reconstruction solely applying the SIRT algorithm was used for the analysis of the nanowire arrangement. To further reduce the impact of artifacts gold nanoparticles were deposited on the sample, as they can be tracked by the software thus facilitating the alignment of tilt series.

The combination of STEM images and histogram slices cut through the reconstruction was used to investigate the junctions in more detail (fig. 5.3a). The analysis yields no thickness variation at T-shaped junctions which agrees well with the findings of local thickness measurements described in chapter 4. In addition, it shows that the nanowires

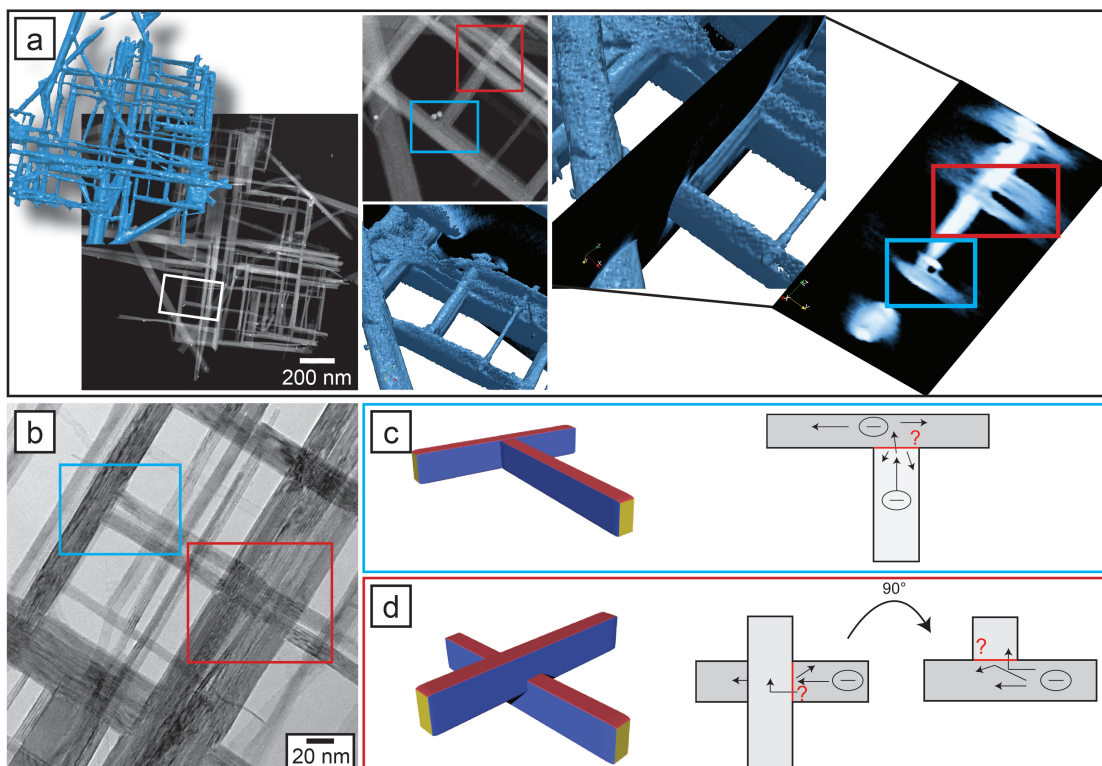


Figure 5.3 Analysis of the 3D nanowire arrangement in the network using electron tomography. a) Electron tomography features the 3D morphology of the nanowire networks. Slices cut through the network were used to investigate the nanowire arrangement (blue square: T-shaped junction; red square: crossing). b) Bright field image of a network, the two junction types are highlighted with two colored squares. Schematic illustrations of the nanowire arrangement at the junctions are given for T-shaped junctions (c) and crossings (d). The charge transfer at the junctions is an open question with high impact on the performance of the nanostructures as photocatalysts.

are in close contact at the junction. This suggests that these junctions either form due to the collision of two nanowires or as starting point of the growth of one nanowire out of the other. The reconstruction shows that two types of crossings have to be distinguished. One type is composed of two overlapping nanowires while the other technically consists of two opposing T-type junctions. No enhanced thickness is detected for the second type while a thickness increase is observed at the overlap region of the classical crossing. This agrees well with the finding of the EELS investigation which likewise yields an increased thickness for crossings. HAADF and HRTEM images indicate a partial intergrowth of the nanowires at the overlap region leading to a slight deformation of the crystal lattice (see chapter 4 and fig. 4.7f). The orthorhombic crystal symmetry of $\text{Nb}_3\text{O}_7(\text{OH})$ allows an expansion of the atomic distances across the overlap which apparently leads to the perpendicular arrangement of the nanowires. This partial intergrowth is most likely responsible for the mechanical stabilization of the networks. As mentioned above these junctions might have a strong impact on the transport properties of the nanostructures which influence their performance in DSSCs or as photocatalysts. Several scenarios are conceivable. At T-shaped junctions no interpenetration occurs and most likely grain boundaries form at the junctions. When a charge reaches the grain boundary it could

either be reflected, recombine or transfer into the other nanowire. The movement of charges perpendicular to the junction in the other nanowire is most likely not affected as no distortion of the crystal lattice was observed for this nanowire (fig. 5.3c). The situation becomes more complex for crossings. A slight deformation of the crystal lattices was observed at the overlap region proposing a partial intergrowth of the nanowires at the junction and a different type of grain boundary occurs. This indicates that charges diffusing close to the overlap region of the nanowires can transfer into the other wire without having to cross a grain boundary (fig. 5.3d). Thus it is expected that these junctions are no strong obstacle for charge-carrier transport.

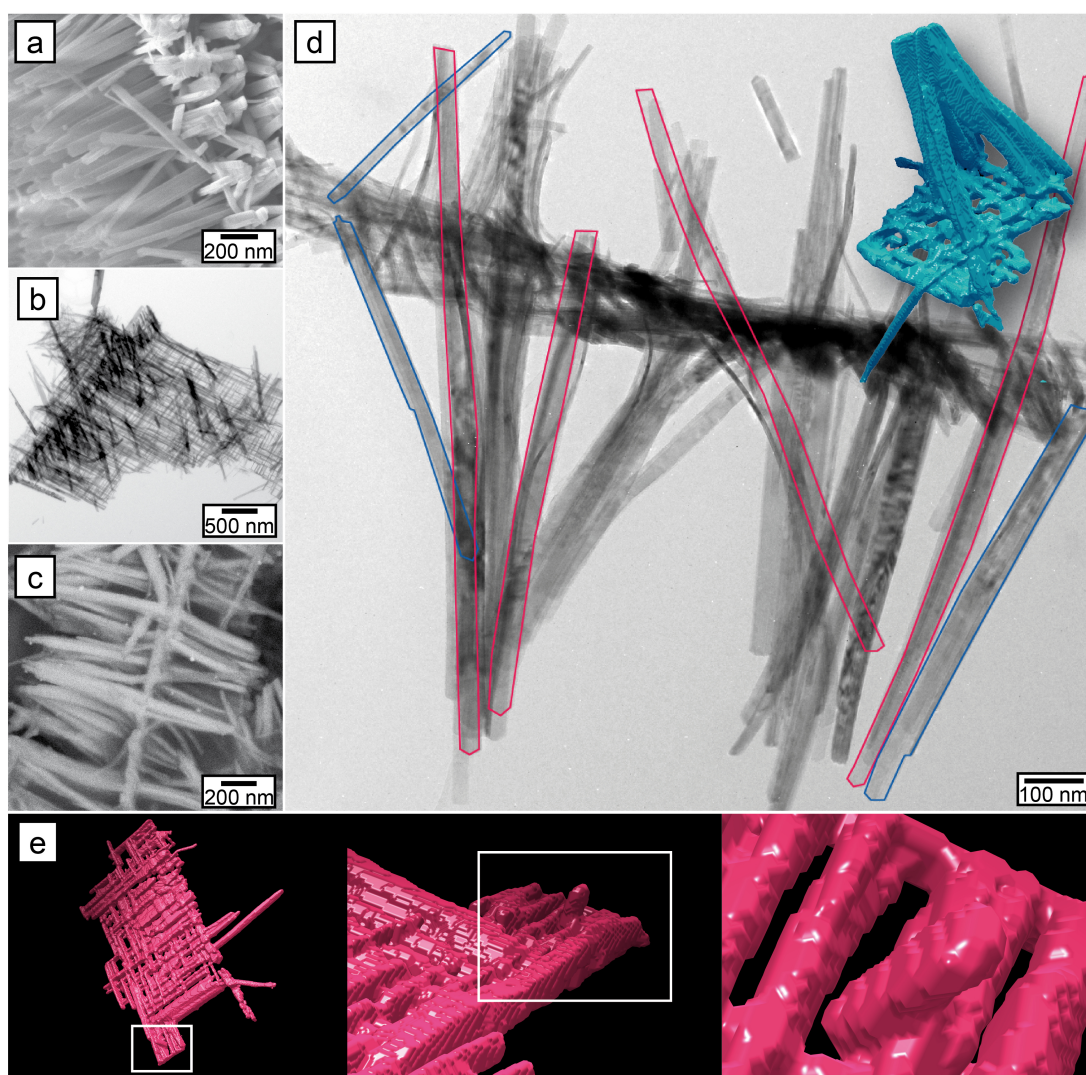


Figure 5.4 Investigation of the nanowire spikes on the cube surface which increase the surface area of the morphology. a) SEM image showing a cube edge. b) TEM image of a wall fragment, revealing the nanowire spikes standing from the surface of the wall. c) SE image of a cross section of one cube wall. The nanowire spikes reach into the interior of the cube. d) BF image of a fragment of a cross section, nanowires penetrating the wall are highlighted in red. e) Tomographic reconstruction of one nanowire showing the connection between network and one single tiny nanowire spike.

SEM images show nanowires which are oriented perpendicular to the nanowire networks and cause the spiky appearance of the superstructures (fig 5.4a-b). SEM and TEM im-

ages of a cross section of the cube wall indicate that most nanowires pass through the cube wall and the ones not passing through might be fragments of broken nanowires (fig 5.4c-d). It was not possible to elucidate their connection to the nanowire network from SEM and TEM images. This information is important as it might help to understand the self-organized formation of the superstructures but also because it reveals to what extent charges generated in the spikes can traverse to the nanowire network. The reconstructions confirms that the spikes pass through the nanowire network. Taking a closer look at the connection between network and spike exhibits that a grain boundary has formed similar as it was described for T-shaped junctions. TEM investigations revealed a larger $\{001\}$ crystal facet compared to the $\{001\}$ facet (see chapter 4). This allows to conclude the grain boundary from the shape of the nanowire spike as the $\{001\}$ lattice plane.

5.3 Conclusion

3D tomography provides new insights into the nanowire arrangement of $\text{Nb}_3\text{O}_7(\text{OH})$ superstructures which completes the picture drawn by local EELS thickness measurements. Due to the grain boundaries at the connections they can act as obstacles but still allow transport throughout the nanowire networks. Conductivity measurements are planned for the future to study this in more detail. The slight distortions observed at the overlap region of crossings indicate that the high degree of ordering characteristic for these nanowire networks is conducted by the orthorhombic crystal lattice of $\text{Nb}_3\text{O}_7(\text{OH})$. In addition the partly intergrowth observed at the overlap regions of crossings seems to be responsible for the mechanical stabilization of the nanowire arrangement. Still a detailed understanding of the initial forces triggering the self-organized formation of these highly ordered superstructures is missing.

5.4 Experimental

$\text{Nb}_3\text{O}_7(\text{OH})$ superstructures were obtained from the hydrothermal synthesis approach described in section 2.4.1 and chapter 4. The powder sample was mixed with ethanol and sonicated for 15 minutes to achieve small network fragments. TEM samples were obtained by drop casting this suspension onto a copper grid with holey carbon support. A *Hummingbird* tomography holder allowing tilt angles of $\pm 90^\circ$ was applied for the acquisition of tilt series with a *FEI Titan* TEM operated in STEM mode at 300 keV. Four series were recorded whose measurement details are listed in table 5.1. In the case of series 2 gold nanoparticles (10 nm) were spray coated on the sample to facilitate the alignment of the tilt series.

Table 5.1 Measurement parameters used for the acquisition of tilt series for 3D tomography of single $\text{Nb}_3\text{O}_7(\text{OH})$ nanowire networks.

	tilt range	step size	
1	-75 – 75°	1.0° ($\pm 60 - 70^\circ$) 1.5° (-60 – 60°)	fig. 5.2
2	-72 – 75°	1.5°	fig. 5.3
3	-65 – 74.5°	1.5°	fig. 5.4d
4	-69 – 73.5°	1.5°	fig. 5.4e

5.5 References

- [1] P. A. Midgley, R. E. Dunin-Borkowski, *Nat. Mater.* **2009**, *8*, 271.
- [2] N. Kawase, M. Kato, H. Nishioka, H. Jinnai, *Ultramicroscopy* **2007**, *107*, 8.
- [3] I. Arslan, J. R. Tong, P. A. Midgley, *Ultramicroscopy* **2006**, *106*, 994.
- [4] W. O. Saxton, W. Baumeister, M. Hahn, *Ultramicroscopy* **1984**, *13*, 57.
- [5] J. Frank, *Methods for Three-Dimensional Visualization of Structures in the Cell*, Springer, **2006**.
- [6] K. M. Hanson, *J. Comput. Assist. Tomo.* **1980**, 361.
- [7] M. Radermacher, T. Wagenknecht, A. Verschoor, J. Frank, *J. Microsc.* **1986**, *141*, RP1.
- [8] R. Gordon, R. Bender, G. T. Herman, *J. Theor. Biol.* **1970**, *29*, 471.
- [9] P. Gilbert, *J. Theor. Biol.* **1972**, *36*, 105.
- [10] A. V. Lakshminarayanan, A. Lent, *J. Theor. Biol.* **1979**, *76*, 267.
- [11] S. Bangliang, Z. Yiheng, P. Lihui, Y. Danya, Z. Baofen, *Chem. Eng. J. (Lausanne)* **2000**, *77*, 37.
- [12] K. J. Batenburg, S. Bals, J. Sijbers, C. Kübel, P. A. Midgley, J. C. Hernandez, U. Kaiser, E. R. Encina, E. A. Coronado, G. Van Tendeloo, *Ultramicroscopy* **2009**, *109*, 730.
- [13] A. Zürner, M. Döblinger, V. Cauda, R. Wei, T. Bein, *Ultramicroscopy* **2012**, *115*, 41.
- [14] E. M. Perassi, C. Hrelescu, A. Wisnet, M. Döblinger, C. Scheu, F. Jäckel, E. A. Coronado, J. Feldmann, *ACS Nano* **2014**, *8*, 4395.
- [15] D. Alloyeau, W. Dachraoui, Y. Javed, H. Belkahla, G. Wang, H. Lecoq, S. Ammar, O. Ersen, A. Wisnet, F. Gazeau, C. Ricolleau, *Nano Lett.* **2015**, *15*, 2574.
- [16] P. R. Buseck, R. E. Dunin-Borkowski, B. Devouard, R. B. Frankel, M. R. McCartney, P. A. Midgley, M. Pósfai, M. Weyland, *Proc. Natl. Acad. Sci. U.S.A.* **2001**, *98*, 13490.
- [17] A. Fihri, R. Sougrat, R. B. Rakhi, R. Rahal, D. Cha, M. N. Hedhili, M. Bouhrara, H. N. Alshareef, V. Polshettiwar, *ChemSusChem* **2012**, *5*, 1241.
- [18] M. C. Scott, C. C. Chen, M. Mecklenburg, C. Zhu, R. Xu, P. Ercius, U. Dahmen, B. C. Regan, J. Miao, *Nature* **2012**, *483*, 444.
- [19] B. Goris, S. Bals, W. Van den Broek, E. Carbó-Argibay, S. Gómez-Graña, L. M. Liz-Marzán, G. Van Tendeloo, *Nat. Mater.* **2012**, *11*, 930.
- [20] R. Xu, C. C. Chen, L. Wu, M. C. Scott, W. Theis, C. Ophus, M. Bartels, Y. Yang, H. Ramezani-Dakhel, M. R. Sawaya, H. Heinz, L. D. Marks, P. Ercius, J. Miao, *Nat. Mater.* **2015**, *14*, 1099.
- [21] C. Messaoudil, T. Boudier, C. O. Sanchez Sorzano, S. Marco, *BMC Bioinform.* **2007**, *8*, 288.
- [22] A. Wisnet, PhD thesis, Ludwig-Maximilians-University, **2014**.

6 In-Depth Characterization of Planar Defects in the Crystal Lattice of $\text{Nb}_3\text{O}_7(\text{OH})$

6.1 Introduction

Hydrothermal conditions feature the crystallization of materials at comparably low temperatures.^[1-3] The crystals form from solution and often complex structures of low enthalpy and entropy occur.^[4] However, the crystal lattices of many nanocrystals obtained from hydrothermal synthesis strategies show complex defect structures.^[5-8] These defects form for two reasons: First as a result of the growth mechanism, like it was shown for TiO_2 nanowires,^[7] or due to impurities introduced via mineralizer added to enhance the solubility of the precursor material.^[6] They affect the performance of the nanostructures in functional devices. For hydrothermally grown TiO_2 nanowires a reduced efficiency of dye-sensitized solar cells was found which was attributed to a confinement of charges by planar defects in the crystal lattice.^[8] Nb_2O_5 is an other metal oxide which is investigated as photoelectrode or photocatalyst material.^[9] Its polymorphs are all based on blocks of corner-sharing NbO_6 octahedra (ReO_3 -type structure units).^[10] The phase variety results from the large amount of possible block arrangements that yield a regular periodic pattern.^[10] The centers of the blocks have a composition of NbO_3 its boundaries one of NbO_2 . Hence, the introduction of smaller blocks and the rearrangement of blocks lead to a compensation of oxygen deficiencies.^[11] This gives rise to the formation of many suboxides observed for Nb_2O_5 ,^[12,13] but to a certain extend also enables the compensation of oxygen loss. Crystallographic shear on the (100) and (001) planes of the ReO_3 substructure allows to adjust the anion/cation ratio so that the corner-sharing NbO_6 blocks are interfaced by crystallographic shear planes.^[14] $\text{H-Nb}_2\text{O}_5$ is the thermodynamically stable Nb_2O_5 polymorph, while the formation of $\text{Nb}_3\text{O}_7(\text{OH})$ is most commonly observed under hydrothermal condition.^[15-20] Like $\text{H-Nb}_2\text{O}_5$ $\text{Nb}_3\text{O}_7(\text{OH})$ is a block structure which is composed of $(3 \times \infty)$ blocks which expand infinitely in b and c -direction. In the following chapter the defect structure of hydrothermally grown $\text{Nb}_3\text{O}_7(\text{OH})$ nanowires is investigated with HRTEM as knowledge about the defect structure of nanomaterials is inevitable for their performance in functional devices.

6.2 Results

The crystal lattice of hydrothermally grown $\text{Nb}_3\text{O}_7(\text{OH})$ is characterized by planar defects visible in $[100]$ viewing direction, but not in $[001]$ direction (fig. 6.1a). A BF image of one nanowire which is composed of a single crystalline and a region with defects is displayed in fig. 6.1b. The defect structure remains unchanged for large regions of the nanowire (fig. 6.1a). The defect structure occurs in a periodic fashion and planar defects appear most commonly every fourth lattice plane. The average defect width between two lattice planes in the defect region is $4.5 \pm 0.7 \text{ \AA}$ (fig. 6.1c). For some nanowires a defect-free region was observed close to their surfaces in addition to defect rich regions in their centers (fig. 6.1a).

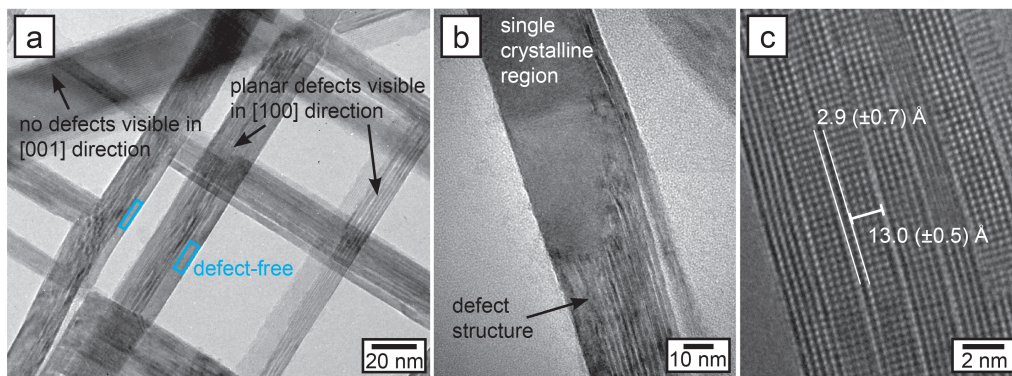


Figure 6.1 TEM images of $\text{Nb}_3\text{O}_7(\text{OH})$ nanowires which reveal planar defects in the crystal lattice of individual nanowires. a) The defects are solely visible for nanowires oriented in $[100]$ direction. b) HRTEM image of a nanowire with a single crystalline and a defected region. c) The defect structure is highly periodic, as planar defects appear for every fourth lattice plane.

A defocus series recorded for a thin nanowire gives further insights into the structure of the defects. Figure 6.2 shows a HRTEM image extracted from this defocus series which contains 42 images acquired at different defocus values (step size 4 nm). The lattice spacing in the undisturbed crystal lattice region is 3.6 \AA and 3.8 \AA which agrees to the lattice distances of $\{010\}$ and $\{001\}$ planes of $\text{Nb}_3\text{O}_7(\text{OH})$, respectively (fig. 6.2a). The image shows two planar defects where the spacing between the adjacent (001) planes is 4.0 \AA and 4.6 \AA . Despite the different width both defects go along with a shift of the (001) planes in $[010]$ direction. For the broader defect (4.6 \AA) the atomic positions shift by $1/2 d[010]$. The schematic drawing given in figure 6.2 illustrates the atomic arrangement. Exit wave reconstruction is applied to obtain further insight into the defects. The amplitude at zero defocus exhibits a dumbbell structure of the main peaks. This is not understood from the crystal structures and therefore might indicate a tilting or deformation of the NbO_6 octahedra in the crystal lattice. Whether this deformation/tilting is connected to the defects is still to be elucidated from exit wave reconstructions of perfect crystal lattice regions.

The amplitude of the exit wave for different defocus values is shown in fig. 6.2d,e for both defects. The wider defect region exhibits a periodic pattern of bright spots for certain defocus values. While no such pattern is visible at zero-defocus, first weak spots

are visible for a defocus value of 10 nm. The symmetry of the defect-free crystal lattice observed for a defocus value of 20 nm resembles the crystal symmetry and the weak spots visible inside the defect appear to be a two-sided extension of the defect-free crystal lattice. This impression is enforced by the amplitude visible for a defocus value of 40 nm, which exhibits white triangles at the border to the defect-free region. At a defocus of 50 nm the spots move to the center of the defect where they form a zigzag line which is also observed at the border of the defect. The pattern observed for the smaller defect is similar to one of the wider defect.

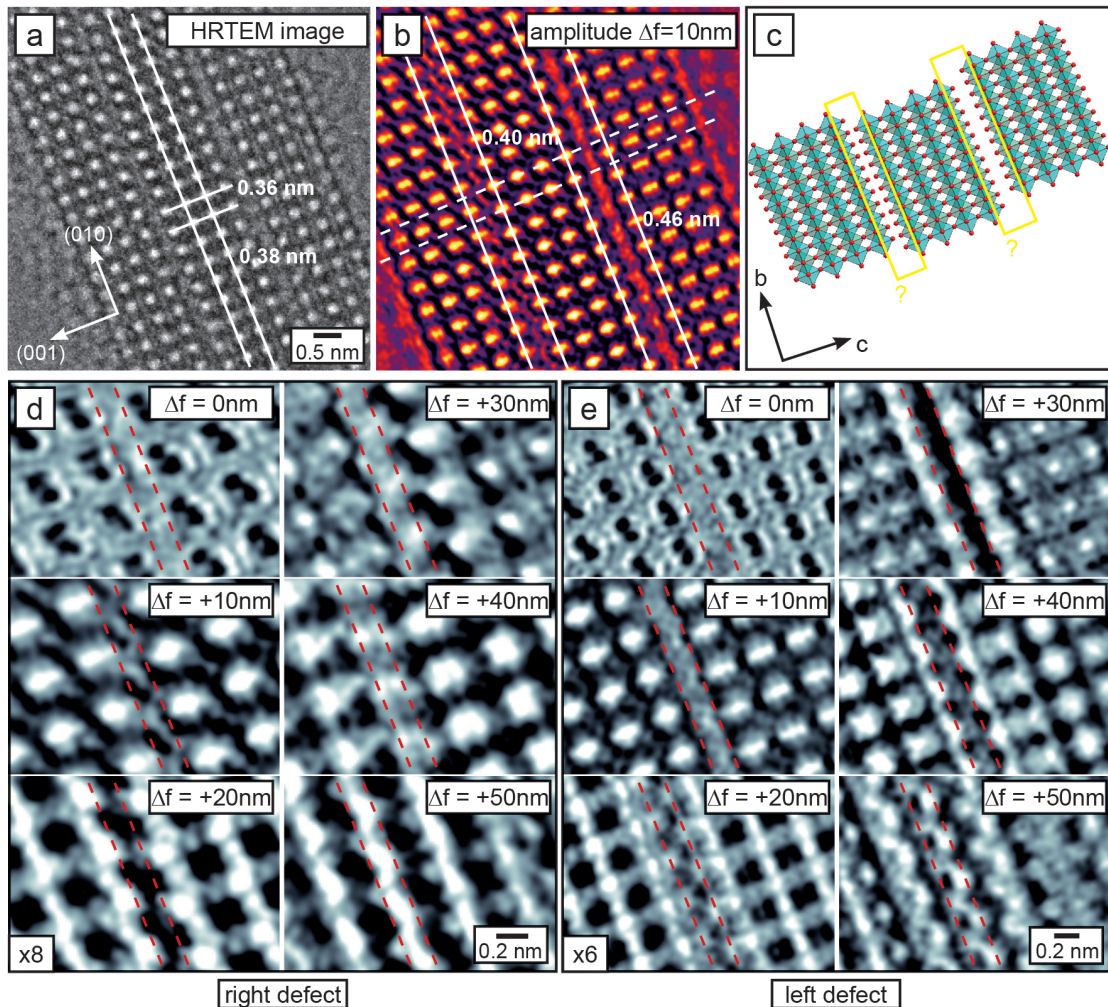


Figure 6.2 HRTEM analysis of the defect structure in a very thin nanowire. a) Unprocessed HRTEM image extracted from a defocus series. b) Amplitude of an exit wave reconstruction based on the defocus series given in a). c) Schematic illustration of the crystal lattice around the defects. d) Higher magnification ($\times 8$) of the amplitude of the exit wave of the crystal lattice surrounding the smaller defect visible on the right side of the nanowire. d) Amplitude of the exit wave for the wider defect visible at the left side of the nanowire at six times magnification. Both d) and e) show amplitude images of different defocus values.

Further insights into the atomic arrangement inside the defects were expected from EELS analysis which allows the investigation of the atomic bonding at the nanoscale. Therefore STEM-EELS experiments were conducted by performing line scans across the defects. Unfortunately the defects exhibit a very low stability and close like a zipper

under the electron beam illumination (see movie 6.1), which is why the ELNES of the Nb_{2,3} and O-K edge do not show significant alteration across the defects.

6.3 Discussion

The crystal lattice of Nb₃O₇(OH) exhibits a fairly regular defect structure composed of planar defects parallel to the {001} planes. Several reasons for the formation of these defects are conceivable. Their formation might help to release mechanical stress in the nanowire networks, but could also be necessary to compensate oxygen deficiency. The formation of planar defects was also observed for hydrothermally grown TiO₂ nanowires where it is associated to the hydrothermal growth process. The preliminary findings of the HRTEM analysis indicate that the defects indeed form due to non-stoichiometry in the crystal lattice. Non-stoichiometric Nb₂O₅ crystal phases are well known for (100) and (001) shear planes along the ReO₃ structure units to compensate the oxygen deficiency. In the case of non-stoichiometric Nb₃O₇(OH) the shear planes would correspond to (001) and (010) planes. Experimentally a shear in [010] direction was observed with the atomic position in {001} planes shifted by 1/2 lattice plane distance for a defect width of 4.6 Å. Furthermore, the observed zipping behavior under the electron beam indicates weak chemical bonding in the defects. From the HRTEM analysis it appears that the structuring observed inside the defects results from the terminal oxygen atoms of the NbO₆ octahedra which reach into the defect. However, it has to be noted that the defects are thermally stable and cannot be removed from the crystal lattice for calcination temperatures of 600 °C (see chapter 7). At higher temperatures a phase transformation to H-Nb₂O₅ occurs which is investigated in detail in the following chapter.

6.4 Experimental

Nb₃O₇(OH) nanowires were obtained from the hydrothermal synthesis approach described in section 2.4.1. The powder sample was mixed with ethanol and sonicated for 25 minutes to achieve small network fragments and single nanowires. For statistical investigation of the defect structure a *Philips CM300FEG/UT* TEM with a field-emission source and an ultra-twin objective lens was applied. HRTEM investigations were performed for ultrathin nanowires with a double corrected *FEI TEAM 0.5* microscope which is based on a *FEI Titan 80–300* microscope modified with a high-brightness emission source, gun monochromator, two *CEOS* hexapole-type spherical aberration correctors and a high-resolution *GIF Tridiem* energy-filter. Exit wave reconstruction was done with the help of Colin Ophus.

6.5 References

- [1] B. Liu, E. S. Aydil, *J. Am. Chem. Soc.* **2009**, *131*, 3985.
- [2] Z. Wang, J. Hou, C. Yang, S. Jiao, K. Huang, H. Zhu, *Phys. Chem. Chem. Phys.* **2013**, *15*, 3249.
- [3] F. Idrees, C. Cao, R. Ahmed, F. K. Butt, S. Butt, M. Tahir, M. Tanveer, I. Aslam, Z. Ali, *Sci. Adv. Mater.* **2015**, *7*, 1298.
- [4] A. Stein, S. W. Keller, T. E. Mallouk, *Science* **1993**, *259*, 7.
- [5] K. H. Tam, C. K. Cheung, Y. H. Leung, A. B. Djurišić, C. C. Ling, C. D. Beling, S. Fung, W. M. Kwok, W. K. Chan, D. L. Phillips, L. Ding, W. K. Ge, *J. Phys. Chem. B* **2006**, *110*, 20865.
- [6] R. Heinhold, H. S. Kim, F. Schmidt, H. von Wenckstern, M. Grundmann, R. J. Mendelsberg, R. J. Reeves, S. M. Durbin, M. W. Allen, *Appl. Phys. Lett.* **2012**, *101*, 062105.
- [7] A. Wisnet, S. B. Betzler, R. V. Zucker, J. Dorman, P. Wagatha, S. Matich, E. Okunishi, L. Schmidt-Mende, C. Scheu, *Cryst. Growth Des.* **2014**, *14*, 4658.
- [8] A. Wisnet, K. Bader, S. B. Betzler, M. Handloser, P. Ehrenreich, T. Pfadler, J. Weickert, A. Hartschuh, L. Schmidt-Mende, C. Scheu, J. A. Dorman, *Adv. Funct. Mater.* **2015**, *25*, 2601.
- [9] Y. Zhao, X. Zhou, L. Ye, S. C. E. Tsang, *Nano Rev.* **2012**, *3*, 1.
- [10] J. S. Anderson, J. M. Browne, J. L. Hutchison, *J. Solid State Chem.* **1972**, *5*, 419.
- [11] R. J. D. Tilley, *Principles and Applications of Chemical Defects*, Taylor & Francis, **1998**.
- [12] J. E. L. Waldron, M. A. Green, D. A. Neumann, *J. Phys. Chem. Solids* **2004**, *65*, 79.
- [13] T. McQueen, Q. Xu, E. N. Andersen, H. W. Zandbergen, R. J. Cava, *J. Solid State Chem.* **2007**, *180*, 2864.
- [14] J. S. Anderson, J. M. Browne, A. K. Cheetham, R. V. Dreele, J. L. Hutchison, F. J. Lincoln, D. J. M. Bevan, J. Straehle, *Nature* **1973**, *243*, 81.
- [15] F. Izumi, H. Kodama, *Z. Anorg. Allg. Chem.* **1978**, *441*, 8.
- [16] H. Zhang, Y. Wang, D. Yang, Y. Li, H. Liu, P. Liu, B. J. Wood, H. Zhao, *Adv. Mater.* **2012**, *24*, 1598.
- [17] J. Wu, J. Wang, H. Li, D. Xue, *Thin Solid Films* **2013**, *544*, 545.
- [18] S. B. Betzler, A. Wisnet, B. Breitbach, C. Mitterbauer, J. Weickert, L. Schmidt-Mende, C. Scheu, *J. Mater. Chem. A* **2014**, *2*, 12005.
- [19] M. Hmadeh, V. Hoepfner, E. Larios, K. Liao, J. Jia, M. Jose-Yacamán, G. A. Ozin, *ChemSusChem* **2014**, *7*, 2104.
- [20] P. Hu, D. Hou, Y. Wen, B. Shan, C. Chen, Y. Huang, X. Hu, *Nanoscale* **2015**, *7*, 1963.

7 Heat Induced Phase-Transformation of 3D Nb₃O₇(OH) Superstructures – Effect of Atmosphere and Electron Beam

This chapter is based on the following publication: S. B. Betzler, T. Harzer, J. Ciston, U. Dahmen, G. Dehm, C. Scheu, *Cryst. Growth & Des.* DOI:10.1021/acs.cgd.6b00386.

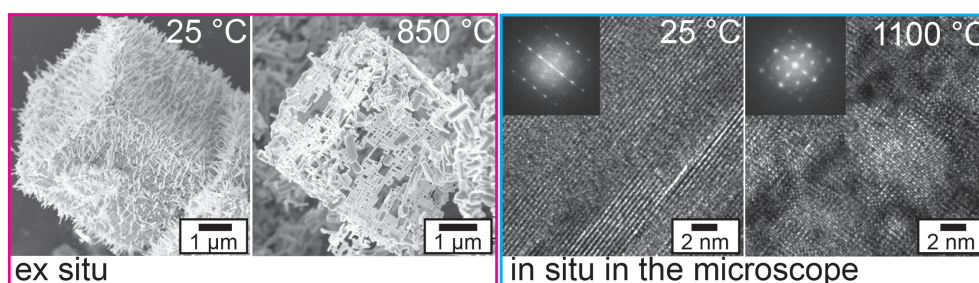


Figure 7.1 Table of contents graphic.

7.1 Introduction

Many different polymorphs are reported for niobium pentoxide with monoclinic H-Nb₂O₅ being the thermodynamically stable high-temperature phase.^[1,2] This phase is observed after calcination of amorphous Nb₂O₅ at 1200 °C via the intermediate formation of T-Nb₂O₅^[3] (T > 600 °C) and M-Nb₂O₅^[4] (T > 1000 °C).^[5] Starting from Nb(IV)O₂ an alternative heat induced transformation pathway to H-Nb₂O₅ occurs with orthorhombic L-Nb₂O₅ forming as intermediate phase which transforms into H-Nb₂O₅ at 850–900 °C.^[6] Other polymorphs include orthorhombic G-Nb₂O₅,^[7] monoclinic R-Nb₂O₅,^[8] and monoclinic zeta-Nb₂O₅.^[9] Most polymorphs are characterized by a common structure element as their crystal structures contain edge- and corner-sharing NbO₆ octahedra. In addition to stoichiometric phases several phases with oxygen deficiency like monoclinic Nb₁₂O₂₉^[10] and Nb₂₂O₅₄ exist.^[11]

Niobium pentoxide can be applied successfully as photocatalyst,^[12–16] photodetector,^[15] electrode material for photoelectrochemical water splitting^[17] and in dye-sensitized solar cells.^[18–21] Recently another class of niobium oxides – Nb₃O₇(OH)^[22] – has attracted attention as very promising photochemical properties are discovered for this phase^[23–28] and its performance as electrode material in dye-sensitized solar cells exceeds Nb₂O₅.^[23] Both orthorhombic Nb₃O₇(OH) ($a = 20.74 \text{ \AA}$, $b = 3.823 \text{ \AA}$, $c = 3.926 \text{ \AA}$)^[22] and monoclinic H-Nb₂O₅ ($a = 21.153 \text{ \AA}$, $b = 3.8233 \text{ \AA}$, $c = 19.356 \text{ \AA}$, $\beta = 119.80^\circ$)^[3] consist of blocks

of corner-sharing NbO_6 octahedra. This structural motif facilitates the phase transformation of $\text{Nb}_3\text{O}_7(\text{OH})$ to $\text{H-Nb}_2\text{O}_5$ as shown by X-ray diffraction studies.^[23,28] In general, all phase transformations are characterized by their thermodynamic (temperature and pressure) and kinetic properties (heating rate).^[29] In situ experiments^[30] performed in the electron microscope have been demonstrated to give insight into the phenomena occurring during heating for numerous materials including silver,^[31] Al_2O_3 ,^[32,33] anatase TiO_2 ^[34] and Al-Si alloy nanoparticles.^[35] However, the conditions inside an electron microscope differ from ex situ laboratory synthesis condition and often result in a reducing environment.^[36–38] This is especially interesting in the case of metal oxides with a covalent component in their bonding as they are known for their ability to accommodate slight reduction by crystallographic shear.^[39]

In the present work, the annealing behavior of complex 3D hierarchical $\text{Nb}_3\text{O}_7(\text{OH})$ superstructures is investigated. They are fabricated by a hydrothermal synthesis strategy^[25] and consist of highly ordered nanowire networks. The superstructures are fully crystalline, phase-pure and have a large surface area which are beneficial properties for photocatalysts and photoelectrodes.^[25] The thermal stability of the morphology and crystal structure of nanostructures is crucial for their application in functional devices. In this work the heat induced phase transformation of $\text{Nb}_3\text{O}_7(\text{OH})$ to $\text{H-Nb}_2\text{O}_5$ and the effect of annealing on the morphology of the superstructures is studied at the atomic scale as a function of pressure and atmosphere. This is important as some niobium oxide polymorphs are reported to tolerate large deviation from stoichiometry.^[11,40,41] In situ experiments carried out in a TEM are furthermore used to directly observe atomic scale phenomena.

7.2 Results and Discussion

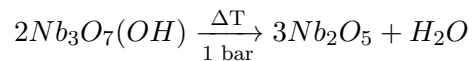
7.2.1 Ex Situ Studies of the Phase Transformation at Ambient Conditions

Figure 7.2a shows a SEM image of the 3D hierarchical $\text{Nb}_3\text{O}_7(\text{OH})$ superstructures investigated in this study. These superstructures were calcined at ambient conditions in the presence of oxygen and analyzed by ex situ XRD and electron microscopy after cooling down to room temperature. XRD reveals changes of the crystallographic structure for an annealing temperature of 500 °C. First a broadening of the reflection at $2\theta_B = 23.6^\circ$ occurs which coincides with a decrease of the intensity of the (001) reflection of $\text{Nb}_3\text{O}_7(\text{OH})$ ($2\theta_B = 22.5^\circ$) (see appendix fig. B.1). For a temperature of 850 °C broad reflections are observed as well which become more pronounced for the sample obtained from calcination at 1200 °C. The comparison with literature^[1,2] shows that the reflections of the sample calcined at 1200 °C perfectly match $\text{H-Nb}_2\text{O}_5$ (see appendix fig. B.2). High resolution imaging performed in the TEM reveals the presence of both crystal phases ($\text{Nb}_3\text{O}_7(\text{OH})$ and $\text{H-Nb}_2\text{O}_5$) in the sample calcined at 600 °C. Hence, an overlap of the strong reflections of $\text{H-Nb}_2\text{O}_5$ at 23.8° ($(110), (\bar{1}11)$) and 23.9° ((011)) with the reflections of $\text{Nb}_3\text{O}_7(\text{OH})$ are responsible for the broadening of the reflections observed in the respective XRD pattern. At the same time SEM images show that the

morphology of the superstructures is preserved up to 850 °C (fig. 7.2b). This is related to the conservation of large parts of the original nanowire networks as obvious from bright field TEM images (fig. 7.2d,e). A comparison of the networks before and after calcination at 850 °C reveals that the nanowire arrangement is preserved while the size of the single wires increases. Electron diffraction pattern acquired for a single nanocrystal of the 850 °C sample confirm that they possess the H-Nb₂O₅ crystal structure with the long dimension being parallel to the [0 1 0] direction (see fig. 7.2f and appendix fig. B.3). The H-Nb₂O₅ nanowires show regions with slightly tilted (2 to 4°) { $\bar{1}01$ } lattice planes as determined from analysis of the FFT. This deviation is compensated by the formation of small-angle grain boundaries (SAGB) consisting of edge dislocations with a spacing of $D = 5.8 \pm 1.3$ nm (fig. 7.2h).

The findings of the TEM investigations indicate a merging of crystallites during the phase transformation which results in larger nanocrystals and suggests that Ostwald ripening occurs (fig. 7.2g). This hypothesis is strengthened by the observation of increased crystal sizes for a higher calcination temperature of 1200 °C as indicated by sharp reflections in the XRD (see appendix fig. B.2). The large crystal size achieved at 1200 °C is also visible in SEM micrographs (fig. 7.2c) which in addition show that the superstructures have collapsed into individual large and compact H-Nb₂O₅ crystals. TEM images reveal the compact nature of these single crystals and electron diffraction experiments indicate the presence of (10 $\bar{1}$) twins in the H-Nb₂O₅ crystal lattice. We propose that these twins form during the merging of small nanocrystals as a result of stress or growth twins (see appendix fig. B.3). The observation of these twins is in accordance with the literature which describes the (10 $\bar{1}$) twin boundary as the only permitted twin boundary in the block structure of H-Nb₂O₅.^[42]

The investigation indicates that surprisingly high temperatures are required to remove water from the crystal lattice of Nb₃O₇(OH) to form H-Nb₂O₅ according to the following equation:



In contrast to a recent study which reported a temperature of 450 °C to suffice for complete transformation of Nb₃O₇(OH) to H-Nb₂O₅^[28] temperatures above 600 °C are required for complete phase-transformation of the Nb₃O₇(OH) superstructures investigated in the present work. Furthermore, we apply in-depth TEM analysis and by this a high thermal stability of both crystal structure and morphology is proven. In situ investigations which allow to directly observe the phase transformation at the atomic scale are performed under reducing conditions in the TEM as described in the following.

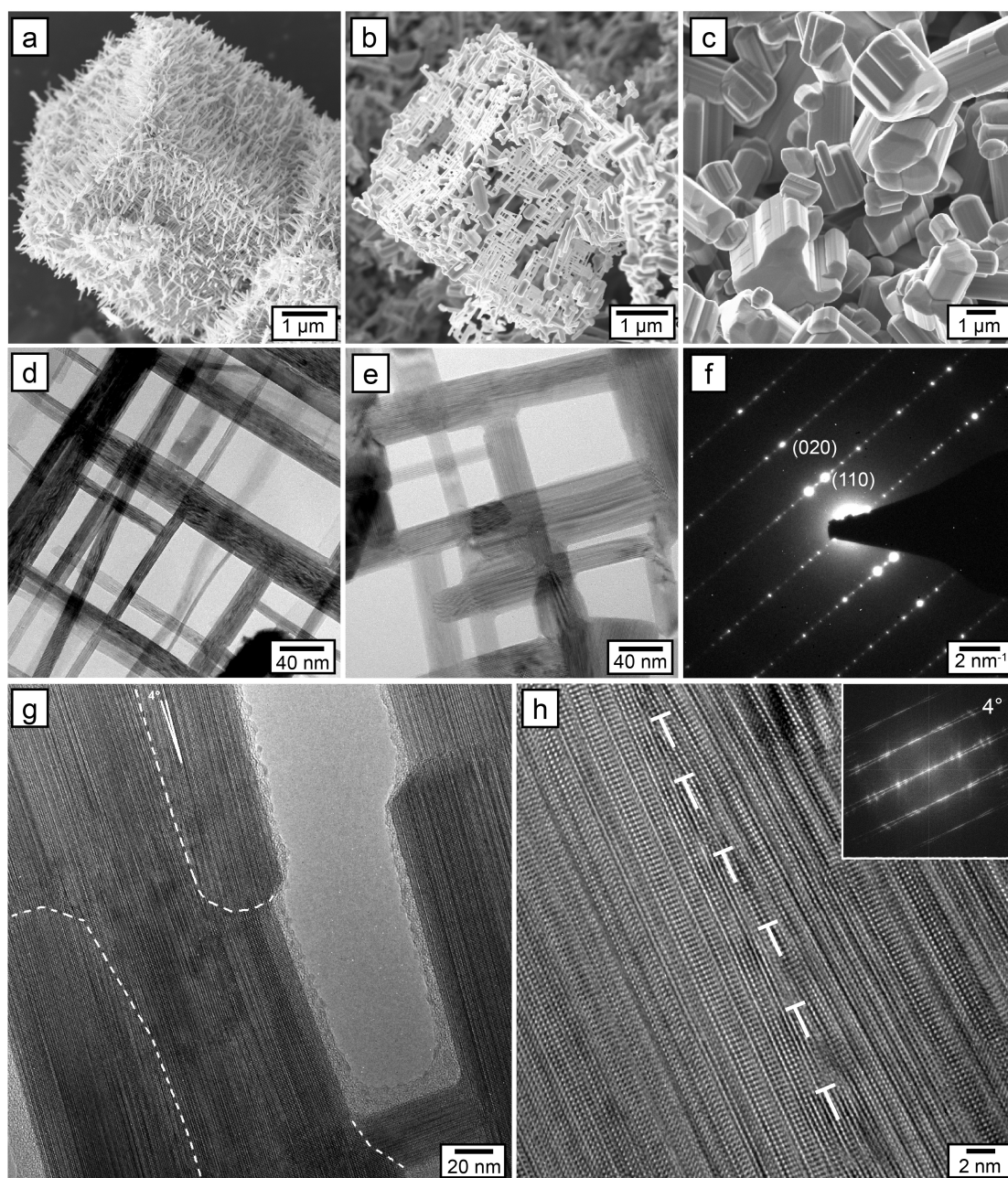


Figure 7.2 Electron micrographs of samples heated ex situ at ambient condition. a) SEM image of the Nb₃O₇(OH) superstructure before the calcination and after the calcination at 850 °C (b) and 1200 °C (c). d) TEM image of the network consisting of the Nb₃O₇(OH) nanowires before calcination. e) TEM image of the nanowire network obtained after calcination at 850 °C. The electron diffraction pattern recorded for one nanocrystal in [001] zone axis is shown in f). g) HRTEM image of an area which shows that the nanowires merged to form larger crystals during calcination at 850 °C. The white lines indicate individual grains. h) Magnified view of the boundary between two nanowires grown together. A miss-tilt of 4° also visible in the FFT is compensated by dislocations (highlighted with white lines) arranged in a small-angle grain boundary.

7.2.2 In Situ TEM Investigation of Phase Transformation in Reducing Atmosphere

The size of the 3D hierarchical $\text{Nb}_3\text{O}_7(\text{OH})$ superstructures (see fig. 7.2a) necessitates the investigation of fragments of nanowire networks or single nanowires with TEM. The high degree of ordering within the large-scale nanowire networks (see fig. 7.2d,7.3a) is apparent from electron diffraction pattern which exhibit distinct reflections typical for single crystals.^[25]

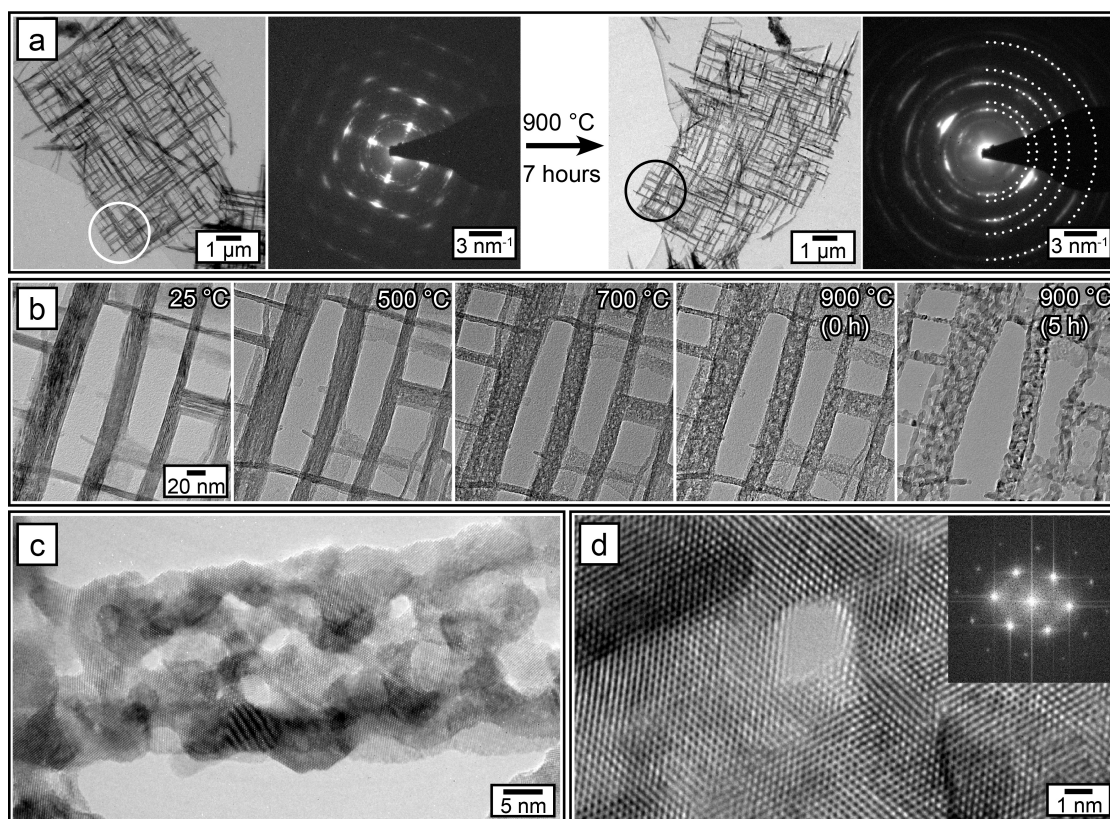


Figure 7.3 In situ TEM heating experiments which shows the effect of heat and electron bombardment on the structure of nanowire networks. a) BF images and electron diffraction pattern of the investigated network before and after the heating experiment. b) BF images recorded during the in situ heating experiment. c) HRTEM images acquired of one nanowire of the investigated network after the in situ experiment. d) HRTEM image conducted on one nanowire after the heating experiment. The inset shows the FFT pattern calculated of the respective HRTEM image.

The effect of heat on the structure of one whole network was monitored in the course of 300 minutes at 900 °C with images recorded every 15 minutes (see fig. 7.3b). To reduce possible electron beam induced radiation damage (acceleration voltage was 300 kV), the beam was moved to a neighboring area in between the measurements (detailed description of the experiment see appendix tab. B.1). No changes are observed for temperatures below 500 °C followed by the formation of a substructure in the nanowires (at 700 °C). This structure becomes more pronounced at 900 °C at which point nanoscale pores develop within the nanowires. These pores are surrounded by small nanocrystals. The shape of the pores changes during the first 135 minutes at 900 °C. Afterwards primar-

ily a bending of the nanowires and only slight changes of the nanocrystalline structure are observed (see appendix movie 7.1). The comparison of electron diffraction patterns from the investigated region before and after the experiment shows that the long-range ordering within the network is lost (fig. 7.3a). Figure 7.3c shows the formation of small nanocrystals which surround the pores. High resolution TEM images recorded after the heating experiment show that all nanocrystals within the pristine nanowire have the same crystal orientation (fig. 7.3d). Although these nanocrystals are aligned along the same zone axis they are slightly rotated relative to each other leading to moiré pattern visible in the HRTEM image. FFT analysis shows that they possess a different crystal structure than the mother compound which cannot definitely be assigned to one specific niobium oxide phase reported in the literature.

In contrast to observations for the $\text{Ni(OH)}_2/\text{NiO}$ system^[43] no changes of the nanowire width are found for the $\text{Nb}_3\text{O}_7(\text{OH})$ nanowire networks in our in situ study (see appendix fig. B.4). It is important to note that despite the pore formation a high thermal stability (no changes up to 500 °C) of the nanowire network is also observed under reducing conditions (fig. 7.3b).

To directly follow the formation of the pores and nanocrystals in situ TEM heating experiments were also conducted at higher magnification for single nanowires oriented parallel to the $[001]$ (fig. 7.4a) and $[100]$ (fig. 7.4b) direction (the $[010]$ direction cannot be investigated as it is the growth direction of the nanowires^[23,25]). In this case, beam damage was not reduced by moving respective nanowires out of the electron beam but by lowering the accelerating voltage to 200 kV. The crystal lattice of $\text{Nb}_3\text{O}_7(\text{OH})$ nanowires is not defect free but contains planar defects parallel to the (001) lattice planes visible in $[100]$ viewing direction (fig. 7.4c). The investigations were performed for regions at the interface between defective and defect-free crystal lattices since the largest changes were expected here (fig. 7.4). First changes of the crystal lattice occur in the form of defects in the temperature range between 400 °C and 500 °C and a shift of the atomic position by $1/2 [001]$ of every third lattice plane is observed (fig. 7.4d). The dislocation leading to the atomic displacements of $1/2[001]$ originate at the planar defect (fig. 7.4b) and move through the single crystalline region towards the surface of the nanowire with a speed of $5.9 \pm \text{nm/min}$ at 450 °C (see appendix movie 7.2). The dislocations form to relieve strain^[44–46] and are believed to initiate the phase transformation which proceeds in the $[001]$ direction. This agrees well with the reported observation that the phase transformation from $\text{Nb}_3\text{O}_7(\text{OH})$ to $\text{H-Nb}_2\text{O}_5$ likewise happens via crystal deformation along the z-direction.^[28] At a temperature of 650 to 750 °C first slight distortions of the crystal lattice cause a blurriness in the FFT pattern and frame the beginning pore formation. With increasing temperatures these pores become more pronounced which coincides with the beginning of a phase transformation as obvious from FFT pattern. The phase transformation proceeds with ongoing heating time and so does the formation of the pores which increase in size. As soon as the phase transformation is completed only minor changes of the pore structure are observed and their sizes remain constant (see appendix fig. B.5). The formation of pores can be provoked directly at a heating

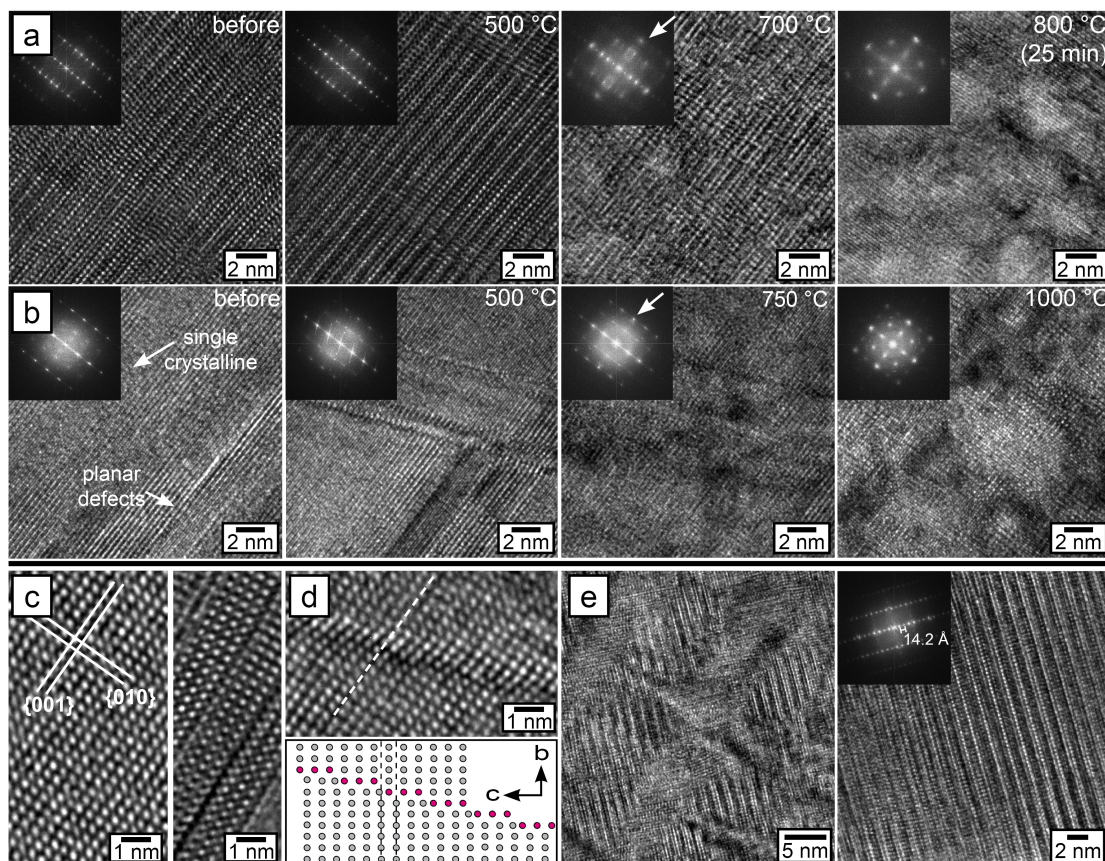


Figure 7.4 HRTEM images detected during the in situ TEM heating experiments. a) Screen shots of a movie recorded for a nanowire in $[001]$ viewing direction at different temperatures. b) Images recorded during an in situ experiment starting from a nanowire in $[100]$ orientation. c) HRTEM images of the crystal structure of a nanowire in $[100]$ direction showing a defect-free area and the planar defects parallel to the (001) lattice planes. d) HRTEM image acquired in $[100]$ direction of one defect forming in the crystal lattice at 450°C and schematic presentation of its structure. e)/f) HRTEM images of two nanowires, which were heated in situ to 950°C in absence of the electron beam. A region composed of different crystal orientations which merged during the recrystallization is visible in the HRTEM image displayed in e) and f) shows a single crystalline region. The FFT yields a d -spacing of 14.2 \AA which does not match $\text{Nb}_3\text{O}_7(\text{OH})$ and $\text{H-Nb}_2\text{O}_5$.

temperature of 900°C by moving the electron beam to a new network which had not been illuminated before (see appendix movie 7.3). In principle several reasons for this pore formation are conceivable. They could form to compensate the volume change occurring during the phase transformation,^[43] due to a movement and agglomeration of defects resulting in Kirkendall voids^[47,48] or be caused by electron beam damage effects which destroy bonds and remove preferentially one atomic species (e.g. oxygen) from the crystal.^[36–38] Of these, the volume change has been shown to be the most likely explanation for numerous decomposition reactions of this type.^[43,49] Many such reactions are found to be topotactic and pseudomorphic, i.e. they maintain crystallographic alignment of the parent and product lattices and leave the external shape of the structure largely unchanged. This implies that the volume difference must be accommodated by internal pores. These pores only form when the sample has reached 500°C and no changes of the nanowire morphology are observed during electron bombardment at lower

temperatures (see appendix movie 7.4). Similar pores were observed for Nb_2O_5 . But other than found for $\text{Nb}_3\text{O}_7(\text{OH})$ in this work the pore formation in Nb_2O_5 is associated with a phase transformation that can be initiated by electron irradiation at room temperature.^[37] The study assumes a reduction of Nb_2O_5 by the electron irradiation but could not match the observed d-values to a known crystal phase. At temperatures of 1200 °C we find a rapid merging of the initial nanowires via oriented attachment and coarsening under strong crystalline anisotropy (see appendix movie 7.5). FFT patterns calculated from HRTEM images acquired at 800 °C (fig. 7.4a) and 1000 °C (fig. 7.4b) are found to be different from the parent phase. The pattern of the nanowires illuminated during the experiment differ dependent on the starting orientation of the nanowire (see appendix fig. B.6). Neither of these pattern fits to the $\text{H-Nb}_2\text{O}_5$ or $\text{Nb}_3\text{O}_7(\text{OH})$ crystal phase and the phase variety of niobium oxide and its ability to accommodate reduction by crystallographic shear complicate the phase identification (the determined d-values are listed in appendix tab. B.2).^[11,40,41,50]

To address the question of the effect of the electron beam irradiation on the phase transformation further nanowires and networks which had not been illuminated during the in situ heating experiment are analyzed after cooling down to room temperature. The investigation show that in the absence of the electron beam a minimum temperature of 900 °C is required to initiate a phase transformation. In that case the networks likewise retain their morphology. Other than in the presence of the electron beam no pore formation is visible but instead the transformation starts with the formation of small nanograins in the initial nanowires. It appears that these nanograins merge in the course of the recrystallization to form larger single crystals (see appendix fig. B.7). It is important to note that at 900 °C not all nanowires have phase transformed and many preserve the $\text{Nb}_3\text{O}_7(\text{OH})$ crystal structure. However, after calcination at 1200 °C all nanowires appear to be transformed into a crystal phase which is different from the mother compound or $\text{H-Nb}_2\text{O}_5$ and besides d-values of 1.9 Å and 3.2 Å a d-value of 14.2 Å is found (fig. 7.4e and appendix tab. B.2). The large d-spacing is solely observed for a few phases which are $\text{M-Nb}_2\text{O}_5$ ($d_{(110)} = 14.5 \text{ Å}$)^[4], $\text{T-Nb}_2\text{O}_5$ ($d_{(020)} = 14.6 \text{ Å}$)^[3] and $\text{L-Nb}_2\text{O}_5$ ($d_{(020)} = 14.7 \text{ Å}$).^[6]

7.2.3 Electron Energy-Loss Spectroscopy Analysis of the Different Samples

The reducing atmosphere in a TEM and the known sensitivity of niobium oxide to be reduced by the electron beam suggest the removal of oxygen during the in situ TEM experiments, thus reducing the oxidation state of niobium. Therefore EELS is applied to determine the oxidation state by analyzing the energy-loss near-edge fine structure of the O-K and Nb-M_{2,3} edge and by quantitative determination of the niobium-to-oxygen ratio.

The ELNES of element specific edges in EEL spectra yields a deeper understanding of the oxidation state and local surrounding of the elements in the crystals. EELS data were recorded with an energy resolution of 0.3–0.4 eV (dispersion 0.07 eV) for $\text{Nb}_3\text{O}_7(\text{OH})$, $\text{Nb}_3\text{O}_7(\text{OH})$ calcined at 600 and 850 °C and $\text{H-Nb}_2\text{O}_5$. The $\text{H-Nb}_2\text{O}_5$ phase was obtained

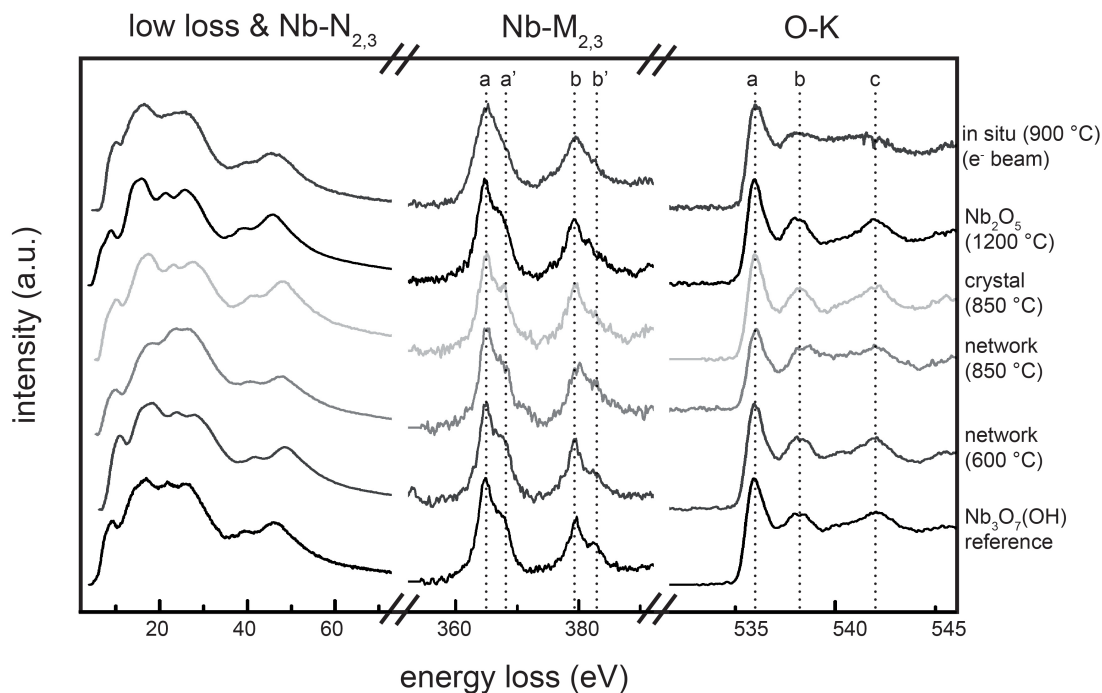


Figure 7.5 EEL spectra recorded for samples obtained from different heat treatments. Different samples were investigated: One $\text{Nb}_3\text{O}_7(\text{OH})$ nanowire network as reference as well as networks calcined ex situ at 600 °C and 850 °C. Furthermore single nanowires observed after calcination at 850 °C and 1200 °C were analyzed in addition to the nanowire network which was heated in situ to temperatures of 900 °C in the presence of the electron beam.

via calcination of $\text{Nb}_3\text{O}_7(\text{OH})$ at 1200 °C. In addition, ELNES data were recorded at the nanowire network heated in situ in the TEM in the presence of the electron beam at 900 °C (fig. 7.5 and tab. 7.1). The low-loss region which contains the plasmon peak and single valence loss excitations is characterized by four main features with additional shoulders and is very similar for all samples (fig. 7.5). Slight deviations between the different samples are most likely caused by carbon contamination and thickness variation. In thick samples multiple scattering events can occur, yielding altered ELNES features.^[51] However, the low loss region for the different samples do not show any sign of a second plasmon and as such the different ELNES features discussed below stem from changes in the oxidation state.

The $\text{Nb-M}_{2,3}$ edge with an edge onset at around 365 eV results from the transition of electrons of the $\text{Nb-}3p$ states to unoccupied $\text{Nb-}4d/\text{Nb-}5s$ states and is characterized by two white lines. The energy difference between M_2 (b) and M_3 (a) originates from the spin-orbital splitting of $3p_{1/2}$ and $3p_{3/2}$ orbitals. The M_2 and M_3 difference is 14.6 ± 0.1 eV for $\text{Nb}_3\text{O}_7(\text{OH})$ and the ex situ heated samples, while a slightly decreased splitting is observed for the sample heated in situ (14.1 ± 0.2 eV) (see tab. 7.1). The ELNES of the $\text{Nb-M}_{2,3}$ edges show high energy loss shoulders (a', b') for all samples (ex situ heated samples, $\text{H-Nb}_2\text{O}_5$ and $\text{Nb}_3\text{O}_7(\text{OH})$) except the one heated in situ in the presence of the electron beam. These high-energy loss shoulders are characteristic for pentavalent niobium, while this double peak structure becomes less pronounced for Nb(IV)O_2 and vanishes for Nb(II)O .^[52,53] Hence, the observed ELNES of the $\text{Nb-M}_{2,3}$

edges proposes the presence of pentavalent niobium in the samples heated ex situ as well as H-Nb₂O₅ and Nb₃O₇(OH). In contrast, the ELNES of the sample heated in situ in the presence of the electron beam indicates the presence of Nb(IV) or Nb(II) in the crystal lattice.

The ELNES of the O-K edge is characterized by three dominant features (*a, b, c*). The splitting of peak *a* and *b* can serve as a fingerprint for the oxidation state.^[53] It is 4.3 ± 0.1 eV for the samples heated ex situ while it decreases to 3.8 ± 0.1 eV for the sample heated in situ in the microscope. The former values agree well with the ones reported for Nb₂O₅ (4.3 eV^[53]) while the latter value indicates a decrease of the niobium oxidation state for the sample heated in situ as a value of 3.5 eV was reported for NbO.^[53] The high similarity between Nb₃O₇(OH) and H-Nb₂O₅ is related to the fact that both crystal structures are based on identical structure units. In this regard, the ELNES of the Nb-M_{2,3} as well as the O-K edge indicate a reduction of the niobium oxidation state due to the combination of electron irradiation and the absence of oxygen. The niobium-to-oxygen (N_{Nb}/N_O) ratio of these samples was quantified based on the intensity of the respective edges $I_{O/Nb}$ using the following equation.^[51]

$$\frac{N_{Nb}}{N_O} = \frac{I_{Nb}}{I_O} \cdot \frac{\sigma_O}{\sigma_{Nb}}$$

Here σ_O and σ_{Nb} are the inelastic cross-section of the O-K and the Nb-M_{2,3} edge, respectively. For Nb₃O₇(OH) a σ_{Nb}/σ_O -factor of 0.86 and for Nb₂O₅ a factor of 0.76 were determined empirical based on the reference sample and H-Nb₂O₅ (1200 °C sample). These factors are used to determine the Nb–O ratio of the sample heated in situ in the microscope in the presence of the electron beam. The Nb–O ratio determined using the cross-section factor ($\sigma_{Nb}/\sigma_O = 0.76$) for Nb₃O₇(OH) is 0.67 while a value of 0.59 was calculated using the σ_{Nb}/σ_O of Nb₂O₅. The values are higher than the ones of Nb₃O₇(OH) ($N_{Nb}/N_O = 0.38$) and Nb₂O₅ ($N_{Nb}/N_O = 0.4$) indicating a lower amount of oxygen. These findings coincide with the altered ELNES of the Nb-M_{2,3} and O-K edge discovered for the sample heated in situ in the microscope proving the removal of oxygen from the crystal structure of the sample due to the combination of heat and reducing condition.

Table 7.1 EELS data recorded for the samples calcined at different temperatures ex situ and in situ in the presence of the electron beam. The peak positions are given relative to the onset of the respective edge which was set to 365 eV for the Nb-M_{2,3} and 532 eV for the O-K edge.

sample	Nb-M _{3,4}		O-K edge		
	a (eV)	b (eV)	a (eV)	b (eV)	c (eV)
Nb ₃ O ₇ (OH) reference	1.5±0.1	16.1±0.2	1.1±0.1	5.6±0.1	13.2±0.2
Nb ₃ O ₇ (OH) 600 °C	1.4±0.2	16.0±0.1	1.1±0.1	5.4±0.1	13.0±0.1
network 850 °C	1.4±0.1	16.0±0.1	1.0±0.1	5.3±0.1	13.0±0.1
crystal 850 °C	1.5±0.2	16.2±0.4	1.1±0.1	5.3±0.1	13.1±0.1
Nb ₂ O ₅ (1200 °C-sample)	1.5±0.1	16.1±0.1	1.0±0.1	5.3±0.1	13.1±0.1
in situ network with e-beam	2.2±0.1	16.5±0.4	1.1±0.1	5.0±0.1	-

7.3 Conclusion

This study investigates the effect of heat on the morphology and crystal structure of 3D hierarchical Nb₃O₇(OH) superstructures at different atmospheric conditions. These superstructures consist of highly ordered nanowire networks. In the presence of oxygen a transformation of Nb₃O₇(OH) to H-Nb₂O₅ is initiated at temperatures above 500 °C and the presence of both crystal phases is observed for a sample calcined at 600 °C. At the same time the morphology of the nanowire networks and with that of the superstructures is preserved up to 850 °C, despite of the merging of the nanowires which goes along with phase transformation. This merging is facilitated by SAGB which form to compensate slight tilting of crystal domains.

The high thermal stability of the nanowire networks is confirmed by in situ investigation in the TEM. However, the reducing condition in the electron microscope has a strong effect on the phase transformation. Prior the phase transformation defects form in the single crystalline region of the nanowires at 450 °C. These defects move through the crystal to its surface starting from planar defects which are characteristic for hydrothermally grown Nb₃O₇(OH) nanowires. The presence of the electron beam during the heating experiment features the formation of an oxygen deficient niobium oxide crystal phase for temperatures above 800 °C. The volume difference between the two crystal phases is compensated by the formation of pores which is observed at temperatures above 700 °C. Solely the presence of the electron beam does not suffice to initiate this pore formation, but at least a temperature of 500 °C is required as well. However, no pores are observed for heating experiments performed in situ in the absence of the electron beam and a side from that under this condition the phase transformation also happens at higher temperatures of 900 °C.

The present study indicates that oxygen has a strong effect on the phase transformation yielding different crystal phases in situ than observed ex situ. The strong effect of the electron beam and the absence of oxygen is explained by the ability of niobium oxide to

form suboxides and accommodate oxygen deficiency via structural strain. While the the absence of oxygen yields a crystal phase with similar crystal symmetry like $\text{H-Nb}_2\text{O}_5$ and $\text{Nb}_3\text{O}_7(\text{OH})$ but different d-values, the additional presence of the electron beam features clearly different crystallographic parameters. All together, this study demonstrates the high thermal stability of $\text{Nb}_3\text{O}_7(\text{OH})$ superstructures related to its crystal structure and morphology. This makes the superstructures especially promising for several functional application performed at higher temperatures.

7.4 Experimental

$\text{Nb}_3\text{O}_7(\text{OH})$ superstructures are obtained from a hydrothermal synthesis approach.^[25] Ex situ calcination experiments at ambient conditions in the presence of oxygen are performed in an oven applying the following procedure: Heating up to the target temperature for six hours (600 °C, 850 °C and 1200 °C), this temperature is kept for another six hours before cooling down to room temperature. The morphology of the different samples is analyzed with a *Zeiss Gemini Ultra Field Emission SEM* equipped with an in-lens detector and operated at 4kV. A thin carbon layer is deposited on the sample with a *BAL-TEC MED020* coating system to reduce charging effects. The crystallographic structure of the powder samples are analyzed with X-ray diffraction using a *STOE* powder diffractometer equipped with a *Dectris Mythen K1* detector, *Seifert ID3003* generator and a *Seifert Long Fine Focus Dx-Cu12x0.4-S* X-ray tube. For the TEM study, the powder samples are mixed with ethanol and sonicated for 5–20 min to break the superstructures. This suspension is drop casted on a TEM grid with holey carbon support. A *Philips CM300FEG/UT* TEM with a field-emission source and an ultra-twin objective lens is used for electron diffraction and HRTEM investigation of the different samples calcined ex situ in the presence of oxygen. Monochromated EELS investigation with an energy resolution of 0.3–0.4 eV are performed at 200 kV on a *Zeiss Libra MC200* microscope equipped with an in-column Omega filter.

For in situ experiments two different heating holder designs are applied. The effect of heat on whole nanowire networks is investigated with a conventional heating holder (*Gatan 652* double tilt) which applies water cooling to minimize drift. The samples are drop casted onto a molybdenum grid prior to the experiment to prevent heat induced decomposition of the TEM grid.^[54] The heating experiments are performed in bright field (BF) mode with a *Jeol 3010* in situ microscope operated at 300 kV. The target networks are furthermore analyzed (electron diffraction, HRTEM) before and after the heating experiment with a *Philips CM300FEG/UT* microscope operated at 300 kV. In situ HRTEM analysis of single nanowires are performed with two different heating holders which use silicon nitride based heating chips. The samples are directly drop casted onto the chip. A *Protochips* single tilt holder with silicon nitride heating chips which allow temperatures up to 1200 °C is used for in situ experiments done with a *FEI Titan 80-300* microscope operated at 200 kV. In addition in situ HRTEM studies are also performed with a *Jeol 2200FS* TEM operated at 200 kV using a *DeNS Solution* double tilt holder and respective silicon nitride chips.

7.5 References

- [1] B. M. Gatehouse, A. D. Wadsley, *Acta Crystallogr.* **1964**, *17*, 1545.
- [2] K. Kato, *Acta Crystallogr. B-Stru.* **1976**, *32*, 764.
- [3] K. Kato, S. Tamura, *Acta Crystallogr. B-Stru.* **1975**, *31*, 673.
- [4] W. Mertin, S. Andersson, R. Gruehn, *J. Solid State Chem.* **1970**, *1*, 419.
- [5] G. Brauer, *Z. anorg. allg. Chem.* **1941**, *248*, 1.
- [6] G. C. Vezzoli, *Phys. Rev. B* **1982**, *26*, 3954.
- [7] O. Yamaguchi, D. Tomihisa, M. Shirai, K. Shimizu, *J. Am. Ceram. Soc.* **1988**, *71*, C-260.
- [8] R. Gruehn, *J. Less-Common Met.* **1966**, *11*, 119.
- [9] T. S. Ercit, *Mineral. Petrol.* **1991**, *43*, 217.
- [10] J. E. L. Waldron, M. A. Green, D. A. Neumann, *J. Phys. Chem. Solids* **2004**, *65*, 79.
- [11] J. B. Goodenough, A. Hamnett, G. Huber, O. Madelung, F. Hullinger, M. Leiß, S. K. Ramasesha, H. Werheit, *Physics of Non-Tetrahedrally Bonded Binary Compounds III / Physik Der Nicht-tetraedrisch Gebundenen Binären Verbindungen III*, Springer, **1984**.
- [12] A. G. S. Prado, L. Bolzon, C. P. Pedroso, A. O. Moura, L. L. Costa, *Appl. Catal. B-Environ.* **2008**, *82*, 219.
- [13] H.-Y. Lin, H.-C. Yang, W.-L. Wang, *Catal. Today* **2011**, *174*, 106.
- [14] Y. Zhao, X. Zhou, L. Ye, S. C. E. Tsang, *Nano Rev.* **2012**, *3*, 1.
- [15] H. Liu, N. Gao, M. Liao, X. Fang, *Scientific reports* **2015**, *5*, 7716.
- [16] F. Idrees, C. Cao, R. Ahmed, F. K. Butt, S. Butt, M. Tahir, M. Tanveer, I. Aslam, Z. Ali, *Sci. Adv. Mater.* **2015**, *7*, 1298.
- [17] H. Cui, G. Zhu, Y. Xie, W. Zhao, C. Yang, T. Lin, H. Gu, F. Huang, *J. Mater. Chem. A* **2015**, *3*, 11830.
- [18] P. Guo, M. A. Aegerter, *Thin Solid Films* **1999**, *351*, 290.
- [19] F. Lenzmann, J. Krueger, S. Burnside, K. Brooks, M. Grätzel, D. Gal, S. Rühle, D. Cahen, *J. Phys. Chem. B* **2001**, *105*, 6347.
- [20] M. Wei, Z.-m. Qi, M. Ichihara, H. Zhou, *Acta Mater.* **2008**, *56*, 2488.
- [21] R. Ghosh, M. K. Brennaman, T. Uher, M.-R. Ok, E. T. Samulski, L. E. McNeil, T. J. Meyer, R. Lopez, *ACS Appl. Mater. Interfaces* **2011**, *3*, 3929.
- [22] F. Izumi, H. Kodama, *Z. Anorg. Allg. Chem.* **1978**, *441*, 8.
- [23] H. Zhang, Y. Wang, D. Yang, Y. Li, H. Liu, P. Liu, B. J. Wood, H. Zhao, *Adv. Mater.* **2012**, *24*, 1598.
- [24] J. Wu, J. Wang, H. Li, D. Xue, *Thin Solid Films* **2013**, *544*, 545.
- [25] S. B. Betzler, A. Wisnet, B. Breitbach, C. Mitterbauer, J. Weickert, L. Schmidt-Mende, C. Scheu, *J. Mater. Chem. A* **2014**, *2*, 12005.
- [26] M. Hmadeh, V. Hoepfner, E. Larios, K. Liao, J. Jia, M. Jose-Yacamán, G. A. Ozin, *ChemSusChem* **2014**, *7*, 2104.
- [27] P. Hu, D. Hou, Y. Wen, B. Shan, C. Chen, Y. Huang, X. Hu, *Nanoscale* **2015**, *7*, 1963.

- [28] H. Zhang, Y. Wang, P. Liu, S. L. Chou, J. Z. Wang, H. Liu, G. Wang, H. Zhao, *ACS Nano* **2016**, *10*, 507.
- [29] P. Kofstad, *J. Phys. Chem. Solids* **1962**, *23*, 1571.
- [30] G. Dehm, J. M. Howe, J. Zweck, *In-situ Electron Microscopy: Applications in Physics, Chemistry and Materials Science*, John Wiley & Sons, Ltd, **2012**.
- [31] M. A. Asoro, D. Kovar, P. J. Ferreira, *ACS Nano* **2013**, *7*, 7844.
- [32] S. H. Oh, Y. Kauffmann, C. Scheu, W. D. Kaplan, M. Rühle, *Science* **2005**, *310*, 661.
- [33] S. H. Oh, M. F. Chisholm, Y. Kauffmann, W. D. Kaplan, W. Luo, M. Rühle, C. Scheu, *Science* **2010**, *330*, 489.
- [34] A. Agrawal, J. Cizeron, V. L. Colvin, *Microsc. Microanal.* **June 1998**, *4*, 269.
- [35] T. Yokota, M. Murayama, J. M. Howe, *Phys. Rev. Lett.* **2003**, *91*, 265504.
- [36] N. J. Long, A. K. Petford-Long, *Ultramicroscopy* **1986**, *20*, 151.
- [37] D. J. Smith, M. R. McCartney, L. A. Bursill, *Ultramicroscopy* **1987**, *23*, 299.
- [38] D. S. Su, M. Wieske, E. Beckmann, A. Blume, G. Mestl, R. Schlögl, *Catal. Lett.* **2001**, *75*, 81.
- [39] J. S. Anderson, J. M. Browne, A. K. Cheetham, R. V. Dreele, J. L. Hutchison, F. J. Lincoln, D. J. M. Bevan, J. Straehle, *Nature* **1973**, *243*, 81.
- [40] U. Balachandran, N. Eror, *J. Mater. Sci.* **1982**, *17*, 1286.
- [41] O. F. Schilling, *J. Phys. Chem. Solids* **1986**, *47*, 595.
- [42] J. S. Anderson, J. M. Browne, J. L. Hutchison, *J. Solid State Chem.* **1972**, *5*, 419.
- [43] A. K. Shukla, P. Ercius, A. R. S. Gautam, J. Cabana, U. Dahmen, *Cryst. Growth Des.* **2014**, *14*, 2453.
- [44] F. Campbell, *Elements of Metallurgy and Engineering Alloys*, ASM International, **2008**.
- [45] D. Hull, D. Bacon in *Introduction to Dislocations (Fourth Edition)*, Butterworth-Heinemann, **2001**.
- [46] J. Wu, C. Jia, K. Urban, J. Hao, X. Xi, *J. Mater. Res.* **2001**, *16*, 3443.
- [47] H. Jin Fan, M. Knez, R. Scholz, K. Nielsch, E. Pippel, D. Hesse, M. Zacharias, U. Gösele, *Nat. Mater.* **2006**, *5*, 627.
- [48] M. T. Buscaglia, V. Buscaglia, M. Viviani, G. Dondero, S. Röhrig, A. Rüdiger, P. Nanni, *Nanotechnology* **2008**, *19*, 225602.
- [49] U. Dahmen, M. G. Kim, A. W. Searcy, *Ultramicroscopy* **1987**, *23*, 365.
- [50] R. J. D. Tilley, *Principles and Applications of Chemical Defects*, Taylor & Francis, **1998**.
- [51] R. Egerton, *Electron Energy-Loss Spectroscopy in the Electron Microscope*, Springer, **2011**.
- [52] D. Bach, H. Störmer, R. Schneider, D. Gerthsen, J. Verbeeck, *Microsc. Microanal.* **2006**, *12*, 416.
- [53] D. Bach, R. Schneider, D. Gerthsen, J. Verbeeck, W. Sigle, *Microsc. Microanal.* **2009**, *15*, 505.
- [54] Z. Zhang, D. Su, *Ultramicroscopy* **2009**, *109*, 766.

8 Titanium Doping and its Effect on the Morphology of 3D Hierarchical $\text{Nb}_3\text{O}_7(\text{OH})$ Nanostructures for Enhanced Light-Induced Water Splitting

This chapter is based on the following publication: S.B. Betzler, F. Podjaski, M. Beetz, K. Bader, K. Hengge, A. Wisnet, M. Handloser, A. Hartschuh, B.V. Lotsch, and C. Scheu, *submitted*.

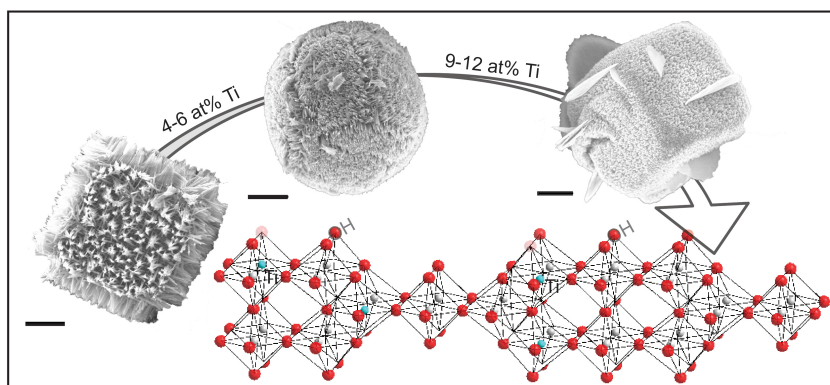


Figure 8.1 Table of content graphic (scale bar 1 μm).

8.1 Introduction

Hydrogen is a key fuel not only for the chemical industry but also as suitable energy source of the future. Photocatalytic water splitting is an environmentally friendly approach for hydrogen production that mimics natural photosynthesis using solar energy to convert water into hydrogen and oxygen gas. The endergonic reaction is catalyzed by a semiconductor: an absorbed photon excites an electron from the valence to the conduction band creating an electron-hole pair. If the potential of this electron-hole pair is sufficient, the electron reduces and the hole oxidizes water to hydrogen and oxygen, respectively.^[1] The photocatalytic activity of a material generally depends on several electronic and morphological factors. The size and energetic position of the band gap with respect to the standard hydrogen electrode determines whether the charge transport from the photocatalyst to water can take place (the theoretical minimum band gap for water splitting is 1.23 eV without overpotential).^[1] TiO_2 is one of the most intensively studied semiconductor in the field of photochemistry,^[2,3] both in the realm of

photocatalysis^[4-6] and solar cell devices.^[7-10] However, the achieved rates are far too low for commercial use,^[11] thus enforcing the research of alternative material systems.^[12,13] Niobium-based metal oxides attract increasing attention in the field of photocatalysis and also serve as possible candidates for water splitting applications.^[14-22] Similar to TiO_2 their crystal structures are built up from NbO_6 octahedra and their band gaps range from 3.1^[23] to 4.9 eV^[24] for different modifications. The capability for photocatalytic water splitting could already be shown for Nb_2O_5 ,^[15,20] $\text{Nb}_3\text{O}_7(\text{OH})$ ^[22] and several other niobates.^[11]

The actual water splitting redox reaction happens at the surface of the semiconductor and accordingly a high surface area is beneficial. The photo-generated electron-hole pair has to diffuse to the surface of the nanostructure, a process threatened by recombination, a major loss mechanism resulting in reduced efficiencies.^[25] A low number of defects in the crystal lattice and nanostructures with small dimensions reduce the probability of electron-hole recombination while large surface areas increase the number of active reaction sites.^[1] Thus, crystalline morphologies consisting of small nanostructures are expected to show the highest turnover rates. In the following we describe hierarchically ordered nanostructures as superstructures. As reported previously by our group, 3D hierarchical $\text{Nb}_3\text{O}_7(\text{OH})$ superstructures can be synthesized using a template-free one-step hydrothermal synthesis approach. The superstructures are composed of nanowire networks and benefit from a large surface area combined with a high crystallinity of the one-dimensional crystals.^[21] This study presents a facile strategy which allows us to rationally modify the morphology and water splitting capability of these $\text{Nb}_3\text{O}_7(\text{OH})$ superstructures via the addition of Ti(IV) to the reaction solution. The presence of Ti(IV) causes decreased nanowire sizes and altered morphologies. The dependence of the morphology and crystallographic properties of $\text{Nb}_3\text{O}_7(\text{OH})$ superstructures and their building blocks on the Ti(IV) concentration was investigated in detail using electron microscopy and X-ray diffraction experiments. The results are correlated with the material properties and hydrogen production rate which increases drastically with the Ti(IV) concentration.

8.2 Results and Discussion

8.2.1 Effect of the Incorporation of Titanium on the Morphology and Crystal Structure

Undoped $\text{Nb}_3\text{O}_7(\text{OH})$ superstructures which grow under hydrothermal conditions at 200 °C form the starting point of this study. The orthorhombic crystal structure of $\text{Nb}_3\text{O}_7(\text{OH})$ is composed of blocks of corner-sharing NbO_6 octahedra. The walls of the hollow, cubic superstructures consist of nanowire networks. Additional nanowires, which point like spikes from their surfaces, further enhance the surface area of the superstructures (fig. 8.2a).^[21] This morphology is named morphology A in the following. EDX spectroscopy shows a linear dependence between the Ti amount incorporated into the superstructures, given relative to Nb, and the Ti(IV) concentration in the reac-

tion solution (see appendix fig. C.1 and C.2). The addition of small Ti(IV) concentrations between 0.03 and 0.06 molL^{-1} cause the formation of a spherical morphology with an average amount of $5.5 \pm 0.7 \text{ at}\%$ titanium incorporated into the crystal lattice of $\text{Nb}_3\text{O}_7(\text{OH})$ (morphology B). This morphology is likewise hollow and built up from nanowires (fig. 8.2b and appendix fig. C.3). SEM images reveal sutures on its surface which might be remainings of former cube edges and propose that the spheres are rounded cubes (see appendix fig. C.4). X-ray diffraction pattern of these samples match the diffraction pattern detected for undoped, phase-pure $\text{Nb}_3\text{O}_7(\text{OH})$ superstructures. With increasing titanium concentration in the reaction solution (0.09 - 0.11 molL^{-1}) a cubic morphology forms (morphology C). In contrast to the cubes found in the absence of Ti(IV) these cubes consist of noticeably smaller nanowires, which arrange to form the walls of hollow cubes (fig. 8.2c). For this sample, the XRD pattern reveal a phase mixture and reflections of the anatase TiO_2 phase are visible in addition to the ones of $\text{Nb}_3\text{O}_7(\text{OH})$. They can be attributed to the formation of large TiO_2 plates on the surface of some of the cubes, as visible in SEM micrographs. EDX measurements in the SEM yield a Ti content of $10.8 \pm 1.5 \text{ at}\%$ for morphology C which is not overgrown by large plates and a significantly higher Ti content of $31 \pm 5 \text{ at}\%$ for morphology C overgrown by TiO_2 plates. Thus two effects are observed: First, the incorporation of titanium yields smaller wire dimensions with the amount of titanium which can be incorporated into the $\text{Nb}_3\text{O}_7(\text{OH})$ crystal lattice being limited. Second, titanium excess leads to the formation of an additional TiO_2 phase.

The XRD pattern show a shifting of the reflections depending on the titanium amount incorporated into the crystal lattice. With increasing Ti concentration in the crystal lattice the different diffraction orders of the (100) planes shift to larger angles, signifying a decreased d -spacing. In contrast, the (001) reflection shifts to smaller angles, related to an expansion of the c -lattice parameter (see appendix fig. C.5). The expansion of the crystal lattice indicates the incorporation of point defects.^[27] The replacement of Nb^{5+} by Ti^{4+} necessitates the removal of anions from the crystal lattice for charge balance. For $\text{Nb}_3\text{O}_7(\text{OH})$ charge balance is most likely obtained by removing hydroxyl groups from the crystal lattice yielding $\text{Nb}_{3-x}\text{Ti}_x\text{O}_7(\text{OH})_{1-x}$. XRD analysis shows a reduced lattice parameter in a -direction for increasing titanium concentration. As the crystal ionic radius of sixfold coordinated Ti(IV) is reported to be 3.5 pm smaller than the radius of sixfold coordinated Nb(V),^[28] the contraction of the crystal lattice in a -direction might result from the replacement of Nb(V) by Ti(IV). This and the distribution of titanium in the crystal lattice of $\text{Nb}_3\text{O}_7(\text{OH})$ is investigated in more detail by transmission electron microscopy and will be discussed below.

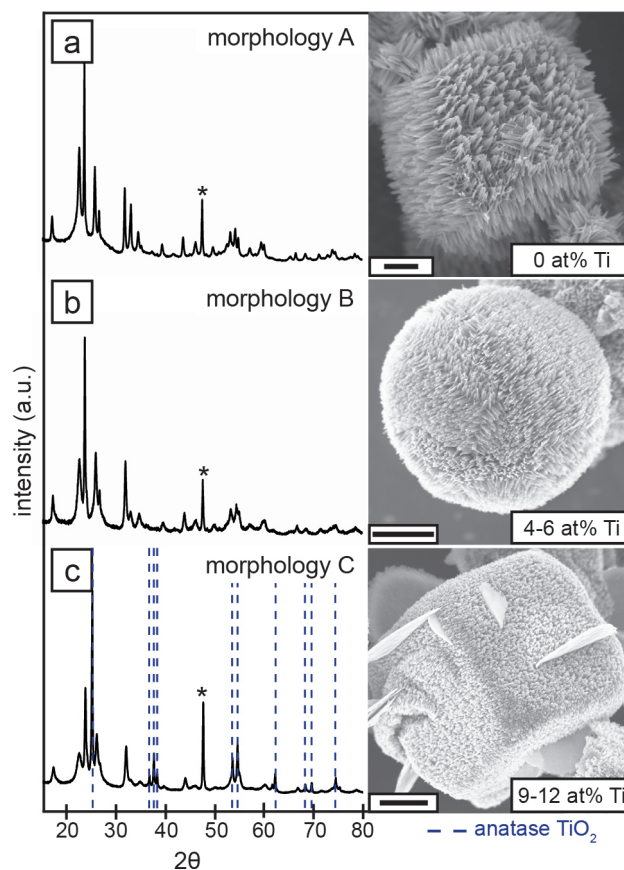


Figure 8.2 Morphology and crystal structure of $\text{Nb}_3\text{O}_7(\text{OH})$ superstructures which form for different Ti(IV) concentrations in the reaction solution. On the right side SEM images of morphology A, B and C are displayed (scale bar 1 μm) with the titanium content averaged over the morphology indicated relative to niobium. The left side shows X-ray diffraction patterns of the respective samples (a-c). The dashed lines belong to reflections of the anatase TiO_2 crystal phase (ICSD, Card No. 44882) all others to $\text{Nb}_3\text{O}_7(\text{OH})$ (isomorphous to $\text{Nb}_3\text{O}_7\text{F}^{[26]}$ (JCPDS, Card No. 74-2363)). A reflection caused by the instrumental setup is marked by an asterisk. The d-values are listed in appendix tab. C.1.

8.2.2 In-Depth TEM Characterization of the Nanowire Networks

TEM investigations are performed for a deeper understanding of the correlation between crystal size and titanium incorporation. As reported previously morphology A consists of highly ordered nanowire networks (fig. 8.2a), which reflects in both BF images and electron diffraction pattern of networks (fig. 8.3b).^[21] The nanowires forming the networks grow in $[010]$ direction and possess larger (001) and slightly smaller (100) crystal facets (true to scale schemes in fig. 8.3d and appendix fig. C.6 and tab. C.2). The indexing of the electron pattern recorded for the nanowire networks proves that they are a superposition of orthogonally aligned nanowires which possess the $[100]$ zone axis.^[21] In addition to the main reflections low intensity reflections appear in the diffraction pattern which originate from detached nanowires.

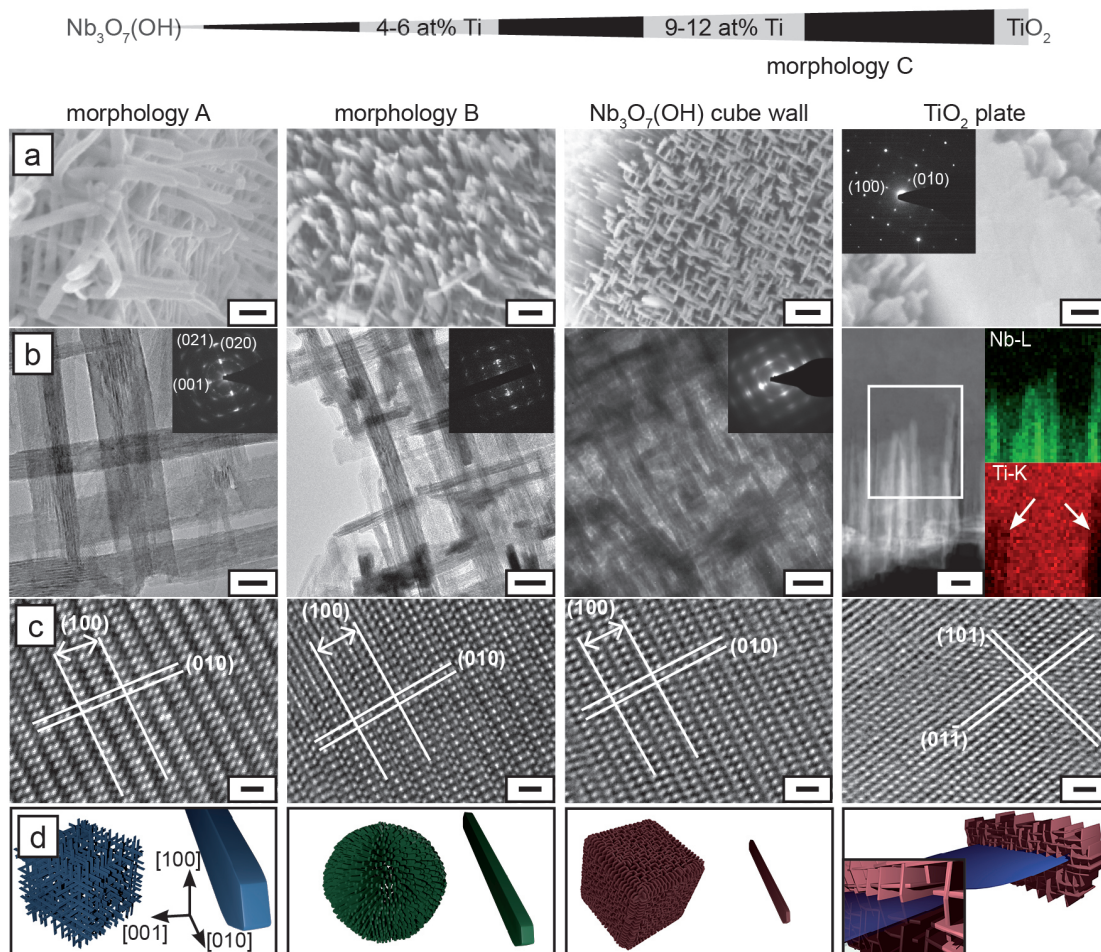


Figure 8.3 Electron microscopy analysis of the superstructures achieved for different Ti(IV) concentrations in the reaction solution. The amount of titanium incorporated into the crystal lattice increases from left to right. SEM images of the different morphologies and the TiO_2 plates are displayed in (a) (scale bars 100 nm). b) TEM images of fragments of the nanowire networks building up the walls of the different morphologies (scale bars 20 nm). The inset shows the diffraction pattern of the respective network observed in $[100]$ direction (scale bar 20 nm). For the TiO_2 plate a scanning TEM image of the conduit region between cube wall and plate is given together with EDX maps (Ti-K and Nb-L line) of the highlighted region (scale bar 20 nm). c) HRTEM images of a nanowire of each morphology (in $[001]$ direction) and the TiO_2 plate (in $[\bar{1}11]$ direction) (scale bars 1 nm). d) Schematic drawings which illustrate the shape of the building blocks true to scale (see appendix. C.2). For the TiO_2 plate the connection between TiO_2 plate and $\text{Nb}_3\text{O}_7(\text{OH})$ cube wall is displayed.

From BF images it is obvious that the walls of morphology B consist of the same nanowire arrangement (fig. 8.3a). However, the nanowires are smaller, shorter and have an altered aspect ratio of the (001) to (100) crystal facets than pristine $\text{Nb}_3\text{O}_7(\text{OH})$ nanowires (see schematic in fig. 8.3d). This trend continues so that the nanowires observed for morphology C are noticeably smaller, shorter and flatter. This causes a rather compact appearance of the cube wall in BF images and broadened reflections in the corresponding electron diffraction pattern of the cube wall. In addition the broadening of the reflections also indicates a slight rotation of the building blocks relative to each other. Still, the overall nanowire arrangement is preserved and the d -spacing of the reflections matches $\text{Nb}_3\text{O}_7(\text{OH})$. Local EDX spectra recorded at the nanowire network of morphology C

yield a titanium concentration of 11.1 at% titanium which is in the range of the titanium amount observed for TiO₂-free cubes of morphology C in the SEM. SEM images reveal large plates on the surface of morphology C (fig. 8.2c and 8.3a). Electron diffraction experiments prove that these plates are single crystalline anatase TiO₂ observed in [001] direction (fig. 8.3c), which matches the results of the XRD analysis (fig. 8.2c). EDX measurements reveal a homogeneous distribution of 23 ± 1 at% niobium within these plates. Figure 8.3a shows a SEM image of the conduit region between cube wall and TiO₂ plate demonstrating that the TiO₂ plate is connected to the Nb₃O₇(OH) nanowires of the cube wall. The combination of scanning TEM and EDX investigations indicate a disruption of the TiO₂ plate by integrated Nb₃O₇(OH) nanowires causing a decreased Ti concentration in these regions, visible in EDX maps of the Ti-K line (marked with white arrows in fig. 8.3b). Nanowires lying on top or below the TiO₂ plate, which are visible in the Nb-EDX map, on the contrary do not cause a strongly modified contrast in the Ti-EDX maps. In this regard, morphology C can actually be regarded as a composition of two morphologies: The Nb₃O₇(OH) cubes form the basis which is partly overgrown by anatase TiO₂ plates.

It is important to find out if titanium is distributed homogeneously in the Nb₃O₇(OH) lattice or enriched in certain areas. Hydrothermally grown Nb₃O₇(OH) nanowires are characterized by planar defects parallel to the {001} lattice planes. These defects have a homogeneous width, which apparently does not change due to the incorporation of titanium into the crystal lattice (see appendix fig. C.7). Figure 8.3c shows HRTEM images detected in [001] direction which do not indicate significant changes of the Nb₃O₇(OH) crystal lattice due to the presence of titanium (fig. 8.3c). These results are confirmed by EDX maps which indicate a homogeneous distribution of titanium throughout the nanowires and no areas of higher Ti concentration are observed including nanowire junctions (see appendix fig. C.8). Together with the XRD analysis these results prove the homogeneous distribution of titanium in the crystal lattice of Nb₃O₇(OH) while an accumulation of titanium at grain boundaries or defects cannot be observed within the detection limit of our measurements. The incorporation of titanium as dopant in the crystal lattice of Nb₃O₇(OH) results in altered crystal sizes and shapes which lead to different morphologies at the microscale. In addition, the findings suggest that the crystal lattice of Nb₃O₇(OH) is not capable of accommodating more than about 12 at% Ti so that the formation of niobium doped anatase TiO₂ is favored for further titanium excess. HRTEM images detected at the conduit region of Nb₃O₇(OH) nanoplate and TiO₂ plate show that this happens via oriented crystal growth (see appendix fig. C.9).

8.2.3 Electron Energy-loss Spectroscopy Study of Titanium Doped Samples

For a better understanding of the local surrounding of doped titanium atoms in the $\text{Nb}_3\text{O}_7(\text{OH})$ lattice electron energy-loss spectroscopy was performed. The energy-loss near edge fine structure of the Ti-L_{2,3}, Nb-M_{2,3} and O-K edge is analyzed for morphology A, morphology B and for both the cube wall and TiO₂ plate of morphology C (fig. 8.4 and appendix tab. C.3). The features in the low loss regime are dominated by plasmon excitations and have a similar shape for all samples. Only intensity ratio of peak *b* and *b'* varies and the decreased intensity of feature *b* observed for morphology A could either result from the absence of titanium in the crystal lattice or be caused by different sample thicknesses.

The Nb-M_{2,3} and Ti-L_{2,3} edges result from the excitation of Nb-3p and Ti-2p electrons to unoccupied Nb-4d or Ti-3d states. The shape of these two edges is characterized by two white lines which reflect the spin-orbital splitting of the 3p orbitals of niobium and 2p orbitals of titanium. The splitting of the Nb-M_{2,3} white lines (peak *a* and *b*) is identical for all investigated samples. Additional high-energy shoulders (*a'* and *b'*) appear for both the Nb-M₃ and Nb-M₂ edge of all samples, indicating the presence of pentavalent niobium [29]. The Ti-L₃ and Ti-L₂ white line (peak *a* and *b*) are further split up to form doublets (additional peak *a'* and *b'*) for morphology B and both the cube wall and the TiO₂ plate of morphology C. This splitting is due to unoccupied t_{2g} levels which hints at the presence of Ti(IV) in the $\text{Nb}_3\text{O}_7(\text{OH})$ crystal lattice.^[30,31] This assumption is strengthened by the measured peak splitting of peak *a* and *b*, which is 5.2 ± 0.1 eV for the three samples. This value fits the literature value of both rutile and anatase TiO₂ (5.4 eV^[30]). The ELNES of the Ti-L_{2,3} edge detected for the TiO₂ plate of morphology C shows an additional high-energy shoulder for peak *a'* (see appendix fig. C.10). This feature is characteristic for anatase TiO₂ and originates from the distortion of the TiO₆ octahedra in the crystal lattice.^[31] The ELNES of the O-K edge of morphology A is dominated by three distinct peaks (*a*, *b*, *c*) with intensities and energy splitting matching to the ones reported for Nb₂O₅.^[29] Neither the intensity nor the splitting of the peaks is strongly affected by the incorporation of titanium into the crystal lattice. However, significant differences are observed for the ELNES of the TiO₂ plate of morphology C which shows a drastically decreased splitting of peak *a* and *b* and the appearance of an additional peak *c'*. The shape and peak splitting of this O-K ELNES matches anatase TiO₂.^[30,31]

The ELNES of the Ti-L_{2,3}, Nb-M_{2,3} and O-K edge do not show significant changes due to the incorporation of titanium into the crystal lattice of $\text{Nb}_3\text{O}_7(\text{OH})$. The unit cell of $\text{Nb}_3\text{O}_7(\text{OH})$ is composed of NbO₆ octahedra. The shape of the Ti-L_{2,3} edge resembles the ELNES of anatase and rutile TiO₂,^[30] both crystal structures consist of TiO₆ octahedra. The ELNES of the Ti-L_{2,3} edge, together with the fact that neither the shape of the O-K nor the Nb-M_{2,3} edge is affected by the incorporated titanium, indicate the replacement of niobium by titanium at its octahedral lattice sites. In the case of the TiO₂ plate both the ELNES of the O-K and the Ti-L_{2,3} edge confirm the results of the diffraction experiments. The TiO₂ plate incorporates niobium and the shape of the Nb-M_{2,3} edge

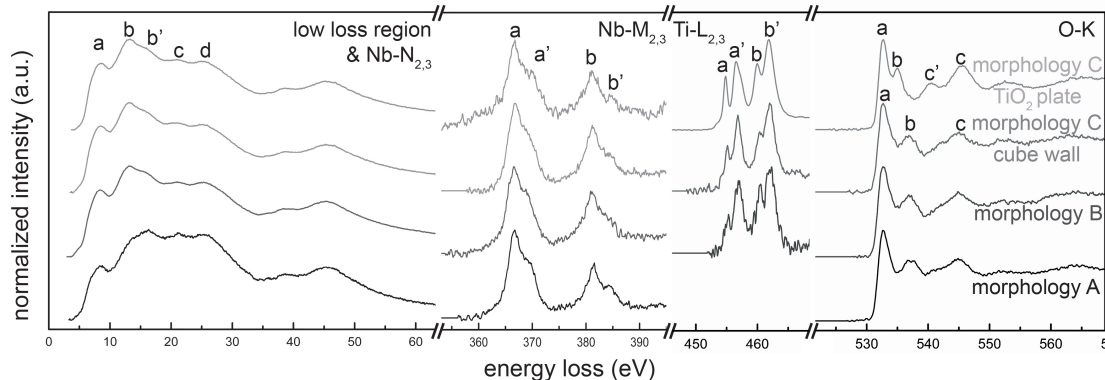


Figure 8.4 EEL spectra detected for morphology A, B and the wall of the cubes and TiO₂ plate of morphology C. The low loss region and the ELNES of the Nb-N_{2,3}, Nb-M_{2,3}, Ti-L_{2,3} and O-K edges are displayed, with significant features marked with letters *a-d* referred to in the text.

indicates the presence of octahedrally coordinated pentavalent niobium suggesting the replacement of titanium by niobium.

8.2.4 Photocatalytic Activity of the Different Morphologies

As expected from the SEM images, BET measurements confirm the high surface area of the different morphologies, yielding $79 \text{ m}^2 \text{ g}^{-1}$ for morphology A, $132 \text{ m}^2 \text{ g}^{-1}$ for morphology B and $173 \text{ m}^2 \text{ g}^{-1}$ for morphology C. Morphology A and B show similar extinction spectra with a strong absorbance below 390 nm , which fits the band gap of 3.2 eV reported for Nb₃O₇(OH).^[21,23] For morphology C the same band gap was measured but an additional slightly enhanced absorbance in the red spectral region ($550\text{--}850 \text{ nm}$) is observed. This is most likely related to the presence of oxygen vacancies in the TiO₂ plates (see appendix fig. C.11). Several studies show the photocatalytic activity of pristine Nb₃O₇(OH).^[21,23,32] However, a recent study proposes that proton reduction is kinetically hindered on the surface of Nb₃O₇(OH) as in most oxides.^[22] In the present work the hydrogen production rate is measured on Pt-decorated 3D hierarchical Nb₃O₇(OH) superstructures. The Pt decoration is achieved by chloroplatinic acid treatment and TEM investigations show homogeneous particle distribution for the different samples. Statistical analysis reveals an average particle diameter of 3.6 nm for morphology A, a diameter of 2.5 nm for morphology B, and 3.3 nm for morphology C, but the overall particle density appears similar (see appendix fig. C.12). Hence, the size variation between the different samples is small and therefore its effect on the water splitting capability is neglected. To account for the size of the band gap and to allow efficient charge-carrier generation, a 600 mWcm^{-2} Xenon lamp, which emits 2.7 to $1.1 \mu\text{Wcm}^{-2}\text{nm}^{-1}$ in the spectral region of 280 to 390 nm (see appendix fig. C.13), is used to measure the hydrogen evolution rate of the different morphologies. Undoped Nb₃O₇(OH) yields a rate of $870 \mu\text{molg}^{-1}\text{h}^{-1}$, which is similar to the rate reported for Pt-decorated Nb₃O₇(OH) nanowires that do not form a 3D arrangement.^[22] This rate increases with increasing Ti-concentration featuring a rate of $1773 \mu\text{molg}^{-1}\text{h}^{-1}$ for morphology B and $1988 \mu\text{molg}^{-1}\text{h}^{-1}$ for morphology C (tab. 8.1).

Table 8.1 H₂ production rate, surface area and PL lifetime for different Nb₃O₇(OH) superstructures which comprise different titanium amounts.

	Ti amount (at%)	Surface area from BET (m ² g ⁻¹)	PL lifetime measured via TCSPC (ps)	H ₂ production Xenon 600 mWcm ⁻² (μmolg ⁻¹ h ⁻¹)
morphology A	0	79	54 ± 2	870
morphology B	5.5 ± 0.7	132	64 ± 2	1773
morphology C	31.2 ± 5.0	173	73 ± 4	1988

To gain further insight into the effect of Ti doping on the photocatalytic properties of the material, we investigated the PL lifetime of the electronic states populated upon optical excitation for the different morphologies (in the absence of platinum) using time-correlated single photon counting (TCSPC) (fig. 8.5a). Two-photon excitation at 730 nm (1.7 eV) was provided by a Ti:Sa oscillator at a repetition rate of 76 MHz and the optical response of the samples was detected for wavelengths shorter than 600 nm. Ultrashort excitation pulses of 150 fs in combination with a fast photodetector and timing electronics (see appendix fig. C.14) lead to a temporal resolution of about 3 ps.^[33] This technique allows to detect changes in the excited state relaxation and helps to distinguish radiative and non-radiative rate modifications. TCSPC transients were recorded at five individual sample spots for each morphology (see appendix fig. C.14) and the extracted PL lifetimes are averaged to minimize the influence of material heterogeneities (fig. 8.5b). All samples showed biexponential decay with time constants of around 10-6 ps and 150-200 ps for the short and long decay time, respectively. For morphology A an intensity averaged lifetime of 54 ± 2 ps is observed. Morphology B feature a somewhat longer lifetime of 64 ± 2 ps. For morphology C, an intensity averaged lifetime of 73 ± 4 ps is recorded. From figure 8.5 it thus becomes evident that for increasing Ti amounts incorporated into the superstructures the excited state lifetime becomes longer. The enhanced PL lifetime for increasing Ti amounts can be attributed to a reduction of non-radiative losses and with that to a lower density of quenching sites existing near the crystal surfaces. The replacement of Nb⁵⁺ by Ti⁴⁺ decreases the amount of hydroxyl groups required for charge neutrality featuring a lower hydroxyl concentration in the crystal lattice of doped samples: (Nb_{3-x}Ti_xO₇(OH)_{1-x}). Hydroxyl groups are known for acting as non-radiative recombination sites.^[34,35] The decreasing amount of recombination sites in combination with the increased surface area of morphology B and C reflect in the H₂ production rate. The rate doubles for morphology B compared to morphology A using the full spectrum illumination of a Xenon lamp. A further increase, but less pronounced, is seen for morphology C which indicates that the presence of TiO₂ plates observed for this morphology does not have a strong effect on the photocatalytic reaction. This is supported by the findings of the TEM investigations which exclude the presence of TiO₂ for morphology B.

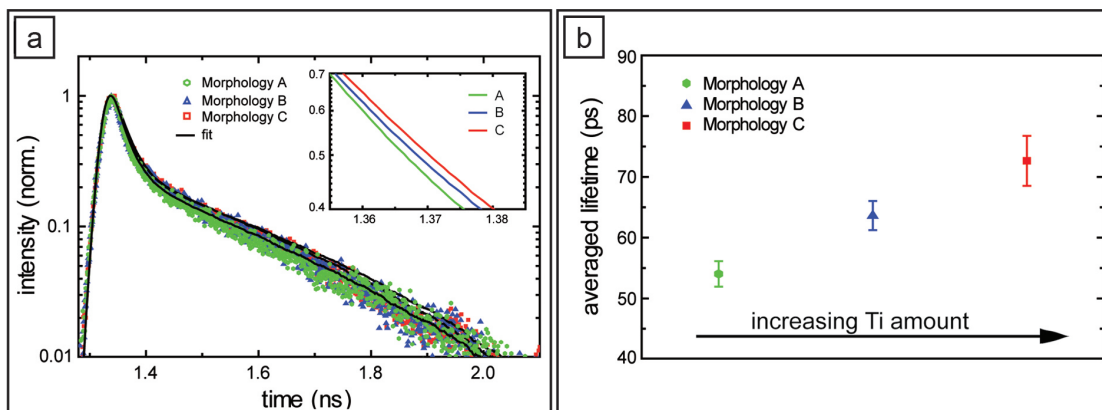


Figure 8.5 a) Semi-log plot of TCSPC transients detected for the three different morphologies after pulsed two-photon excitation at 1.7 eV. The inset, a zoom-in of the biexponential fits of the PL decay dynamics, shows longer PL decay times for increasing Ti amount incorporated in the superstructures. b) Intensity averaged lifetimes for the three different morphologies (for further details see appendix fig. C.14). An increase of the intensity averaged lifetime can be observed with increasing Ti amount in the material.

8.3 Conclusion

This study investigates the effect of titanium doping on the morphology and properties of 3D hierarchical $\text{Nb}_3\text{O}_7(\text{OH})$ superstructures and their performance as photocatalyst material. The integration of titanium at the octahedral lattice sites of $\text{Nb}_3\text{O}_7(\text{OH})$ affects its crystallization leading to reduced growth rates whereas the growth in *a*- and *b*-direction is affected more strongly than the one in *c*-direction. It seems that the modified shapes of the nanowires or altered surface charges influence the interparticular forces which drive the organized self-assembly of the superstructures, as the findings of this study yield no evidence for an involvement of TiO_2 -islands at nanowire junctions. In the absence of titanium hollow cubes which consist of highly-ordered nanowire networks form. For a doping degree of 5.5 ± 0.7 at% Ti the formation of hollow spheres constituted by smaller nanowires is observed, while 10.8 ± 1.5 at% Ti lead to cubic superstructures built up from small nanoplates. The amount of titanium which can be incorporated into the crystal lattice is limited to around 12 at%, with further titanium excess resulting in the formation of niobium doped anatase TiO_2 plates. These TiO_2 plates grow on the surface of $\text{Nb}_3\text{O}_7(\text{OH})$ nanowires, which integrate into the anatase TiO_2 plate, via oriented crystal growth.

Morphologies formed in the presence of titanium show higher photocatalytic H_2 evolution rates than pristine $\text{Nb}_3\text{O}_7(\text{OH})$ superstructures. PL lifetime measurements indicate a lower density of quenching sites at the surface of the crystals in the presence of titanium. This is attributed to a reduced density of hydroxyl groups required to achieve charge neutrality. The substitution of Nb^{5+} by Ti^{4+} means that fewer hydroxyl groups are needed for charge balance ($\text{Nb}_{3-x}\text{Ti}_x\text{O}_7(\text{OH})_{1-x}$) which reflects in enhanced PL lifetimes observed for morphology B and C. For morphology B no TiO_2 crystal phase was discovered so that the doubled H_2 evolution rate observed for this morphology ($1773 \mu\text{molh}^{-1}\text{g}^{-1}$) compared to pristine $\text{Nb}_3\text{O}_7(\text{OH})$ superstructures ($870 \mu\text{molh}^{-1}\text{g}^{-1}$)

can be attributed to a combination of a reduced density of quenching sites near the surface and the increased surface area of morphology B. Morphology C is overgrown by TiO_2 plates which form due to excess Ti(IV) in the reaction solution. However, the H_2 evolution rate observed for this morphology is only slightly higher than the one of morphology B indicating that the presence of TiO_2 does not significantly enhance the photocatalytic activity.

Still, active band gap engineering is required to extend the optical absorption of $\text{Nb}_3\text{O}_7(\text{OH})$ more towards the visible regime which would yield higher efficiencies.

8.4 Experimental

The synthesis of doped $\text{Nb}_3\text{O}_7(\text{OH})$ superstructures is based on the procedure used to obtain $\text{Nb}_3\text{O}_7(\text{OH})$ superstructures.^[21] Titanium butoxide was added under vigorous stirring to a mixture of NbCl_4 , water and HCl prior to hydrothermal treatment at 200°C (detailed description of the synthesis procedure section 2.4.2). A *Zeiss Gemini Ultra Field Emission* SEM equipped with an In-lens detector was operated at 4 keV to investigate the morphology of the superstructures. To reduce charging effects during the measurements the samples were sputtered with carbon using a *BAL-TEC MED020* coating system. The doping degree was determined from EDX measurements performed in the SEM using a *Jeol JSM-6500F* SEM equipped with an *Oxford Instruments Inca Energy* EDX detector. An acceleration voltage of 15 keV and an acquisition time of 60–120 s was used to record the spectra. XRD analysis were carried out in transmission mode on a *STOE* powder diffractometer equipped with a *Dectris Mythen K1* detector, *Seifert ID3003* generator and *Seifert Long Fine Focus Dx-Cu12x0.4-S* X-ray tube. TEM investigation were performed on cube fragments achieved by sonicating a mixture of powder sample and ethanol for 5–15 minutes. The suspension was drop casted onto a copper grid with holey carbon support. A *Jeol JEM-2011* and a *FEI Tecnai G2 20 S-TWIN* microscope both operated at 200 keV were used for bright field imaging and electron diffraction experiments. A *Philips CM300FEG/UT* with a field-emission source and an ultra-twin objective lens was applied for HRTEM analysis. EDX analysis in the TEM were performed at 300 keV in STEM mode using a *FEI Titan 80–300* equipped with a *EDAX* ultra thin window Si(Li) EDX detector and a *FEI TitanX 60–300* equipped with a *Bruker* windowless EDX detector with a solid angle of 0.7 steradians. A *Zeiss Libra 200MC* microscope which was operated at 200 keV and equipped with an in-column omega filter was used for monochromated EEL spectra investigations. All spectra were recorded in TEM mode using identical settings with a dispersion of 0.07 eV/channel and an energy resolution of 0.3–0.4 eV.

UV/Vis spectra were recorded in transmission mode with a *Perkin Elmer Lambda 1050* UV/Vis/NIR spectrometer for a spectral region of 250 to 1200 nm (step size 1 nm). The hydrogen production by the superstructures was measured under full spectrum illumination at 600 mWcm^{-2} achieved with a *Newport 300 W* Xenon lamp. For the measurement 10 mg of the powder sample, 9 mL water, 1 mL methanol and 2.5 μL chloroplatinic acid (8 wt%) were added together with a stirring beat in a glass reactor. The filled reac-

tor was evacuated and flushed with Argon five times prior to every measurement series in order to degas the solution. The sample illumination was carried out in top geometry through a Quartz window while the solution was kept at 25 °C and stirred. The amount of hydrogen produced was measured with a *Thermo Fischer Trace GC Ultra*.

8.5 References

- [1] A. Kudo, Y. Miseki, *Chem. Soc. Rev.* **2009**, *38*, 253.
- [2] X. Chen, S. S. Mao, *Chem. Rev.* **2007**, *107*, 2891.
- [3] Z. Weng, H. Guo, X. Liu, S. Wu, K. W. K. Yeung, P. K. Chu, *RSC Adv.* **2013**, *3*, 24758.
- [4] A. Fujishima, K. Honda, *Nature* **1972**, *238*, 37.
- [5] M. Ni, M. K. H. Leung, D. Y. C. Leung, K. Sumathy, *Renew. Sust. Energ. Rev.* **2007**, *11*, 401.
- [6] M. Wang, J. Ioccozia, L. Sun, C. Lin, Z. Lin, *Energ. Environ. Sci.* **2014**, *7*, 2182.
- [7] B. O'Regan, M. Grätzel, *Nature* **1991**, *353*, 737.
- [8] H. J. Snaith, L. Schmidt-Mende, *Adv. Mater.* **2007**, *19*, 3187.
- [9] A. Hagfeldt, G. Boschloo, L. Sun, L. Kloo, H. Pettersson, *Chem. Rev.* **2010**, *110*, 6595.
- [10] F. Sauvage, F. Di Fonzo, A. Li Bassi, C. S. Casari, V. Russo, G. Divitini, C. Ducati, C. E. Bottani, P. Comte, M. Grätzel, *Nano Lett.* **2010**, *10*, 2562.
- [11] F. E. Osterloh, *Chem. Mater.* **2008**, *20*, 35.
- [12] M. D. Hernández-Alonso, F. Fresno, S. Suárez, J. M. Coronado, *Energy Environ. Sci.* **2009**, *2*, 1231.
- [13] L. Yang, H. Zhou, T. Fan, D. Zhang, *Phys. Chem. Chem. Phys.* **2014**, *16*, 6810.
- [14] R. Jose, V. Thavasi, S. Ramakrishna, *J. Am. Ceram. Soc.* **2009**, *92*, 289.
- [15] H.-Y. Lin, H.-C. Yang, W.-L. Wang, *Catal. Today* **2011**, *174*, 106.
- [16] B. Gao, J. Fu, K. Huo, W. Zhang, Y. Xie, P. K. Chu, *J. Am. Ceram. Soc.* **2011**, *94*, 2330.
- [17] H. Zhang, Y. Wang, D. Yang, Y. Li, H. Liu, P. Liu, B. J. Wood, H. Zhao, *Adv. Mater.* **2012**, *24*, 1598.
- [18] Y. Zhao, X. Zhou, L. Ye, S. C. E. Tsang, *Nano Rev.* **2012**, *3*, 1.
- [19] L. Li, J. Deng, R. Yu, J. Chen, Z. Wang, X. Xing, *J. Mater. Chem. A* **2013**, *1*, 11894.
- [20] H. Luo, W. Song, P. G. Hoertz, K. Hanson, R. Ghosh, S. Rangan, M. K. Brennaman, J. J. Concepcion, R. A. Binstead, R. A. Bartynski, R. Lopez, T. J. Meyer, *Chem. Mater.* **2013**, *25*, 122.
- [21] S. B. Betzler, A. Wisnet, B. Breitbach, C. Mitterbauer, J. Weickert, L. Schmidt-Mende, C. Scheu, *J. Mater. Chem. A* **2014**, *2*, 12005.
- [22] M. Hmadeh, V. Hoepfner, E. Larios, K. Liao, J. Jia, M. Jose-Yacamán, G. A. Ozin, *ChemSusChem* **2014**, *7*, 2104.
- [23] J. Wu, J. Wang, H. Li, D. Xue, *Thin Solid Films* **2013**, *544*, 545.
- [24] G. Agarwal, G. B. Reddy, *J. Mater. Sci.: Mater. in Electronics* **2005**, *16*, 21.

-
- [25] A. Wisnet, K. Bader, S. B. Betzler, M. Handloser, P. Ehrenreich, T. Pfadler, J. Weickert, A. Hartschuh, L. Schmidt-Mende, C. Scheu, J. A. Dorman, *Adv. Funct. Mater.* **2015**, *25*, 2601.
- [26] F. Izumi, H. Kodama, *Z. Anorg. Allg. Chem.* **1978**, *441*, 8.
- [27] F. Zhang, S.-W. Chan, J. E. Spanier, E. Apak, Q. Jin, R. D. Robinson, I. P. Herman, *Appl. Phys. Lett.* **2002**, *80*, 127.
- [28] R. D. Shannon, *Acta Crystallogr. A* **1976**, *32*, 751.
- [29] D. Bach, R. Schneider, D. Gerthsen, J. Verbeeck, W. Sigle, *Microsc. Microanal.* **2009**, *15*, 505.
- [30] R. Brydson, H. Sauer, W. Engel, J. M. Thomas, E. Zeitler, N. Kosugi, H. Kuroda, *J. Phys.: Condens. Matter.* **1989**, *1*, 797.
- [31] E. Stoyanov, F. Langenhorst, G. Steinle-Neumann, *Am. Mineral.* **2007**, *92*, 577.
- [32] P. Hu, D. Hou, Y. Wen, B. Shan, C. Chen, Y. Huang, X. Hu, *Nanoscale* **2015**, *7*, 1963.
- [33] T. Gokus, A. Hartschuh, H. Harutyunyan, M. Allegrini, F. Hennrich, M. Kappes, A. A. Green, M. C. Hersam, P. T. Araújo, A. Jorio, *Appl. Phys. Lett.* **2008**, *92*, 153116.
- [34] H. Zhou, H. Alves, D. M. Hofmann, W. Kriegseis, B. K. Meyer, G. Kaczmarczyk, A. Hoffmann, *Appl. Phys. Lett.* **2002**, *80*, 210.
- [35] G. Xiong, U. Pal, J. G. Serrano, *J. Appl. Phys.* **2007**, *101*, 024317.

9 Summary and Conclusion

In this study a hydrothermal synthesis procedure was developed to fabricate novel 3D hierarchical $\text{Nb}_3\text{O}_7(\text{OH})$ superstructures with appealing properties for photocatalysis and as electrode material. The superstructures are achieved from a template-free one-step hydrothermal synthesis strategy. This synthesis approach is sensitive towards minor changes of the pH conditions, synthesis temperature and time resulting in different morphologies. Amongst these hollow 3D hierarchical $\text{Nb}_3\text{O}_7(\text{OH})$ superstructures stand out. The walls of this cubic morphology are composed of highly ordered nanowire networks featuring large surface areas (up to $77\text{ m}^2\text{g}^{-1}$) combined with high crystallinity as observed by XRD and electron diffraction. Despite their complexity these superstructures form self-organized starting from amorphous hollow cubes discovered in the reaction solution prior to the hydrothermal treatment. Hydrothermal conditions provoke the formation of tiny nanoparticles on the surface of these cubes. These particles most likely serve as seed-crystals for the subsequent nanowire growth yielding highly ordered nanowire networks. EELS investigations show that the $\text{Nb}_3\text{O}_7(\text{OH})$ crystal lattice contains pentavalent niobium which is coordinated octahedrally by oxygen. However, HRTEM analysis reveals a highly periodic defect structure in the crystal lattice, which is composed of planar defects parallel to $\{001\}$ planes. These defects feature a shift of $1/2d[010]$ of neighboring crystal domains. The tendency of niobium oxide crystal phases to compensate non-stoichiometry via crystallographic shear planes indicates that these defects form to compensate small oxygen deficiency. The 3D arrangement of the nanowires in the network was elucidated by local thickness measurements performed by STEM-EELS. The knowledge was further expanded by 3D tomography which led to the distinction of two junction types: T-shaped junctions and crossings. No thickness variation was discovered for T-shaped junctions which most likely result from a nanowire collision or as starting point for the growth of one nanowire. An enhanced thickness was found at the overlap region of nanowire crossings indicating partial intergrowth of the nanowires. It seems that nanowire crossings conduct the perpendicularity of the nanowire arrangement enabled by the orthorhombic crystal lattice. The surface area of these superstructures is increased by additional nanowires oriented orthogonal to the nanowire networks. These nanowires most likely attach to the nanowire network via $\{001\}$ crystal faces.

$\text{Nb}_3\text{O}_7(\text{OH})$ can be phase-transformed to monoclinic $\text{H-Nb}_2\text{O}_5$ starting at 500°C . Despite the phase transformation the superstructure morphology remains exceptionally stable for temperatures up to 850°C . Still, a merging of the nanowires via LAGBs was observed for this temperature by HRTEM analysis. At temperatures of 1200°C solely large $\text{H-Nb}_2\text{O}_5$ crystals are observed which form at the expense of collapsing superstruc-

tures. These findings indicate that the phase transformation goes along with an Ostwald ripening process. The high stability of the networks is confirmed by in situ heating experiments performed in the TEM, which do not yield significant changes for nanowire networks calcined at 900 °C. Higher magnification images taken during in situ heating yield the formation of defects at temperatures of 500 °C. They are related to the planar defects commonly observed in the Nb₃O₇(OH) nanowires. Above 700 °C the formation of pores starts which is most likely related to a combination of phase transformation and reduction of the oxide by the electron beam. The tendency of niobium oxides to form suboxides is well known in literature and reflects in this study as the presence or absence of oxygen affects the crystal phase achieved from calcination of Nb₃O₇(OH). UV/Vis spectroscopy yields a band gap of 3.16 eV for the Nb₃O₇(OH) superstructures averaged over a large sample volume. This value is confirmed by low-loss EEL spectroscopy performed for single nanowires. Together with their large surface area and high crystal quality their absorption properties render these superstructures attractive for photochemical applications. Furthermore, their ability to photocatalytically degrade different dyes could be proven at different pH values. Accordingly promising H₂ production rates of 870 μmolg⁻¹h⁻¹ were observed for Pt decorated Nb₃O₇(OH) superstructures under 600 mWcm⁻² Xenon irradiation.

To further improve the performance of the superstructures, the effect of dopants on the crystallographic and photophysical properties of Nb₃O₇(OH) was analyzed. Doping was achieved by simply adding titanium-butoxide to the reaction solution. The addition of Ti(IV) leads to its homogeneous incorporation into the crystal lattice, with a maximum of about 12 at%. Further titanium excess leads to the formation of anatase TiO₂ plates on the surface of the superstructures. The presence of Ti(IV) in the reaction solution results in the formation of different superstructure morphologies composed of smaller nanowires, which have higher surface areas than the undoped superstructures. For a doping degree of 5.5 ± 0.7 at% Ti hollow spheres form, while the formation of hollow cubes composed of small nanowires is observed for a doping degree of 10.8 ± 1.5 at% Ti. In addition to the altered morphology, the presence of titanium at the surface of the superstructures also yields fewer surface defects which reflects in enhanced PL lifetimes. The combination of these two effects features enhanced H₂ production rates observed for these superstructures. Using 600 mWcm² Xenon radiation a doubled rate was observed for a doping degree of 5.5 ± 0.7 at% Ti compared to undoped Nb₃O₇(OH). The highest rate of 1900 μmolg⁻¹h⁻¹ is found for Nb₃O₇(OH) superstructures which comprise 10.8 ± 1.5 at% titanium and are overgrown by anatase TiO₂ plates.

Several properties of the superstructures still leave room for improvement which might result in even higher efficiencies in the future. First the size of the band gap is still rather large for photochemistry. On this account doping with other elements – maybe non-metal ions – could help at modulating the band gap size to allow the absorption of light from the visible spectrum. Furthermore, planar defects were observed in the crystal lattice of Nb₃O₇(OH). Other than it was reported for planar defects in hydrothermally grown TiO₂ nanowires, these defects cannot be removed by calcination. Therefore, to date it

was not possible to elucidate their effect on the performance of the superstructures. This is important, as a confinement of charge transport by planar defects was observed for the TiO_2 nanowires. The complexity of the 3D arrangement might further affect the motion of carriers throughout the superstructures. 3D reconstruction of the nanowire networks yield a first hint how the nanowire junctions might affect the charge transport. Still local conductivity measurements are required to prove the assumption. Together with an understanding of the forces that trigger the self-assembly of 3D hierarchical superstructures, these findings could help to modulate the optimal morphology for future application.

Appendices

A Template-Free Synthesis of Novel, Highly-Ordered 3D Hierarchical $\text{Nb}_3\text{O}_7(\text{OH})$ Superstructures

A.1 Quantitative Analysis of the Cube Sizes

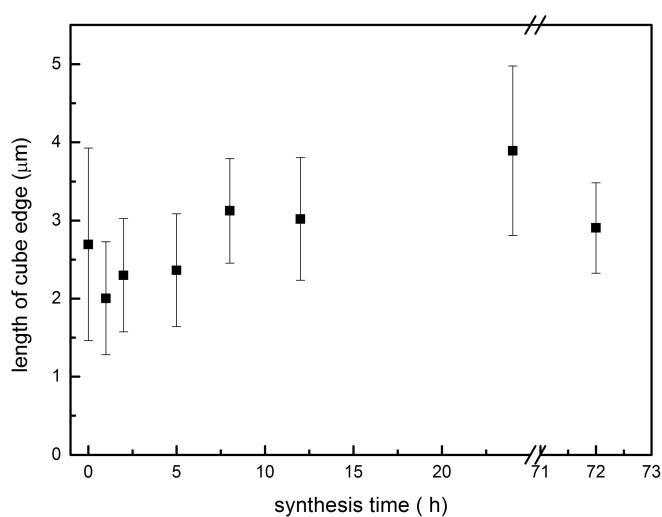


Figure A.1 Quantitative analysis of the cube size in dependence of the duration of the hydrothermal synthesis analyzing the edge length of 60 cubes.

A.2 Determination of the Band Gap from UV/Vis Data

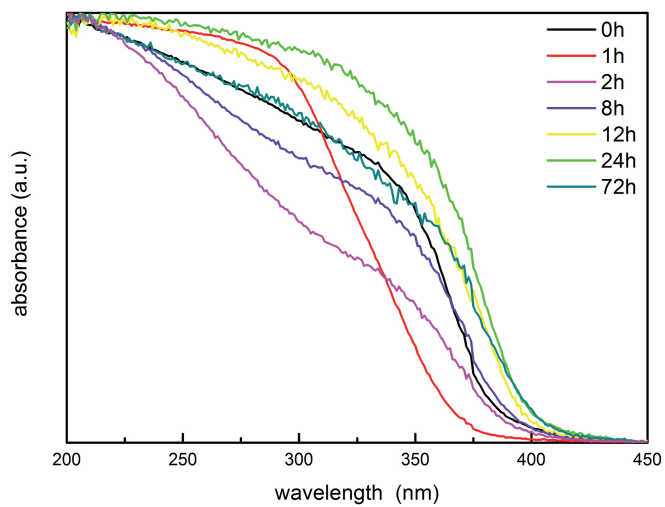


Figure A.2 Normalized UV/Vis spectra detected for different synthesis times.

Table A.1 Direct band gaps determined from UV/Vis data applying the Tauc method ($m = 1$) for different synthesis times.

growth time (h)	band gap (eV)
0	3.30 ± 0.05
1	3.52 ± 0.05
2	3.28 ± 0.05
8	3.25 ± 0.05
12	3.21 ± 0.05
24	3.19 ± 0.05
72	3.16 ± 0.05

A.3 EDX Data Detected of one Single Nanowire

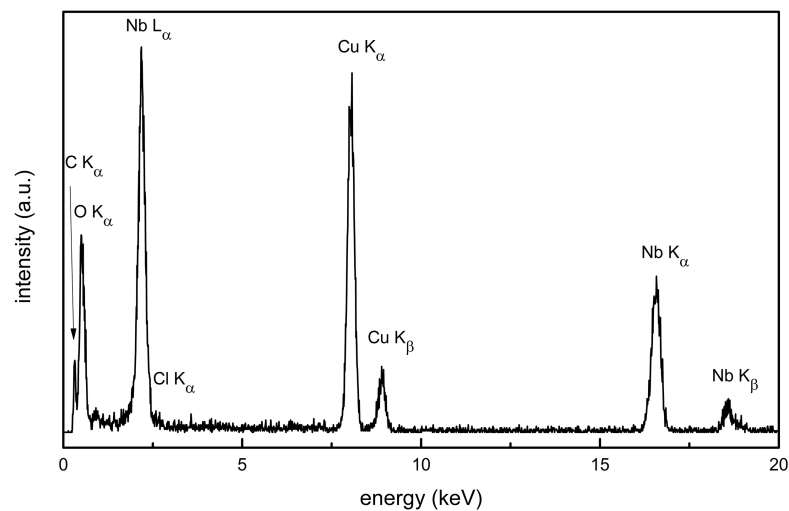


Figure A.3 EDX spectrum detected of one single $\text{Nb}_3\text{O}_7(\text{OH})$ nanowire in TEM showing peaks of niobium, oxygen and the copper support.

A.4 Simulations of the Electron Diffraction Pattern with JEMS

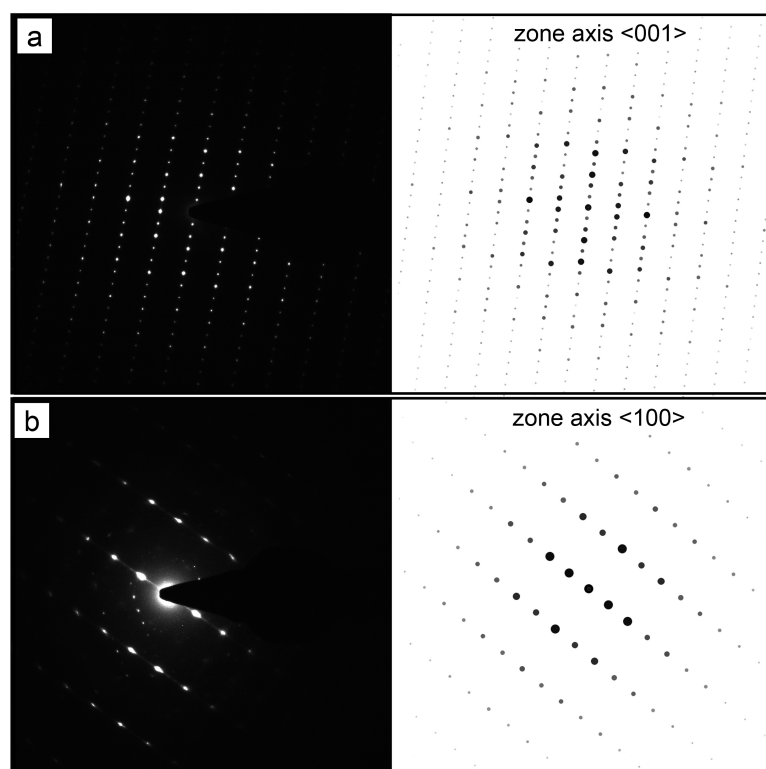


Figure A.4 Experimental and with JEMS simulated electron diffraction patterns of $\text{Nb}_3\text{O}_7(\text{OH})$ observed in $[001]$ (a) and $[100]$ direction (b).

A.5 Photocatalytic Degradation of Dyes Under UV Irradiation

Reference measurements were performed to exclude bleaching of the dyes due to the UV irradiation and to ensure that the decreasing dye concentration results from degradation photocatalyzed by $\text{Nb}_3\text{O}_7(\text{OH})$. In this regard bleaching experiments with pure dye solutions were performed, the achieved results are shown in figure A.5a–c related to the measured photocatalytic degradation applying $\text{Nb}_3\text{O}_7(\text{OH})$. To investigate adsorption of dye on the $\text{Nb}_3\text{O}_7(\text{OH})$ surfaces, the concentration of the used dye solution is compared to the dye concentration of the $\text{Nb}_3\text{O}_7(\text{OH})$ -dye-mixture (fig. A.5d).

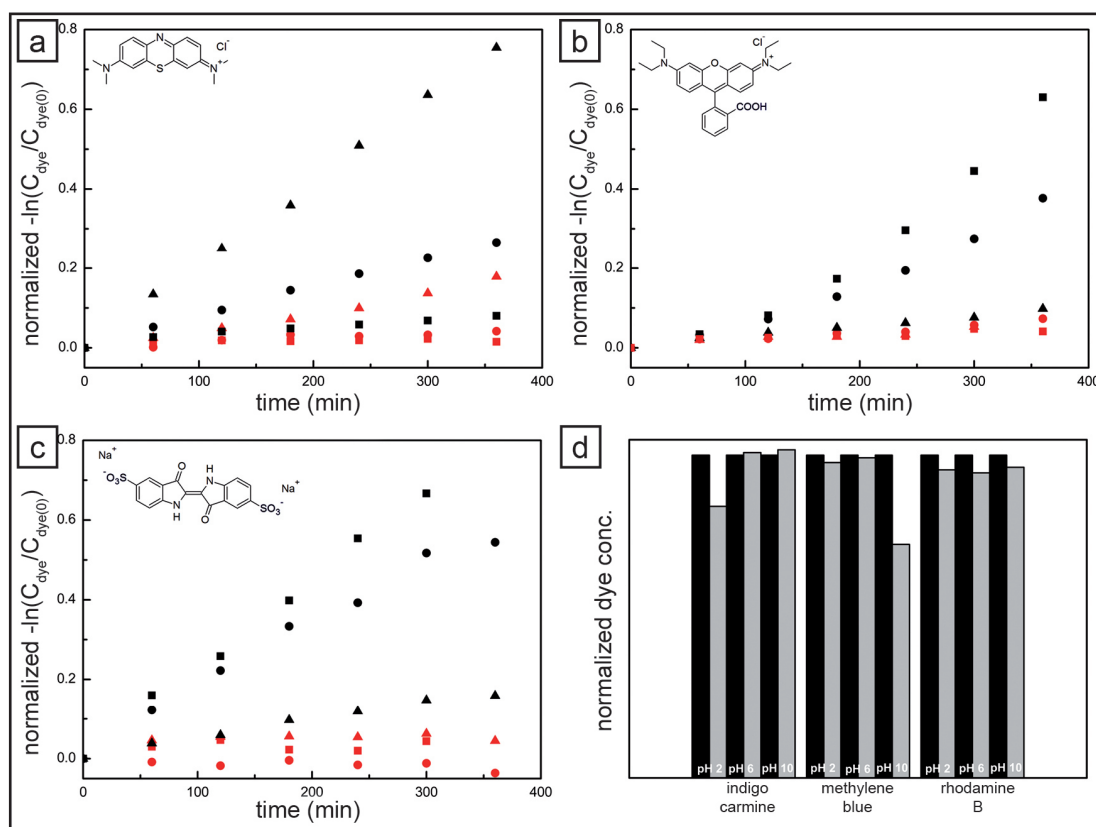


Figure A.5 Reference measurements related to the photocatalytic dye degradation measurements. a-c) Bleaching of the dye due to UV irradiation (methylene blue (a), rhodamine B (b) and indigo carmine (c)) at different pH-values (pH 2 (■), pH 6 (●) and pH 10 (▲)). The measured bleaching (red symbols) is related to the results of the photocatalytic degradation measurements (black symbols). d) Investigation of dye adsorption onto the $\text{Nb}_3\text{O}_7(\text{OH})$ surface in dependence of the dye type and the pH value, via measurement of the dye concentration in the solution. The concentration was determined from UV/Vis spectra, the original concentration of the dye is given as black columns, while the dye concentration after incubation with $\text{Nb}_3\text{O}_7(\text{OH})$ for 1.5 hours is given in light gray.

B Heat Induced Phase-Transformation of 3D $\text{Nb}_3\text{O}_7(\text{OH})$ Superstructures – Effect of Atmosphere and Electron Beam

B.1 X-ray Diffraction Analysis Tracing the Effect of Heat on the Crystal Structure

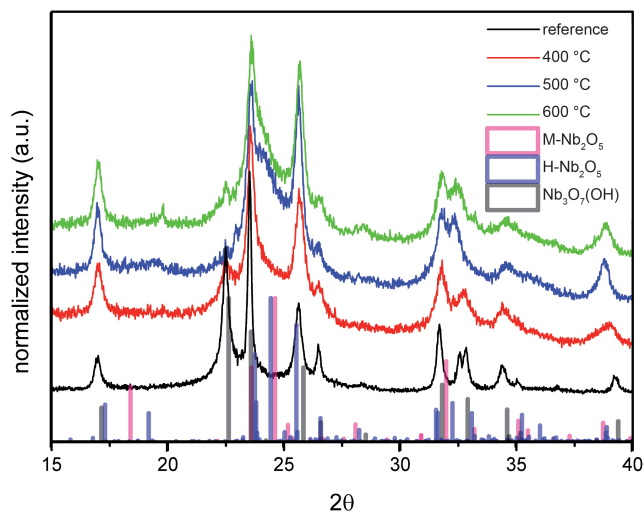


Figure B.1 X-ray diffraction pattern for samples which were calcined at 400, 500 and 600 °C for one hour. In addition a reference pattern of $\text{Nb}_3\text{O}_7(\text{OH})$ is given. The calculated positions of the lattice spacing of $\text{M-Nb}_2\text{O}_5$, $\text{H-Nb}_2\text{O}_5$ and $\text{Nb}_3\text{O}_7(\text{OH})$ are also included.

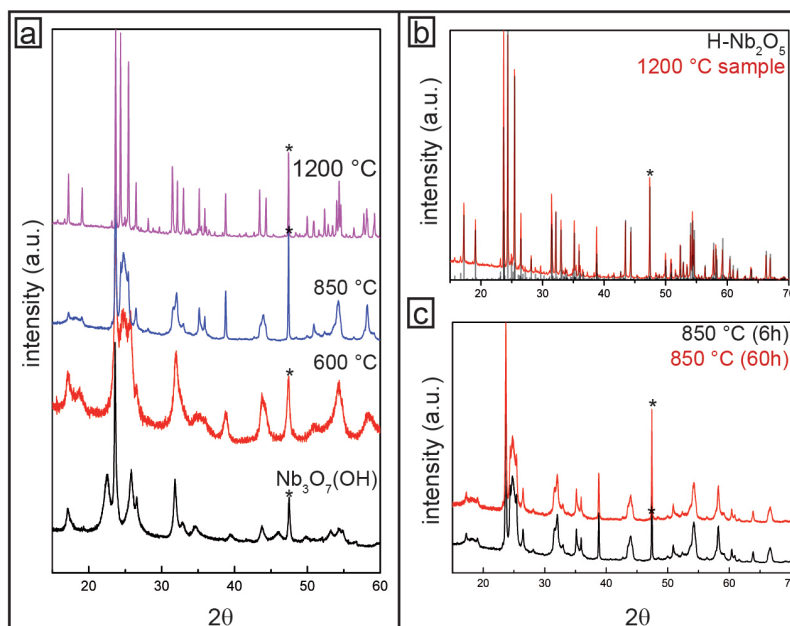


Figure B.2 X-ray diffraction pattern detected for samples calcined at temperatures between 600 °C and 1200 °C. a) The pattern detected for a calcination temperature of 600 °C (6h) shows a phase mixture of Nb₃O₇(OH) and a new crystal phase. At a calcination temperature of 850 °C (6h) only reflections of the new crystal phase are visible, their broadness indicates small crystallites. The sample calcined at 1200 °C (6h) exhibits sharp reflections of the new crystal phase. b) Comparison of the sample calcined at 1200 °C with a reference pattern of monoclinic H-Nb₂O₅. c) An increase of the calcination time does not affect the XRD pattern of the respective sample. A reflection caused by the measurement setup is marked with an asterisk.

B.2 Electron Diffraction Investigation of H-Nb₂O₅ After Ex Situ Calcination

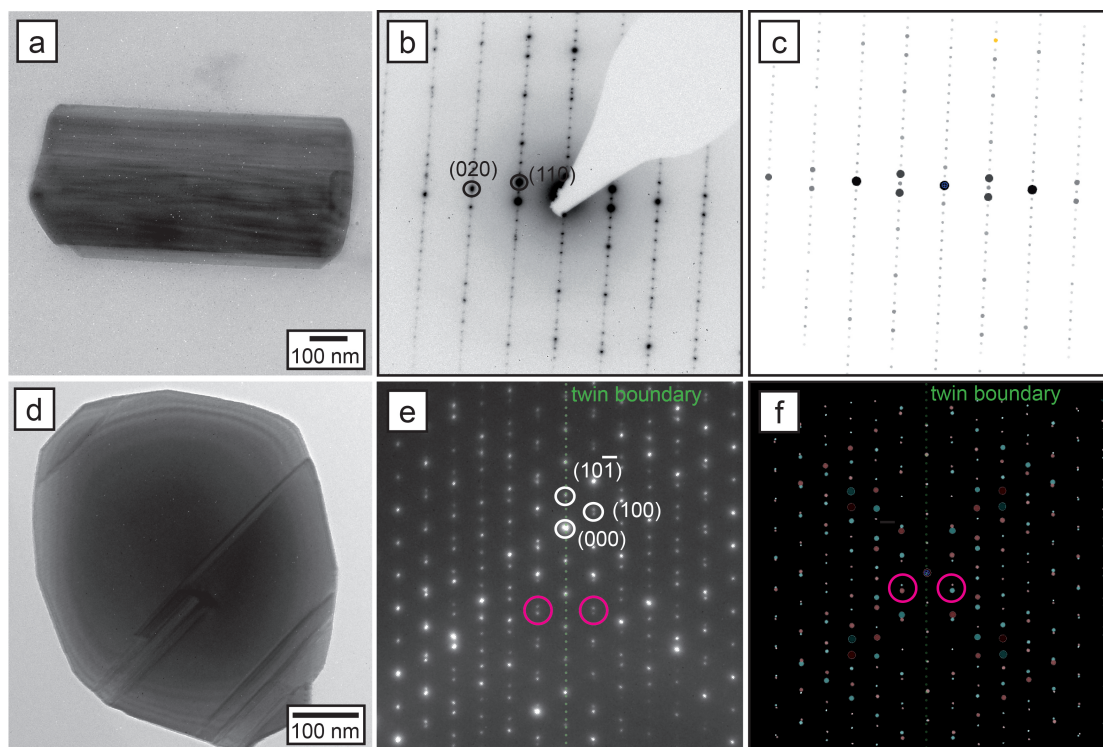


Figure B.3 TEM of crystals obtained at a calcination temperature of 850 °C and 1200 °C. a) Bright field image of one crystal observed for the 850 °C sample. b) Corresponding electron diffraction pattern indexed for H-Nb₂O₅ in $\langle 001 \rangle$ zone axis. c) Simulation of the electron diffraction of H-Nb₂O₅ in $\langle 001 \rangle$ zone axis, featuring a close agreement with the experiment. d) Bright field image of one crystal obtained after calcination at 1200 °C. The image shows the compact nature of the crystal and exhibits defects in the crystal lattice. e) Corresponding electron diffraction pattern indexed for H-Nb₂O₅ in $\langle 010 \rangle$ zone axis. Please note that the diffraction pattern is rotated with respect to the bright field image. f) Simulated electron diffraction pattern of H-Nb₂O₅ in $\langle 010 \rangle$ zone axis considering the presence of a twin boundary in the crystal (red and blue reflections) with the $(10\bar{1})$ as common plane. The experimental pattern is reproduced.

B.3 In Situ Heating Experiment Performed on a Network

Table B.1 Details of the in situ heating experiment of a nanowire network.

RT \rightarrow 500 °C	20 minutes (24 °C/min)
500 °C	8 minutes
500 °C \rightarrow 700 °C	9 minutes (22 °C/min)
700 °C	9 minutes
700 °C \rightarrow 900 °C	9 minutes (22 °C/min)
900 °C	300 minutes (images every 15 min)
900 °C	120 minutes (investigation of other parts of the sample)
900 °C \rightarrow 40 °C	11 minutes

B.4 Comparison of the Nanowire Width Before and After the Heating Experiment

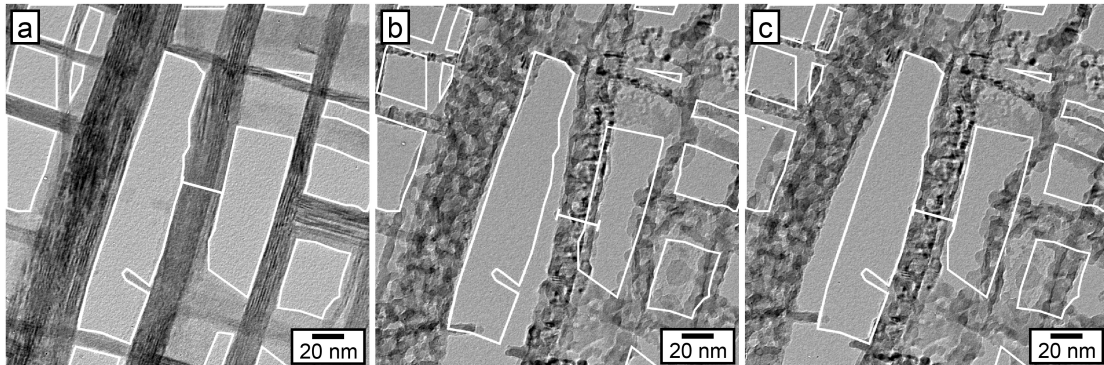


Figure B.4 BF images of the network before and after the in situ heating experiment. a) The outline of the nanowire network before the heating experiment is highlighted with white lines. These white lines are included into BF images acquired for the same network region after the experiment. b) The width of the thick nanowire on the left is analyzed and in c) the width of the thin nanowire in the center.

B.5 Lattice Spacings Determined from Fast Fourier Transformation Pattern of Calcined Samples

Table B.2 Lattice plane distances observed for different samples after in situ heating experiments in the TEM. The values are determined from FFT pattern.

experiment parameters	d_1 (Å)	d_2 (Å)	d_3 (Å)	$\angle_{1,2}$	$\angle_{2,3}$
network; max. T 900 °C	2.6	1.4	2.3	30°	26°
starting orientation [001]; max. T 850 °C	2.5	2.5	1.2	87°	45°
starting orientation [100]; max. T 1000 °C	3.8	3.8	2.7	90°	44°
in situ without electron beam; max. T 900 °C	2.5	1.4	1.5	68°	32°
in situ without electron beam; max. T 1000 °C & 1200 °C	14.2	1.9	3.2	32°	58°

B.6 In Situ Heating of One Single Nanowire – Observation of Pore Formation

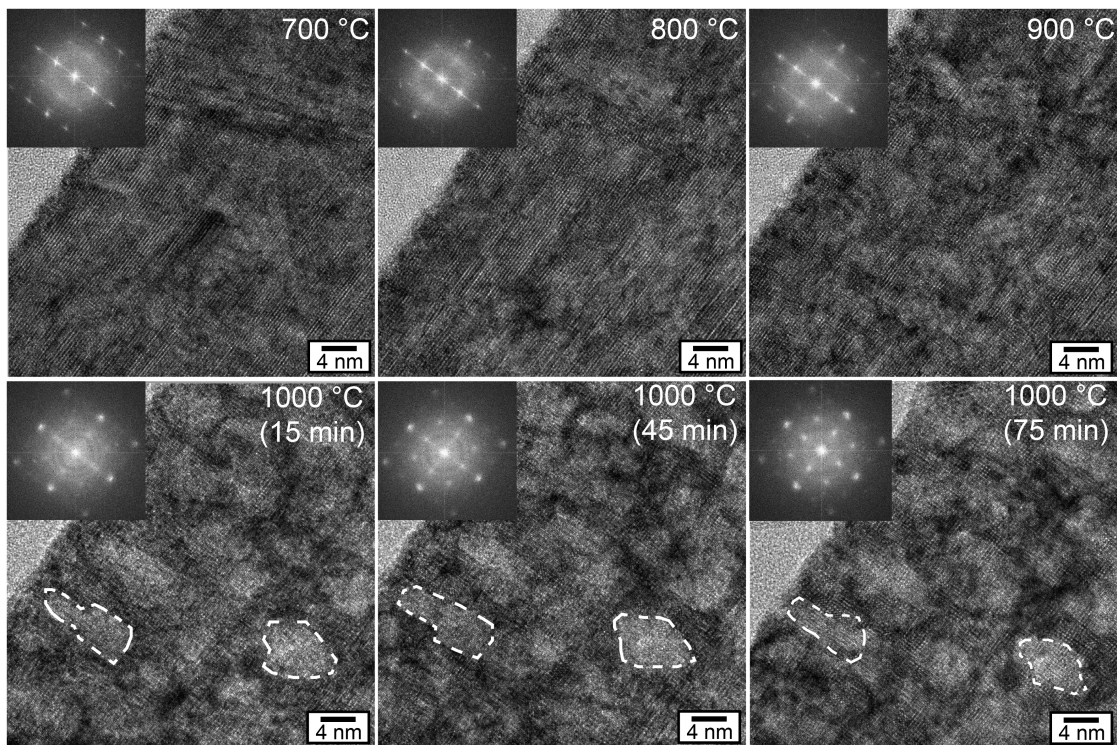


Figure B.5 HRTEM images detected at different times and temperatures of the in situ experiment. The screen shots were taken at one nanowire which was oriented in [100] direction before the in situ heating experiment.

B.7 FFT of Nanowires After the Calcination – Detected for Both Starting Crystal Orientation

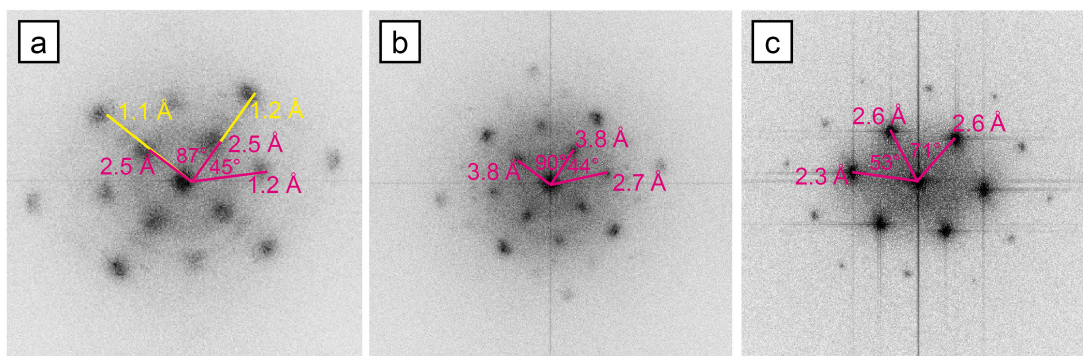


Figure B.6 FFT of different nanowires after the in situ heating experiment. a) FFT of a nanowire after in situ heating to 800 °C. Original viewing direction is [001]. b) FFT of a nanowire calcined in situ at 1000 °C. The nanowire was oriented in [100] direction before the experiment. c) FFT of one single nanowire in a nanowire network which was heated in situ to 900 °C.

B.8 HRTEM Images of Nanowires Heated In Situ in Absence of the Electron Beam

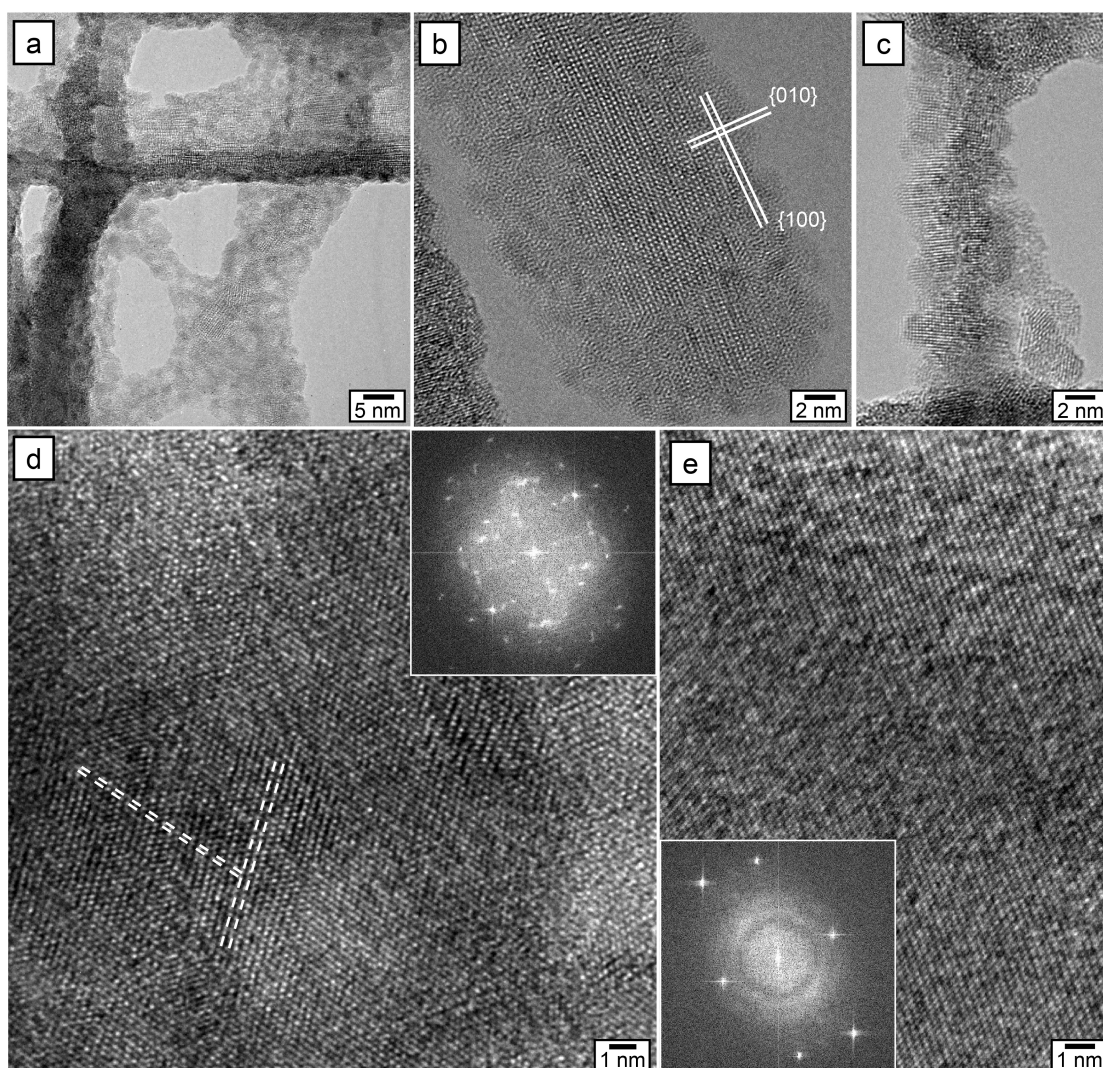


Figure B.7 HRTEM and FFT images of a nanowire network heated in situ for 7 hours at 900 °C in absence of the electron beam. a) Small nanocrystals appear concurrently with the phase transformation. b) Not all nanowire are phase transformed but some remain $\text{Nb}_3\text{O}_7(\text{OH})$. However at the surface of these nanowires the formation of small nanocrystals is observed. c) Nanowire, which is composed of small nanocrystals. d) Phase transformed nanowire, the nanograins are still visible. e) Larger nanocrystal of the new crystal phase, FFT pattern demonstrate that it is a different crystal phase than the mother compound $\text{Nb}_3\text{O}_7(\text{OH})$.

C Titanium Doping and its Effect on the Morphology of 3D Hierarchical Nb₃O₇(OH) Nanostructures for Enhanced Light-Induced Water Splitting

C.1 EDX Spectra Detected for Nanowires Synthesized in the Presence of Ti(IV)

The average amount of titanium incorporated into the different superstructures was determined in the SEM since this allowed to chose specific morphologies. In addition, local EDX measurements were performed in the TEM, focussing on fragments of the superstructures. The EDX spectra show a small additional chloride peak, which results from remaining precursor. Both methods yield similar results. Due to the low fluorescence yield and absorption in the detector the oxygen K-line was not used for quantification.

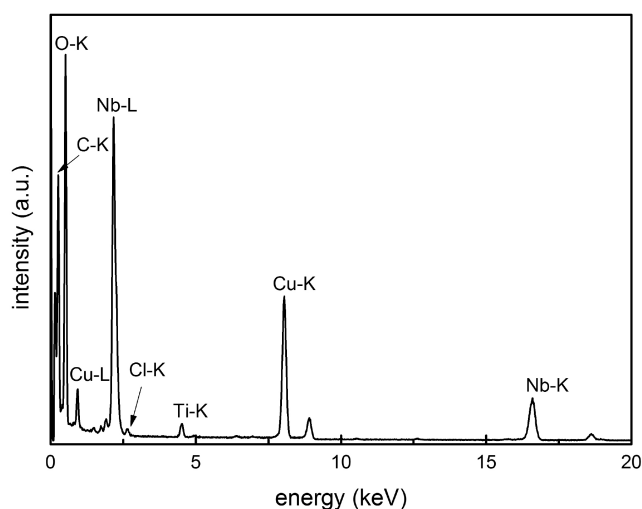


Figure C.1 Exemplary EDX spectrum detected of a network of morphology B in TEM. The quantitative analysis gives a Ti-doping amount of 3.9 at% relative to Nb. The copper peak results from the TEM support grid and the chloride peak is due to the original precursor.

C.2 Correlation Between Doping Degree and Ti(IV) Concentration in the Reaction Solution

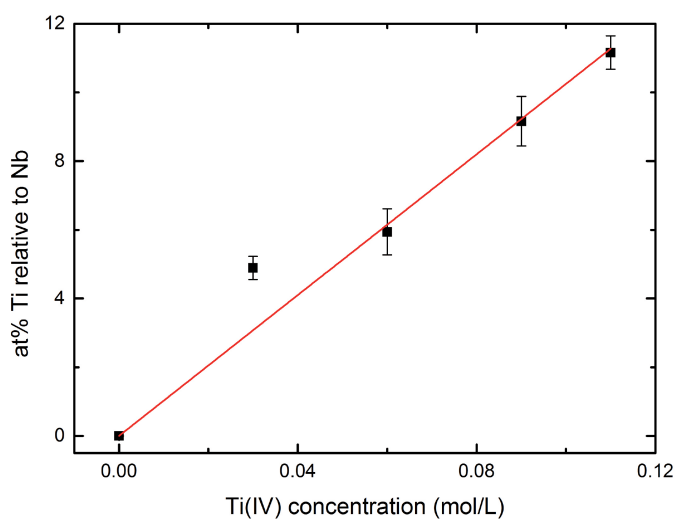


Figure C.2 Doping degree of the $\text{Nb}_3\text{O}_7(\text{OH})$ superstructures dependent on the Ti(IV) concentration in the reaction solution. The doping degree is given in at% Ti relative to Nb, which was determined from EDX measurements performed in the SEM.

C.3 Hollowness of $\text{Nb}_3\text{O}_7(\text{OH})$ Superstructures

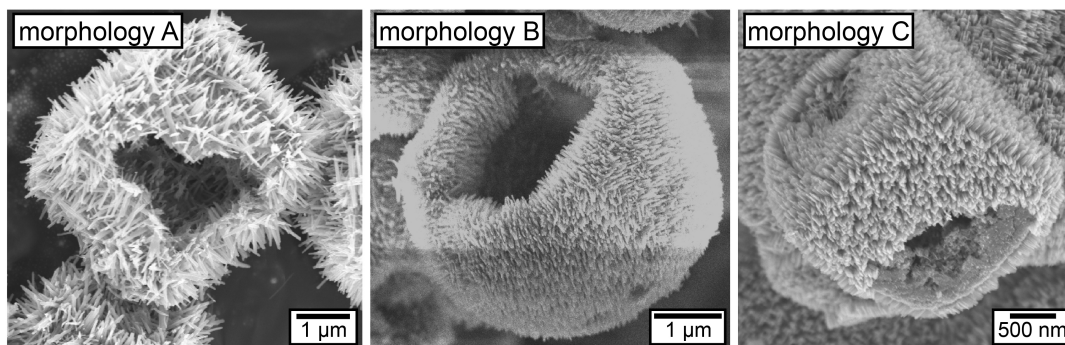


Figure C.3 SEM images of the different $\text{Nb}_3\text{O}_7(\text{OH})$ superstructures morphologies proving their hollowness.

C.4 X-ray Diffraction Analysis in Dependence on the Ti(IV) Concentration

Table C.1 Measured $2\theta_B$ values and calculated d-spacings which were assigned to $\text{Nb}_3\text{O}_7(\text{OH})$ (isomorphous to $\text{Nb}_3\text{O}_7\text{F}$, ICSD-28461) and anatase TiO_2 (ICSD 44882).

2θ	d-spacing [\AA]	hkl	crystal phase
17.1	5.17	(400)	$\text{Nb}_3\text{O}_7(\text{OH})$
22.6	3.92	(001)	$\text{Nb}_3\text{O}_7(\text{OH})$
23.7	3.76	(110)	$\text{Nb}_3\text{O}_7(\text{OH})$
25.1	3.50	(011)	anatase TiO_2
26.0	3.45	(600)	$\text{Nb}_3\text{O}_7(\text{OH})$
26.7	3.35	(310)	$\text{Nb}_3\text{O}_7(\text{OH})$
31.8	2.81	(510)	$\text{Nb}_3\text{O}_7(\text{OH})$
32.8	2.72	(111)	$\text{Nb}_3\text{O}_7(\text{OH})$
34.5	2.59	(601)	$\text{Nb}_3\text{O}_7(\text{OH})$
36.6	2.40	(013)	anatase TiO_2
37.5	2.40	(004)	anatase TiO_2
38.3	2.30	(112)	anatase TiO_2
39.3	2.29	(511)	$\text{Nb}_3\text{O}_7(\text{OH})$
43.7	2.07	(1000)	$\text{Nb}_3\text{O}_7(\text{OH})$
46.2	1.97	(002)	$\text{Nb}_3\text{O}_7(\text{OH})$
49.5	1.83	(1001)	$\text{Nb}_3\text{O}_7(\text{OH})$
52.5	1.74	(112)	$\text{Nb}_3\text{O}_7(\text{OH})$
53.6	1.70	(015)	anatase TiO_2
54.1	1.69	(1110)	$\text{Nb}_3\text{O}_7(\text{OH})$
54.5	1.67	(121)	anatase TiO_2
54.8	1.67	(620)	$\text{Nb}_3\text{O}_7(\text{OH})$
57.1	1.61	(512)	$\text{Nb}_3\text{O}_7(\text{OH})$
59.3	1.55	(1111)	$\text{Nb}_3\text{O}_7(\text{OH})$
59.9	1.54	(621)	$\text{Nb}_3\text{O}_7(\text{OH})$
62.1	1.48	(024)	anatase TiO_2
68.8	1.36	(116)	anatase TiO_2
70.3	1.34	(022)	anatase TiO_2

C.5 Spherical morphology B

SEM images of the spherical morphology which contains 5.5 ± 0.7 at% titanium show remainings of corners indicating that they result from rounded cubes.

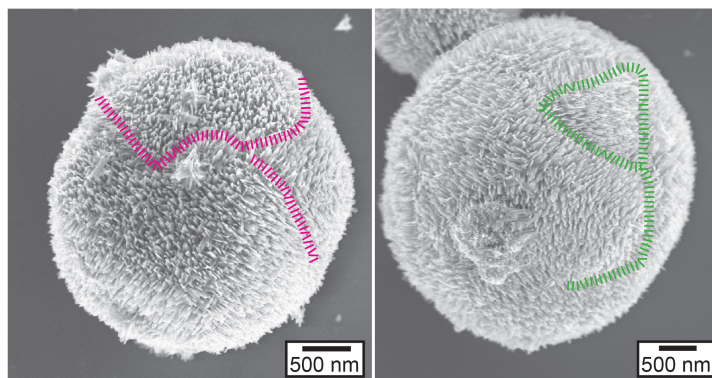


Figure C.4 SEM images of the spherical morphology B containing 5.5 ± 0.7 at% titanium. Possible edge remainings are highlighted.

C.6 Shift of Reflections in the XRD Pattern

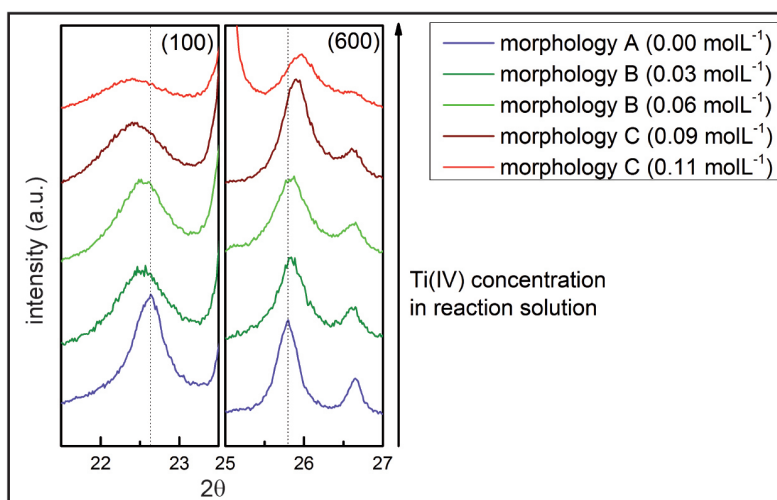


Figure C.5 Shifting of the (001) and (600) reflexes with increasing Ti(IV) concentration in the reaction solution.

C.7 Quantitative Analysis of the Wire Thickness from TEM Images

The thickness t and width w of the nanowires were measured from TEM images. Quantitative analysis was performed by measuring and averaging the thickness of 10 nanowires for the $\langle 100 \rangle$ and $\langle 001 \rangle$ zone axis of the respective sample. The length l of the nanowires was estimated from SEM images of broken cubes. The results are summarized in Table C.2.

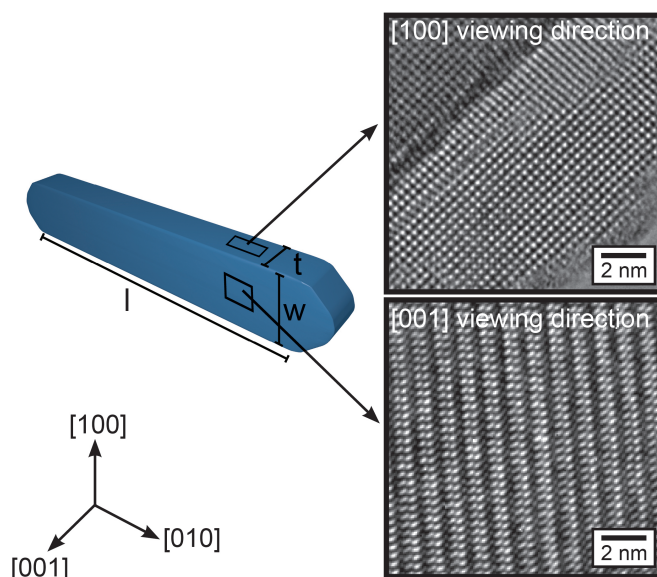


Figure C.6 Schematic drawing of the wires and corresponding crystallographic directions. HRTEM images of $\text{Nb}_3\text{O}_7(\text{OH})$ nanowires observed in two different viewing directions. HRTEM image of a nanowire oriented parallel to the $[100]$ direction, the nanowire width in this crystal direction is called thickness t of the nanowire. The width of a nanowire oriented in $[001]$ direction is called width w .

Table C.2 Width, thickness, w -to- t aspect ratio and length l of nanowires for the different morphologies were measured from SEM and TEM images, averaging 10 data points per sample.

	width w (nm)	thickness t (nm)	w -to- t aspect ratio	length l (nm)
morphology A	45 (± 14)	28 (± 10)	1.6 : 1.0	848 (± 75)
morphology B	24 (± 9)	12 (± 5)	2.0 : 1.0	250 (± 30)
morphology C	15 (± 6)	4 (± 1)	3.8 : 1.0	165 (± 16)

C.8 HRTEM Images Showing Planar Defects Parallel to $\{001\}$ Lattice Planes

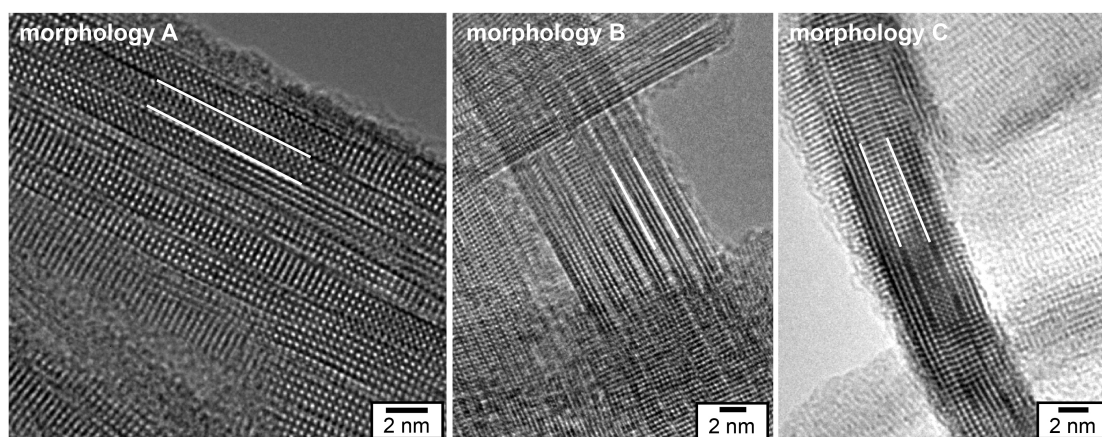


Figure C.7 HRTEM images of nanowires observed in $[100]$ viewing direction for morphology A, B and C. The width of the planar defects parallel to the $\{001\}$ lattice plane is similar for the different morphologies.

C.9 EDX Mapping Experiments Performed for Morphology B

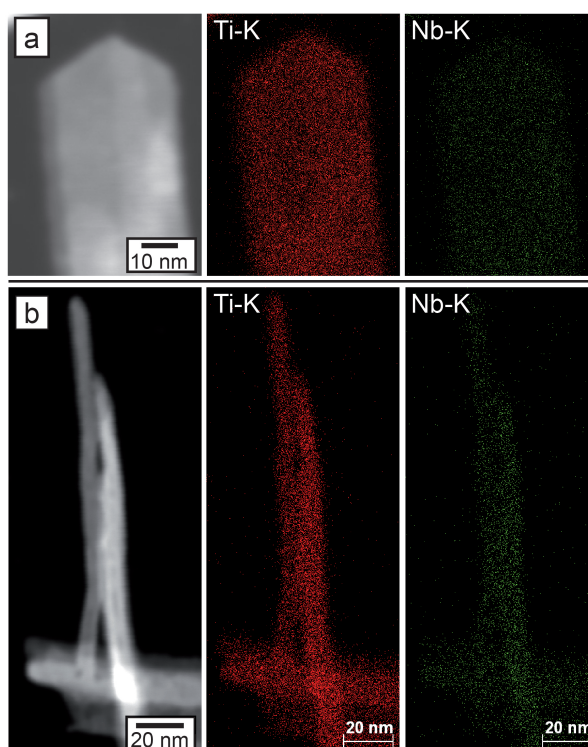


Figure C.8 EDX mappings based on the Ti-K and the Nb-K line are displayed for two different sample regions. a) Scanning TEM image and Ti and Nb distribution within one nanowire. Systematic quantification analysis of selected areas of this map yields a constant titanium distribution over the nanowire, with a titanium amount of 4 at%. b) Junction of four nanowires. The quantitative analysis does not show significant changes of the titanium distribution at the overlap region. Again 4 at% titanium are incorporated into the crystal lattice.

C.10 HRTEM Investigation of the Connection Region Between $\text{Nb}_3\text{O}_7(\text{OH})$ Nanowires and Anatase TiO_2 Plate

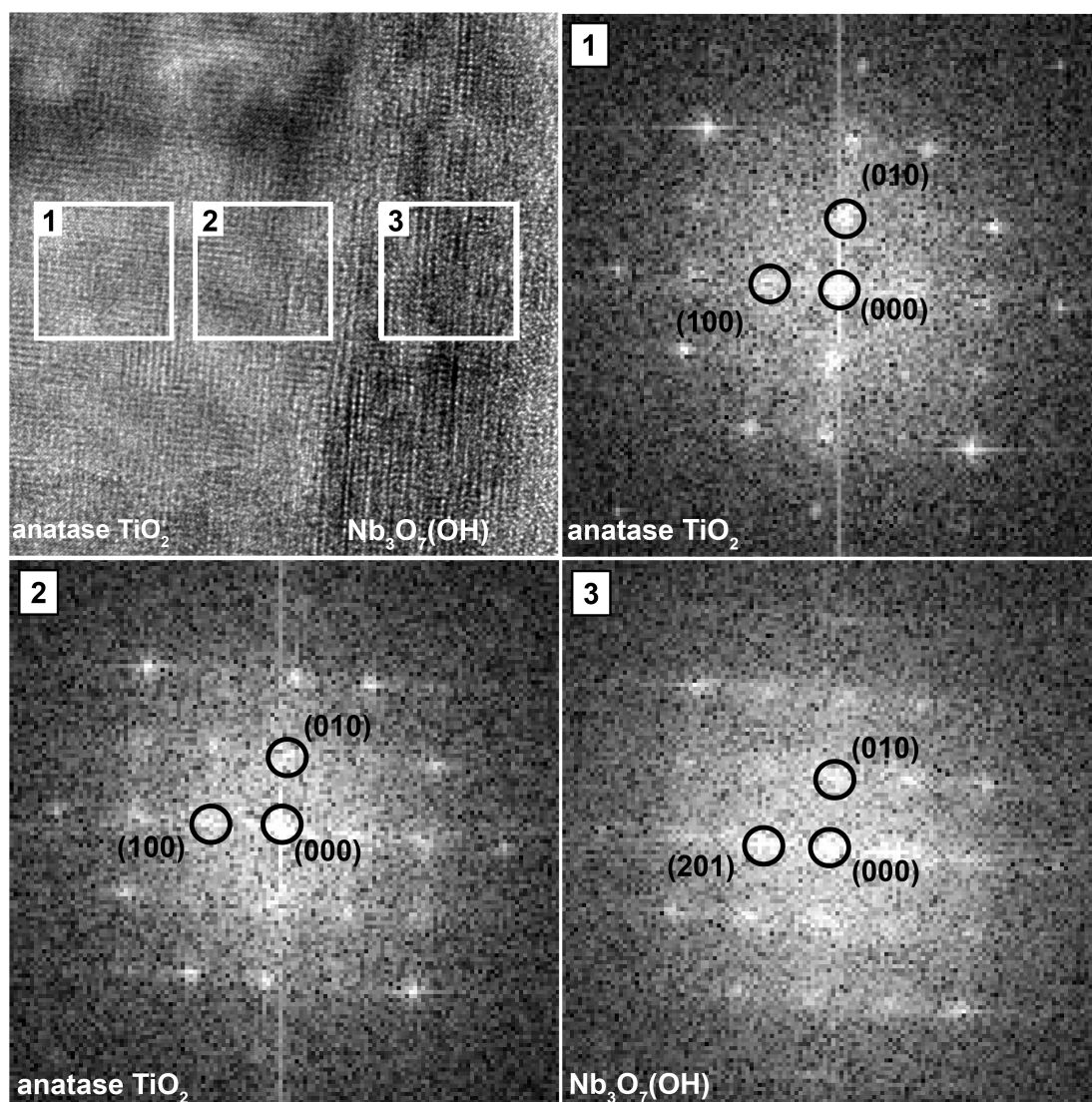


Figure C.9 FFT analysis of the interface between incorporated $\text{Nb}_3\text{O}_7(\text{OH})$ nanowire and TiO_2 plate. The area for which the FFT pattern were calculated are marked.

C.11 Analysis of EEL Spectra Detected for the Different Samples

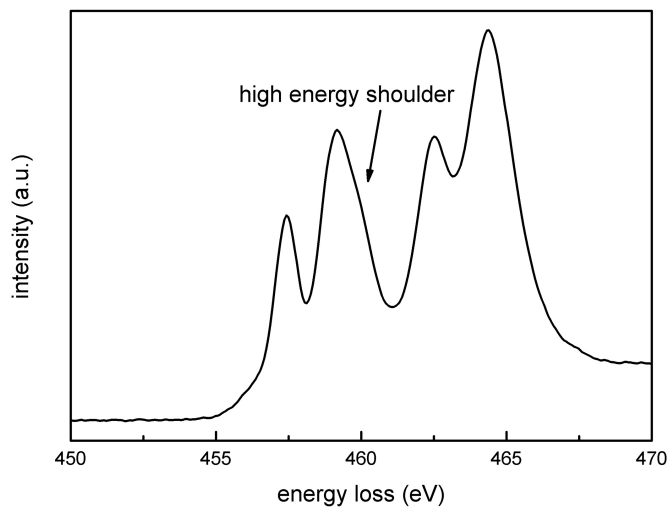


Figure C.10 ELNES of the Ti-L_{2,3} edge measured for anatase TiO₂ plates which form for excessive Ti(IV) in the reaction solution. The characteristic high-energy shoulder is marked.

Table C.3 Qualitative analysis of the ELNES of the Ti-L_{2,3}, Nb-M_{2,3} and O-K edge. Comparison of measured spectra with literature data. The peak position is given relative to the onset of the respective edge.

		a	a'	b	b'
Nb-M _{2,3}	lit. Nb ₂ O ₅	366.9	+2.5	+15.0	+17.8
	morphology A (Nb ₃ O ₇ (OH))		+2.6 ± 0.1	+14.7 ± 0.1	+17.7 ± 0.2
	morphology B (5 at% Ti)		+2.2 ± 0.1	+14.6 ± 0.1	+17.3 ± 0.1
	morphology C (10 at% Ti)		-	+14.6 ± 0.1	-
	anatase TiO ₂		+3.1 ± 0.1	+14.6 ± 0.1	+18.2 ± 0.3
		a	a'	b	b'
Ti-L _{2,3}	morphology A (Nb ₃ O ₇ (OH))		-	-	-
	morphology B (5 at% Ti)		+1.7 ± 0.1	+5.2 ± 0.1	+6.9 ± 0.1
	morphology C (10 at% Ti)		+1.7 ± 0.1	+ 5.3 ± 0.1	+6.8 ± 0.1
	anatase TiO ₂		+1.7 ± 0.1	+ 5.1 ± 0.1	+7.1 ± 0.1
	lit. anatase TiO ₂	458.2	+1.8 (B1) + 2.5 (B2)	+5.4	+7.4
	lit. rutile TiO ₂	458.2	+2.0 (B1) + 2.9 (B2)	+5.4	+7.9
		a	b	c	c'
O-K	Nb ₂ O ₅	533.5	+4.6	-	+ 13.0
	morphology A (Nb ₃ O ₇ (OH))		+4.5 ± 0.1	-	+12.8 ± 0.1
	morphology B (5 at% Ti)		+4.3 ± 0.1	-	+12.3 ± 0.2
	morphology C (10 at% Ti)		+4.3 ± 0.1	-	+12.2 ± 0.1
	anatase TiO ₂		+ 2.4 ± 0.1	+7.7 ± 0.2	-
	lit. anatase TiO ₂	531.1	+ 2.6	+8.0	+13.5
	lit. rutile TiO ₂	530.9	+ 2.6	+9.0	+14.0

C.12 UV/Vis Spectra Recorded for the Different Samples

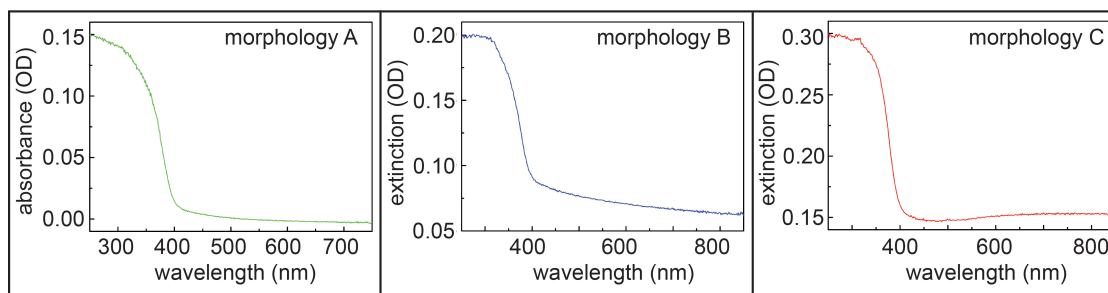


Figure C.11 UV/Vis spectra recorded for the different morphologies. All have a steep rise at 400 nm. The tail in the data of morphology B results from scattering due to the measurement geometry. The extinction spectrum of morphology C shows slight absorption between 550 and 850 nm.

C.13 TEM Investigation of Pt-Nb₃O₇(OH) Structures

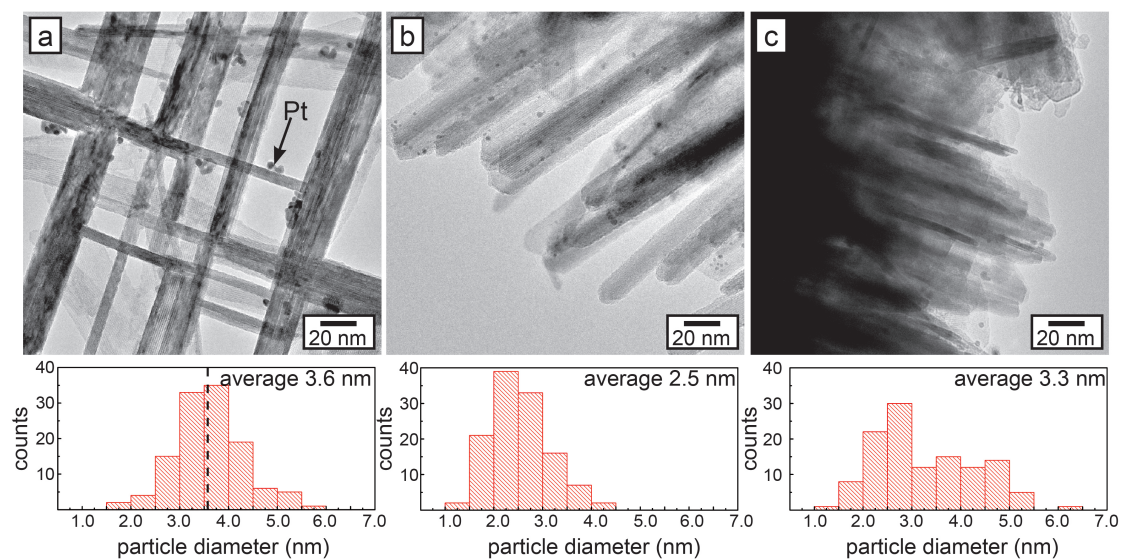


Figure C.12 TEM investigation of the Pt particle distribution on the different morphologies and statistical analysis of their sizes. For morphology A an average particle size of 3.6 nm was found (a), for morphology B 2.5 nm (b) and for morphology C 3.3 nm (c).

C.14 Spectrum of the 600 mWcm^{-2} Xenon Lamp Used to Measure the H_2 Evolution

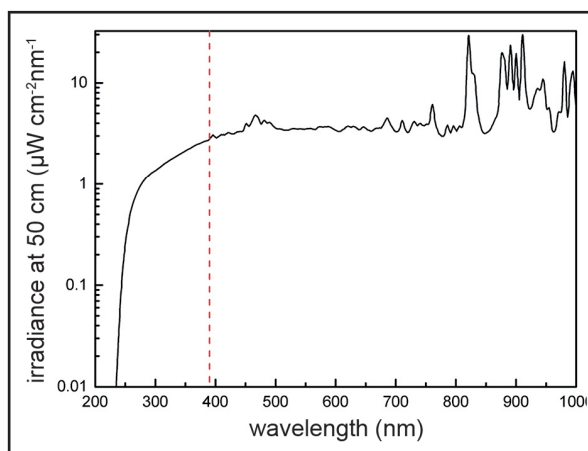


Figure C.13 Spectrum of the 600 mWcm^{-2} Xenon lamp used to measure H_2 evolution. The dotted red line marks the wavelength limit for the $\text{Nb}_3\text{O}_7(\text{OH})$ absorption.

C.15 PL Lifetime Characterization Performed for the Different Morphologies

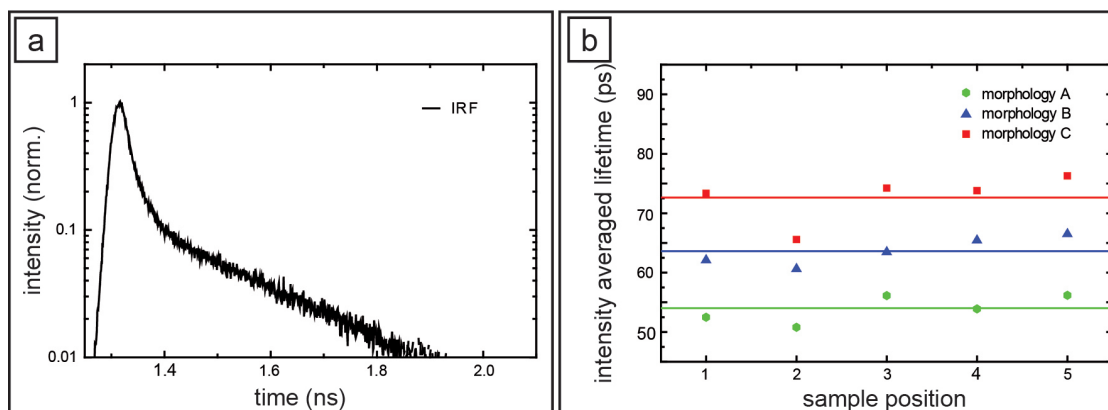


Figure C.14 PL lifetime characterization of the different morphologies. a) Instrument response function of the used setup. b) The intensity averaged lifetimes were measured at five different sample positions per morphology.

Bibliography

References from Chapter 1

- [1] R. E. Morris, P. S. Wheatley, *Angew. Chem.* **2008**, *47*, 4966.
- [2] I. Moreels, K. Lambert, D. Smeets, D. De Muynck, T. Nollet, J. C. Martins, F. Vanhaecke, A. Vantomme, C. Delerue, G. Allan, Z. Hens, *ACS Nano* **2009**, *3*, 3023.
- [3] D. B. Williams, C. B. Carter, *Transmission Electron Microscopy: A Textbook for Materials Science*, Springer, **2013**.
- [4] A. Wisnet, K. Bader, S. B. Betzler, M. Handloser, P. Ehrenreich, T. Pfadler, J. Weickert, A. Hartschuh, L. Schmidt-Mende, C. Scheu, J. A. Dorman, *Adv. Funct. Mater.* **2015**, *25*, 2601.
- [5] J. H. Fendler, F. C. Meldrum, *Adv. Mater.* **1995**, *7*, 607.
- [6] Y. Wang, A. S. Angelatos, F. Caruso, *Chem. Mater.* **2008**, *20*, 848.
- [7] Q. Yang, Z. Lu, J. Liu, X. Lei, Z. Chang, L. Luo, X. Sun, *Prog. Nat. Sci.* **2013**, *23*, 351.
- [8] C. C. Yec, H. C. Zeng, *J. Mater. Chem. A* **2014**, *2*, 4843.
- [9] M. R. Kim, Z. Xu, G. Chen, D. Ma, *Chemistry* **2014**, *20*, 11256.
- [10] S. K. Tripathi, N. Shukla, V. N. Kulkarni, *Nanotechnology* **2009**, *20*, 075304.
- [11] S. M. George, *Chem. Rev.* **2010**, *110*, 111.
- [12] S. S. Parkin, M. Hayashi, L. Thomas, *Science* **2008**, *320*, 190.
- [13] O. Salata, *J. Nanobiotechnology* **2004**, *2*, 3.
- [14] D. A. Giljohann, D. S. Seferos, W. L. Daniel, M. D. Massich, P. C. Patel, C. A. Mirkin, *Angewandte Chemie* **2010**, *49*, 3280.
- [15] In *Nanostructured Semiconductor Oxides for the Next Generation of Electronics and Functional Devices*, (Ed.: S. Zhuiykov), Woodhead Publishing, **2014**, pp. 267–320.
- [16] Mauna Loa Observatory, Scripps CO₂ data, **Oct. 2015**, <http://co2now.org/Current-CO2/CO2-Now/scripps-co2-data-mauna-loa-observatory.html>.
- [17] K. Yu, J. Chen, *Nanoscale Res. Lett.* **2008**, *4*, 1.
- [18] A. Hagfeldt, G. Boschloo, L. Sun, L. Kloo, H. Pettersson, *Chem. Rev.* **2010**, *110*, 6595.
- [19] B. O'Regan, M. Grätzel, *Nature* **1991**, *353*, 737.
- [20] A. Fujishima, K. Honda, *Nature* **1972**, *238*, 37.
- [21] M. G. Walter, E. L. Warren, J. R. McKone, S. W. Boettcher, Q. Mi, E. A. Santori, N. S. Lewis, *Chem. Rev.* **2010**, *110*, 6446.
- [22] X. Chen, S. Shen, L. Guo, S. S. Mao, *Chem. Rev.* **2010**, *110*, 6503.
- [23] F. E. Osterloh, *Chem. Soc. Rev.* **2013**, *42*, 2294.

- [24] A. C. Dodd, A. J. McKinley, M. Saunders, T. Tsuzuki, *J. Nanopart. Res.* **2006**, *8*, 43.
- [25] G. Xiong, U. Pal, J. G. Serrano, *J. Appl. Phys.* **2007**, *101*, 024317.
- [26] K. Kočí, L. Obalová, L. Matějová, D. Plachá, Z. Lacný, J. Jirkovský, O. Šolcová, *Appl. Catal. B-Environ* **2009**, *89*, 494.
- [27] A. K. Ghosh, C. Fishman, T. Feng, *J. Appl. Phys.* **1980**, *51*, 446.
- [28] C. R. M. Grovenor, *J. Phys. C: Solid State Phys.* **1985**, *18*, 4079.
- [29] P. Docampo, S. Guldin, U. Steiner, H. J. Snaith, *J. Phy. Chem. Lett.* **2013**, *4*, 698.
- [30] A. Testino, I. R. Bellobono, V. Buscaglia, C. Canevali, M. D'Arienzo, S. Polizzi, R. Scotti, F. Morazzoni, *J. Am. Chem. Soc.* **2007**, *129*, 3564.
- [31] W. A. Goddard, D. Brenner, S. E. Lyshevski, G. J. Iafrate, *Handbook of Nanoscience, Engineering, and Technology, Third Edition*, Taylor & Francis, **2012**.
- [32] J. Jiu, F. Wang, S. Isoda, M. Adachi, *Chem. Lett.* **2005**, *34*, 1506.
- [33] J. Jiu, S. Isoda, F. Wang, M. Adachi, *J. Phys. Chem. B* **2006**, *110*, 2087.
- [34] B. Liu, E. S. Aydil, *J. Am. Chem. Soc.* **2009**, *131*, 3985.
- [35] E. J. W. Crossland, N. Noel, V. Sivaram, T. Leijtens, J. A. Alexander-Webber, H. J. Snaith, *Nature* **2013**, *495*, 215.
- [36] J. Albero, P. Atienzar, A. Corma, H. Garcia, *Chem. Rec.* **2015**, *15*, 803.
- [37] S. Mathew, A. Yella, P. Gao, R. Humphry-Baker, B. F. Curchod, N. Ashari-Astani, I. Tavernelli, U. Rothlisberger, M. K. Nazeeruddin, M. Grätzel, *Nat Chem* **2014**, *6*, 242.
- [38] D. O. Scanlon, C. W. Dunnill, J. Buckeridge, S. A. Shevlin, A. J. Logsdail, S. M. Woodley, C. R. Catlow, M. J. Powell, R. G. Palgrave, I. P. Parkin, G. W. Watson, T. W. Keal, P. Sherwood, A. Walsh, A. A. Sokol, *Nat. Mater.* **2013**, *12*, 798.
- [39] H. Zhang, Y. Wang, D. Yang, Y. Li, H. Liu, P. Liu, B. J. Wood, H. Zhao, *Adv. Mater.* **2012**, *24*, 1598.

References from Chapter 2

- [1] A. Fujishima, K. Honda, *Nature* **1972**, *238*, 37.
- [2] B. O'Regan, M. Grätzel, *Nature* **1991**, *353*, 737.
- [3] X. Chen, S. S. Mao, *Chem. Rev.* **2007**, *107*, 2891.
- [4] D. O. Scanlon, C. W. Dunnill, J. Buckeridge, S. A. Shevlin, A. J. Logsdail, S. M. Woodley, C. R. Catlow, M. J. Powell, R. G. Palgrave, I. P. Parkin, G. W. Watson, T. W. Keal, P. Sherwood, A. Walsh, A. A. Sokol, *Nat. Mater.* **2013**, *12*, 798.
- [5] M. Dürr, S. Rosselli, A. Yasuda, G. Nelles, *J. Phys. Chem. B* **2006**, *110*, 21899.
- [6] I. Concina, A. Vomiero, *Small* **2015**, *11*, 1744.
- [7] A. K. Chandiran, M. Abdi-Jalebi, M. K. Nazeeruddin, M. Grätzel, *ACS Nano* **2014**, *8*, 2261.
- [8] Ü. Özgür, Y. I. Alivov, C. Liu, A. Teke, M. Reshchikov, S. Doan, V. Avrutin, S.-J. Cho, H. Morkoç, *J. Appl. Phys.* **2005**, *98*, 041301.
- [9] A. Janotti, C. G. Van de Walle, *Rep. Prog. Phys.* **2009**, *72*, 126501.

- [10] M. Liu, C.-Y. Nam, C. T. Black, J. Kamcev, L. Zhang, *J. Phys. Chem. C* **2013**, *117*, 13396.
- [11] W. Zhou, Y. Liu, Y. Yang, P. Wu, *J. Phys. Chem. C* **2014**, *118*, 6448.
- [12] P. Tiwana, P. Docampo, M. B. Johnston, H. J. Snaith, L. M. Herz, *ACS Nano* **2011**, *5*, 5158.
- [13] A. Birkel, Y.-G. Lee, D. Koll, X. V. Meerbeek, S. Frank, M. J. Choi, Y. S. Kang, K. Char, W. Tremel, *Energy Environ. Sci.* **2012**, *5*, 5392.
- [14] N. J. Jeon, J. H. Noh, W. S. Yang, Y. C. Kim, S. Ryu, J. Seo, S. I. Seok, *Nature* **2015**, *517*, 476.
- [15] J. H. Noh, S. H. Im, J. H. Heo, T. N. Mandal, S. I. Seok, *Nano Lett.* **2013**, *13*, 1764.
- [16] G. E. Eperon, S. D. Stranks, C. Menelaou, M. B. Johnston, L. M. Herz, H. J. Snaith, *Energy Environ. Sci.* **2014**, *7*, 982.
- [17] D. Shi, V. Adinolfi, R. Comin, M. Yuan, E. Alarousu, A. Buin, Y. Chen, S. Hoogland, A. Rothenberger, K. Katsiev, Y. Losovyj, X. Zhang, P. Dowben, O. F. Mohammed, E. Sargent, O. M. Bakr, *Science* **2015**, *347*, 519.
- [18] A. Hagfeldt, G. Boschloo, L. Sun, L. Kloo, H. Pettersson, *Chem. Rev.* **2010**, *110*, 6595.
- [19] B. E. Hardin, H. J. Snaith, M. D. McGehee, *Nat. Photonics* **2012**, *6*, 162.
- [20] E. P. Meagher, G. A. Lager, *Can. Mineral.* **1979**, *17*, 77.
- [21] F. Schoßberger, *Z. Kristallogr.* **1942**, *104*.
- [22] L. Pauling, J. H. Sturdivant, *Z. Kristallogr.* **1928**, *68*.
- [23] T. Mitsuhashi, O. J. Kleppa, *J. Am. Ceram. Soc.* **1979**, *62*, 356.
- [24] T. Dittrich, E. A. Lebedev, J. Weidmann, *Phys. Status Solidi A* **1998**, *165*, R5.
- [25] E. Hendry, M. Koeberg, B. O'Regan, M. Bonn, *Nano Lett.* **2006**, *6*, 755.
- [26] Y. Zhao, X. Zhou, L. Ye, S. C. E. Tsang, *Nano Rev.* **2012**, *3*, 1.
- [27] M. Mozetič, U. Cvelbar, M. K. Sunkara, S. Vaddiraju, *Adv. Mater.* **2005**, *17*, 2138.
- [28] M. Wei, Z.-m. Qi, M. Ichihara, H. Zhou, *Acta Mater.* **2008**, *56*, 2488.
- [29] C. Yan, D. Xue, *Adv. Mater.* **2008**, *20*, 1055.
- [30] C. Yan, L. Nikolova, A. Dadvand, C. Harnagea, A. Sarkissian, D. F. Perepichka, D. Xue, F. Rosei, *Adv. Mater.* **2010**, *22*, 1741.
- [31] A. Le Viet, M. V. Reddy, R. Jose, B. V. R. Chowdari, S. Ramakrishna, *J. Phys. Chem. C* **2010**, *114*, 664.
- [32] B. Gao, J. Fu, K. Huo, W. Zhang, Y. Xie, P. K. Chu, *J. Am. Ceram. Soc.* **2011**, *94*, 2330.
- [33] J. Wu, D. Xue, *CrystEngComm* **2011**, *13*, 1966.
- [34] J. He, Y. Hu, Z. Wang, W. Lu, S. Yang, G. Wu, Y. Wang, S. Wang, H. Gu, J. Wang, *J. Mater. Chem. C* **2014**, *2*, 8185.
- [35] F. Idrees, C. Cao, R. Ahmed, F. K. Butt, S. Butt, M. Tahir, M. Tanveer, I. Aslam, Z. Ali, *Sci. Adv. Mater.* **2015**, *7*, 1298.
- [36] H.-Y. Lin, H.-C. Yang, W.-L. Wang, *Catal. Today* **2011**, *174*, 106.
- [37] L. Li, J. Deng, R. Yu, J. Chen, Z. Wang, X. Xing, *J. Mater. Chem. A* **2013**, *1*, 11894.

- [38] H. Zhang, Y. Wang, D. Yang, Y. Li, H. Liu, P. Liu, B. J. Wood, H. Zhao, *Adv. Mater.* **2012**, *24*, 1598.
- [39] R. Ghosh, M. K. Brennaman, T. Uher, M.-R. Ok, E. T. Samulski, L. E. McNeil, T. J. Meyer, R. Lopez, *ACS Appl. Mater. Interfaces* **2011**, *3*, 3929.
- [40] K. Sayama, H. Sugihara, H. Arakawa, *Chem. Mater.* **1998**, *10*, 7.
- [41] H. Luo, W. Song, P. G. Hoertz, K. Hanson, R. Ghosh, S. Rangan, M. K. Brennaman, J. J. Concepcion, R. A. Binstead, R. A. Bartynski, R. Lopez, T. J. Meyer, *Chem. Mater.* **2013**, *25*, 122.
- [42] H. Paritong, I. Wadsworth, L. A. Donohue, W.-D. Münz, *Trans. Inst. Met. Finish.* **1998**, *76*, 4.
- [43] M. Ziolk, *Catal. Today* **2003**, *78*, 47.
- [44] A. G. S. Prado, L. Bolzon, C. P. Pedroso, A. O. Moura, L. L. Costa, *Appl. Catal. B-Environ.* **2008**, *82*, 219.
- [45] G. Agarwal, G. B. Reddy, *J. Mater. Sci.: Mater. in Electronics* **2005**, *16*, 21.
- [46] B. M. Gatehouse, A. D. Wadsley, *Acta Crystallogr.* **1964**, *17*, 1545.
- [47] J. S. Anderson, J. M. Browne, J. L. Hutchison, *J. Solid State Chem.* **1972**, *5*, 419.
- [48] J. S. Anderson, J. M. Browne, A. K. Cheetham, R. V. Dreele, J. L. Hutchison, F. J. Lincoln, D. J. M. Bevan, J. Straehle, *Nature* **1973**, *243*, 81.
- [49] K. Kato, S. Tamura, *Acta Crystallogr. B-Stru.* **1975**, *31*, 673.
- [50] J. Wu, J. Wang, H. Li, D. Xue, *Thin Solid Films* **2013**, *544*, 545.
- [51] F. Izumi, H. Kodama, *Z. Anorg. Allg. Chem.* **1978**, *441*, 8.
- [52] W. Khan, S. B. Betzler, O. Šipr, J. Ciston, P. Blaha, C. Scheu, J. Minar, *submitted* **2016**.
- [53] Q. Yang, Z. Lu, J. Liu, X. Lei, Z. Chang, L. Luo, X. Sun, *Prog. Nat. Sci.* **2013**, *23*, 351.
- [54] L. N. Demianets, A. N. Lobachev, *Krist. Tech.* **1979**, *14*, 16.
- [55] A. Stein, S. W. Keller, T. E. Mallouk, *Science* **1993**, *259*, 7.
- [56] B. Liu, E. S. Aydil, *J. Am. Chem. Soc.* **2009**, *131*, 3985.
- [57] J. S. Beck, J. C. Vartuli, W. J. Roth, M. E. Leonowicz, C. T. Kresge, K. D. Schmitt, C. T.-W. Chu, D. H. Olson, E. W. Sheppard, *J. Am. Chem. Soc.* **1992**, *114*, 10834.
- [58] M.-M. Titirici, M. Antonietti, A. Thomas, *Chem. Mater.* **2006**, *18*, 3808.
- [59] S. B. Betzler, C. Scheu in *Materials Development for Solar Fuels and Energy Conversion in Fuel Cells*, (Eds.: U. Kramm, H.-J. Lewerenz, D. Schmeißer), Springer Science to be printed, **2016**.

References from Chapter 3

- [1] P. J. Goodhew, J. Humphreys, R. Beanland, *Electron Microscopy and Analysis, Third Edition*, Taylor & Francis, **2000**.
- [2] P. Goodhew in *Aberration-Corrected Analytical Transmission Electron Microscopy*, John Wiley & Sons, Ltd, **2011**, pp. 1–19.
- [3] D. B. Williams, C. B. Carter, *Transmission Electron Microscopy: A Textbook for Materials Science*, Springer, **2013**.
- [4] M. Knoll, E. Ruska, *Z. Physik* **1932**, *76*, 21.

- [5] C. Kisielowski, B. Freitag, M. Bischoff, H. van Lin, S. Lazar, G. Knippels, P. Tiemeijer, M. van der Stam, S. von Harrach, M. Stekelenburg, M. Haider, S. Uhlemann, H. Müller, P. Hartel, B. Kabius, D. Miller, I. Petrov, E. A. Olson, T. Donchev, E. A. Kenik, A. R. Lupini, J. Bentley, S. J. Pennycook, I. Anderson, A. M. Minor, A. K. Schmid, T. Duden, V. Radmilovic, Q. M. Ramasse, M. Watanabe, R. Erni, E. A. Stach, P. Denes, U. Dahmen, *Microsc. Microanal.* **Oct. 2008**, *14*, 469.
- [6] W. H. Bragg, W. L. Bragg, *Proc R. Soc. Lond. A* **1913**, *88*, 428.
- [7] CEOS, Phase contrast and information limit, **Oct. 2015**, <http://www.ceos-gmbh.de/English/FAQ/informationlimit.html>.
- [8] G. Dehm, J. M. Howe, J. Zweck, *In-situ Electron Microscopy: Applications in Physics, Chemistry and Materials Science*, John Wiley & Sons, Ltd, **2012**.
- [9] S. H. Oh, Y. Kauffmann, C. Scheu, W. D. Kaplan, M. Rühle, *Science* **2005**, *310*, 661.
- [10] S. H. Oh, M. F. Chisholm, Y. Kauffmann, W. D. Kaplan, W. Luo, M. Rühle, C. Scheu, *Science* **2010**, *330*, 489.
- [11] Z. Zhang, D. Su, *Ultramicroscopy* **2009**, *109*, 766.
- [12] T. E. Everhart, R. F. M. Thornley, *J. Sci. Instrum.* **1960**, *37*, 246.
- [13] R. Egerton, *Electron Energy-Loss Spectroscopy in the Electron Microscope*, Springer, **2011**.
- [14] J. Goldstein, D. E. Newbury, D. C. Joy, C. E. Lyman, P. Echlin, E. Lifshin, L. C. Sawyer, J. R. Michael, *Scanning Electron Microscopy and X-ray Microanalysis: Third Edition*, Springer, **2002**.
- [15] S. B. Betzler, A. Wisnet, B. Breitbach, C. Mitterbauer, J. Weickert, L. Schmidt-Mende, C. Scheu, *J. Mater. Chem. A* **2014**, *2*, 12005.
- [16] T. Malis, S. C. Cheng, R. F. Egerton, *J. Electron. Microsc. Tech.* **1988**, *8*, 193.
- [17] J. Park, S. Heo, J.-G. Chung, H. Kim, H. Lee, K. Kim, G.-S. Park, *Ultramicroscopy* **2009**, *109*, 1183.
- [18] M. Stöger-Pollach, H. Franco, P. Schattschneider, S. Lazar, B. Schaffer, W. Grogger, H. W. Zandbergen, *Micron* **2006**, *37*, 396.
- [19] L. Gu, V. Srot, W. Sigle, C. Koch, P. van Aken, F. Scholz, S. B. Thapa, C. Kirchner, M. Jetter, M. Rühle, *Phys. Rev. B* **2007**, *75*.
- [20] W. Khan, S. B. Betzler, O. Šipr, J. Ciston, P. Blaha, C. Scheu, J. Minar, *submitted* **2016**.
- [21] D. Bach, H. Störmer, R. Schneider, D. Gerthsen, J. Verbeeck, *Microsc. Microanal.* **2006**, *12*, 416.
- [22] D. Bach, R. Schneider, D. Gerthsen, J. Verbeeck, W. Sigle, *Microsc. Microanal.* **2009**, *15*, 505.
- [23] R. D. Leapman, L. A. Grunes, P. L. Fejes, *Phys. Rev. B* **1982**, *26*, 614.
- [24] S. D. Berger, J. M. Macaulay, L. M. Brown, *Philos. Mag. Lett.* **1987**, *56*, 179.
- [25] R. Brydson, H. Sauer, W. Engel, J. M. Thomas, E. Zeitler, N. Kosugi, H. Kuroda, *J. Phys.: Condens. Matter.* **1989**, *1*, 797.
- [26] C. Heiliger, F. Heyroth, F. Syrowatka, H. S. Leipner, I. Maznichenko, K. Kokko, W. Hergert, I. Mertig, *Phys. Rev. B* **2006**, *73*.
- [27] E. Stoyanov, F. Langenhorst, G. Steinle-Neumann, *Am. Mineral.* **2007**, *92*, 577.

- [28] M. Yoshiya, I. Tanaka, K. Kaneko, H. Adachi, *J. Phys.: Condens. Matter* **1999**, *11*, 3217.
- [29] S. B. Betzler, F. Podjaski, K. Bader, M. Beetz, A. Wisnet, M. Handloser, A. Hartschuh, B. V. Lotsch, C. Scheu, *submitted* **2016**.
- [30] G. Cliff, G. W. Lorimer, *J. Microsc.* **1975**, *103*, 203.
- [31] Z. Chen, H. N. Dinh, E. Miller, *Photoelectrochemical Water Splitting Standards, Experimental Methods, and Protocols*, Springer, **2013**.
- [32] B. E. Warren, *X-ray Diffraction*, Dover Publications, **1969**.
- [33] C. S. S. R. Kumar, *UV-VIS and Photoluminescence Spectroscopy for Nanomaterials Characterization*, Springer, **2013**.
- [34] W. Borchardt-Ott, *Kristallographie*, Springer, **2009**.
- [35] P. Scherrer, *NGWG Math.-Phys.* **1918**, *1918*, 98.
- [36] D. Ariosa, F. Elhordoy, E. A. Dalchiele, R. E. Marotti, C. Stari, *J. App. Phys.* **2011**, *110*, 124901.
- [37] H. M. Rietveld, *J. Appl. Crystallogr.* **1969**, *2*, 65.
- [38] J. Tauc, R. Grigorovici, A. Vancu, *Phys. Status Solidi B* **1966**, *15*, 627.
- [39] P. Sharma, I. Sharma, S. C. Katyal, *J. Appl. Phys.* **2009**, *105*, 053509.

References from Chapter 4

- [1] R. Ladj, A. Bitar, M. Eissa, Y. Mugnier, R. Le Dantec, H. Fessi, A. Elaissari, *J. Mater. Chem. B* **2013**, *1*, 1381.
- [2] H.-N. Kim, J. H. Moon, *ACS Appl. Mater. Interfaces* **2012**, *4*, 5821.
- [3] H. Cölfen, M. Antonietti, *Angew. Chem. Int. Ed. Engl.* **2005**, *44*, 5576.
- [4] Q. Gong, X. Qian, X. Ma, Z. Zhu, *Cryst. Growth Des.* **2006**, *6*, 1821.
- [5] R. Q. Song, H. Cölfen, *Adv. Mater.* **2010**, *22*, 1301.
- [6] K. J. M. Bishop, C. E. Wilmer, S. Soh, B. A. Grzybowski, *Small* **2009**, *5*, 1600.
- [7] S. J. Sedlmaier, T. Dennenwaldt, C. Scheu, W. Schnick, *J. Mater. Chem.* **2012**, *22*, 15511.
- [8] A. S. Wochnik, A. Frank, C. Heinzl, J. Häusler, J. Schneider, R. Hoffmann, S. Matich, C. Scheu, *Solid State Sci.* **2013**, *26*, 23.
- [9] L. Zhang, X. Zhao, W. Ma, M. Wu, N. Qian, W. Lu, *CrystEngComm* **2013**, *15*, 1389.
- [10] B. Liu, E. S. Aydil, *J. Am. Chem. Soc.* **2009**, *131*, 3985.
- [11] X. Chen, S. S. Mao, *Chem. Rev.* **2007**, *107*, 2891.
- [12] P. Docampo, S. Guldin, U. Steiner, H. J. Snaith, *J. Phy. Chem. Lett.* **2013**, *4*, 698.
- [13] R. Jose, V. Thavasi, S. Ramakrishna, *J. Am. Ceram. Soc.* **2009**, *92*, 289.
- [14] M. D. Hernández-Alonso, F. Fresno, S. Suárez, J. M. Coronado, *Energy Environ. Sci.* **2009**, *2*, 1231.
- [15] M. Wang, J. Iocozia, L. Sun, C. Lin, Z. Lin, *Energ. Environ. Sci.* **2014**, *7*, 2182.
- [16] J. Wu, J. Wang, H. Li, D. Xue, *Thin Solid Films* **2013**, *544*, 545.
- [17] G. Agarwal, G. B. Reddy, *J. Mater. Sci.: Mater. in Electronics* **2005**, *16*, 21.

- [18] M. Wei, Z.-m. Qi, M. Ichihara, H. Zhou, *Acta Mater.* **2008**, *56*, 2488.
- [19] J. Liu, D. Xue, K. Li, *Nanoscale Res. Lett.* **2011**, *6*, 138.
- [20] C. Yan, L. Nikolova, A. Dadvand, C. Harnagea, A. Sarkissian, D. F. Perepichka, D. Xue, F. Rosei, *Adv. Mater.* **2010**, *22*, 1741.
- [21] D. Xue, F. Liu, *Modern Phys. Lett. B* **2009**, *23*, 3769.
- [22] K. Sayama, H. Sugihara, H. Arakawa, *Chem. Mater.* **1998**, *10*, 7.
- [23] P. Guo, M. A. Aegerter, *Thin Solid Films* **1999**, *351*, 290.
- [24] R. Ghosh, M. K. Brennaman, T. Uher, M.-R. Ok, E. T. Samulski, L. E. McNeil, T. J. Meyer, R. Lopez, *ACS Appl. Mater. Interfaces* **2011**, *3*, 3929.
- [25] H. Zhang, Y. Wang, D. Yang, Y. Li, H. Liu, P. Liu, B. J. Wood, H. Zhao, *Adv. Mater.* **2012**, *24*, 1598.
- [26] T. Maruyama, S. Arai, *Appl. Phys. Lett.* **1993**, *63*, 869.
- [27] N. Özer, D.-G. Chen, C. Lampert, *Thin Solid Films* **1996**, *277*, 162.
- [28] Y. Zhao, X. Zhou, L. Ye, S. C. E. Tsang, *Nano Rev.* **2012**, *3*, 1.
- [29] M. Žumer, V. Nemanič, B. Zajec, M. Remškar, A. Mrzel, D. Mihailovič, *Appl. Phys. Lett.* **2004**, *84*, 3615.
- [30] B. Varghese, S. C. Haur, C.-T. Lim, *J. Phys. Chem. C* **2008**, *112*, 10008.
- [31] D. Rosenfeld, P. E. Schmid, S. Széles, F. Lévy, V. Demarne, A. Grisel, *Sens. Actuators B* **1996**, *37*, 83.
- [32] A. Le Viet, M. V. Reddy, R. Jose, B. V. R. Chowdari, S. Ramakrishna, *J. Phys. Chem. C* **2010**, *114*, 664.
- [33] F. Izumi, H. Kodama, *Z. Anorg. Allg. Chem.* **1978**, *441*, 8.
- [34] D. Bach, R. Schneider, D. Gerthsen, J. Verbeeck, W. Sigle, *Microsc. Microanal.* **2009**, *15*, 505.
- [35] M. Anpo, T. Shima, S. Kodama, Y. Kubokawa, *J. Phys. Chem.* **1987**, *91*, 4305.
- [36] H. Perron, C. Domain, J. Roques, R. Drot, E. Simoni, H. Catalette, *Theor. Chem. Acc.* **2007**, *117*, 565.
- [37] M. Ramamoorthy, D. Vanderbilt, R. D. King-Smith, *Phys. Rev. B* **1994**, *49*, 16721.
- [38] L. Li, J. Deng, R. Yu, J. Chen, Z. Wang, X. Xing, *J. Mater. Chem. A* **2013**, *1*, 11894.
- [39] T. Wang, H. Cölfen, M. Antonietti, *J. Am. Chem. Soc.* **2005**, *127*, 3246.
- [40] H. Zhang, Y. Li, Y. Wang, P. Liu, H. Yang, X. Yao, T. An, B. J. Wood, H. Zhao, *J. Mater. Chem. A* **2013**, *1*, 6563.
- [41] U. G. Akpan, B. H. Hameed, *J. Hazard. Mater.* **2009**, *170*, 520.
- [42] J. Park, S. Heo, J.-G. Chung, H. Kim, H. Lee, K. Kim, G.-S. Park, *Ultramicroscopy* **2009**, *109*, 1183.

References from Chapter 5

- [1] P. A. Midgley, R. E. Dunin-Borkowski, *Nat. Mater.* **2009**, *8*, 271.
- [2] N. Kawase, M. Kato, H. Nishioka, H. Jinnai, *Ultramicroscopy* **2007**, *107*, 8.
- [3] I. Arslan, J. R. Tong, P. A. Midgley, *Ultramicroscopy* **2006**, *106*, 994.
- [4] W. O. Saxton, W. Baumeister, M. Hahn, *Ultramicroscopy* **1984**, *13*, 57.

- [5] J. Frank, *Methods for Three-Dimensional Visualization of Structures in the Cell*, Springer, **2006**.
- [6] K. M. Hanson, *J. Comput. Assist. Tomo.* **1980**, 361.
- [7] M. Radermacher, T. Wagenknecht, A. Verschoor, J. Frank, *J. Microsc.* **1986**, *141*, RP1.
- [8] R. Gordon, R. Bender, G. T. Herman, *J. Theor. Biol.* **1970**, *29*, 471.
- [9] P. Gilbert, *J. Theor. Biol.* **1972**, *36*, 105.
- [10] A. V. Lakshminarayanan, A. Lent, *J. Theor. Biol.* **1979**, *76*, 267.
- [11] S. Bangliang, Z. Yiheng, P. Lihui, Y. Danya, Z. Baofen, *Chem. Eng. J. (Lausanne)* **2000**, *77*, 37.
- [12] K. J. Batenburg, S. Bals, J. Sijbers, C. Kübel, P. A. Midgley, J. C. Hernandez, U. Kaiser, E. R. Encina, E. A. Coronado, G. Van Tendeloo, *Ultramicroscopy* **2009**, *109*, 730.
- [13] A. Zürner, M. Döblinger, V. Cauda, R. Wei, T. Bein, *Ultramicroscopy* **2012**, *115*, 41.
- [14] E. M. Perassi, C. Hrelescu, A. Wisnet, M. Döblinger, C. Scheu, F. Jäckel, E. A. Coronado, J. Feldmann, *ACS Nano* **2014**, *8*, 4395.
- [15] D. Alloeyau, W. Dachraoui, Y. Javed, H. Belkahla, G. Wang, H. Lecoq, S. Ammar, O. Ersen, A. Wisnet, F. Gazeau, C. Ricolleau, *Nano Lett.* **2015**, *15*, 2574.
- [16] P. R. Buseck, R. E. Dunin-Borkowski, B. Devouard, R. B. Frankel, M. R. McCartney, P. A. Midgley, M. Pósfai, M. Weyland, *Proc. Natl. Acad. Sci. U.S.A.* **2001**, *98*, 13490.
- [17] A. Fihri, R. Sougrat, R. B. Rakhi, R. Rahal, D. Cha, M. N. Hedhili, M. Bouhrara, H. N. Alshareef, V. Polshettiwar, *ChemSusChem* **2012**, *5*, 1241.
- [18] M. C. Scott, C. C. Chen, M. Mecklenburg, C. Zhu, R. Xu, P. Ercius, U. Dahmen, B. C. Regan, J. Miao, *Nature* **2012**, *483*, 444.
- [19] B. Goris, S. Bals, W. Van den Broek, E. Carbó-Argibay, S. Gómez-Graña, L. M. Liz-Marzán, G. Van Tendeloo, *Nat. Mater.* **2012**, *11*, 930.
- [20] R. Xu, C. C. Chen, L. Wu, M. C. Scott, W. Theis, C. Ophus, M. Bartels, Y. Yang, H. Ramezani-Dakhel, M. R. Sawaya, H. Heinz, L. D. Marks, P. Ercius, J. Miao, *Nat. Mater.* **2015**, *14*, 1099.
- [21] C. Messaoudil, T. Boudier, C. O. Sanchez Sorzano, S. Marco, *BMC Bioinform.* **2007**, *8*, 288.
- [22] A. Wisnet, PhD thesis, Ludwig-Maximilians-University, **2014**.

References from Chapter 6

- [1] B. Liu, E. S. Aydil, *J. Am. Chem. Soc.* **2009**, *131*, 3985.
- [2] Z. Wang, J. Hou, C. Yang, S. Jiao, K. Huang, H. Zhu, *Phys. Chem. Chem. Phys.* **2013**, *15*, 3249.
- [3] F. Idrees, C. Cao, R. Ahmed, F. K. Butt, S. Butt, M. Tahir, M. Tanveer, I. Aslam, Z. Ali, *Sci. Adv. Mater.* **2015**, *7*, 1298.
- [4] A. Stein, S. W. Keller, T. E. Mallouk, *Science* **1993**, *259*, 7.

- [5] K. H. Tam, C. K. Cheung, Y. H. Leung, A. B. Djurišić, C. C. Ling, C. D. Beling, S. Fung, W. M. Kwok, W. K. Chan, D. L. Phillips, L. Ding, W. K. Ge, *J. Phys. Chem. B* **2006**, *110*, 20865.
- [6] R. Heinhold, H. S. Kim, F. Schmidt, H. von Wenckstern, M. Grundmann, R. J. Mendelsberg, R. J. Reeves, S. M. Durbin, M. W. Allen, *Appl. Phys. Lett.* **2012**, *101*, 062105.
- [7] A. Wisnet, S. B. Betzler, R. V. Zucker, J. Dorman, P. Wagatha, S. Matich, E. Okunishi, L. Schmidt-Mende, C. Scheu, *Cryst. Growth Des.* **2014**, *14*, 4658.
- [8] A. Wisnet, K. Bader, S. B. Betzler, M. Handloser, P. Ehrenreich, T. Pfadler, J. Weickert, A. Hartschuh, L. Schmidt-Mende, C. Scheu, J. A. Dorman, *Adv. Funct. Mater.* **2015**, *25*, 2601.
- [9] Y. Zhao, X. Zhou, L. Ye, S. C. E. Tsang, *Nano Rev.* **2012**, *3*, 1.
- [10] J. S. Anderson, J. M. Browne, J. L. Hutchison, *J. Solid State Chem.* **1972**, *5*, 419.
- [11] R. J. D. Tilley, *Principles and Applications of Chemical Defects*, Taylor & Francis, **1998**.
- [12] J. E. L. Waldron, M. A. Green, D. A. Neumann, *J. Phys. Chem. Solids* **2004**, *65*, 79.
- [13] T. McQueen, Q. Xu, E. N. Andersen, H. W. Zandbergen, R. J. Cava, *J. Solid State Chem.* **2007**, *180*, 2864.
- [14] J. S. Anderson, J. M. Browne, A. K. Cheetham, R. V. Dreele, J. L. Hutchison, F. J. Lincoln, D. J. M. Bevan, J. Straehle, *Nature* **1973**, *243*, 81.
- [15] F. Izumi, H. Kodama, *Z. Anorg. Allg. Chem.* **1978**, *441*, 8.
- [16] H. Zhang, Y. Wang, D. Yang, Y. Li, H. Liu, P. Liu, B. J. Wood, H. Zhao, *Adv. Mater.* **2012**, *24*, 1598.
- [17] J. Wu, J. Wang, H. Li, D. Xue, *Thin Solid Films* **2013**, *544*, 545.
- [18] S. B. Betzler, A. Wisnet, B. Breitbach, C. Mitterbauer, J. Weickert, L. Schmidt-Mende, C. Scheu, *J. Mater. Chem. A* **2014**, *2*, 12005.
- [19] M. Hmadeh, V. Hoepfner, E. Larios, K. Liao, J. Jia, M. Jose-Yacaman, G. A. Ozin, *ChemSusChem* **2014**, *7*, 2104.
- [20] P. Hu, D. Hou, Y. Wen, B. Shan, C. Chen, Y. Huang, X. Hu, *Nanoscale* **2015**, *7*, 1963.

References from Chapter 7

- [1] B. M. Gatehouse, A. D. Wadsley, *Acta Crystallogr.* **1964**, *17*, 1545.
- [2] K. Kato, *Acta Crystallogr. B-Stru.* **1976**, *32*, 764.
- [3] K. Kato, S. Tamura, *Acta Crystallogr. B-Stru.* **1975**, *31*, 673.
- [4] W. Mertin, S. Andersson, R. Gruehn, *J. Solid State Chem.* **1970**, *1*, 419.
- [5] G. Brauer, *Z. anorg. allg. Chem.* **1941**, *248*, 1.
- [6] G. C. Vezzoli, *Phys. Rev. B* **1982**, *26*, 3954.
- [7] O. Yamaguchi, D. Tomihisa, M. Shirai, K. Shimizu, *J. Am. Ceram. Soc.* **1988**, *71*, C-260.
- [8] R. Gruehn, *J. Less-Common Met.* **1966**, *11*, 119.
- [9] T. S. Ercit, *Mineral. Petrol.* **1991**, *43*, 217.

- [10] J. E. L. Waldron, M. A. Green, D. A. Neumann, *J. Phys. Chem. Solids* **2004**, *65*, 79.
- [11] J. B. Goodenough, A. Hamnett, G. Huber, O. Madelung, F. Hullinger, M. Leiß, S. K. Ramasesha, H. Werheit, *Physics of Non-Tetrahedrally Bonded Binary Compounds III / Physik Der Nicht-tetraedrisch Gebundenen Binären Verbindungen III*, Springer, **1984**.
- [12] A. G. S. Prado, L. Bolzon, C. P. Pedroso, A. O. Moura, L. L. Costa, *Appl. Catal. B-Environ.* **2008**, *82*, 219.
- [13] H.-Y. Lin, H.-C. Yang, W.-L. Wang, *Catal. Today* **2011**, *174*, 106.
- [14] Y. Zhao, X. Zhou, L. Ye, S. C. E. Tsang, *Nano Rev.* **2012**, *3*, 1.
- [15] H. Liu, N. Gao, M. Liao, X. Fang, *Scientific reports* **2015**, *5*, 7716.
- [16] F. Idrees, C. Cao, R. Ahmed, F. K. Butt, S. Butt, M. Tahir, M. Tanveer, I. Aslam, Z. Ali, *Sci. Adv. Mater.* **2015**, *7*, 1298.
- [17] H. Cui, G. Zhu, Y. Xie, W. Zhao, C. Yang, T. Lin, H. Gu, F. Huang, *J. Mater. Chem. A* **2015**, *3*, 11830.
- [18] P. Guo, M. A. Aegerter, *Thin Solid Films* **1999**, *351*, 290.
- [19] F. Lenzmann, J. Krueger, S. Burnside, K. Brooks, M. Grätzel, D. Gal, S. Rühle, D. Cahen, *J. Phys. Chem. B* **2001**, *105*, 6347.
- [20] M. Wei, Z.-m. Qi, M. Ichihara, H. Zhou, *Acta Mater.* **2008**, *56*, 2488.
- [21] R. Ghosh, M. K. Brennaman, T. Uher, M.-R. Ok, E. T. Samulski, L. E. McNeil, T. J. Meyer, R. Lopez, *ACS Appl. Mater. Interfaces* **2011**, *3*, 3929.
- [22] F. Izumi, H. Kodama, *Z. Anorg. Allg. Chem.* **1978**, *441*, 8.
- [23] H. Zhang, Y. Wang, D. Yang, Y. Li, H. Liu, P. Liu, B. J. Wood, H. Zhao, *Adv. Mater.* **2012**, *24*, 1598.
- [24] J. Wu, J. Wang, H. Li, D. Xue, *Thin Solid Films* **2013**, *544*, 545.
- [25] S. B. Betzler, A. Wisnet, B. Breitbach, C. Mitterbauer, J. Weickert, L. Schmidt-Mende, C. Scheu, *J. Mater. Chem. A* **2014**, *2*, 12005.
- [26] M. Hmadeh, V. Hoepfner, E. Larios, K. Liao, J. Jia, M. Jose-Yacamán, G. A. Ozin, *ChemSusChem* **2014**, *7*, 2104.
- [27] P. Hu, D. Hou, Y. Wen, B. Shan, C. Chen, Y. Huang, X. Hu, *Nanoscale* **2015**, *7*, 1963.
- [28] H. Zhang, Y. Wang, P. Liu, S. L. Chou, J. Z. Wang, H. Liu, G. Wang, H. Zhao, *ACS Nano* **2016**, *10*, 507.
- [29] P. Kofstad, *J. Phys. Chem. Solids* **1962**, *23*, 1571.
- [30] G. Dehm, J. M. Howe, J. Zweck, *In-situ Electron Microscopy: Applications in Physics, Chemistry and Materials Science*, John Wiley & Sons, Ltd, **2012**.
- [31] M. A. Asoro, D. Kovar, P. J. Ferreira, *ACS Nano* **2013**, *7*, 7844.
- [32] S. H. Oh, Y. Kauffmann, C. Scheu, W. D. Kaplan, M. Rühle, *Science* **2005**, *310*, 661.
- [33] S. H. Oh, M. F. Chisholm, Y. Kauffmann, W. D. Kaplan, W. Luo, M. Rühle, C. Scheu, *Science* **2010**, *330*, 489.
- [34] A. Agrawal, J. Cizeron, V. L. Colvin, *Microsc. Microanal.* **June 1998**, *4*, 269.
- [35] T. Yokota, M. Murayama, J. M. Howe, *Phys. Rev. Lett.* **2003**, *91*, 265504.

- [36] N. J. Long, A. K. Petford-Long, *Ultramicroscopy* **1986**, *20*, 151.
- [37] D. J. Smith, M. R. McCartney, L. A. Bursill, *Ultramicroscopy* **1987**, *23*, 299.
- [38] D. S. Su, M. Wieske, E. Beckmann, A. Blume, G. Mestl, R. Schlögl, *Catal. Lett.* **2001**, *75*, 81.
- [39] J. S. Anderson, J. M. Browne, A. K. Cheetham, R. V. Dreele, J. L. Hutchison, F. J. Lincoln, D. J. M. Bevan, J. Straehle, *Nature* **1973**, *243*, 81.
- [40] U. Balachandran, N. Eror, *J. Mater. Sci.* **1982**, *17*, 1286.
- [41] O. F. Schilling, *J. Phys. Chem. Solids* **1986**, *47*, 595.
- [42] J. S. Anderson, J. M. Browne, J. L. Hutchison, *J. Solid State Chem.* **1972**, *5*, 419.
- [43] A. K. Shukla, P. Ercius, A. R. S. Gautam, J. Cabana, U. Dahmen, *Cryst. Growth Des.* **2014**, *14*, 2453.
- [44] F. Campbell, *Elements of Metallurgy and Engineering Alloys*, ASM International, **2008**.
- [45] D. Hull, D. Bacon in *Introduction to Dislocations (Fourth Edition)*, Butterworth-Heinemann, **2001**.
- [46] J. Wu, C. Jia, K. Urban, J. Hao, X. Xi, *J. Mater. Res.* **2001**, *16*, 3443.
- [47] H. Jin Fan, M. Knez, R. Scholz, K. Nielsch, E. Pippel, D. Hesse, M. Zacharias, U. Gösele, *Nat. Mater.* **2006**, *5*, 627.
- [48] M. T. Buscaglia, V. Buscaglia, M. Viviani, G. Dondero, S. Röhrig, A. Rüdiger, P. Nanni, *Nanotechnology* **2008**, *19*, 225602.
- [49] U. Dahmen, M. G. Kim, A. W. Searcy, *Ultramicroscopy* **1987**, *23*, 365.
- [50] R. J. D. Tilley, *Principles and Applications of Chemical Defects*, Taylor & Francis, **1998**.
- [51] R. Egerton, *Electron Energy-Loss Spectroscopy in the Electron Microscope*, Springer, **2011**.
- [52] D. Bach, H. Störmer, R. Schneider, D. Gerthsen, J. Verbeeck, *Microsc. Microanal.* **2006**, *12*, 416.
- [53] D. Bach, R. Schneider, D. Gerthsen, J. Verbeeck, W. Sigle, *Microsc. Microanal.* **2009**, *15*, 505.
- [54] Z. Zhang, D. Su, *Ultramicroscopy* **2009**, *109*, 766.

References from Chapter 8

- [1] A. Kudo, Y. Miseki, *Chem. Soc. Rev.* **2009**, *38*, 253.
- [2] X. Chen, S. S. Mao, *Chem. Rev.* **2007**, *107*, 2891.
- [3] Z. Weng, H. Guo, X. Liu, S. Wu, K. W. K. Yeung, P. K. Chu, *RSC Adv.* **2013**, *3*, 24758.
- [4] A. Fujishima, K. Honda, *Nature* **1972**, *238*, 37.
- [5] M. Ni, M. K. H. Leung, D. Y. C. Leung, K. Sumathy, *Renew. Sust. Energ. Rev.* **2007**, *11*, 401.
- [6] M. Wang, J. Ioccozia, L. Sun, C. Lin, Z. Lin, *Energ. Environ. Sci.* **2014**, *7*, 2182.
- [7] B. O'Regan, M. Grätzel, *Nature* **1991**, *353*, 737.
- [8] H. J. Snaith, L. Schmidt-Mende, *Adv. Mater.* **2007**, *19*, 3187.

- [9] A. Hagfeldt, G. Boschloo, L. Sun, L. Kloo, H. Pettersson, *Chem. Rev.* **2010**, *110*, 6595.
- [10] F. Sauvage, F. Di Fonzo, A. Li Bassi, C. S. Casari, V. Russo, G. Divitini, C. Ducati, C. E. Bottani, P. Comte, M. Grätzel, *Nano Lett.* **2010**, *10*, 2562.
- [11] F. E. Osterloh, *Chem. Mater.* **2008**, *20*, 35.
- [12] M. D. Hernández-Alonso, F. Fresno, S. Suárez, J. M. Coronado, *Energy Environ. Sci.* **2009**, *2*, 1231.
- [13] L. Yang, H. Zhou, T. Fan, D. Zhang, *Phys. Chem. Chem. Phys.* **2014**, *16*, 6810.
- [14] R. Jose, V. Thavasi, S. Ramakrishna, *J. Am. Ceram. Soc.* **2009**, *92*, 289.
- [15] H.-Y. Lin, H.-C. Yang, W.-L. Wang, *Catal. Today* **2011**, *174*, 106.
- [16] B. Gao, J. Fu, K. Huo, W. Zhang, Y. Xie, P. K. Chu, *J. Am. Ceram. Soc.* **2011**, *94*, 2330.
- [17] H. Zhang, Y. Wang, D. Yang, Y. Li, H. Liu, P. Liu, B. J. Wood, H. Zhao, *Adv. Mater.* **2012**, *24*, 1598.
- [18] Y. Zhao, X. Zhou, L. Ye, S. C. E. Tsang, *Nano Rev.* **2012**, *3*, 1.
- [19] L. Li, J. Deng, R. Yu, J. Chen, Z. Wang, X. Xing, *J. Mater. Chem. A* **2013**, *1*, 11894.
- [20] H. Luo, W. Song, P. G. Hoertz, K. Hanson, R. Ghosh, S. Rangan, M. K. Brennaman, J. J. Concepcion, R. A. Binstead, R. A. Bartynski, R. Lopez, T. J. Meyer, *Chem. Mater.* **2013**, *25*, 122.
- [21] S. B. Betzler, A. Wisnet, B. Breitbach, C. Mitterbauer, J. Weickert, L. Schmidt-Mende, C. Scheu, *J. Mater. Chem. A* **2014**, *2*, 12005.
- [22] M. Hmadeh, V. Hoepfner, E. Larios, K. Liao, J. Jia, M. Jose-Yacaman, G. A. Ozin, *ChemSusChem* **2014**, *7*, 2104.
- [23] J. Wu, J. Wang, H. Li, D. Xue, *Thin Solid Films* **2013**, *544*, 545.
- [24] G. Agarwal, G. B. Reddy, *J. Mater. Sci.: Mater. in Electronics* **2005**, *16*, 21.
- [25] A. Wisnet, K. Bader, S. B. Betzler, M. Handloser, P. Ehrenreich, T. Pfadler, J. Weickert, A. Hartschuh, L. Schmidt-Mende, C. Scheu, J. A. Dorman, *Adv. Funct. Mater.* **2015**, *25*, 2601.
- [26] F. Izumi, H. Kodama, *Z. Anorg. Allg. Chem.* **1978**, *441*, 8.
- [27] F. Zhang, S.-W. Chan, J. E. Spanier, E. Apak, Q. Jin, R. D. Robinson, I. P. Herman, *Appl. Phys. Lett.* **2002**, *80*, 127.
- [28] R. D. Shannon, *Acta Crystallogr. A* **1976**, *32*, 751.
- [29] D. Bach, R. Schneider, D. Gerthsen, J. Verbeeck, W. Sigle, *Microsc. Microanal.* **2009**, *15*, 505.
- [30] R. Brydson, H. Sauer, W. Engel, J. M. Thomas, E. Zeitler, N. Kosugi, H. Kuroda, *J. Phys.: Condens. Matter.* **1989**, *1*, 797.
- [31] E. Stoyanov, F. Langenhorst, G. Steinle-Neumann, *Am. Mineral.* **2007**, *92*, 577.
- [32] P. Hu, D. Hou, Y. Wen, B. Shan, C. Chen, Y. Huang, X. Hu, *Nanoscale* **2015**, *7*, 1963.
- [33] T. Gokus, A. Hartschuh, H. Harutyunyan, M. Allegrini, F. Hennrich, M. Kappes, A. A. Green, M. C. Hersam, P. T. Araújo, A. Jorio, *Appl. Phys. Lett.* **2008**, *92*, 153116.

-
- [34] H. Zhou, H. Alves, D. M. Hofmann, W. Kriegseis, B. K. Meyer, G. Kaczmarczyk, A. Hoffmann, *Appl. Phys. Lett.* **2002**, *80*, 210.
- [35] G. Xiong, U. Pal, J. G. Serrano, *J. Appl. Phys.* **2007**, *101*, 024317.

Curriculum Vitae – Sophia Betzler

Education

2007	CARL-ORFF-GYMNASIUM (Unterschleißheim) General qualification for university entrance
10/07 – 12/10	LUDWIG-MAXIMILIANS-UNIVERSITY (LMU) MUNICH Bachelor degree Chemistry and Biochemistry (B.Sc.)
Bachelor thesis	<i>EGF Rezeptor Targeting therapeutischer Nanopartikel</i>
12/10 – 12/12	LMU MUNICH Master degree Chemistry (M.Sc.)
Master thesis	<i>Synthesis and characterization of TiO₂ and Nb_xO_y nanostructures</i>
02/13 – 12/15	LMU MUNICH, CENTER FOR NANOSCIENCE (CeNS) & NANOSYSTEMS INITIATIVE MUNICH (NIM) PhD study in the group of Prof. Scheu
10/14 – 04/15	NATIONAL CENTER FOR ELECTRON MICROSCOPY (NCEM) at the Lawrence Berkeley National Laboratory, (California, USA)

Awards and Honors

2012	3RD PLACE IMAGE CONTEST of the Royal Microscopical Society
2013	BEST POSTER AWARD NIM Summer Retreat
2013	BEST POSTER AWARD Microscopy Conference 2013
2013	AWARD OF THE DR. KLAUS RÖMER FOUNDATION for outstanding performance in master studies
2014	TRAVEL AWARD of CeNS for the European Materials Research Society (EMRS) Spring meeting 2014
2014	1ST PLACE BEST POSTER AWARD EMRS Spring meeting 2014, Session Z: Materials development for solar fuel production and energy conversion.
2014	NIM TRAVEL AWARD for the research stay at NCEM, USA
2015	TRAVEL AWARD of the Deutsche Gesellschaft für Elektronenmikroskopie for the Microscopy Conference 2015

List of Publication

1. A. Ranft, S.B. Betzler, F. Haase, B. V. Lotsch, *Additive-mediated size control of MOF nanoparticles*, Cryst. Eng. Commun. (2013), **15**, 9296-9300.
2. R. Hoffmann, A. Wochnik, C. Heinzl, S.B. Betzler, S. Matich, E. Griesshaber, H. Schulz, M. Kučera, J.R. Young, C. Scheu, W.W. Schmahl, *Nanoprobe crystallographic orientation studies of isolated shield elements of the coccolithophore species *Emiliana huxleyi**, Eur. J. Mineral. (2014), **26**, 473-483.
3. R. Hoffmann, A.S. Wochnik, S.B. Betzler, S. Matich, E. Griesshaber, W.W. Schmahl, C. Scheu, *TEM preparation methods and influence of radiation damage on the beam sensitive CaCO_3 shell of *Emiliana huxleyi**, Micron (2014), **62**, 28-36.
4. S.B. Betzler, A. Wisnet, B. Breitbach, C. Mitterbauer, J. Weickert, L. Schmidt-Mende, C. Scheu, *Template-free synthesis of novel, highly-ordered 3D hierarchical $\text{Nb}_3\text{O}_7(\text{OH})$ superstructures with semiconductive and photoactive properties*, J. Mater. Chem. A. (2014) **2**, 12005-12013.
5. A. Wisnet, S.B. Betzler, R. Zucker, J. Dorman, P. Wagatha, S. Matich, L. Schmidt-Mende, C. Scheu, *A model for hydrothermal growth of rutile wires and its correlated development of defect structures*, Cryst. Growth. Des. (2014) **14**, 4658-4663.
6. A. Wisnet, K. Bader, S.B. Betzler, M. Handloser, J. Weickert, A. Hartschuh, L. Schmidt-Mende, C. Scheu, J. A. Dorman, *Understanding Defects in Quasi-Single Crystal Electrode Materials – A Study on TiO_2 Nanowires*, Adv. Funct. Mater. (2015) **25**, 2601-2608.
7. S.B. Betzler, F. Podjaski, K. Bader, M. Beetz, A. Wisnet, M. Handloser, A. Hartschuh, B. V. Lotsch, C. Scheu, *Tuning the morphology of 3D hierarchical $\text{Nb}_3\text{O}_7(\text{OH})$ superstructures with titanium for enhanced light-induced water splitting*, submitted.
8. S.B. Betzler, C. Scheu, in *Materials Development for Solar Fuels and Energy Conversion in Fuel Cells*, Springer Science, to be printed **2016**.
9. S.B. Betzler, T. Harzer, J. Ciston, U. Dahmen, G. Dehm, C. Scheu, *Heat induced phase-transformation of 3D $\text{Nb}_3\text{O}_7(\text{OH})$ superstructures – the effect of atmosphere and the electron beam*, Cryst. Growth Des. (2016) DOI:10.1021/acs.cgd.6b00386.

10. W. Khan, S.B. Betzler, O. Šipr, J. Ciston, P. Blaha, C. Scheu, J. Minar, *Theoretical and experimental study of the optoelectronic properties of Nb₃O₇(OH) and Nb₂O₅ for photochemistry*, submitted.

List of Oral Presentation

- 06/2013 MECHANICS MEETS ENERGY (Düsseldorf, Germany)
S.B. Betzler, A. Folger, *More than just beautiful, metal oxides at the nanoscale.*
- 01/2014 MECHANICS MEETS ENERGY II (Winterberg, Germany)
S.B. Betzler, *Beautiful 3D hierarchical niobium oxide superstructures.*
- 10/2014 NCEM (Berkeley, California)
S.B. Betzler, A. Wisnet, C. Scheu, *Electron microscopic investigation of highly-ordered 3D Nb₃O₇(OH) superstructures for photochemical applications.*
- 06/2015 SCANDEM (Jyväskylä, Finland)
S.B. Betzler, T. Harzer, A. Wisnet, J. Ciston, U. Dahmen, C. Scheu, *Transmission electron microscopy study of 3D hierarchical Nb₃O₇(OH) superstructures for water splitting application.*
- 09/2015 MICROSCOPY CONFERENCE (Göttingen, Germany)
S.B. Betzler, T. Harzer, J. Ciston, A. Wisnet, U. Dahmen, G. Dehm, C. Scheu, *Transmission electron microscopy study of novel 3D hierarchical Nb₃O₇(OH) superstructures, performing in-situ heating experiments and tomography reconstruction.*

List of Poster Presentation

- 03/2007 SCHÜLERKONFERENZ (TU Munich, Germany)
S. Betzler, *Joghurtherstellung – Verfolgung der Säureentwicklung.*
- 09/2012 NANOSCIENCES: SOFT, SOLID, ALIVE AND KICKING (Venice, Italy)
S. Betzler, A. Wisnet, J. Reindl, A. Müller, J. Weickert, L. Schmidt-Mende, C. Scheu, *Growth and analysis of rutile nanowires for applications in hybrid solar cells.*
- 03/2013 NIM WINTERSCHOOL (Kirchberg, Austria)
S.B. Betzler, A. Wisnet, A. Müller, J. Weickert, L. Schmidt-Mende, C. Scheu, *Analysis and modification of TiO₂ rutile nanowires for application in hybrid solar cells.*
- 07/2013 NANOSYSTEMS FOR SOLAR CONVERSION (Munich, Germany)
S. Betzler, A. Folger, A. Wisnet, J. Weickert, J. Reindl, L. Schmidt-Mende, C. Scheu, *Titanium dioxide nanostructures for application in hybrid solar cells.*
- 08/2013 MICROSCOPY CONFERENCE 2013 (Regensburg, Germany)
S.B. Betzler, A. Folger, A. Wisnet, V. Falkowski, J. Weickert, L. Schmidt-Mende, C. Scheu, *Electron microscopic investigation of TiO₂ rutile nanowires for application in hybrid solar cells.*
- 10/2013 WORKSHOP: ADVANCES IN SEMICONDUCTOR NANOWIRE-BASED PHOTONICS (Munich, Germany)
S.B. Betzler, A.M. Folger, A. Wisnet, L. Schmidt-Mende, C. Scheu, *Investigation of rutile TiO₂/Nb_xO_y core-shell nanowires for application in hybrid solar cells.*
- 05/2014 EMRS SPRING MEETING (Lille, France)
S.B. Betzler, A. Wisnet, C. Scheu,
Investigation of novel 3D hierarchical niobiumoxide superstructures.
- 07/2015 IAM NANO (Hamburg, Germany)
S.B. Betzler, J. Ciston, A. Wisnet, U. Dahmen, C. Scheu, *Investigation of the heat-induced phase-transformation of 3D hierarchical Nb₃O₇(OH) superstructures to Nb₂O₅ via ex-situ and in-situ electron microscopy.*

Acknowledgments

Time to say thank you...



Liebe Tina, vielen Dank für diese tolle Zeit. Ich hatte unglaublich viel Spaß während meiner Doktorarbeit, hab sehr viel gelernt und gesehen und hatte das mit Abstand hübscheste Thema. Du hast mich immer unterstützt und es ermöglicht dass ich mir den Traum von einem Leben in den USA erfüllen konnte. Danke danke danke!

Lieber Achim, vielen Dank dass du das Zweitgutachten dieser Arbeit übernimmst. Aber vor allem, vielen vielen Dank dass du mich als Gast in deinem Arbeitskreis aufgenommen hast.

Obwohl auf zwei Städte aufgeteilt hatte ich eine wunderschöne Zeit im AK Scheu. Begonnen hat alles bei der lieben Ramona. Liebe Ramona, vielen Dank für die schöne Zeit und die moralische Unterstützung! Weiter gings zum Andi, ohne den es diese Arbeit in dieser Form nicht geben würde. Lieber Andi ich habe super viel von dir gelernt, von deinem Wissen gezehrt und neuen Nerd-Kram kennengelernt. Danke dass du dein Knowhow immer so großzügig mit mir geteilt hast. Ich wünsch dir alles erdenklich Gute für deine Zukunft in der großen weiten Welt. Die Zweigstelle Süd war dann die nächste Station, lieber Christoph und liebe Katha, obwohl wir schlagartig geschrumpft waren war man nie alleine. Ich wünsche euch beiden alles gute und hoffe dass wir uns noch oft über den Weg laufen, z.B. in der Boulderhalle. Liebe Anna, vielen Dank für alles, für die Bespaßung per Skype, die Nächte auf deiner blauen Couch, deine Geduld und Fürsorge.

Zusammen mit der Teresa hast du viel dazu beigetragen dass ich mittlerweile durchaus überlebensfähig bin. Liebe Angi vielen Dank für deine Geduld mit der ihr mich in die Tücken des Lebens eingeweiht habt. Vielen Dank für die vielen schönen Momente auch an Alena, Stephan und Stefan. Ich bin immernoch davon überzeugt dass der AK Scheu der netteste AK der Chemie war!

Lieber Michi, nicht viele Menschen können von sich sagen einen eigenen EDVler zu haben und einen Experten für so ziemlich alle Fragestellungen. Ich hoffe dass wir noch oft zusammen arbeiten und bin unglaublich stolz darauf was aus meinem niemals wirklich kleinen Bacheloranten/Goldfisch geworden ist. Im Herzen folgen hierauf noch 50 Seiten, aus Platzgründen muss ich leider darauf verzichten.

I had a great time in Berkeley and learned so many new things. Dear Jim, Uli, Colin, Karin, Song, Peter, Marissa, Mary and Matt thank you all a lot for making my stay so unforgettable and sharing all your knowledge with me. I hope that I will meet you all again someday.

Lieber AK Hartschuh, danke für das Asyl. Ich habe mich bei euch immer sehr gut aufgehoben gefühlt. Ein besonders großes Dankeschön geht an Matze, Kathi, Irene, Harald und Julia die mich bei meinem Endspurt tatkräftig unterstützt haben. Vielen vielen Dank!

Außerdem möchte ich mich auch bei den lieben Konstanzern bedanken von denen ich viel über Solarzellen gelernt habe.

Natürlich haben zu dieser Arbeit noch viele weitere fleißige Heinzelmännchen beigetragen. Leider kann ich hier nicht jeden namentlich erwähnen, mein Dank ist euch alle jedoch sicher.

Last but not least. Ein großer Dank geht an das Team Betzler das mir während meines gesamten Studiums zur Seite stand. Außerdem hab ich die besten und treuesten Freunde der Welt, liebe Gagas und alle anderen danke dass ihr immer zur Stelle seid wenn es brennt. Und ohne meinen Fels der immer da ist zum anlehnen wenn man ihn braucht wäre ich wohl auch nicht so weit gekommen. Danke Matthias.